



City Research Online

City, University of London Institutional Repository

Citation: Rane, S. (2015). Grid Generation and CFD Analysis of Variable Geometry Screw Machines. (Unpublished Doctoral thesis, City University London)

This is the accepted version of the paper.

This version of the publication may differ from the final published version.

Permanent repository link: <https://openaccess.city.ac.uk/id/eprint/15129/>

Link to published version:

Copyright: City Research Online aims to make research outputs of City, University of London available to a wider audience. Copyright and Moral Rights remain with the author(s) and/or copyright holders. URLs from City Research Online may be freely distributed and linked to.

Reuse: Copies of full items can be used for personal research or study, educational, or not-for-profit purposes without prior permission or charge. Provided that the authors, title and full bibliographic details are credited, a hyperlink and/or URL is given for the original metadata page and the content is not changed in any way.



**CITY UNIVERSITY
LONDON**

Grid Generation and CFD Analysis of Variable Geometry Screw Machines

By

Sham Ramchandra Rane

Thesis submitted for the degree of Doctor of Philosophy
in Mechanical Engineering

City University London
School of Mathematics, Computer Science and Engineering

August 2015

"Having considerable confidence in the method I was using in deducing the equations of motion from the fundamental assumption; it naturally occurred to me to re-examine the fundamental assumptions, to see if these had been introduced into the theory in their fullness. It was then I observed that the theory, both as applied by Maxwell, and myself, neglected any possible dimensions of a molecule, and it became clear that by neglecting this we had neglected that which made it possible for the boundary to produce an acceleration on the fluid."

— Professor Osborne Reynolds

On the equations of motion and the boundary conditions for viscous fluids

(Read before Section A at the " British Association", 1883)

Table of Contents

List of Figures	v
List of Tables.....	x
Acknowledgement.....	xi
Declaration	xii
Abstract	xiv
Nomenclature	xv
Chapter 1 – Introduction.....	1
1.1 Introduction	1
1.2 Twin Screw Compressor	2
1.3 Single Screw Compressor	4
1.4 Variable Geometry Screw Machines.....	6
1.4.1 Variable pitch twin screw compressor	7
1.4.2 Variable profile parallel axis twin screw compressor	10
1.4.3 Tri-rotor screw compressors	11
1.4.4 Single screw compressor variants	11
1.4.5 Spiral compressor and expander	12
1.4.6 Internal Conical Rotary Screw Compressor.....	13
1.5 Computational methods for fluid flow calculations	13
1.6 Grid generation approaches in practise	15
1.7 Motivation to investigate grid generation in numerical methods.....	17
Chapter 2 – Literature Review	19
2.1 Numerical analysis of Screw machines using lumped parameter models	20
2.2 CFD analysis of Screw Compressors and Expanders	23
2.3 Summary	26
Chapter 3 – Research Aims and Contribution to Knowledge.....	27
3.1 Aims of research.....	27
3.2 Methodology	27
3.3 Contribution to knowledge.....	28
Chapter 4 Grid Deformation Schemes for Screw Machines.....	30

4.1	Introduction	30
4.2	Governing equations for deforming domains.....	30
4.3	Solution of governing equations	34
4.3.1	Diffusion equation based mesh smoothing	35
4.3.2	User defined nodal displacement	35
4.3.3	Key-Frame grid re-meshing	36
4.4	Investigation of Key-frame grid remeshing technique.....	37
4.5	Algebraic approach for grid generation of twin screw machines.....	43
4.6	Differential approach for grid generation of twin screw machines.....	45
4.7	Comparison of the two approaches	47
4.8	Summary	49
Chapter 5	– Grid Generation for Variable Geometry Screw Machines	50
5.1	Introduction	50
5.2	Development of the algebraic approach to improve cross section grid	52
5.2.1	Distribution from outer boundary to inner boundary	53
5.2.2	Coordinate transformation of the full rotor region.....	55
5.2.3	Regularisation by skewed sine function.....	58
5.2.4	Example of grids with conformal interface.....	63
5.2.5	Regularisation by background block distribution	65
5.2.6	Example of grids with interlobe refinement	72
5.2.7	Example of grid with one to one connected interface	73
5.2.8	Comparison of grid quality parameters.....	74
5.3	Grid generation for variable pitch and variable profile screw rotors	79
5.3.1	Integration of 2D grid sections into a 3D mesh	79
5.3.2	Grid generation for variable lead rotors	84
5.3.3	Grid generation for variable profile rotors	87
5.3.4	Examples of grids with variable pitch and uniform profile	90
5.3.5	Examples of grid with uniform pitch and variable profile	91
5.3.6	Example of grid for internal conical rotary compressor	93
5.4	Development of inflation layer grid	94
5.4.1	Calculation of the node spacing	95
5.5	Summary	97
Chapter 6	- Case Studies and Discussion	98

6.1	Introduction	98
6.2	Analysis of a 3/5 synchronised Dry Air Compressor.....	100
6.2.1	Case description.....	100
6.2.2	Pressure based coupled solver	101
6.2.3	Pressure based segregated solver	103
6.2.4	Experimental measurement.....	104
6.2.5	Results and discussion	107
6.2.6	Inference from comparison of solvers	112
6.2.7	Influence of interlobe grid refinement on performance prediction	113
6.2.8	Influence of inflation layer on the performance prediction.....	118
6.3	Analysis of a 3/5 synchronised Dry Air Expander.....	124
6.3.1	Case description.....	125
6.3.2	Simulation.....	126
6.3.3	Results and Discussion	128
6.3.4	Evaluation of overall performance characteristics	134
6.3.5	Influence of inflation layer grid on performance	136
6.3.6	Inference	140
6.4	Analysis of Variable Geometry Dry Air Screw Compressor.....	142
6.4.1	Case description.....	143
6.4.2	Simulation.....	147
6.4.3	Results and Discussion	147
6.4.4	Inference	156
6.5	Closure	157
Chapter 7	– Conclusions and Recommendation for Future Work.....	158
7.1	Summary of the research.....	158
7.2	Conclusions	159
7.3	Recommendations for future work.....	161
References	163	
Appendices.....	177	
Appendix A.	Screw compressor performance parameters	178
Appendix B.	Fundamentals of Grid Generation Approaches	181

B.1	Algebraic grid generation.....	181
B.2	Coordinate transformation.....	181
B.3	Lagrange basis polynomial interpolation	183
B.4	Hermite interpolation polynomial	184
B.5	Differential grid generation.....	187
B.6	Variational grid generation.....	192
Appendix C. Characteristic domain decomposition.....		194
C.1	Analytical rack	196
C.2	Numerical rack	197
C.3	Differential division line	199
Appendix D. Algebraic approach for Grid Generation of Twin Screw Rotors		201
D.1	Coordinate transformation of interlobe rotor space	201
D.2	Rotor boundary adaptation.....	202
D.3	Outer boundary regularisation.....	205
D.4	Interior nodes distribution	209
D.5	Grid orthogonalisation.....	212
D.6	Grid smoothing.....	213
Appendix E. Differential approach for Grid Generation of Twin Screw Rotors		215
E.1	Solution of the Laplace equation.....	215

List of Figures

Figure 1.1 Classification of common industrial compressors.....	2
Figure 1.2 Oil injected twin screw compressor and its working chamber.....	2
Figure 1.3 Operating stages in a twin screw compressor.....	3
Figure 1.4 Typical pressure and volume variation in a twin screw compressor.....	4
Figure 1.5 Geometry and basic components of a single-screw compressor	5
Figure 1.6 Single screw compressor rotors.....	5
Figure 1.7 Operating stages in a single screw compressor	6
Figure 1.8 Concept of variable geometry screw machines	7
Figure 1.9 Meshing of uniform pitch twin screw rotors	8
Figure 1.10 Meshing of variable pitch twin screw rotors	8
Figure 1.11 Comparison of displacement curve	8
Figure 1.12 Comparison of compression curve	8
Figure 1.13 Cylinder and port development of a rotor pair	9
Figure 1.14 Meshing of variable profile parallel axis twin screw rotors	10
Figure 1.15 Tri rotor screw compressor.....	11
Figure 1.16 Single screw compressor configuration variants	12
Figure 1.17 Spiral compressor and expander configuration	12
Figure 1.18 Internal twin screw compressor configuration	13
Figure 1.19 Basic grid generation techniques.....	16
Figure 1.20 Non-conformal interface between the two rotors	18
Figure 1.21 Merged nodes at the CUSP point to capture blow-hole	18
Figure 2.1 Conical rotors with SRM 4/6 profile.....	23
Figure 3.1 Research methodology	28
Figure 4.1 Flow chart of solution process with deforming domains	34
Figure 4.2 Grid deformation using Diffusion equation mesh smoothing	35
Figure 4.3 Grid deformation using User defined nodal displacement	36
Figure 4.4 Grid deformation using Key-Frame grid re-meshing	36
Figure 4.5 Hexahedral mesh using Diffusion smoothing (SH1).....	38
Figure 4.6 Tetrahedral mesh used in Key-frame re-meshing (KR1)	39
Figure 4.7 Piston displacement plot.....	39
Figure 4.8 Cyclic pressure history	40
Figure 4.9 Cyclic temperature history	40

Figure 4.10 Error in pressure predictions of adiabatic cycles.....	41
Figure 4.11 Error in temperature predictions of adiabatic cycles	42
Figure 4.12 Simplified block diagram – Algebraic rotor grid generation	44
Figure 4.13 Simplified block diagram – Differential rotor grid generation	46
Figure 5.1 Grid generation developments for twin screw rotors	51
Figure 5.2 Non-conformal interface between the two rotors	52
Figure 5.3 Merged nodes at the CUSP point to capture blow-hole	53
Figure 5.4 Distribution of nodes on the outer boundary	55
Figure 5.5 Point distribution on inner boundary and outer circle	56
Figure 5.6 Forward transformation of full rotor region to computational domain	57
Figure 5.7 Reverse transformation of full rotor region to physical domain	58
Figure 5.8 Use of skewed sine function to regularise distribution	60
Figure 5.9 Effect of skewness of skewed sine function on distribution	60
Figure 5.10 Effect of amplitude of skewed sine function on distribution	61
Figure 5.11 Regularised distribution obtained with skewed sine function.....	62
Figure 5.12 Reverse transformation of the regularised distribution	62
Figure 5.13 Conformal grids generated with sine function in a Roots blower rotor	63
Figure 5.14 Conformal grid generated with sine function in a Screw Compressor rotor.....	64
Figure 5.15 Notch defects on the rotor surface in 3D grids	65
Figure 5.16 Background blocking for the main and gate rotors	67
Figure 5.17 Using blocks to get rotor profile distribution	68
Figure 5.18 Refinement in the rack segment and superimposition of rack curve.....	69
Figure 5.19 Grid generated with background blocking in screw compressor rotor.....	70
Figure 5.20 Surface mesh on the rotor, casing and the rack interface	71
Figure 5.21 Examples of grids with interlobe refinement	73
Figure 5.22 Example of grids with one to one connected interface.....	74
Figure 5.23 Comparison of Grid A and Grid B - % cells vs Quality factor	75
Figure 5.24 Comparison of cells with Equi-angle Skew factor < 0.15	76
Figure 5.25 Comparison of regions with aspect ratio > 200.....	77
Figure 5.26 Comparison of cells with Determinant < 0.1.....	77
Figure 5.27 Comparison of cells with MaxWarp factor > 50	78
Figure 5.28 Grid generation for rotors with uniform lead	80
Figure 5.29 Grid assemblies in 3D from data of 2D sections	81

Figure 5.30 Axial spacing difference between uniform pitch and variable pitch grids	82
Figure 5.31 SCORG structure for variable pitch and variable profile rotors.....	83
Figure 5.32 Section angular rotation with axial distance for different Pitch Functions	84
Figure 5.33 Variable pitch and variable profile grid generation.....	88
Figure 5.34 Grid assembly in 3D for variable pitch and variable profile rotors.....	89
Figure 5.35 Examples of variable pitch grid with uniform profile on 5/6 ‘N’ rotors	90
Figure 5.36 Example of variable geometry rotor grid with uniform pitch	91
Figure 5.37 Grid sections of variable geometry rotor, 3/5 ‘Rotor generated N’ profile	92
Figure 5.38 Grid of the working chamber for conical internal screw rotors	93
Figure 5.39 Construction of inflation layer adjacent to rotor surface	94
Figure 5.40 Inflation layer subroutine with the main grid generation	95
Figure 5.41 Example inflation layer with 8 divisions and growth rate 1.2.....	96
Figure 6.1 Screw compressor – a) The machine and b) Extracted flow model	101
Figure 6.2 Overview of the pressure based solver	101
Figure 6.3 Tetrahedral mesh in Solver-1	103
Figure 6.4 Body-fitted binary tree mesh in Solver-2	103
Figure 6.5 Experimental setup for performance measurement.....	105
Figure 6.6 Location of interlobe pressure transducers on the compressor	105
Figure 6.7 Pressure-Angle diagram a) 6000 rpm, b) 8000 rpm	107
Figure 6.8 Comparison of mass flow rate and indicated power	108
Figure 6.9 Comparison of full range mass flow rate and indicated power	108
Figure 6.10 Comparison of specific power and volumetric efficiency.....	109
Figure 6.11 Comparison of full range specific power and volumetric efficiency	110
Figure 6.12 Comparison of velocity and density in leakage gaps	111
Figure 6.13 CFD Model Domain and Grid refinements in the interlobe clearance.....	114
Figure 6.14 Pressure contours on the rotor surface with Base grid and Grid – 4	115
Figure 6.15 Pressure variation in the chamber with at 6000 and 8000rpm	115
Figure 6.16 Comparison of Indicated power and Flow rate	116
Figure 6.17 Comparison of Volumetric efficiency and Indicated Specific power	117
Figure 6.18 Example of Inflation layer grid on the two rotors	119
Figure 6.19 Comparison of velocity profile close to discharge port.....	120
Figure 6.20 Comparison of gas velocity adjacent to Male Rotor	120
Figure 6.21 Comparison of y^+ based on first grid point coordinate from the Male Rotor....	121

Figure 6.22 Comparison of Wall Shear proximate to the Male Rotor.....	122
Figure 6.23 Pressure Angle diagram with Inflation layer grid	123
Figure 6.24 Numerical grid of the GL-51.2 screw expander rotors.....	124
Figure 6.25 Flow domains for analysis of the twin screw expander	125
Figure 6.26 Variation of pressure in a twin screw expander	128
Figure 6.27 Influence of clearance variation on P-Angle at 4000rpm.....	130
Figure 6.28 Influence of clearance variation on P-Angle at 10000rpm.....	130
Figure 6.29 Influence of the location of high pressure boundary on P-Angle.....	131
Figure 6.30 Influence of high pressure boundary condition on P-Angle.....	132
Figure 6.31 Influence of laminar and turbulence model on P-Angle	133
Figure 6.32 Mass flow rate Vs CFD case variants.....	134
Figure 6.33 Indicated power Vs CFD case variants	134
Figure 6.34 Power vs. Speed at different filling pressures	135
Figure 6.35 Mass flow rate vs. Speed at different filling pressures.....	135
Figure 6.36 Cross section grid of the expander with inflation layer on the rotors	136
Figure 6.37 Comparison of velocity profile close to high pressure port	137
Figure 6.38 Comparison of gas velocity adjacent to Male Rotor	138
Figure 6.39 Comparison of Pressure Angle diagram with Inflation layer grid	139
Figure 6.40 Comparison of power and mass flow rate with inflation layer grid	140
Figure 6.41 Twin screw compressor and its working chamber	142
Figure 6.42 CFD model – flow domain of the twin screw compressor.....	143
Figure 6.43 Meshing of Uniform Pitch Twin Screw Rotors.....	143
Figure 6.44 Meshing of Variable Pitch Twin Screw Rotors.....	143
Figure 6.45 Reduced discharge port area in <i>Case 2</i> compared with <i>Case 1</i>	144
Figure 6.46 Variable pitch grid – 3/5 ‘N’ rotors	144
Figure 6.47 Variable profile grid – 3/5 ‘N’ rotors	145
Figure 6.48 Three levels of grid refinements shown for one section.....	146
Figure 6.49 Pressure variation on variable pitch rotor with discharge at 2.0bar.	148
Figure 6.50 Indicator diagram for cases calculated on fine grid with discharge at 2.0 bar ..	148
Figure 6.51 Indicator diagram for cases calculated on fine grid with turbulence models.	149
Figure 6.52 Effect of grid refinement on integral parameters	150
Figure 6.53 Effect of grid refinement on pressure diagram.....	150
Figure 6.54 Influence of turbulence models on performance parameters	151

Figure 6.55 Comparison of interlobe sealing line lengths	152
Figure 6.56 Comparison of Blow-hole area.....	153
Figure 6.57 Comparison of performance parameters	155
Figure B.1 Mapping of a curved physical region onto a rectangle.....	182
Figure B.2 Mapping of a unit square onto a curved four sided region	185
Figure B.3 Mapping of a unit square by projector $\mathbf{P}\eta$	186
Figure B.4 TFI mapping of a unit square by composite projector $\mathbf{P}\xi \oplus \mathbf{P}\eta$	187
Figure B.5 Differential construction of a 2D curvilinear grid	188
Figure B.6 Specification of first mesh interval and angle in Sorenson's method.....	191
Figure C.1 Characteristic decomposition of a screw compressor.....	195
Figure C.2 Main rotor, Gate rotor and Rack curves in meshing condition.....	197
Figure C.3 Analytical rack as a splitting curve for O blocks.....	197
Figure C.4 Rack cut from rotor profile using DDS	199
Figure C.5 Differential equipotential as a splitting curve for O blocks.....	200
Figure D.1 Coordinate transformation from rotor region to computational region	201
Figure D.2 Coordinate transformation from interlobe region to computational region	202
Figure D.3 Sinus adaptation function on the gate rotor profile	205
Figure D.4 Point distribution on inner boundary and outer circle	206
Figure D.5 Transformation of interlobe region to computational domain.....	207
Figure D.6 Regularised distribution on the outer boundary	209
Figure D.7 Explicit orthogonalisation of grid lines	212
Figure D.8 Orthogonalisation of the gate rotor mesh	213
Figure D.9 Influence of iterative smoothing on grid lines.....	214
Figure E.1 Solution to Laplace equation with fixed boundary conditions	215
Figure E.2 Transition of division line	217
Figure E.3 Basic grid generated by the differential approach	218
Figure E.4 Radial spacing with geometric redistribution	219

List of Tables

Table 4.1 Conservative form of the governing equations of the flow of a compressible Newtonian fluid	31
Table 4.2 Error in Pressure, Temperature and Gas Mass	41
Table 4.3 Comparison of algebraic and differential approach for screw rotor grids	47
Table 6.1 Solver-1 modelling parameters (used by ANSYS CFX)	102
Table 6.2 Solver-2 modelling parameters (used by PumpLinx)	104
Table 6.3 Test rig instrumentation details.....	106
Table 6.4 Grid levels and number of divisions.....	113
Table 6.5 Grid size comparison with inflation layers	118
Table 6.6 Rotor tangential velocity at root diameter	119
Table 6.7 Comparison of results with inflation layer grid	123
Table 6.8 Cases evaluated for the analysis in <i>Stage I</i>	127
Table 6.9 Experimental test results for Expander GL 51.2.....	128
Table 6.10 CFD model performance prediction of GL 51.2.....	134
Table 6.11 Rotor grid size comparison with inflation	136
Table 6.12 Rotor tangential velocity at root diameter	138
Table 6.13 Comparison of results with inflation layer grid	139
Table 6.14 Grid refinement as number of computational nodes.....	147
Table 6.15 Comparison of Interlobe Sealing Line Length	152
Table 6.16 Comparison of Blow-hole area	154
Table 6.17 Comparison of variable geometry rotor efficiencies	154
Table D.1 Rotor profile adaptation functions	205

Acknowledgement

Presented thesis is a result of research carried out at the Centre for Positive Displacement Compressor Technology of City University London between 2011 and 2015. I am very thankful to the University for granting me financial assistance and allowing me to use the computational resources for this investigation.

Professor Ahmed Kovačević has been an inspiration and his work on the subject of grid generation and CFD in screw machines forms the basis of the presented study. I am grateful to him that he encouraged and supported my research with perseverance and generosity.

Professor Nikola Stošić has been a remarkable teacher. His explanations of the physical processes inside screw machines helped in interpretation of results and I am very thankful to him for his enthusiasm and support.

Professor Ian Smith has helped me from time to time to shape the thesis in its meaningful form with corrections in English and scientific terminologies. I am grateful for his support and kindness.

Design and experimental data for expander performance was provided by TU Dortmund and I am thankful to Professor Andreas Brümmer for his help.

I am highly indebted to my wife, my mother and my father who supported me and gave me all the help that could have been possible during this period. My elder brother and my twin sister encouraged my ideas cheerfully. My father through his manufacturing firm Maya Engineering Works; generously funded my studies. Without my family's love I would not have the same courage.

I also thank all my colleagues and friends for their help and advices. Dr Ashvin Dhunput, Ms Madhulika Kethidi, Ms Ekaterina Chukanova, Dr Matthew Read, Mr Mohammed Arjeneh and laboratory technicians Mr Mike Smith, Mr Jim Ford are a few of them to mention.

Sham Ramchandra Rane

City University London, 2015

Declaration

COVERED WORK

I, Sham Ramchandra Rane, 2 Loring Road, London TW76QA , “the Depositor”, would like to deposit “**Grid Generation and CFD Analysis of Variable Geometry Screw Machines**”, here after referred to as the “Work”, in the City University Institutional Repository and agree to the following:

NON-EXCLUSIVE RIGHTS

Rights granted to the City University Institutional Repository through this agreement are entirely non-exclusive and royalty free. I am free to publish the Work in its present version or future versions elsewhere. I agree that the City University Institutional Repository administrators or any third party with whom the City University Institutional Repository has an agreement to do so may, without changing content, translate the Work to any medium or format for the purpose of future preservation and accessibility.

DEPOSIT IN THE CITY UNIVERSITY INSTITUTIONAL REPOSITORY

I understand that work deposited in the City University Institutional Repository will be accessible to a wide variety of people and institutions - including automated agents - via the World Wide Web. I also agree to an electronic copy of my thesis being included in the British Library Electronic Theses On-line System (EThOS).

I understand that once the Work is deposited, a citation to the Work will always remain visible. Removal of the Work can be made after discussion with the City University Institutional Repository, who shall make best efforts to ensure removal of the Work from any third party with whom the City University Institutional Repository has an agreement.

I AGREE AS FOLLOWS:

- That I am the author or co-author of the work and have the authority on behalf of the author or authors to make this agreement and to hereby give the City University Institutional Repository administrators the right to make available the Work in the way described above.
- That I have exercised reasonable care to ensure that the Work is original, and does not to the best of my knowledge break any UK law or infringe any third party's copyright or other Intellectual Property Right. Where I have included third party copyright material, I have fully acknowledged its source.
- The administrators of the City University Institutional Repository do not hold any obligation to take legal action on behalf of the Depositor, or other rights holders, in the event of breach of intellectual property rights, or any other right, in the material deposited.

Sham Ramchandra Rane

London, 2015

Abstract

This thesis describes the development of grid generation and numerical methods for predicting the flow in variable geometry, positive displacement screw machines.

It has been shown, from a review of available literature, that the two main approaches available to generate deforming grids for the CFD analysis of 3D transient flow in screw machines are algebraic and differential. Grids that maintain the cell count and connectivity, during solution, provide the highest accuracy and customised grid generation tools have the capability to accommodate large mesh deformations. For the analysis of screw rotors with a variable lead or varying profile, these techniques are suitable but are required to be developed further with new procedures that can define the three dimensional variation of geometry of the rotors onto the computational grid.

An algebraic grid generation method was used for deforming grid generation of variable lead and varying profile rotors. Functions were developed for correlating a specified lead variation along the rotor axis with the grid spacing. These can be used to build a continuously variable lead with linear, quadratic or higher order functions. For variable profile rotors, a novel approach has been developed for three dimensional grid structuring. This can be used to specify a continuously variable rotor profile, a variable lead, and both internal and external rotor engagement, thus making it possible to generate rotor domains with conical and variable lead geometries. New grid distribution techniques were developed to distribute boundary points on the rotors from the fixed points on the rack and the casing. These can refine the grid in the region of interlobe leakage gaps between the rotors, produce a one to one connected interface between them and improve the cell quality. Inflation layers were applied and tested for mesh refinement near the rotor boundaries. Case studies have been presented to validate the proposed grid generation techniques and the results have been compared with experimental data. Simulated results agreed well with measured data and highlighted the conditions where deviations are highest. Results with variable geometry rotors showed that they achieve steeper internal pressure rise and a larger discharge port area could be used. With variable lead rotors the volumetric efficiency could be improved by reducing the sealing line length in the high pressure zone. Calculations with inflation layers showed that local velocities were better predicted but there was no substantial influence on the integral performance parameters.

Nomenclature

a, b, c	- transformation parameters	$q_{\emptyset s}$	- flux source in general transport equation
$\mathbf{a}_l, \mathbf{b}_l$	- boundary points	$q_{\emptyset v}$	- volume source in general transport equation
A_{sk}	- amplitude of sine function	\mathbf{r}	- radius vector
b_i	- constant	$\mathbf{rb}(x, y)$	- Blocking node position vector
\mathbf{B}_i	- Blocking index	r, θ	- polar coordinates of a point
c_i	- concentration of species	rpm	- rotor speed
c_1-c_4	- tension spline coefficients	Re	- Reynolds number
C_1, C_2	- coefficients of orthogonalisation procedure	S	- cell surface
C_p	- specific heat at constant pressure	s	- transformed coordinate
C, σ	- constants in $k \varepsilon$ turbulence model	S_{ci}	- source term of species
D	- outer diameter	\mathbf{S}	- viscous part of stress tensor
div	- divergence operator	t	- time
$f^i(s)$	- adaptation variable	T	- temperature
$F^i(s)$	- integrated adaptation variable	\mathbf{T}	- stress tensor
$f(t)$	- skewed sine function	T_{gate}	- gate rotor torque
$f(\xi, \eta)$	- stretching functions	T_{main}	- main rotor torque
$grad$	- gradient operator	\mathbf{u}	- displacement vector
gr	- Growth rate of inflation	n_{layers}	- Number of layers in inflation
h_1-h_4	- blending functions of Hermite interpolation	u_i	- Cartesian component of velocity vector
h	- enthalpy	\mathbf{v}	- fluid velocity
i	- internal energy	\mathbf{v}_b	- surface velocity
j_a	- number of angular divisions of φ	V	- cell Volume
k	- turbulent kinetic energy	V_i	- built in volume index
k_p	- point count	V_s	- suction closure volume

K	- number of points	V_d	- discharge open volume
L	- rotor length	\dot{V}	- volumetric flow rate
m	- mass	w	- weight factor
\dot{m}	- mass flow rate	W	- weight function
n	- rotor speed	W_{ind}	- indicated work
n_{sk}	- frequency of sine function	x, y, t	- rotor profile parameters
\mathbf{n}	- cell face normal vector	X_ξ	- grid spacing
p	- pressure	x, y, z	- Cartesian coordinates
p_i	- local lead	X, Y, Z	- points on physical boundaries
p_s	- starting lead	x_p, y_p	- coordinates of calculation point P
p_e	- ending lead	y_p', y_p''	- first and second derivatives in vicinity of the point P
p_{st}	- starting pitch	z_1	- Number of lobes on main rotor
p_{en}	- ending pitch	z_2	- Number of lobes on gate rotor
$p(x)$	- polynomial	Δt	- time step
P_{ind}	- indicated power	Δz	- increment in rotor axial direction
$\mathbf{P}_\xi, \mathbf{P}_\eta$	- projector functions	$\mathbf{P}_\xi \oplus \mathbf{P}_\eta$	- composite mapping

Greek symbols

α, β	- tension spline coefficients	ρ	- density
α_1, β_1	- blending functions	σ	- tension spline parameter
α_i	- male rotor rotation angle	ϕ_w	- wrap angle
$\Delta\alpha$	- step of male rotor rotation angle	ϕ	- intrinsic transport property
γ	- adiabatic index	φ	- interlobe angle of male rotor
$\delta_{k,l}$	- Kronecker delta function	ξ, η	- computational coordinate
δ	- displacement	Ω	- control volume
ε	- dissipation of turbulent kinetic energy	Γ	- diffusion coefficient in general transport equation
μ	- viscosity	σ_{sk}	- skewness of sine function
π	- pi	ω	- angular velocity

η_v	- volumetric efficiency	ζ_i	- distance of control point
η_{ad}	- adiabatic efficiency	$\hat{\eta}_{i,j}$	- arc lengths
η_{iso}	- isothermal efficiency		

Subscripts

1	- main rotor	iso	- isothermal
2	- gate rotor	max	- maximum
0,1	- suction conditions	min	- minimum
2	- discharge conditions	s	- grid values
ad	- adiabatic	$sind$	- specific indicated
eff	- effective	t	- theoretical
ind	- indicated		

Superscripts

n	- time step or iteration level
-----	--------------------------------

Abbreviations

- ALE – Arbitrary Lagrangian-Eulerian
 CFD – Computational Fluid Dynamics
 SCORPATH – Screw Compressor Rotor Profiling and Thermodynamics
 SCORG – Screw Compressor Rotor Grid Generator
 PDE – Partial Differential Equation
 TFI – Transfinite Interpolation
 GGI – Generalised Grid Interface
 RANS – Reynolds Averaged Navier-Stokes

Chapter 1 – Introduction

1.1 Introduction

Rotary Twin Screw Compressors have been in industrial usage for a long time and were first proposed in 1878 by Heinrich Krigar in Germany (*Stošić et al.*, 2005a). They are widely used in the oil and gas, process gas extraction, refrigeration and industrial air industries. For a long period, their development, as compressors or expanders, was limited by their low efficiency and high manufacturing cost. The asymmetric rotor profile, developed in 1973 (*Stošić et al.*, 2005a), greatly reduced leakage through the blow-hole and, at about the same time, the introduction of CNC machine tools made it possible to produce helical rotors with complex profiles. Single screw compressors of the Zimmern type are another type of rotary positive displacement machine which originated around 1962 (*Zimmern*, 1984). Today screw machines are regarded as highly reliable and compact systems for energy conversion. Continuing demands for reduced energy losses and higher gas pressure differences in compact machines have led to the use of modern analytical tools to predict the flow characteristics and performance of non-conventional types of screw machine, such as those with rotors of variable geometry.

The remainder of this chapter contains a basic introduction to various types of screw compressors, their mode of operation, and some computational methods that can be used for their performance prediction.

Figure 1.1 shows a classification of commonly used industrial compressors. This is based on the principle by which the working gas is pressurised and as seen, screw compressors fall in the category of positive displacement machines. The meaning of positive displacement is that the gas is compressed by reduction of its volume. This is achieved by simply reducing the volume of a chamber containing the gas. This chamber is called the working chamber of a compressor. For a piston-cylinder configuration the working chamber is just a cylinder but for a screw compressor the working chamber volume is more complex and is formed by two or more meshing lobed rotors enclosed in a casing. There are two main types of screw compressor in industrial operation, namely; the twin screw and the single screw.

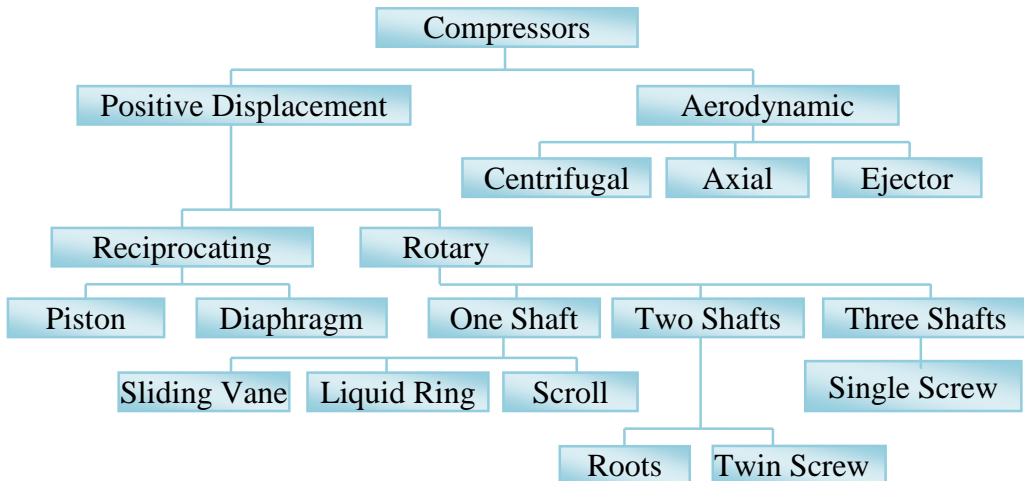


Figure 1.1 Classification of common industrial compressors

Screw compressors are further classified as Oil free and Oil injected based on the presence or absence of oil in the working chamber. The operating principle of both types is the same but in the oil free compressor the gas is compressed without any contact with the lubricant, whereas in the oil injected compressor the lubricant is injected into the gas during compression and removed downstream. Oil free compressors require additional timing gears on the rotor shafts to maintain contact free operation whereas in oil injected compressors the male rotor usually drives the female rotor directly.

1.2 Twin Screw Compressor

Figure 1.2 shows an example of an oil injected twin screw compressor. The main elements of the machine and working chamber have been highlighted.

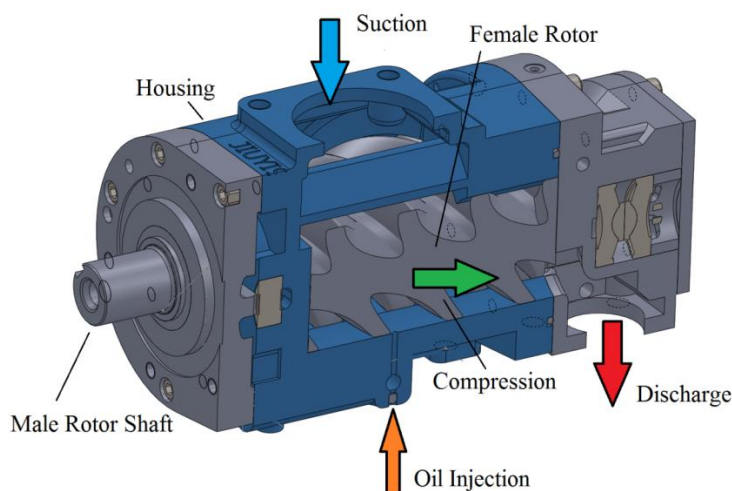


Figure 1.2 Oil injected twin screw compressor and its working chamber

There are six leakage paths identified in this type of machine (*Fleming et. al.*, 1994, 1998, *Hanjalić and Stošić*, 1997) the rotor interlobe leakage, rotor leading edge tip leakage, trailing edge tip leakage, the high pressure side and low pressure side axial end leakage and the high pressure side blow-hole leakage.

Operating Principle

The working principle of these machines with the rotors in the form of helical lobed screws is simple. The male rotor engages with the female rotor forming a closed interlobe space with the housing. The working chamber of the compressor between the rotors and the casing is shown in Figure 1.3-1.

Figure 1.4 shows the volume and pressure variation in the working chamber in one compression cycle. The numbers on the diagram indicate the state of gas in the process. When the lobes disengage at one end, suction is created. As the volume between the lobes continuously increases it draws in the working fluid – Figure 1.4 – 2. Further rotation of the rotor traps this volume between the rotors and the casing. Because of the helical twist on the lobes, the rotation of the rotor causes an axial displacement of fluid – Figure 1.4 – 4.

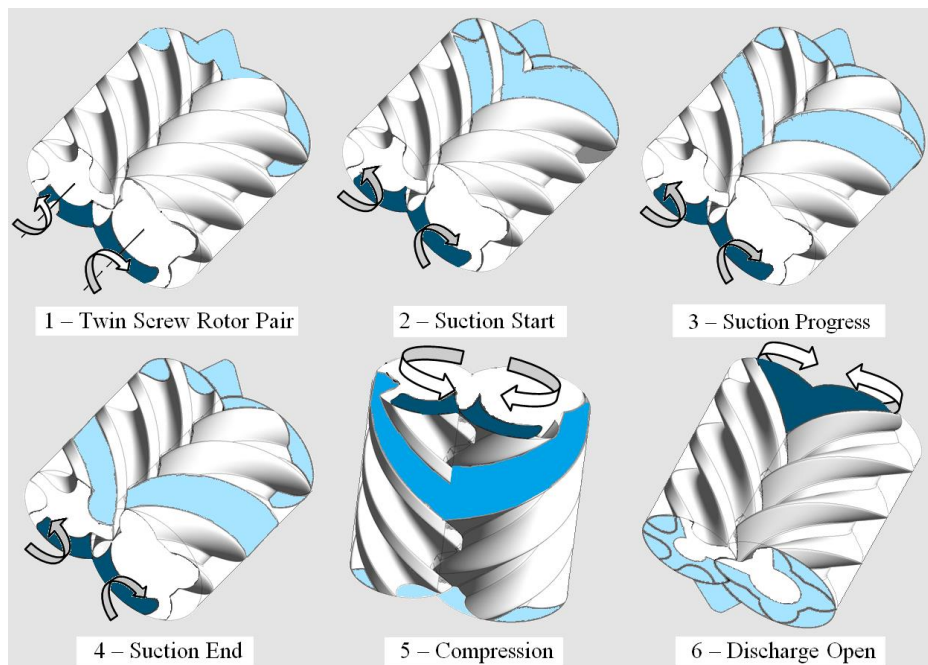


Figure 1.3 Operating stages in a twin screw compressor

The volume of the gas trapped is denoted as V_s . This is the end on suction process. The opening area of the port is cut to match with the helix on the rotor lobes and hence at a fixed angle of the rotor rotation the suction port is cut-off from the rotor volume. After closing of the exposure to suction port, the gate rotor lobe starts to overlap onto the main rotor lobes on the underside

and thereby the trapped volume starts reducing when the lobes mesh – Figure 1.4 – 5. This increases the pressure. Further rotation exposes the pressurised fluid to the outlet port and the fluid is delivered – Figure 1.4 – 6. The minimum volume of the gas before it is exposed to the discharge port is denoted as V_d . The ratio $V_i = \frac{V_s}{V_d}$ is the built in volume index of the machine.

Depending on the gas being compressed, V_i determines the maximum pressure internally developed in the compressor.

The compression process takes place between positions 4 and 6, when the pressure rises. Leakage is in the reverse direction to that of the main flow. If the direction of rotation is reversed the path from 6 – 4 is an expansion process and the pressure drops between 6 – 4. In that case, the leakage is in the direction of the main flow.

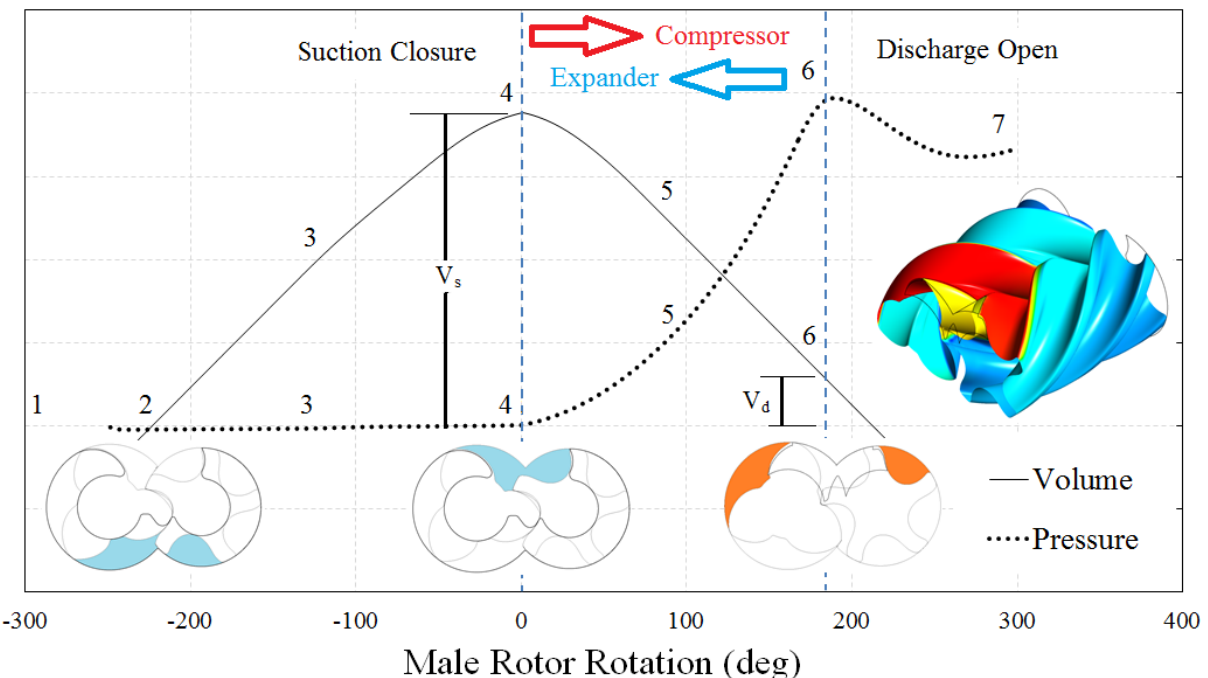


Figure 1.4 Typical pressure and volume variation in a twin screw compressor

1.3 Single Screw Compressor

Single Screw Compressors are another type of rotary positive displacement machine, originating from around 1962. Figure 1.5 shows the basic components of a typical Single Screw compressor (*Wei-feng Wu and Quan-ke Feng, 2008*). As the name suggests a single screw rotor is externally driven in the form of a cylinder with helical grooves (Globoid). Two or more gate rotors act as idlers driven by the main rotor. The gate rotors are in the form of stars whose teeth

envelope the flutes of the main rotor, during operation. The axis of the star rotors in this configuration is perpendicular to the main screw axis.

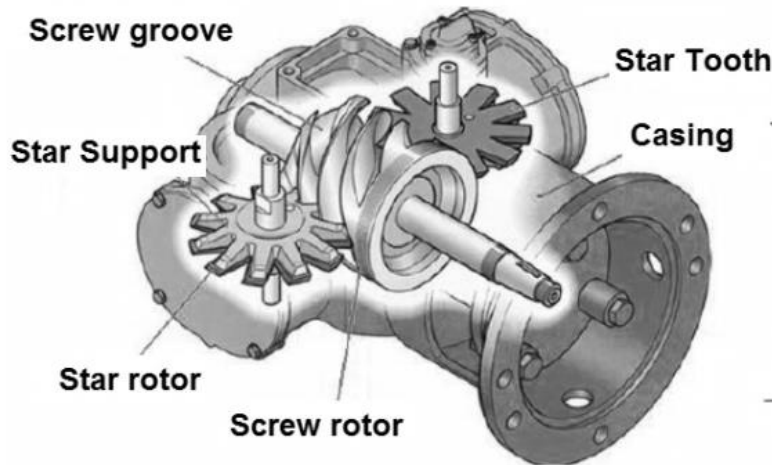


Figure 1.5 Geometry and basic components of a single-screw compressor

The advantage of this arrangement is that the radial forces on the main rotor are balanced (Zimmern, 1984, Zimmern and Patel, 1972). The end faces of the main rotor are exposed to the suction pressure which reduces the axial force exerted on the main rotor. Pressure force is exerted on the star teeth due to the pressure difference between the top and bottom of the star rotors.

Operating Principle

Figure 1.6 shows the meshing of single screw compressor rotors, viewed from the top. Figure 1.7 – 1 shows the meshing from side. A working chamber is formed each time a screw flute starts to engage with a star tooth. This happens simultaneously on both star rotors. The compressor consists of three stages namely suction, compression and discharge.

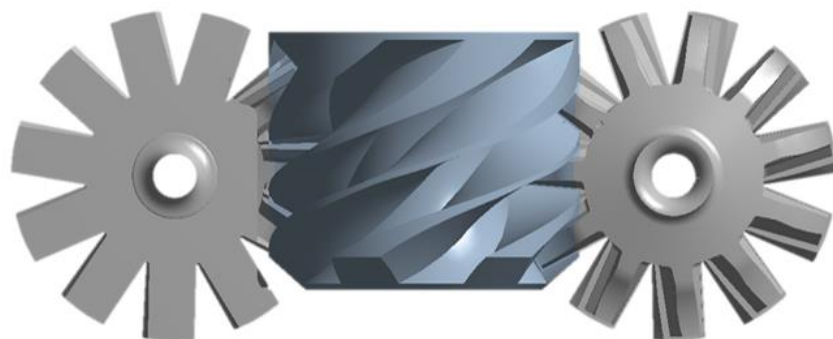


Figure 1.6 Single screw compressor rotors

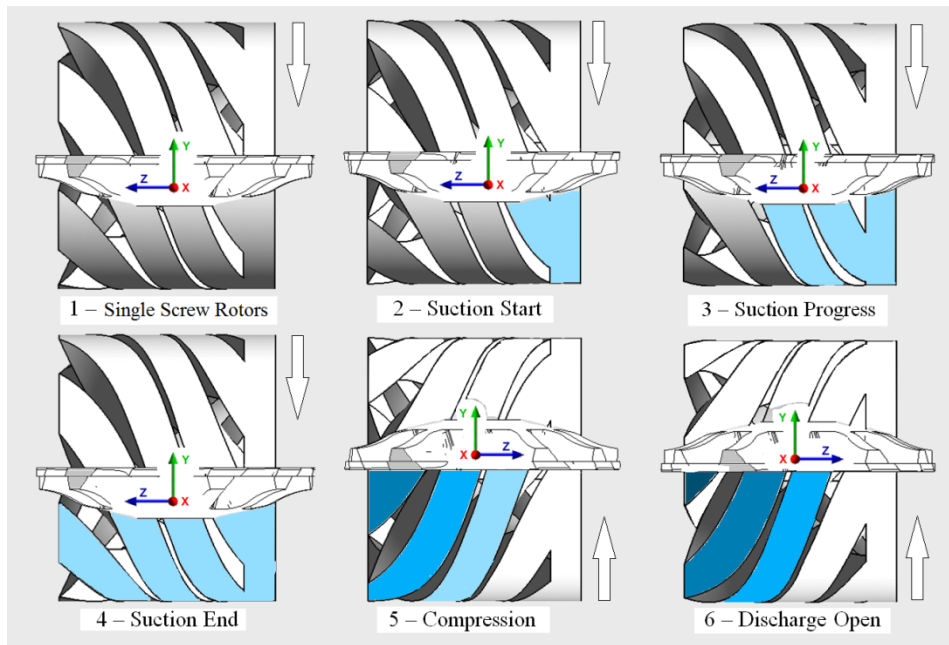


Figure 1.7 Operating stages in a single screw compressor

Figure 1.7 also shows the operating principle of the compressor. Gas enters the flute-casing enclosed volume from the suction side simultaneously at the top-left and the bottom-right – Figure 1.7 – 2. As rotation progresses, this flute engages with a Star tooth and slowly the volume gets trapped between the Screw flute, housing and the Star Tooth (In both upper – not shown and lower halves) – Figure 1.7 – 4. Further rotation starts the compression process – Figure 1.7 – 5. As the trapped volume is reduced, it becomes exposed to the small triangular discharge port and high pressure gas is delivered – Figure 1.7 – 6. This compression process takes place in each of the flutes of the main rotor. There are nine leakages paths identified in this type of geometry (*Thomas and Hamilton, 1982, Boblitt and Moore, 1984, Wei-feng Wu, Quan-ke Feng, 2008*). Capacity control is provided by a variable-return port controlled by a sliding vane that regulates the position where compression begins.

1.4 Variable Geometry Screw Machines

The twin screw and single screw compressors, described above, are the most widely used types of industrial compressor. Apart from these basic designs there are some variants described in literature and under research. These non-conventional screw machines are based on the same operating principles but there are differences in the geometry, the number of rotors or the rotor mutual orientations. Theoretically, some improvements in performance and design benefits can

be obtained by these non-conventional machines over those already described. Figure 1.8 presents possible arrangements of variable geometry screw machines.

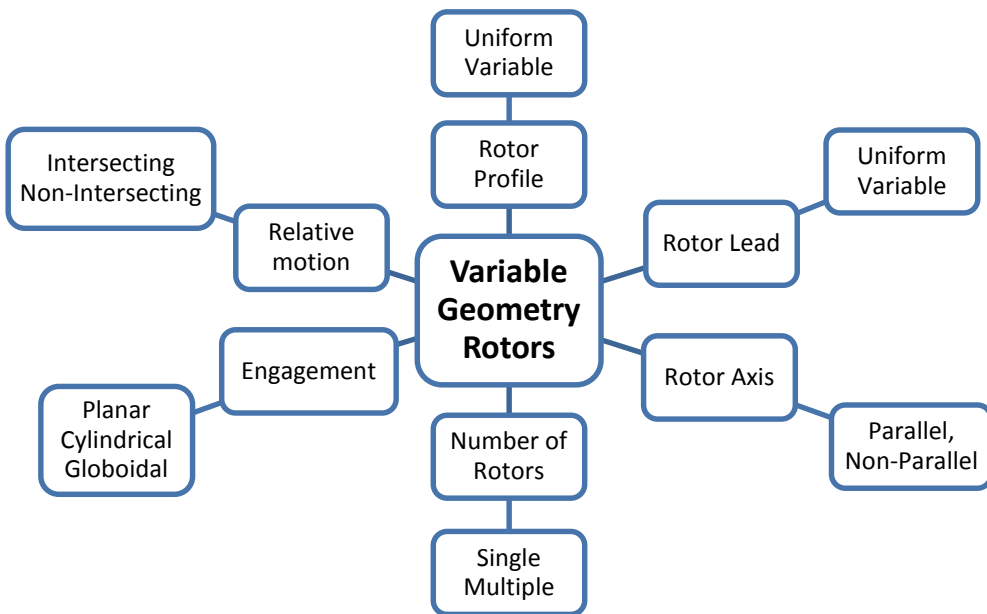


Figure 1.8 Concept of variable geometry screw machines

1.4.1 Variable pitch twin screw compressor

Screw compressor rotors with a variable lead are still at the research stage, but a patent on this concept dates back to 1969 (*Gardner, 1969*). This describes a helical screw compressor with a continuously variable lead for the lobes of the male and gate rotors. A method of assembly of such rotors is also proposed by fusion of a stack of metal plates using a template to get the desired variable lead. Figure 1.9 shows the meshing of twin screw rotors with constant helical pitch, whereas Figure 1.10 shows the meshing of twin screw rotors with the same dimensions but with a variable helical pitch. It has been shown in the literature that for the same rotor lengths, diameter, wrap angles and lobe profiles the variable pitch rotors can be designed to provide higher pressure ratios and larger discharge port opening areas, thus reducing the exit throttling losses (*Gardner, 1969*).

The screw compressor efficiency depends upon the profile of the rotors, the combination of the number of lobes on the male and gate rotors, the length and diameter, the wrap angle and the clearances (*Fleming and Tang, 1994, 1998, Hanjalić and Stošić, 1997*). The difficulty in obtaining high efficiencies at higher compression ratios is related to the discharge throttling due to the small discharge port areas and to the increased leakage losses that occur in the high pressure zones near the discharge end of the rotor.

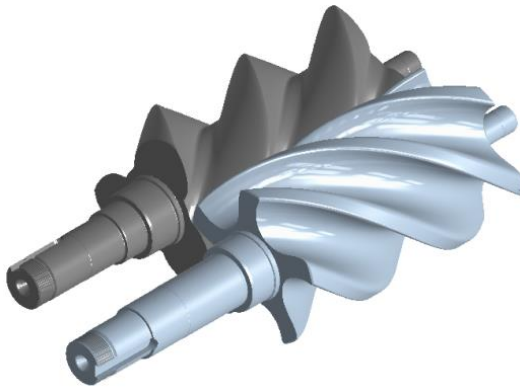


Figure 1.9 Meshing of uniform pitch twin screw rotors

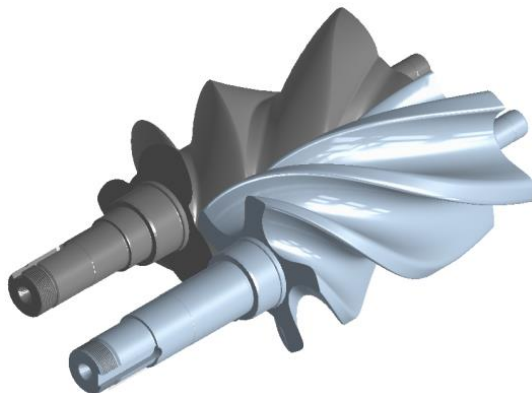


Figure 1.10 Meshing of variable pitch twin screw rotors

If all other variables other than the lead angle are equal, the sealing line length can be altered by varying the rotor lead angle along its length. Since the leakage loss in a compressor is directly proportional to the length of the sealing line segment that bounds the compression volume, decreasing it from the low pressure inlet end to the higher pressure discharge end, by varying the helix lead angle, makes it possible to achieve greater efficiencies. This is illustrated in Figure 1.11 which shows a comparison between the expected volumetric displacement of constant and variable lead rotor compressors in machines with otherwise identical dimensions.

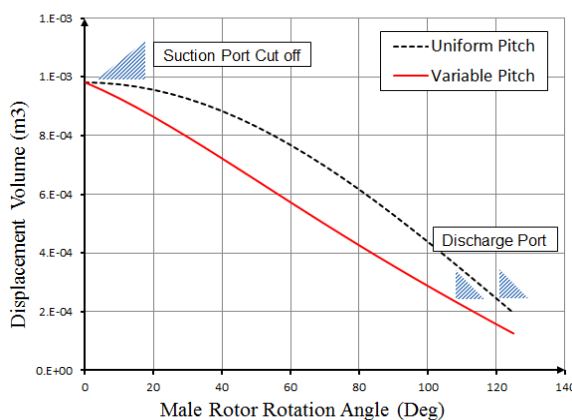


Figure 1.11 Comparison of displacement curve

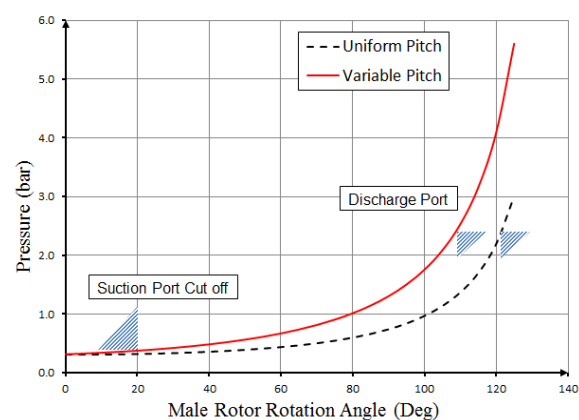


Figure 1.12 Comparison of compression curve

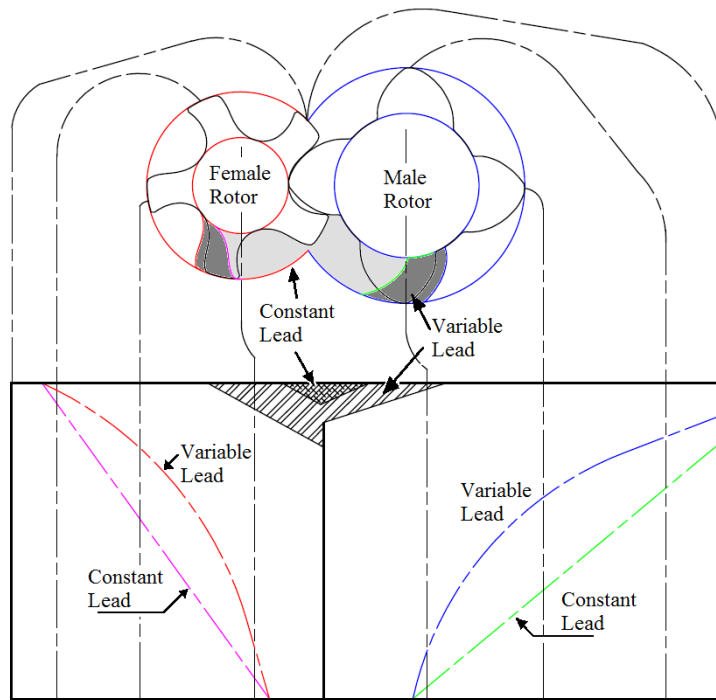


Figure 1.13 Cylinder and port development of a rotor pair

It can be seen that with the same rotor wrap angle and suction cut-off volume, the same built-in volume index can be obtained, from variable lead rotors, with earlier opening of the discharge port. This is also apparent from Figure 1.12 which shows a comparison of the compression characteristics of the two rotors. As an example for a male rotor with 3 lobes, of diameter 127.45mm, L/D ratio 1.6 and wrap angle 285°, pairing with a female rotor with 5 lobes, diameter of 120.38mm and discharge ports designed for a $V_i = 1.8$, when the male rotor pitch is varied linearly from 130mm to 40mm the V_i increases to 2.19 for the same discharge port and wrap angle.

Throttling loss is the energy lost due to inability of the compressed gas to be readily delivered and this loss reduces if discharge area is increased. In the case of the variable lead rotors, the discharge pressure will be reached earlier in the compression chambers. Assuming no over compression in the working chamber, for the same discharge pressure, the discharge port will be larger in the case of variable lead rotors. Hence the throttling losses will be reduced.

Figure 1.13 shows the cylinder and port development of a rotor pair. On the end plates the highlighted areas are the axial discharge ports for a uniform lead and a variable lead rotor and on the cylinder development, the hatched areas are the radial discharge ports. The axial and radial ports are timed such that the compression chamber opens to the discharge pressure at a set internal volume ratio. These projections show the increase in area for a variable lead rotor.

Thus three main advantages of varying the lead on screw rotors can be identified as:

- a. Improved compression characteristics. i.e. an increase in the built-in volume index for a comparable size of rotors.
- b. Less throttling losses due to increase in discharge port area for a given pressure ratio.
- c. Decreased leakage losses due to reduction in sealing line length towards high compression zones.

Theoretically the maximum volume of gas that can be sucked into a screw compressor is the gas region cross-section area multiplied by the rotor length. Any twist on the lobes creates a material overlap, reducing the fluid volume confined between the inter-lobes and the casing. Hence if rotor pairs of constant lead, but otherwise identical dimensions, are compared with variable lead rotors, it is possible that the reduced lead at the discharge end of the rotors may improve the compression characteristics but, in turn, reduce the suction cut-off volume, thereby reducing the compressor delivery. This can be a disadvantage of the design. The manufacture of variable lead rotors is not possible on a commercial scale because the form milling process adopted for uniform lead rotors is not applicable. The use of the latest technologies like 5-Axis machine tools is still under investigation but currently such rotors have not been manufactured.

1.4.2 Variable profile parallel axis twin screw compressor

The operating behaviour and advantages, described for variable pitch rotors, can also be realised if the rotor diameters are made to vary from suction to the discharge. Figure 1.14 shows an example of a parallel axis variable profile twin screw rotor.

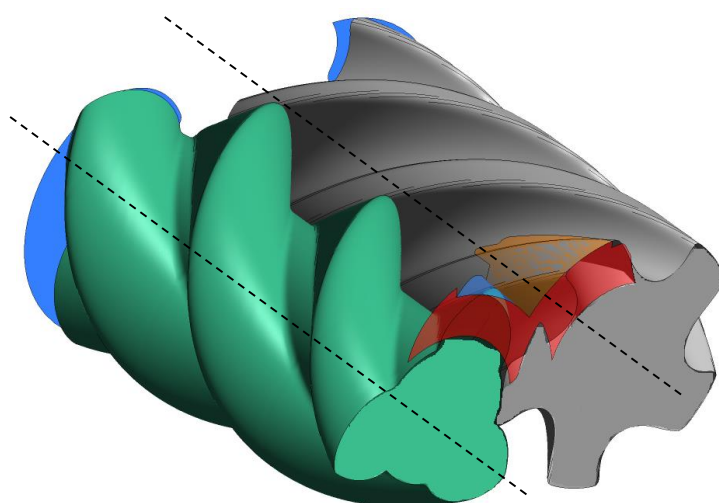


Figure 1.14 Meshing of variable profile parallel axis twin screw rotors

1.4.3 Tri-rotor screw compressors

As the pressure difference between suction and discharge is increased in screw compressors, the rotor root diameter has to increase, in order to be able to endure bending loads and avoid rotor damage. Also, the number of rotor lobes has to be increased. As a consequence, there is a decrease in the mass flow rate achieved by a given size of machine.

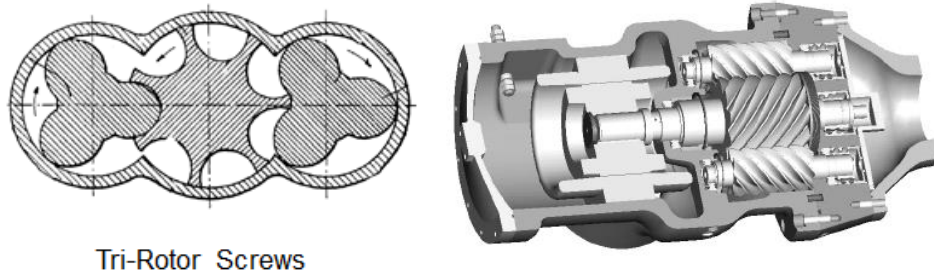


Figure 1.15 Tri rotor screw compressor

One of the methods of achieving higher mass flows is by running two or more compressors in parallel. Another approach is to utilize a single male rotor and multiple female rotors to effectively increase the number of compression chambers and boost the mass flow rate. One arrangement for two female rotors is shown in Figure 1.15 (*Nilsson, 1949*). The suction and discharge in this configuration happen on both axial ends of the male rotor and this can help in reducing the radial load on it. The design of the ports is challenging because the end plates have to accommodate heavy bearings. This increases the chances of having the full pressure difference across a clearance leakage path, increasing the effective leakage as compared to just twin screw arrangement. Such a possibility and also the port design can be investigated further in detail by CFD analysis.

1.4.4 Single screw compressor variants

Some non-conventional single screw configurations are also available in theory as shown in Figure 1.16 (*Zimmern, 1984*). The name convention is based on the form and relative axial arrangement of the gate and main rotors. These are namely: Planar Screw – Cylindrical Gate (PC type), Cylindrical Screw – Planar Gate (CP type), Planar Screw – Planar Gate (PP type) and Cylindrical Screw – Cylindrical Gate (CC type). The most widely used arrangement is the CP type. The CFD analysis of Single Screw Compressors is still unexplored and there are numerous aspects that may be improved if the detailed physics of flow in these machines is examined.

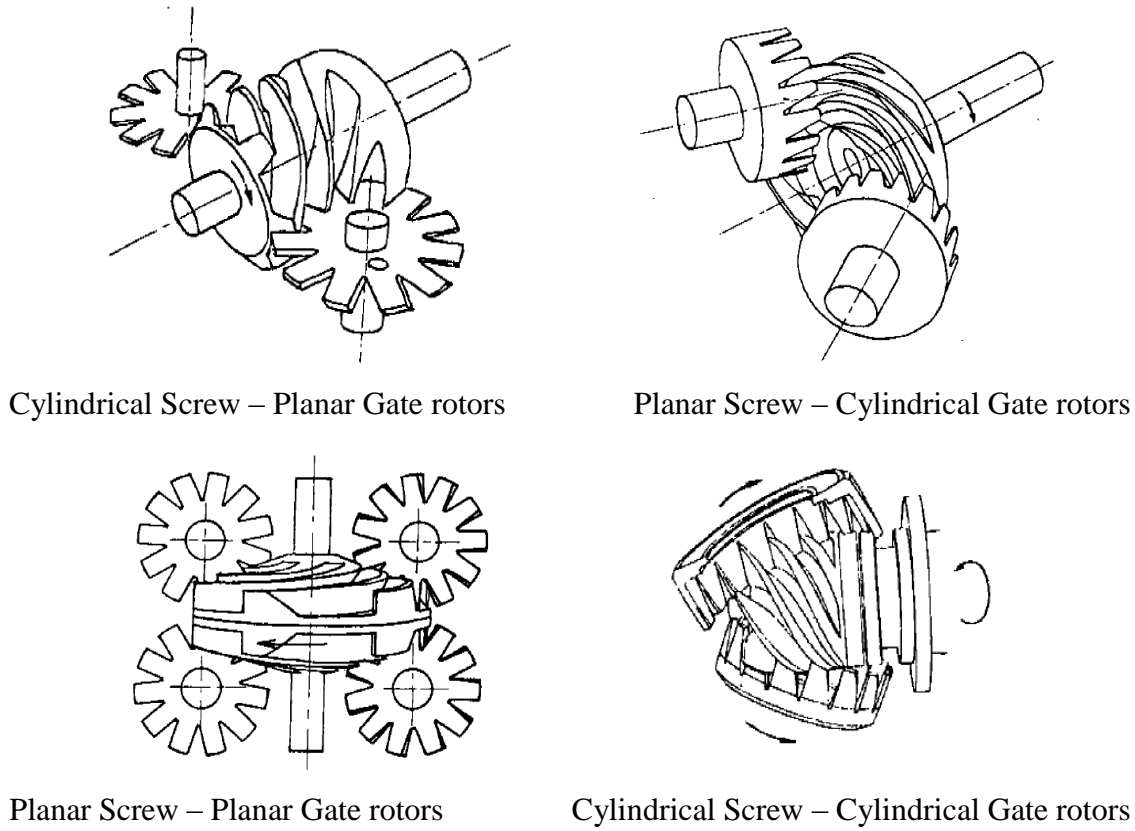


Figure 1.16 Single screw compressor configuration variants

1.4.5 Spiral compressor and expander

In his patent, *Perna* (2003) described a combination of variable lead, variable diameter mutually interacting rotors. A combination of two or more rotors was included as well as an integral arrangement for interlobe chamber volume reduction or expansion. A nonparallel axis of meshing has also been proposed, as shown in Figure 1.17.

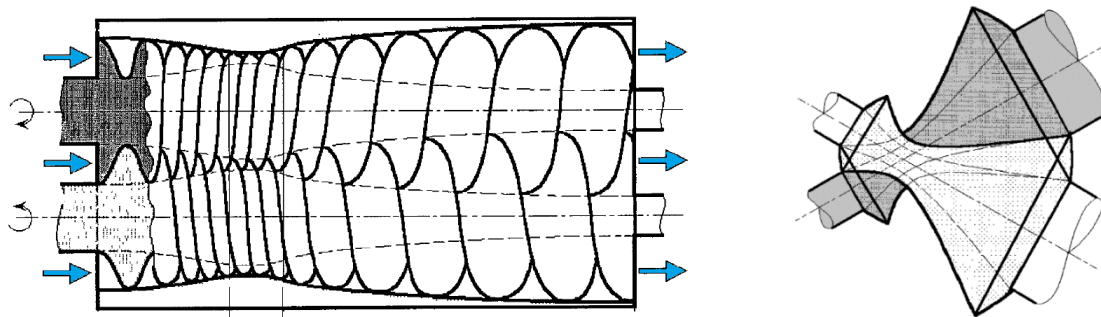


Figure 1.17 Spiral compressor and expander configuration

1.4.6 Internal Conical Rotary Screw Compressor

Recently Vert-Rotors (Vertrotors, 2011) developed a non-classical design of a screw type compressor with two conical helical rotors of which one is internal and another is external. The two rotors form a pair of epicycloid /hypocycloid conical screws with a configuration of a 3 lobe internal gear and a 4 lobe external gear, as shown in Figure 1.18. The volume is reduced during rotation because of the progressive reduction of the rotor diameter. CFD analysis would help in evaluating the feasibility of obtaining a high pressure ratio in a single stage and in estimating its performance.

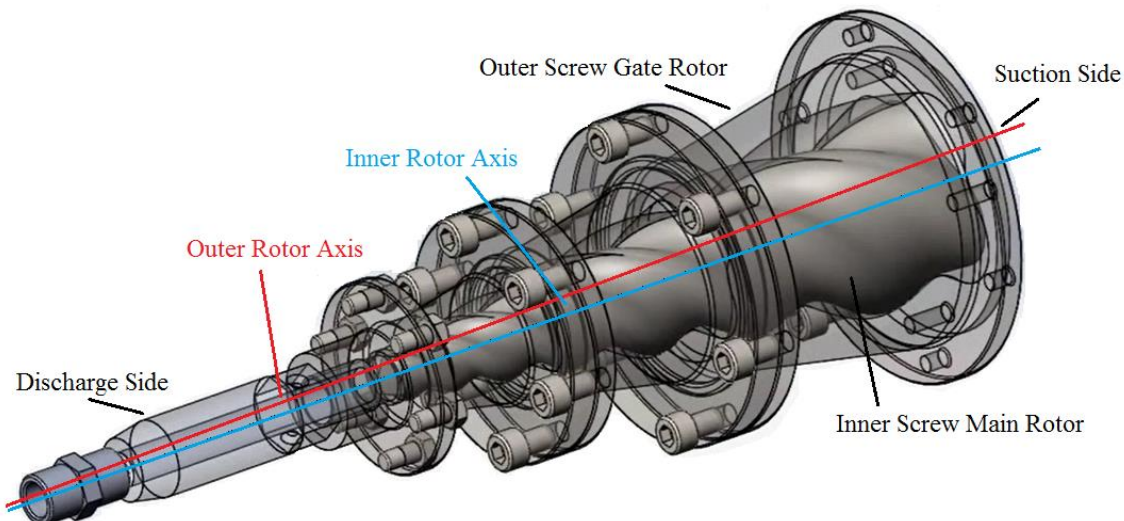


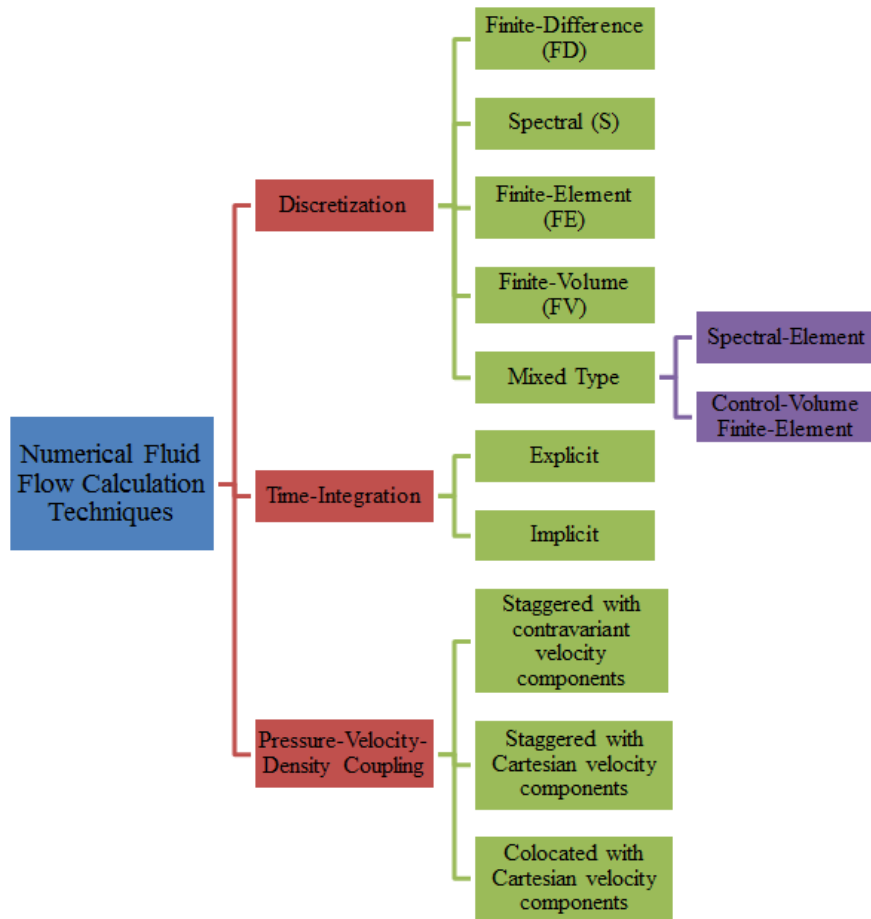
Figure 1.18 Internal twin screw compressor configuration

1.5 Computational methods for fluid flow calculations

General fluid flow is mathematically defined by PDE's, describing the conservation of mass, momentum and other scalar quantities of a physical system. These equations are closely coupled; time dependent partial differential equations, with strong dependence on fluid properties, and numerical methods are essential for obtaining their solution. A control volume approach in which the flow within a certain spatial volume is studied is preferred in case of fluid flow calculations. Numerical methods for fluid flow calculation can be classified using several features like:

- Discretisation method used to approximate the differential or integral conservative equations into a system of algebraic equations.
- Time-integration method.
- Method of pressure-velocity-density coupling.

Some of the methods are listed below:



Finite Difference method is the oldest method for numerical solution of a PDE's applicable for simple geometries. The generic conservation equations are considered in their differential form as:

$$\frac{\partial(\rho \phi)}{\partial t} + \frac{\partial(\rho u_j \phi)}{\partial x_j} = \frac{\partial}{\partial x_j} \left(\Gamma \frac{\partial \phi}{\partial x_j} \right) + q_\phi \quad (1.1)$$

The domain geometry is covered with grid points at which the differential equation is applied. Partial derivatives in the equation are approximated in terms of the nodal values of the function at these grid points. The disadvantage of FD formulation is that conservation is not always enforced.

Finite Volume method, on the other hand, treats the domain geometry as split into a number of small, regular, contiguous volumes and the centroids of these volumes act as integration points. The faces of each control volume are shared by adjacent cells. The generic conservation equations are considered in integral form and hence global as well as local conservation is enforced (*Ferziger and Perić, 1996*).

$$\frac{\partial}{\partial t} \int_{\Omega} \rho \phi d\Omega + \int_S \rho \phi \mathbf{v} \cdot \mathbf{n} dS = \int_S \Gamma \operatorname{grad} \phi \cdot \mathbf{n} dS + \int_{\Omega} q_{\phi} d\Omega \quad (1.2)$$

FV formulations can accommodate a variety of cell structures in domain discretisation and hence are suitable for most of the industrial flow applications.

Finite Element method combines the conservation equation with a weighing function and a solution is sought such that minimum residuals are attained. The variation of the dependent function within a control volume called an element is assumed to follow a specified shape function.

Text such as *Tannehill, Anderson and Pletcher* (1997), *Ferziger and Perić* (1996), *Versteeg and Malalasekera* (1995), *Patankar* (1980), *Date* (2005) provide an extensive treatment on the subject of computational fluid dynamics. A variety of numerical algorithms and modelling practises are available in the literature. Also a number of commercial software packages are available for flow calculation with these included in many real world industrial applications. Even the process of grid generation has matured enough to the point where physicists can use commercially available tools directly and generate the type or size of grid required for an application. The situation for applications like screw machines is not so favourable. Given the complexity of the fluid geometry, the grid requirements are much more stringent and hardly any commercially available grid generator has been found suitable for these applications (*Kovačević*, 2002). Under these constraints and also due to the nature of the governing equations, that need to be solved when the computational domains deform with time, FV methods are most suitable for screw machine numerical flow calculations.

Discretisation methods are used to approximate the differential or integral conservative equations into a system of algebraic equations. In the FV method this discretisation is the division of the physical computational domain into small non-overlapping discrete volumes that share faces and together represent the grid of the geometry with all boundaries. These volumes are used for the solution of the conservation equations and it is important that the grid achieves the desired cell type and quality required for accurate solution of the numerical method employed.

1.6 Grid generation approaches in practise

Figure 1.19 shows a breakdown of some of the basic grid generation techniques in practise today. They are broadly dependent upon the type of grids required and the grid data structure. Based on data structure the grid can be structured or unstructured (*Liseikin*, 1999). Structured

grids are preferred from consideration of solver accuracy and discretisation, but it is difficult to generate structured grids in complex practical geometries using common algorithms.

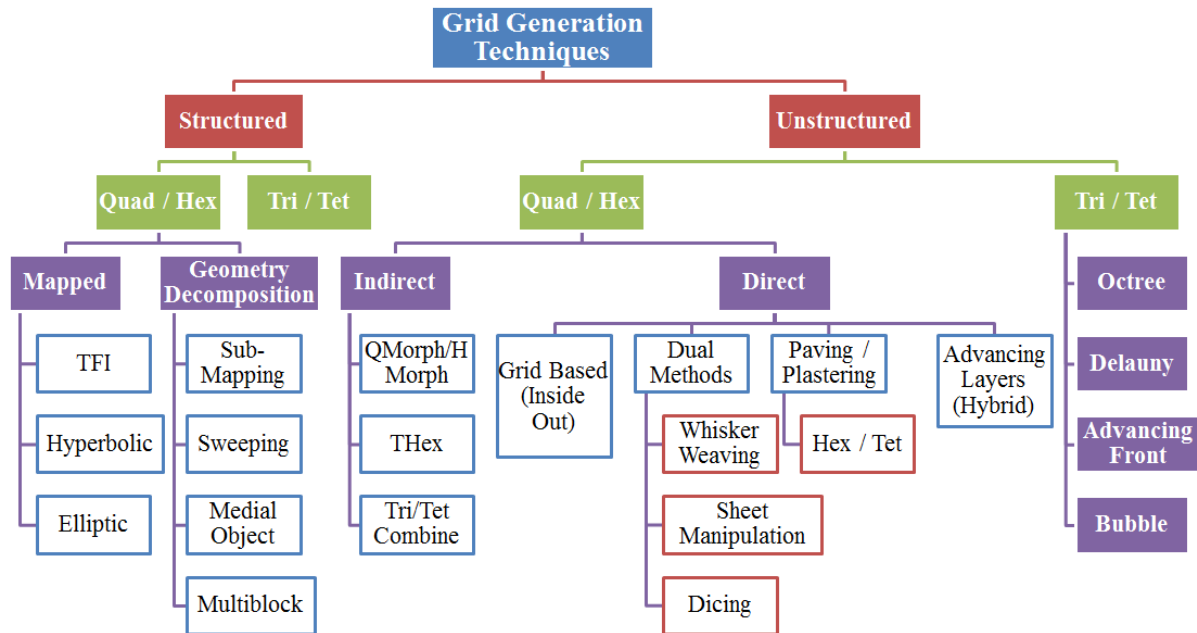


Figure 1.19 Basic grid generation techniques

Unstructured grids with tetrahedral geometry have been the most successful because of their ease of generation and adaptation, even in complex geometries but they suffer from lack of high accuracy, solution instabilities and a high cell count compared to hexahedral geometry grids. Based on the cell geometry, grids can be classified as Quadrilateral, Hexahedral, Triangular, Tetrahedral, Prism, Pyramid or Polyhedral (not shown in Figure 1.19). It is also possible to construct a hybrid structured-unstructured grid with a combination of different cell geometries as suitable in a particular region of the computational domain.

Such methods of grid generation are widely applied in commercial grid generators for FV formulations. When the geometry of a twin screw compressor's working chamber or other types of screw machine's working chambers is considered, the grid has to deform in operation and also needs to capture the large variation in the size of the domain from core flow region to the leakage flow region in clearances. Due to these reasons, commercial grid generators have not been successful in producing deforming grids for screw machine flow domains. Out of the techniques presented in Figure 1.19, structured methods with mapped topologies and using TFI or Elliptic solutions have been possible when implemented into customised grid generation tools. Also some multi-blocking and unstructured grids with remeshing solutions have been

attempted in practise. The literature review, presented in Section 2.2, presents some studies using these methods.

1.7 Motivation to investigate grid generation in numerical methods

The objective of using CFD models for analysing flow in screw machines is to get complete details of the flow field and trace sites where designers can improve the dynamics of the fluid flow. Such information is not available from classical methods of modelling such as chamber analysis. With the available technology, CFD analysis of dry running twin screw compressors and expanders has been made possible. This was mainly achieved due to the introduction of customised grid generation tools and commercial solvers capable of integrating seamlessly with them.

The motivation for this research has been twofold in this respect.

- The methods of grid generation currently used for deforming rotor domains have been developed for uniform rotor geometry and parallel axis alignment. When it comes to the analysis of new variants of design such as those described in Section 1.4, there are still many challenges in constructing a CFD model. This is because the customised grid generation tools are not generic in nature and need further modification when the basic rotor or compression chamber designs change. Hence it was necessary to develop new procedures of grid generation for rotors with variable geometry.
- With the approach for screw rotor grid generation in which the node distribution on the rotor profiles is fixed, there are two features of the grid that require attention.
 - a) The interface between the two O blocks is Non-Conformal
 - b) At the CUSP points there exist nodes that are merged with other nodes.

Figure 1.20 shows an example of a non-conformal interface between the two rotor blocks. Such a grid is generated when completely discontinuous O Blocks are constructed. They give flexibility to improve the cell quality in the individual blocks by orthogonalisation and smoothing and at the same time improve the robustness of the control parameters used for profile adaptation and distribution regularisation, but the presence of a non-conformal interface raises concerns about the stability of the solver and quality of flux balance that will be achieved with any additional physical equations, as in oil injection or water cooling. Moreover not all solvers are capable of defining an interface with such high node movements as are required in a helical screw grid.

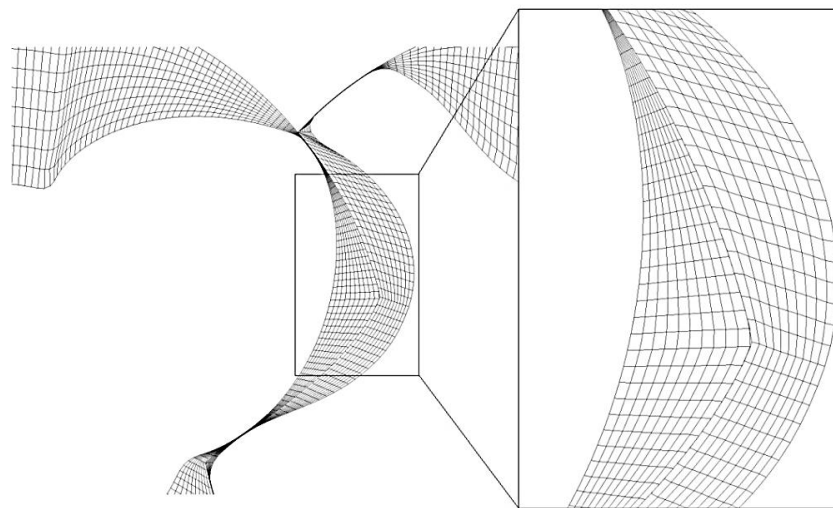


Figure 1.20 Non-conformal interface between the two rotors

Similarly the reason for having nodes merged at the CUSP points is to capture a straight line in the axial direction and the blow-hole area accurately as shown in Figure 1.21.

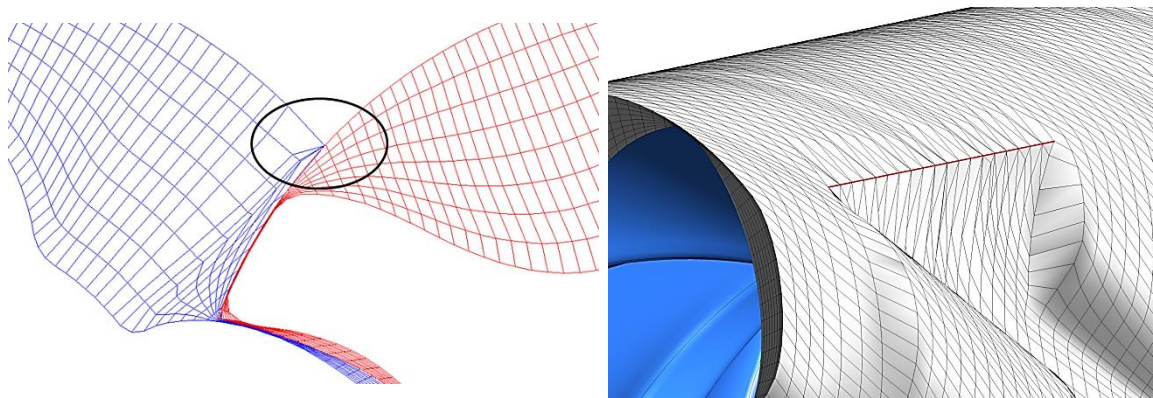


Figure 1.21 Merged nodes at the CUSP point to capture blow-hole

This results in the creation of Pyramid or Prism cell topology at the CUSP's. This is not an error, because the conservation equations are solved by the solver treating the respective element topologies. However there are some solvers like ANSYS FLUENT, STAR CCM+ that result into degenerated cells when the nodes are merged during the solution.

Hence it was necessary to develop or try other possibilities of grid generation in the rotor cross section such that these grid quality features could be improved.

Accordingly this study was focused on the development of grids for variable geometry rotors and device improvements in the cross section grids being finally used to construct a three dimensional computational domain.

Chapter 2 – Literature Review

Screw machines have been traditionally designed using thermodynamic lumped parameter models. These models have remarkably helped in the evaluation of the machine performance and for optimisation of rotor profiles for a given application. A lot of literature is currently available that focuses on such lumped parameter models. Some of the research published in the area has been discussed here. These studies have highlighted the capabilities that can be achieved by a simplified model and also the important physical phenomenon that have been idealised and need to be accounted by higher order numerical flow models.

The main sources of literature have been the three major international conferences dedicated to compressor technology. These are:

- *International Compressor Engineering Conference* held at Purdue University, USA.
- *International Conference on Screw Machines* held at TU Dortmund, Germany.
- *International Conference on Compressors and their Systems* held at City University London, UK.

Apart of these conferences there are many journals like the *International Journal of Refrigeration* that have regularly provided technological updates on Screw machine systems. A large number of Patents have been published on rotor profiles, flow control systems and rotor configurations like twin screw or multi screw arrangements. A few good books have also been published on Screw machine technology, such as those of *Sakun* (1960), *Andreev* (1961) and *Amosov* (1977) in Russian, *Rinder* (1979) and *Konka* (1988) in German, *Xing* (2000) in Chinese and by *O'Neill* (1993), *Arbon* (1994) and *Stošić et al.* (2005a) in English. More recently, 3D numerical models employing CFD have been investigated and a few papers have been published in these conference proceedings. Only one book by *Kovačević et al.* (2007) is available, which is focused on the CFD analysis of twin screw machines while a few journal papers are available presenting screw machine grid generation technology.

In this chapter, the practise and application of Computational Fluid Dynamics for screw machines has been critically reviewed. Modelling approaches published in some of the journals and conferences and typical results achieved have been highlighted. Special attention has been given to grid generation techniques. A detailed review of the algebraic and differential approach of deforming grid generation for twin screw machines has been presented. For the

algebraic approach of grid generation, the PhD thesis by *Kovačević* (2002), the monograph by *Kovačević et al.* (2007) and associated technical papers have been the primary source. For the differential approach of grid generation, the PhD thesis by *Vande Voorde* (2005) and associated technical papers have been the primary source.

From the available techniques for deforming grid generation it was found that Arbitrary Lagrangian Eulerian (ALE) formulations with customised grid generation tools have been successfully used for twin screw machines. A comparatively new approach of Key-Frame remeshing is available with commercial flow solvers and has been investigated in Section 4.4 for its accuracy and applicability to screw machines.

The review of available literature and CFD practises have confirmed the need for further development of numerical models and grid generation techniques for screw machines. Presently available approaches of grid generation need to be extended to produce better quality computational cells and also make them suitable for non-conventional screw machines like variable geometry rotors.

2.1 Numerical analysis of Screw machines using lumped parameter models

For oil free or oil injected twin screw compressors, *Fujiwara et al.* (1974, 1984), *Fujiwara and Osada* (1990), *Fukazawa and Ozawa.* (1980), *Sangfors* (1982 and 1984), *Singh et al.* (1984 and 1990), *Dagang et al.* (1986), *Kauder and Rau* (1994) and *Janicki* (2007) presented numerical models. These were based on the classical approach of solving the equations of conservation of mass and energy applied to a control volume. The use of uniform parameter values, within the whole volume, enabled ordinary differential equations to be used. Because of the coupled nature of these equations, they could not be solved analytically and a numerical approach had to be adopted. The challenging part of the modelling has been to calculate accurately the geometric properties of the machine, such as the change in volume with time and estimation of the various leakage gaps.

Stošić and Hanjalić (1977) developed models, by solving numerically the internal energy and mass conservation differential equations using Runge – Kutta fourth order procedure and this was applied to calculate the performance of two stage reciprocating compressors. In 1988 the procedure was extended and implemented in the program SCORPATH[®] - Screw Compressor Rotor Profiling and Thermodynamics (*Stošić*, 1988) for twin screw compressors.

Hanjalić and Stošić (1997) have presented design optimisation of the rotor profile using such models. The optimisation technique was based on Box method and for the given objective function considered variables such as rotor profile parameters, number of lobes, oil injection parameters and operating conditions. All these developments were later collected into a text book on mathematical modeling of twin screw compressor by *Stošić et al.* (2005).

Fleming and Tang (1994) and *Fleming et al.* (1998) have presented model for development and performance improvement of twin screw compressors. *Tang* (1995) in his thesis, has provided a detailed account of these developments and application of numerical chamber models to optimize refrigeration screw compressors.

Sauls, Powel and Weathers (2006) have used a thermodynamic chamber models to predict the compressor performance and then provide boundary conditions for a 3D FEM thermal analysis for calculation of rotor deformation and clearance variation.

French engineer *Bernard Zimmern* (1984) has presented an historical review of the oil-injection free Single screw compressors. Similar to Twin screw compressors, for Single screw compressors, *Bein and Hamilton* (1982), *Boblitt and Moore* (1984), *Jianhua and Guangxi* (1988), *Li Hong Qi and Jin Li Wen* (2004) presented computer chamber model for oil flooded single screw compressors.

Lundberg and Glanvall (1978) presented similar chamber models and also compared the performance of twin and single screw type of compressors at full load operation.

For twin screw expanders *Smith et al.* (1996) have presented thermodynamic models for the development of a trilateral flash cycle system. In 2004, *Smith et al.* (2004) presented an improved system for power recovery using twin screw expander which were analysed using chamber models. The analysis of screw expanders using chamber models has been reported in several papers like *Stošić and Hanjalić* (1994) and *Stošić et al.* (2002).

Bruemmer and Huther (2009), used a chamber model, based on the conservation of mass and energy, to predict the performance of screw expanders, in order to evaluate the influence of internal volume ratio V_i , length to diameter (L/D) ratio, rotor wrap angle Φ_w , size of leakage path and some other parameters.

Nikolov et al. (2012), estimated the influence of rotor and casing thermal deformation on the performance of a screw expander in an ORC system, based on the iterative coupling of a thermodynamic chamber model and 3D FEM thermal analysis.

Most recently, *Read, Stošić and Smith* (2014) presented a full multivariable optimisation of screw expander geometry and operating conditions for an ORC system to establish the most efficient expander design for a given duty using chamber models. The application was in waste heat recovery from low grade sources.

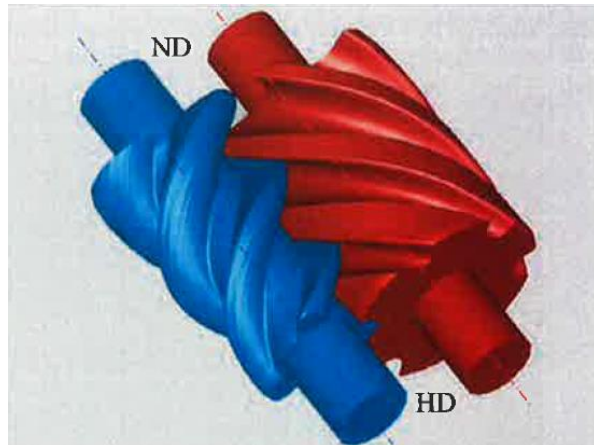
Grieb and Brügger (2014) have presented an integral design approach using chamber models for the design of screw expanders for closed-loop cycles showing that system parameters should be correlated with expander geometry in order to maximise their overall thermal efficiency.

In case of non-conventional screw machines, a patent by *Gardner* (1969) proposes a helical screw compressor with continuously variable lead for the lobes on the male and gate rotors. Recently, *Schulze-Beckinghausen et al.* (2014) have presented a thermodynamic chamber model and compared the results of the variable lead compressor performance with constant lead rotors. Their model predicted higher compression with rotors of varying pitch. The volumetric efficiency showed an improvement compared to constant lead rotors but the indicated power was high due to non-optimal internal pressure rise, which increased the specific power.

Utri and Brügger (2014) presented a thermodynamic comparison of screw expanders with constant and variable pitch in an ORC system. Instead of a continuous lead variation, they considered a stepped variation which gives a larger port area for the high pressure filling part of the cycle. The overall wrap angle on the rotors was maintained equal to 245°. A multi chamber thermodynamic model was then used to evaluate and compare the performance of different configurations. Rotors with variable rotor pitch showed an increase of up to 5% in effective power output.

Kauder and Fost (2002) and *Fost* (2006) evaluated options to modify screw rotors to improve the filling process in screw expanders and proposed a few non-conventional concepts like conical rotors and rotors with inlet discs, each with a different pitch. Conical rotors had a variable rotor profile, as shown in Figure 2.1, and showed an improvement in chamber filling mainly influenced by a reduction in pressure loss at the inlet. For the same built in volume index $V_i = 5$, the max inlet area showed an increase from 540mm² to 1080mm². The performance of a cylindrical rotor was compared with a conical rotor over a range of wrap angles from 150° to 300° with a filling pressure of 15bar at 250° C. In the case of the cylindrical rotors the volumetric efficiency decreased from 82% at a wrap angle of 300° to 34 % at a wrap

angle of 150° . In the case of conical rotors the reduction was lower from 88% at 300° to 78% at a wrap angle of 150° . The isentropic efficiency in the case of cylindrical rotors reduced from 94% at a wrap angle of 300° to 78% at a wrap angle of 150° . While in the case of conical rotors the isentropic efficiency reduced slightly from 94% at 300° to 92% at a wrap angle of 150° .



Reproduced from *Kauder and Fost* (2002)

Figure 2.1 Conical rotors with SRM 4/6 profile.

All these studies were done with the intention of predicting the performance and characteristics of screw machines at the design stage and optimizing the geometry and control parameters for a given application and operating condition. With vast improvements in computational technology and availability of more accurate calculation methods, the use of Computational Fluid Dynamics for screw machine design has been encouraged as it would provide better insight into the flow dynamics within them.

2.2 CFD analysis of Screw Compressors and Expanders

As the rotors of a screw machine turn during operation of the compressor, the fluid volume in between them is deformed (compressed or expanded) and the CFD grid which represents the fluid volume also needs to deform. Without capturing this deformation it is not possible to capture the real three dimensional fluid characteristics inside the working chamber.

The report on the application of CFD in analysis of screw machines can be found in *Stošić, Smith and Zagorac* (1996). They presented a solution in both screw and scroll compressor geometry without full grid deformation but by the addition of a representative momentum source in the conservation equations. The results were encouraging for pressure distribution but did not provide full flow properties. A breakthrough was achieved in 1999 by *Kovačević*

with the use of an analytical rack generation method, proposed by *Stošić* (1998), applied to generate an algebraic, adaptive, block structured, deforming grid calculation for twin screw rotors. Since then there have been several activities reported on the CFD analysis of twin screw compressors. The use of this method for screw compressor applications is justified by its ease of use and its speed. The analysis of the working chamber is transient in nature and requires a grid representing every time step rotor position and domain deformation. In this respect, algebraic methods can be used to recalculate the grid quickly. *Kovačević, Stošić and Smith* (1999 and 2000) successfully used an algebraic grid generation method together with boundary adaptation and transfinite interpolation which has been implemented in the program SCORG – (Screw Compressor Rotor Grid Generator). This has been written in FORTRAN with a C# front end application. In his thesis, *Kovačević* (2002) presented the grid generation aspects in detail. *Kovačević et al.* (2002a, 2002b, 2003, 2005 and 2006) have reported CFD simulations of twin screw machines to predict flow, heat transfer, fluid-structure interaction, etc. *Kovačević et al.* (2007) also published a textbook on the CFD analysis of screw compressors.

Pascu et al. (2012) have reported optimisation of the discharge port of a Twin screw compressor using the SCORG grid generator and ANSYS CFX solver. Optimisation was based on the selection of the port geometry by relative comparison of flow fields predicted by the CFD models.

Sauls and Branch (2013) used the results from CFD calculations to develop an improved one-dimensional thermodynamic model for refrigerant screw compressors, by extracting calibration coefficients that influence the pressure variation during the discharge process.

Kethidi et al. (2011) conducted further studies on the influence of turbulence modelling on the CFD prediction of local velocity fields in twin screw compressors. *Nouri et al.* (2006) carried out cycle-resolved velocity measurements within a screw compressor using LDV and these data have been used by *Kethidi et al.* (2012) to compare with the results from 3D CFD models.

Mujić et al. (2008) have presented an optimisation of the discharge port area based on flow behaviour in the discharge chamber. They used CFD for relative comparison of port geometry modifications and their influence on predicted pressure pulsations has been used to judge sound spectrum and noise level from the compressor. These noise levels predicted by CFD solutions have been used for designing discharge ports with reduced noise levels.

Mujić (2009) in his thesis presented a 3D CFD coupled model in which the boundary conditions for the discharge port were obtained as time varying data from 1D thermodynamic chamber

models. The procedure was implemented for Star CCM+ solver. It was found that the results predicted by the coupled model for sound pressure levels were closer to the full 3D CFD models and also in close agreement with the experimental measurements. Such an approach simplified the numerical analysis and also provided faster results from the CFD models.

Recently, *Arjeneh et al.* (2014) have presented the analysis of flow through the suction port of a compressor with water injection. It was reported that it was difficult to stabilise the solver in a full 3D analysis with both deforming rotor domains and multiphase models. A simplified suction port model, with time varying boundary conditions, obtained from a full 3D single phase analysis was successful in predicting pressure variation in the suction port that agreed closely with experimental results. Also wetting of the port walls by the injected water was well predicted.

Vande Voorde, Vierendeels and Dick (2004 and 2005) were the first to implement a grid generation algorithm for block structured mesh from the solution of the Laplace equation for twin screw compressors and pumps using differential methods. The use of differential methods requires the PDE to be solved for every rotor position and then the grid generation has to be repeated from the equipotential and gradient lines. In his thesis, *Vande Voorde* (2005) presented the principles of solving the initial Laplace equation and then using it to construct a block structured deforming mesh. Based on this grid generation, flow in a double tooth compressor and a twin screw compressor was analysed and the results were compared with experimental data over a range of discharge pressures and rotor speeds.

Papes, Degroote and Vierendeels (2013 and 2014) presented a 3D CFD analysis of an oil injected twin screw expander using the same differential grid generation approach. A real gas model for the working fluid R245fa was used and results for the different leakage flows were presented together with chamber pressure variation curves and performance analysis at different pressure ratios.

Recently CFX Berlin (2014) has introduced a software tool called *TwinMesh* to link with ANSYS CFX solver and this tool generates a grid for twin rotor machines on similar lines to that of the algebraic and differential approaches. *Hesse et al.* (2014) have presented the application of such a deforming grid for the analysis of an oil free twin screw compressor.

2.3 Summary

CFD has found an increasing usage and many research groups have started investigating their screw machines using full 3D CFD models. From the available techniques for deforming grid generation it was found that only ALE formulations with Finite Volume Methods and customised grid generation tools, have been successfully used for twin screw machines. Most of the screw machine CFD work on grid generation and analysis has either been performed at, or originates from City University London and, apart from these works, there are only a few reports available on transient three dimensional CFD analyses of screw machines. So far no published works are available on the 3D numerical analysis of twin screw compressors with variable pitch rotors, variable profile rotors, single screw machines, tri-rotor screw machines or other complex screw machines. *Prasad* (2004) highlighted that one of the main reasons for CFD analysis not being utilised to its full potential for screw machines is the difficulty of pre-processing i.e. grid generation. Literature and CFD practises have confirmed that there is need for further development of numerical models and grid generation techniques for variable geometry screw machines.

Chapter 3 – Research Aims and Contribution to Knowledge

There is a great demand from industry to improve fluid machine performance by exploring novel concepts through the use of computer simulation models that give a better insight into the flow. 3D CFD simulation makes such insights into different aspects of flow fields possible. However, within the current state of the art, it is difficult to generate the computational grids required for this purpose in screw machine geometries. For novel variable geometry rotor designs like variable lead or variable profile, no method is yet available for deforming grid generation.

3.1 Aims of research

The main aim of this research is to develop computational fluid dynamics models with deforming grids for variable geometry screw machines.

The activities undertaken to achieve this are as follows:

- Explore and evaluate fluid flow calculation techniques currently available and applicable for screw machine flow predictions.
- Develop grid generation techniques for 3D numerical analysis of variable geometry screw machines such as variable pitch rotors and variable profile rotors.
- Develop new techniques that will help in improving the quality of deforming grids generated for screw machines.
- Perform calculations on different types of screw machines using the new developments and compare the numerical results with experimental measurements.

3.2 Methodology

Figure 3.1 shows the research approach. Design and performance parameters for variable geometry screw machines that can be evaluated using CFD analysis were identified from the literature. The current state of art for analysis of screw machines were studied and case studies were conducted to analyse the possibilities of developments for variable geometry machines.

The main challenge identified was grid generation and hence focus was on techniques available for grid generation.

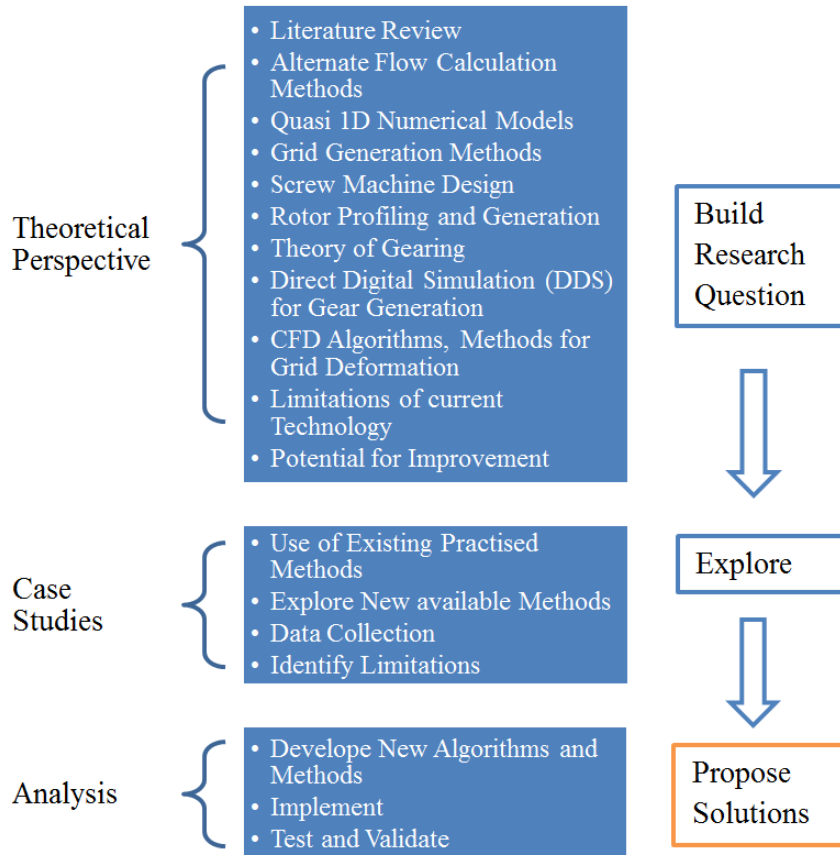


Figure 3.1 Research methodology

3.3 Contribution to knowledge

The research described in this thesis has resulted in the extension of the role of computational fluid dynamics to variable geometry screw machines such as variable pitch rotors and variable profile rotors by means of the following developments.

- An algebraic grid generation, in which the deforming rotor blocks are generated from the outer boundary (the casing) to the inner boundary (the rotor profile), has been developed. This type of distribution generates fully quadrilateral cells in the grids of the rotor cross section and also avoids rotation of the mesh blocks. This development improves the quality of cells and also refines the grids, selectively, in the interlobe region.

- Techniques for distributing grids in a cross section have been developed that make it possible to improve the interface between the rotors to remain in one to one conformity.
- The algebraic method of grid generation has been extended by new procedures to include rotors with variable lead by controlling the cross section spacing. For this purpose, functions for uniform, linear or a stepped lead can be prescribed.
- A new algorithm, capable of generating grids for rotors with variable profiles, has been implemented. A continuously variable rotor profile can be prescribed. This makes it possible to analyse flow in domains with conical rotors and parallel axes. Rotors can be engaged either externally or internally to form the working chamber.
- A new simplified technique of generating inflation layer grids has been developed that can refine the cells adjacent to the rotors.
- Case studies have been carried out to investigate the relative performance of twin screw compressors with three different rotor designs. The three geometries considered were rotors with constant lead and profile, rotors with a linearly variable lead and rotors with a uniform lead but with a linearly variable profile i.e. conical main and gate rotors. Grid independence studies were conducted to serve as a reference for screw compressor design engineers exploring rotor modifications for performance improvement.
- Additional case studies using the new grid developments are reported for compressors and expanders and results have been compared with experimental measurements. A variety of modelling parameters and grid generation techniques were explored. These studies will be useful for flow analysts practising CFD in screw machines.

To summarise, it is hoped that the developments presented in this thesis will extend the role played by computational methods in innovative screw machine designs.

Chapter 4 Grid Deformation Schemes for Screw Machines

4.1 Introduction

Commercial flow solvers can account for flow solutions in applications with deforming domains, but, in general, cannot be applied to screw machine flow simulations, due to the need for large magnitude deformation of the domain while retaining geometrical accuracy, for physically valid capture of the processes involved. Hence only customised grid generators that work alongside the numerical solvers have been successful for such cases.

In this chapter the governing equations for deforming domains and schemes of mesh movement have been reviewed and a relatively new approach of remeshing using external grids called key-frame remeshing has been analysed. This method provides the potential to handle large mesh deformations with unstructured tetrahedral grids. Current methods of grid generation, used in customised grid generators, have also been reviewed. These techniques mainly use algebraic and differential approaches. A comparative study between the two approaches helped in the selection of techniques that can improve the grid quality and also implement grids for variable geometry rotors.

4.2 Governing equations for deforming domains

CFD solvers commonly use the Finite Volume Method and, applied to screw compressors, this requires the solution of unsteady flow regimes with moving boundaries. The FVM has been used to solve problems of this type for a long time. *Perić* (1985) introduced a finite volume methodology for prediction of three-dimensional flows in complex ducts for orthogonal and non-orthogonal grids. *Demirdžić* and *Perić* (1990) presented an implementation of finite volume method for the prediction of fluid flow in domains of arbitrary shape with moving boundaries. *Demirdžić* and *Muzafferija* (1995) applied the method to fluid flow and solid body stress analysis simultaneously.

In an Eulerian reference, the conservation of mass, momentum, energy and other intensive properties applied to fluid flow in a control volume (CV) can be defined by coupled, time dependent, partial differential equations. These equations form the basis for all fluid flow

computations employing the Finite Volume Method of numerical solution. Table 4.1 presents the conservative form of the governing equations of the flow of a compressible Newtonian fluid. The equations of state relates the thermodynamic variables ρ, p, i, T to the two state variables ρ and T , with assumption of thermodynamic equilibrium.

Table 4.1 Conservative form of the governing equations of the flow of a compressible Newtonian fluid

Mass	$\frac{\partial \rho}{\partial t} + \operatorname{div}(\rho \mathbf{v}) = 0$
x-momentum	$\frac{\partial(\rho u)}{\partial t} + \operatorname{div}(\rho u \mathbf{v}) = -\frac{\partial p}{\partial x} + \operatorname{div}(\mu \operatorname{grad} u) + S_{Mx}$
y-momentum	$\frac{\partial(\rho v)}{\partial t} + \operatorname{div}(\rho v \mathbf{v}) = -\frac{\partial p}{\partial y} + \operatorname{div}(\mu \operatorname{grad} v) + S_{My}$
z-momentum	$\frac{\partial(\rho w)}{\partial t} + \operatorname{div}(\rho w \mathbf{v}) = -\frac{\partial p}{\partial z} + \operatorname{div}(\mu \operatorname{grad} w) + S_{Mz}$
Internal energy	$\frac{\partial(\rho i)}{\partial t} + \operatorname{div}(\rho i \mathbf{v}) = -p \operatorname{div} \mathbf{v} + \operatorname{div}(k \operatorname{grad} T) + \Phi + S_i$
Equations of state	$p = p(\rho, T)$ and $i = i(\rho, T)$ e.g. for perfect gas $p = \rho RT$ and $i = C_v T$

S_{Mx}, S_{My} and S_{Mz} are the body force source terms of x, y and z momentum respectively per unit volume per unit time. Φ represents a dissipation function for all the effects due to viscous stresses in the internal energy equation. The thermodynamic equilibrium assumption with introduction of Newtonian fluid model makes the system of seven equations and seven unknowns that can be solved with provided initial and boundary conditions.

On similar principles, for a general variable ϕ the conservative form of the so called transport equation can be written as,

$$\frac{\partial(\rho \phi)}{\partial t} + \operatorname{div}(\rho \phi \mathbf{v}) = \operatorname{div}(\Gamma \operatorname{grad} \phi) + S_\phi$$

Integral form of the conservation equation can be represented by the general transport equation, (Ferziger and Perić, 1996)

$$\frac{\partial}{\partial t} \int_{\Omega} \rho \phi d\Omega + \int_S \rho \phi \mathbf{v} \cdot \mathbf{n} dS = \int_S \Gamma \operatorname{grad} \phi \cdot \mathbf{n} dS + \int_{\Omega} q_\phi d\Omega$$

transient *convection* *diffusion* *source*

(4.1)

When the control volume is not fixed in space, the solution domain changes with time, due to movement of the boundaries. This movement is defined either as a function of time or is dependent on the current solution field. The convective fluxes such as the mass flux are calculated in such cases, using relative velocity components at the cell faces. If the coordinate system remains fixed and Cartesian velocity components are used, the only change in the conservation equations is the appearance of the relative velocity ($\mathbf{v} - \mathbf{v}_b$) in all convective terms, where \mathbf{v}_b is the velocity vector at the cell's face.

$$\frac{\partial}{\partial t} \int_{\Omega} \rho \phi d\Omega = \frac{d}{dt} \int_{\Omega} \rho \phi d\Omega - \int_S \rho \phi \mathbf{v}_b \cdot \mathbf{n} dS \quad (4.2)$$

$$\frac{d}{dt} \int_{\Omega} \rho \phi d\Omega + \int_S \rho \phi (\mathbf{v} - \mathbf{v}_b) \cdot \mathbf{n} dS = \int_S \Gamma \operatorname{grad} \phi \cdot \mathbf{n} dS + \int_{\Omega} q_{\phi} d\Omega \quad (4.3)$$

transient *convection* *diffusion* *source*

Application of Leibnitz rule (Equation 4.2) for differentiation under the integral sign to transient terms of equation (4.1) gives the integral form of a general conservation equation in Arbitrary Lagrangian-Eulerian formulation – equation (4.3). This is arbitrary, because the grid velocity \mathbf{v}_b and grid motion is independent of fluid motion. However, when the cell faces move, the conservation of mass and other conserved quantities are not necessarily ensured if the grid velocities are calculated explicitly and, in turn, are used to calculate the convective fluxes. To ensure that these equations are completely conserved, the Space Conservation Law needs to be satisfied.

Space conservation or Geometric conservation is given by,

$$\frac{d}{dt} \int_{\Omega} d\Omega + \int_S \mathbf{v}_b \cdot \mathbf{n} dS = 0 \quad (4.4)$$

Space conservation can be regarded as mass conservation with zero fluid velocity. The unsteady terms involving integral over control volume Ω , in the governing equation, which is now changing with time, need to be treated in a way to be consistent with the space conservation equation with deforming and/or moving grid. Grid velocities and change in CV volumes are required to be calculated that confirm with the space conservation. If the implicit Euler scheme is used for temporal discretisation, the transient term can be discretised as:

$$\frac{d}{dt} \int_{\Omega} \rho \phi d\Omega = \frac{(\rho \phi \Omega)^{n+1} - (\rho \phi \Omega)^n}{\Delta t} \quad (4.5)$$

Where, n and $n + 1$ represent current and next time level respectively. The $n + 1$ volume Ω^{n+1} is computed from

$$\Omega^{n+1} = \Omega^n + \frac{d\Omega}{dt} \Delta t \quad (4.6)$$

Where, $d\Omega/dt$ is the rate of change of volume of CV and in order to satisfy equation (4.4) it is calculated as,

$$\frac{d\Omega}{dt} = \int_S \mathbf{v}_b \cdot \mathbf{n} dS = \sum_j^{n_f} \mathbf{v}_{b,j} \cdot S_j \quad (4.7)$$

n_f is the number of faces on the control volume and S_j is the j^{th} face area vector. The dot product $\mathbf{v}_{b,j} \cdot S_j$ on each control volume face is calculated from the volume swept out $-\partial\Omega_j$ by that face over the time step Δt as $\partial\Omega_j/\Delta t$. Therefore mass flux \dot{m}_j can be calculated using $\partial\Omega_j/\Delta t$ instead of explicitly calculated grid velocity $\mathbf{v}_{b,j}$.

$$\dot{m}_j = \int_{S_j} \rho (\mathbf{v} - \mathbf{v}_{b,j}) \cdot \mathbf{n} dS_j \approx \rho_j (\mathbf{v} \cdot \mathbf{n})_j S_j - \frac{\rho_j \partial\Omega_j}{\Delta t} \quad (4.8)$$

If the volume change and mass fluxes are calculated as above, space conservation is conformed. The requirement for space conservation in flow equations at moving integration points was introduced by *Trulio and Trigger* (1961) when applied to a finite difference calculation framework. *Thomas and Lombard* (1979) presented the implementation of space conservation for a density based finite difference scheme on structured meshes. The importance of the space conservation law was discussed by *Demirdžić and Perić* (1990) also *Demirdžić, Issa and Lilek* (1990). They showed that the error in mass conservation due to non-conformance of space conservation is proportional to the time step size for constant grid velocities and is not influenced by the grid refinement size. *Gosman and Watkins* (1977), *Gosman and Johns* (1978) and *Gosman* (1984) presented applications of this to reciprocating In-Cylinder problems with moving boundaries.

When the equations of conservation are applied to control volumes of finite dimensions, there are limitations to the resolution of length scales beyond a certain size, or capturing near-wall boundary layer phenomena or shocks where the gradients are high. So, in addition to these equations, models can be introduced into the calculation like turbulence models, near wall functions, species transport etc. These models can be analogously represented by the general transport equation and are not discussed here. When FVM is applied to screw compressors, it faces a major challenge in the grids required for transient simulations. These grids have to capture the complex geometry formed by the fluid enveloping the screw rotors and at the same time they need to change their shape.

4.3 Solution of governing equations

Figure 4.1 represents a flow chart of the solution process for a FVM with deforming domains. The solver used in this analysis is a pressure based coupled solver which solves for pressure based on the balancing of mass and momentum conservation.

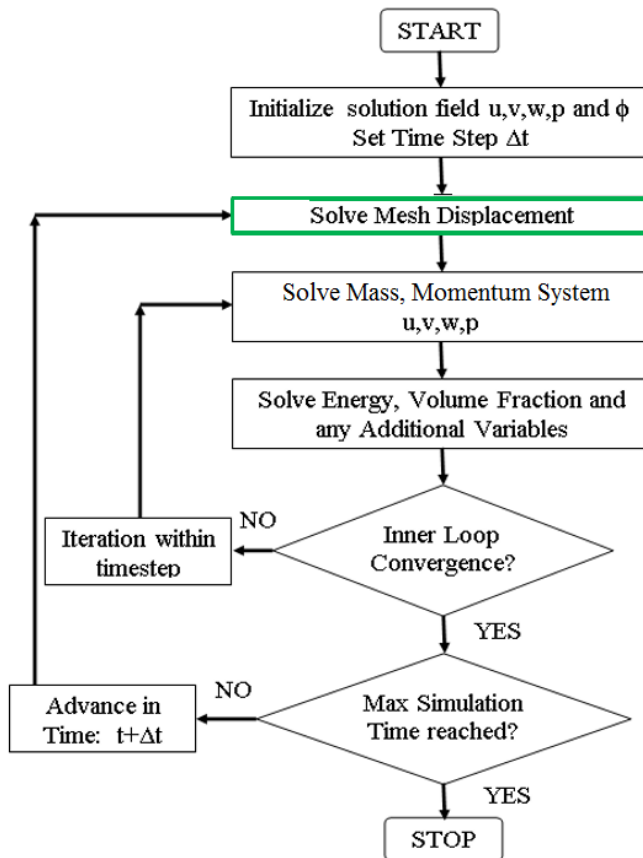


Figure 4.1 Flow chart of solution process with deforming domains

For compressible flows, where the density varies, an equation of state is used to obtain the relationship between density and pressure and the mass conservation equation is linearised in terms of pressure. Hence a coupled system of equations, involving three Cartesian velocity components and pressure, is solved for every iteration in a time step. The highlighted block, named ‘Solve Mesh Displacement’ in Figure 4.1, is of interest for this work. This step should allow for the movement of the initial grid to the new position in time, during which the control volume deforms. The mesh should retain the same number of nodes, cells and topology while the cell deformation should be defined by the movement of its nodes. The integration process and the solution of the governing equations, as described in the previous section, will ensure that the space conservation is retained at the new time instance. The node displacement can be

solved using different strategies, for example a) Spring smoothing, b) Diffusion equation smoothing or c) User defined nodal displacements through external subroutines.

4.3.1 Diffusion equation based mesh smoothing

In the diffusion equation based mesh smoothing, the specified displacement on the boundary nodes is propagated to the interior nodes by solving equation (4.9) internally in the solver.

$$\nabla \cdot (\Gamma_{disp} \nabla \delta) = 0 \quad (4.9)$$

Here, Γ_{disp} is the mesh stiffness that depends on local cell volumes and distance of the nodes from deforming boundaries. This method is graphically presented in the Figure 4.2.

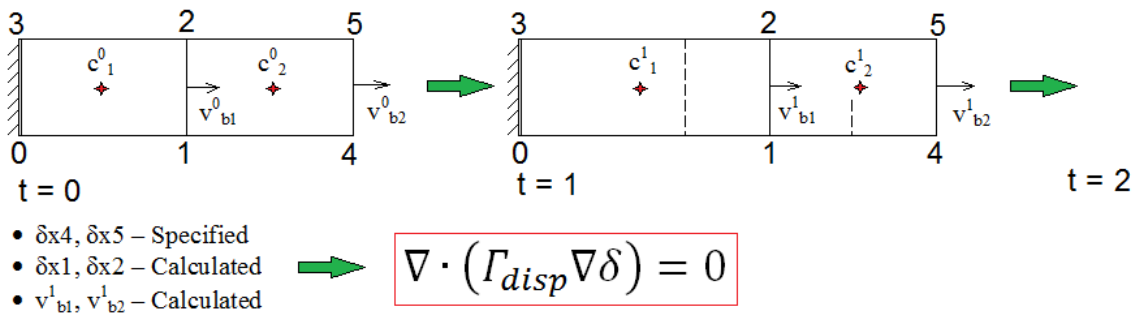


Figure 4.2 Grid deformation using Diffusion equation mesh smoothing

The number of cells and their connectivity remains constant for the duration of the calculation, with the grid being deformed at the beginning of each time step. A mesh smoothing method is not suitable for large boundary displacements because it produces cells with high skewness and there are chances of element failure due to negative volumes after high nodal displacements. This limitation is dependent on the type of cells, the grid size relative to the magnitude of the boundary displacement, the relative orientation of the cells and the boundary displacement, the position of the non-deforming boundaries etc. For example, for tetrahedral types of cell the skewness quality degrades faster with boundary displacements, compared to hexahedral cells. Hence for cases with simple geometries like a piston-cylinder this method can be used even with large displacements with hexahedral grids, but it fails for complex geometries like screw compressors.

4.3.2 User defined nodal displacement

Customised grid generators can be used to generate a set of grids representing nodal locations for every time step externally, prior to the numerical solution of flow in the calculation domain.

The numerical grid is replaced at the beginning of each time step by the use of appropriate user subroutines, often called ‘Junction Boxes’. This method is called User defined nodal displacement and is shown graphically in Figure 4.3.

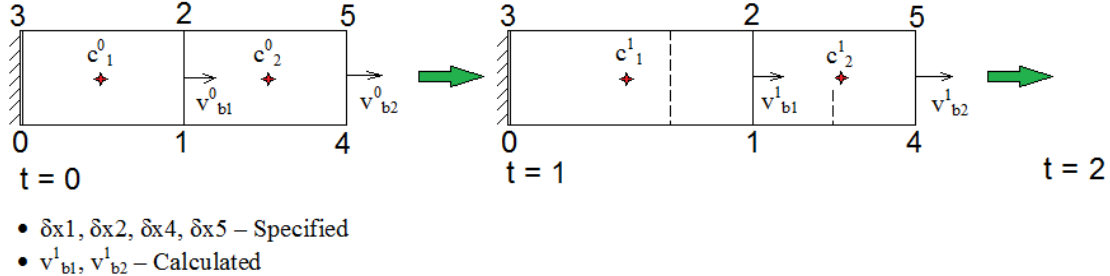


Figure 4.3 Grid deformation using User defined nodal displacement

In principle, it achieves the same result as the Diffusion equation mesh smoothing but it is suitable for large boundary displacements because the nodal positions are controlled externally.

4.3.3 Key-Frame grid re-meshing

Figure 4.4 shows another strategy suitable for high grid deformations which uses general purpose grid generators.

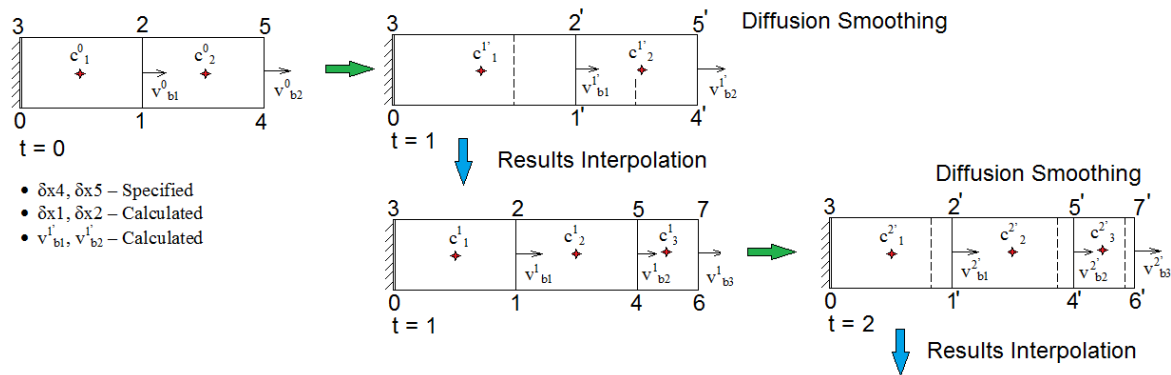


Figure 4.4 Grid deformation using Key-Frame grid re-meshing

After every time step, Diffusion smoothing is performed to obtain the new geometry. A check is then performed to determine whether the control volume cells can absorb further deformation without generating negative volume elements. Upon the discovery of irregular cells, groups of cells are selectively re-meshed locally, retaining the boundary geometry but with a change in the number of cells and their connectivity. This process is called Key-Frame re-meshing

(ANSYS, 2011). Re-meshing is followed by the next time step calculations similar to those in Figure 4.2 but an intermediate interpolation of the solution from the previous time step is required because generally all cells will have changed connectivity.

In Section 4.4, a comparison of the solution from the mentioned methods of grid deformation has been presented to study the accuracy of calculations for problems with positive displacement nature of flow physics.

4.4 Investigation of Key-frame grid remeshing technique

The discussion so far focused on techniques available for generating a grid for the rotor domain outside the flow solver. There are a few methods available which are built inside the solver and provide a certain level of control on when to replace the current computational grid with an external grid. Key-Frame grid remeshing is one such method available in most numerical solvers but it has never been tried for the calculation of flow in a screw machine. Figure 4.4, presented in Section 4.3, shows the strategy used with Key-Frame remeshing.

A case study has been presented here to assess the applicability of the key-frame re-meshing method to positive displacement calculations. A reversible adiabatic compression process in a piston cylinder was solved by the use of three grid deformation techniques: diffusion smoothing, user defined nodal displacements and key-frame grid re-meshing. Such a simplistic geometry and thermodynamic process was chosen because it forms the fundamental mechanism for calculating performance by CFD in positive displacement machines and analytical results are available for error estimation.

The isentropic compression-expansion process in a reciprocating piston cylinder can be modelled by a polytropic process equation relating the gas pressure and volume. Since the process is both adiabatic and reversible there will be no energy losses or gains in the control volume and the gas will return to its initial state given by equation 4.10.

$$\left(\frac{p_2}{p_1}\right) = \left(\frac{V_1}{V_2}\right)^{\gamma} = \left(\frac{T_2}{T_1}\right)^{\frac{\gamma}{(\gamma-1)}} \quad (4.10)$$

Consider a hypothetical piston cylinder arrangement with a sinusoidal displacement given to the piston. For this trial, a cylinder with diameter 100 mm and length 100 mm was considered. The initial position of the piston was for a maximum volume of 7.854×10^{-4} mm³. The Piston displacement was 70 mm, varying sinusoidally with a frequency of 50Hz. The final minimum cylinder volume was 2.356×10^{-4} mm³. This gave a fixed volume ratio of 3.333 for the system.

Based on equation (4.10), for an initial absolute pressure in the cylinder of 2.013 bar the expected peak pressure is 10.86 bar. Similarly, for an initial temperature of 298 K, the expected peak temperature is 482.35 K.

In order to make the CFD model isentropic, all boundaries were defined as adiabatic and the calculation of the viscous dissipation term in the conservation equation of total energy was turned off. This took reversibility, due to the turbulent viscosity dissipation factor, into account. Molecular viscosity and no slip conditions at walls were retained for the formulation to be close to physical conditions.

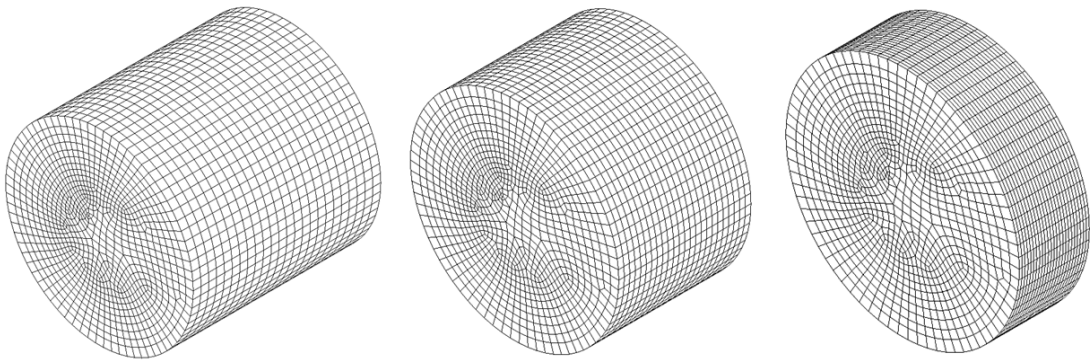


Figure 4.5 Hexahedral mesh using Diffusion smoothing (SH1)

The most suitable configuration for diffusion smoothing is a hexahedral mesh since the cell quality does not deteriorate much when boundaries deform. Figure 4.5 shows the hexahedral mesh generated by diffusion smoothing at three different time steps. The hexahedral meshes generated by diffusion smoothing were identified as **SH**. The mesh shown in Figure 4.5 is a coarse mesh consisting of 22752 cells identified as **SH1**. Two refined meshes were generated by the same method and named **SH2** consisting of 49962 cells and **SH3** consisting of 74720 cells (Table 4.2).

For the key-frame based re-meshing a tetrahedral mesh was selected, as shown in Figure 4.6. Three different cases were generated, namely coarse **KR1**, medium **KR2** and fine **KR3** consisting of similar number of cells and nodes (Table 4.2).

For the User Defined Nodal Displacement, a hexahedral mesh was selected and three grid sizes were generated to correspond to sizes of the Diffusion smoothing. These were named **UH1**, **UH2** and **UH3** respectively, as listed in Table 4.2.

The time step was 2.8571×10^{-4} sec while each cycle contained 70 time steps which corresponded to 50 cycles per second. Mesh deformation was applied after each time step. The

implicit second order backward Euler discretisation was used within the pressure based coupled solver. The advection scheme was high resolution and the turbulence model was k-epsilon. An r.m.s. residual target of 1.0×10^{-4} was maintained for all the equations. The fluid was air, assumed to be an ideal gas, with a molar mass of $28.96 \text{ kg kmol}^{-1}$, Specific Heat Capacity of $1004.4 \text{ J kg}^{-1} \text{ K}^{-1}$, Dynamic Viscosity of $1.831 \times 10^{-5} \text{ kg m}^{-1} \text{ s}^{-1}$ and Thermal Conductivity of $2.61 \times 10^{-2} \text{ W m}^{-1} \text{ K}^{-1}$.

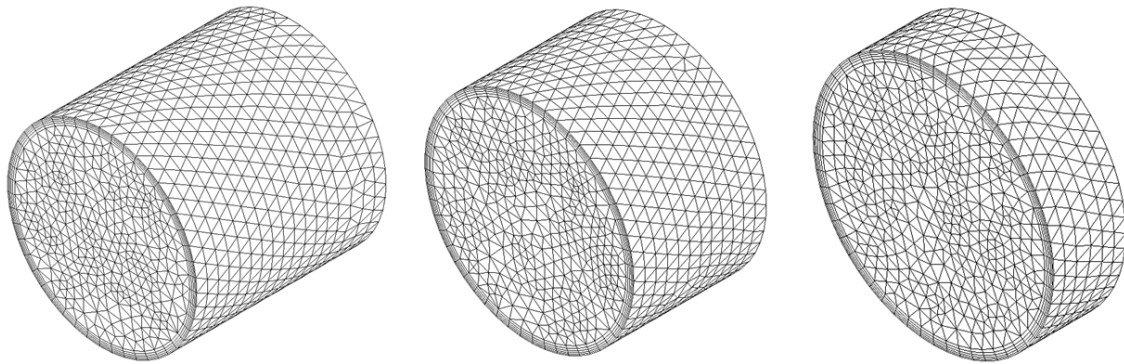


Figure 4.6 Tetrahedral mesh used in Key-frame re-meshing (KR1)

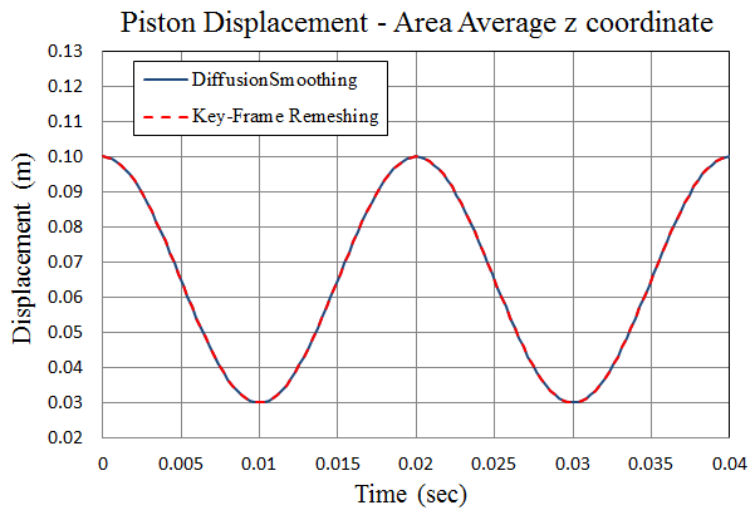


Figure 4.7 Piston displacement plot

Figure 4.7 shows the variation of piston displacement with time for the same volume ratio in cases SH1 and KR1. Figure 4.8 shows the change of pressure with time in cases SH1 and KR1. The results obtained with user defined nodal displacement UH1 were identical to that of SH. All case grid details and results are presented in Table 4.2. Although both, diffusion smoothing (SH1) and key-frame re-meshing (KR1) follow the same change of volume during compression and expansion, the calculated peak pressures are not equal. In the case of diffusion smoothing

the pressure in the first cycle achieved the theoretical peak of 10.86 bar and consistently repeated itself in the following cycles. But in the case of key-frame re-meshing the maximum pressure in the first cycle was higher than the theoretical value and it continued to increase in the following cycles. Similarly the initial state of pressure at the end of expansion did not return to its base value as it did in the case of diffusion smoothing.

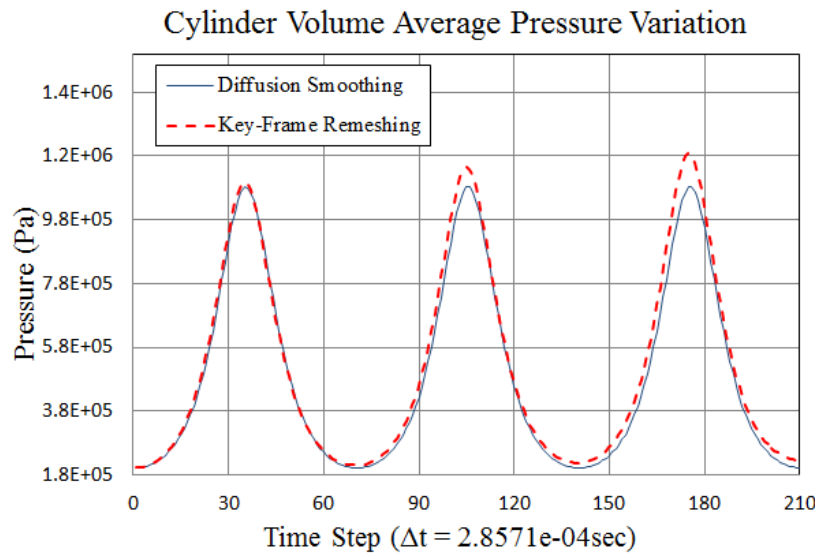


Figure 4.8 Cyclic pressure history

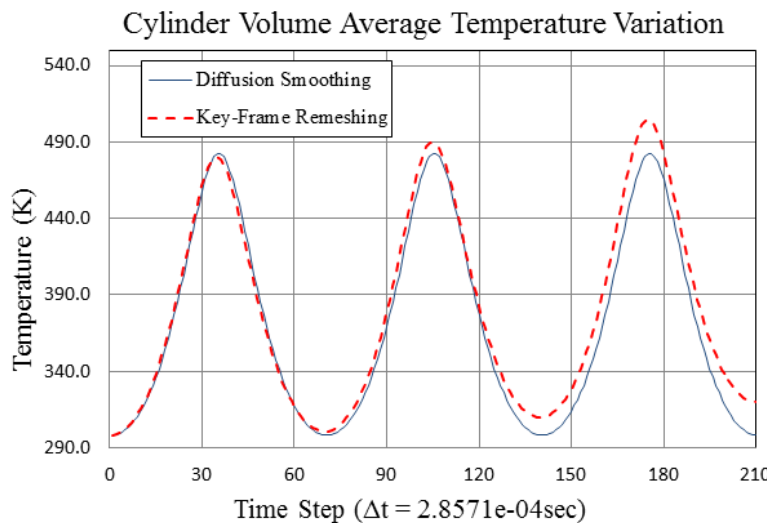


Figure 4.9 Cyclic temperature history

Figure 4.9 shows the temperature change with time in the cylinder for both cases. The peak temperatures are not equal in the two cases. In the case of diffusion smoothing the temperature in the first cycle rises to the theoretical peak of 482.35 K and repeats itself in the following cycles consistently. In the case of key-frame re-meshing the peak temperature in the first cycle

is similar to the theoretical value but it continues to increase in the following cycles. Similarly the initial state of temperature, at the end of expansion does not return to its base level of 298 K as it does in the case of diffusion smoothing. Table 4.2 shows the error in the prediction of pressure and temperature obtained from the three different grid deformation strategies with three different grid sizes and over multiple consecutive compression cycles.

Table 4.2 Error in Pressure, Temperature and Gas Mass

	Cycle	SH1	SH2	SH3	KR1	KR2	KR3	UH1	UH2	UH3
Number of Cells		22752	49962	74720	42098	118749	211418	22752	49962	74720
Number of Nodes		24650	53244	79171	11849	31514	53148	24650	53244	79171
Error in Pressure [%]	I	-0.44	-0.44	-0.44	1.17	1.34	1.11	-0.44	-0.44	-0.44
	II	-0.42	-0.42	-0.42	6.23	7.26	7.41	-0.42	-0.42	-0.42
	III	-0.41	-0.41	-0.41	10.55	12.95	14.41	-0.41	-0.41	-0.41
Error in Temperature [%]	I	-0.08	-0.08	-0.08	0.05	0.32	0.25	-0.08	-0.08	-0.08
	II	-0.07	-0.07	-0.07	3.44	4.18	3.74	-0.07	-0.07	-0.07
	III	-0.05	-0.05	-0.05	8.56	9.80	10.24	-0.05	-0.05	-0.05
Error in Mass [%]	I	-0.38	-0.32	-0.30	1.78	1.91	2.27	-0.38	-0.32	-0.30
	II	-0.38	-0.32	-0.30	2.91	3.21	3.88	-0.38	-0.32	-0.30
	III	-0.38	-0.32	-0.30	2.15	3.29	4.43	-0.38	-0.32	-0.30

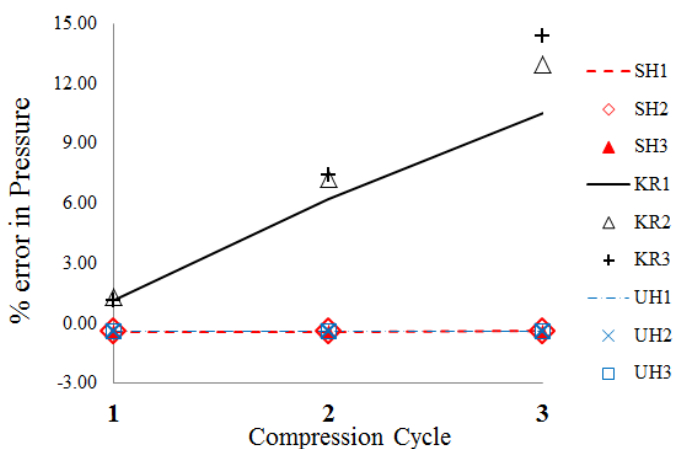


Figure 4.10 Error in pressure predictions of adiabatic cycles

The error in the pressure predictions over three consecutive compression cycles for the various grid deformation strategies is shown in Figure 4.10, while Figure 4.11 shows the error in the temperature calculation over the compression cycles for these three cases.

The results show that the Diffusion smoothing (SH) based method of grid displacement and the User defined nodal displacement (UH) based method of grid displacement produce the same, highly accurate predictions which conform with the theoretical results for this deforming boundary formulation. However, errors in the pressure and temperature prediction exist when the key-frame re-meshing based method of grid deformation is used. For the key-frame re-meshing method, the error increases with the grid refinement.

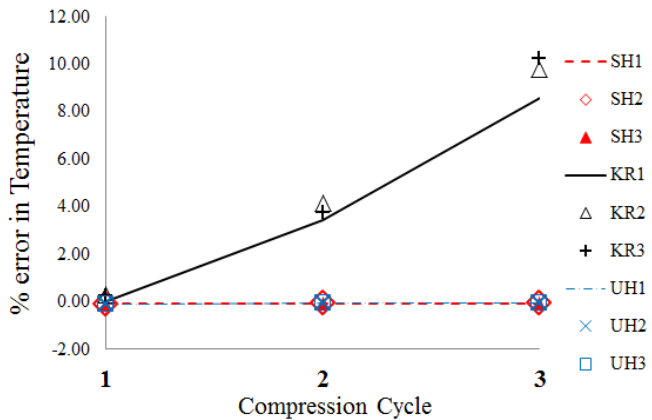


Figure 4.11 Error in temperature predictions of adiabatic cycles

Since the mesh is replaced for each time step it is quite possible that it induces an increase in calculation error. As pointed out in *Ferziger and Perić (1996)*, this can lead to artificial mass source errors in the continuity equation that can also accumulate with flow time. Table 4.2 shows the error in mass over multiple consecutive compression cycles for the three different grid deformation strategies. Limiting the mesh, to be replaced, only when the cell quality is severely reduced, should help to reduce the error, but in the case of complex topologies, as in screw machines, this is very difficult.

In conclusion, the Key-Frame Re-Meshing method gave inconsistent results with increasing error in pressure and temperature predictions in successive compression cycles. Grid refinement also did not improve the accuracy of Key-Frame Re-Meshing while reducing the time step made excessive demands on pre-processing. However Diffusion Smoothing and User Defined Nodal Displacement produced identical results with accurate estimates of pressure and temperature.

Thus for further work on grid generation for non-conventional screw machines, such as single screw rotors, variable pitch and profile machines and tri-rotor screws , it was necessary to extend the customised grid generation techniques and use a strategy such as the User Defined Nodal Displacement during the ALE calculations.

4.5 Algebraic approach for grid generation of twin screw machines

The principles of algebraic grid generation are presented in this section with their application to a twin screw machine for generating a block structured grid. Figure 4.12 shows the main stages of the procedure developed by *Kovačević et al.* (2002). The domain of the working chamber is decomposed into the low pressure port, the rotor domain and the high pressure port, as shown in Figure C.1. The rotor domain, which deforms with time, consists of a hexahedral grid, and a set of grids representing the entire compression cycle is required to be supplied to the solver for continuous simulation. The low pressure and high pressure ports can be meshed using general purpose grid generators and it is easier to have a tetrahedral grid with fine prism layers covering the boundaries. These tetrahedral grids interface with a structured grid, built on the rotor domain via non-conformal conservative interfaces in the flow solver.

An algebraic grid generation method employing multi parameter one dimensional adaptation and transfinite interpolation is used to construct the hexahedral grid in the rotor domain. A block structured numerical mesh is desired in the rotor domain. In order to construct an O grid it is necessary to subdivide the topology of the male rotor, the female rotor and the casing together into two. One O grid is constructed on the male side and other on the female side. It is most convenient to do this, splitting in 2D cross section of the rotors, and the envelope method of gearing is used to construct a rack curve between the male and the female rotor profiles to split into two O grid primitives as described in [Appendix C](#).

Consecutive 2D cross sections are calculated individually using following steps (*Kovačević, 2002 and 2005*):

1. Transformation from the ‘physical’ domain to the numerical non-dimensional domain.
2. Definition of the edges by applying an adaptive technique.
3. Selection and matching of four non-contacting boundaries.
4. Calculation of the curves, which connect the facing boundaries by transfinite interpolation.
5. Application of a stretching function to obtain the distribution of the grid points.
6. Orthogonalisation, smoothing and final checking of the grid consistency.

This procedure is the most important function of the framework and provides flexibility to extend it to more complex rotor designs like variable pitch or variable profiles. A detailed description of the algebraic approach for screw rotors is given in [Appendix D](#).

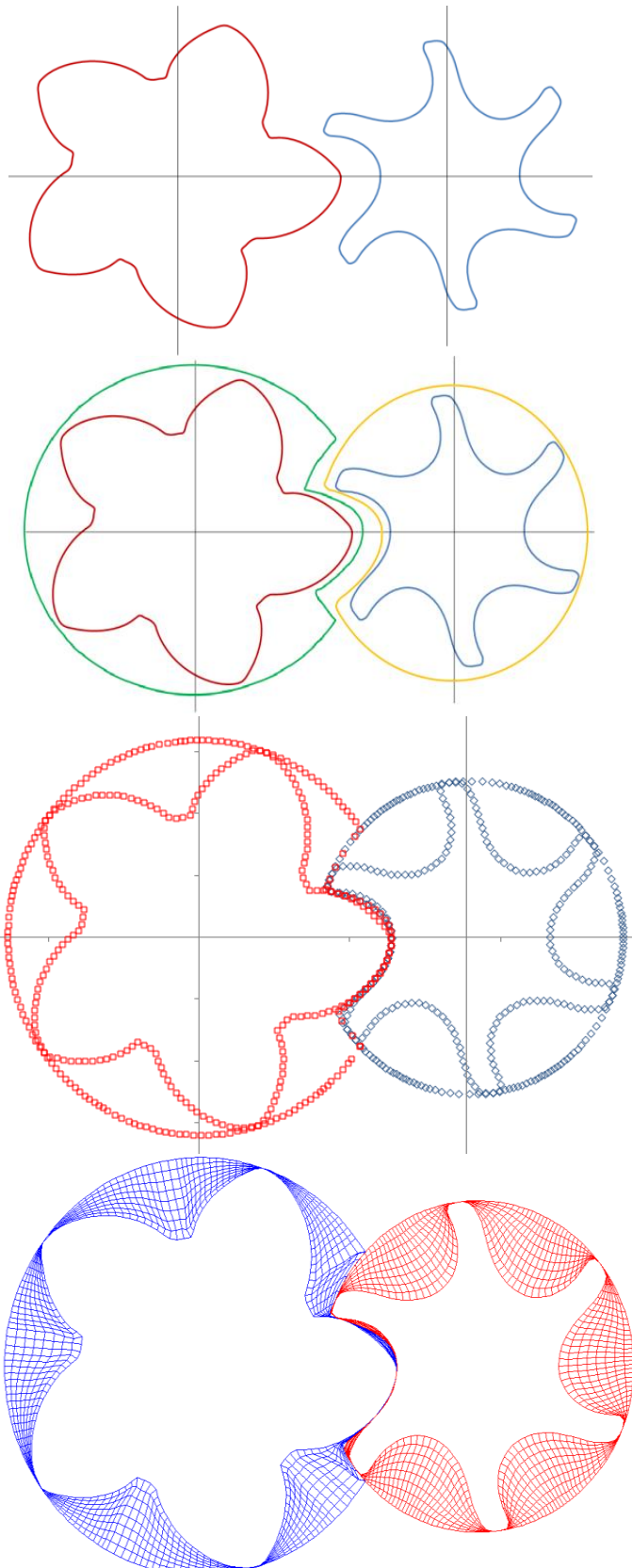
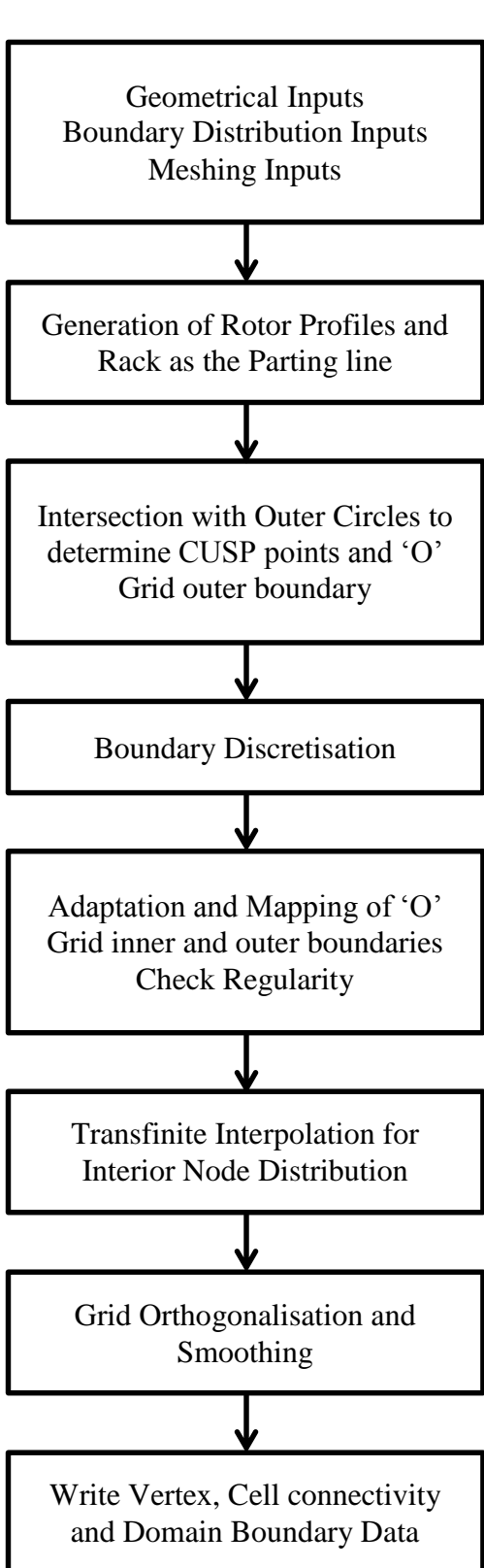


Figure 4.12 Simplified block diagram – Algebraic rotor grid generation

4.6 Differential approach for grid generation of twin screw machines

The differential equation based decomposition is a generic method that can be applied to a variety of twin rotor machines like lobe pumps, tooth compressors, screw compressors etc. the working chamber is again split into the deforming domain of the rotors and the static domains of the low pressure and high pressure ports as shown in Figure C.1. The compression chamber is defined using the rotor profile and the casing and a block structure grid is generated by the stages shown in Figure 4.13.

The beneficial properties of the differential solution are well known and were first utilised by *Crowley and Winslow* for generating a triangular 2D mesh (*Winslow*, 1964, 1966) in the numerical solution of PDE's for static magnetic fields. *Winslow* did not have to solve the Laplace equation, but by inverting the equations (B.22) and (B.23) as shown in Section B.5, with stretching functions equal to 0, the grid coordinates in the physical domain were obtained directly, using the finite-difference method.

With the differential approach, the grid for main flow calculations is in turn generated from the solution of an elliptic PDE like the Laplace equation $\nabla^2 \phi = 0$. Hence the first task after representing the compression chamber is to slice it into a number of 2D cross sections. Depending on the lead of the helical rotor, each 2D section spacing is such that it corresponds to a unit degree of rotation of the main rotor. This allows for smooth representation of the rotor lead as well as physical rotation of the rotors during simulation. Figure C.5 shows the splitting curve or division line obtained in a 2D cross section of the compression chamber.

An FVM can be used to solve the Laplace equation in the 2D domain so formed. Since the rotor profiles have close tolerances, the region formed between the casing and the two profiles has a very complex boundary. The distance between the rotor and the casing can vary from a few millimetres in the core region to a few micrometres in the clearance regions. Hence, discretisation, using unstructured triangular cells is the most appropriate. The gaps can be highly refined to capture the iso-potential lines conforming with the boundary, accurately. Figure 4.13 shows a triangular mesh generated using the commercial grid generator ANSYS. In practise 10 – 15 times higher refinement is necessary. *Vande Voorde et al.* (2005) used a customised Delaunay triangulation program (*Riemslagh et al.*, 1998, 2000) for this initial triangular grid construction. Further details of this approach are given in [Appendix E](#).

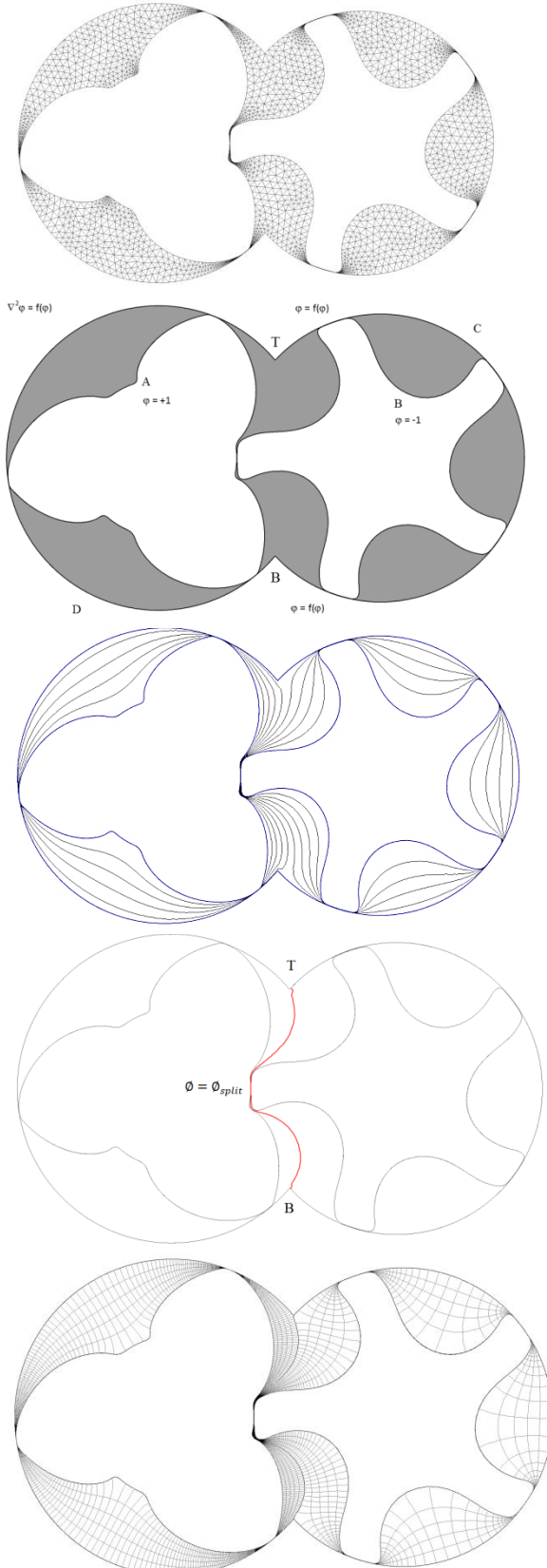
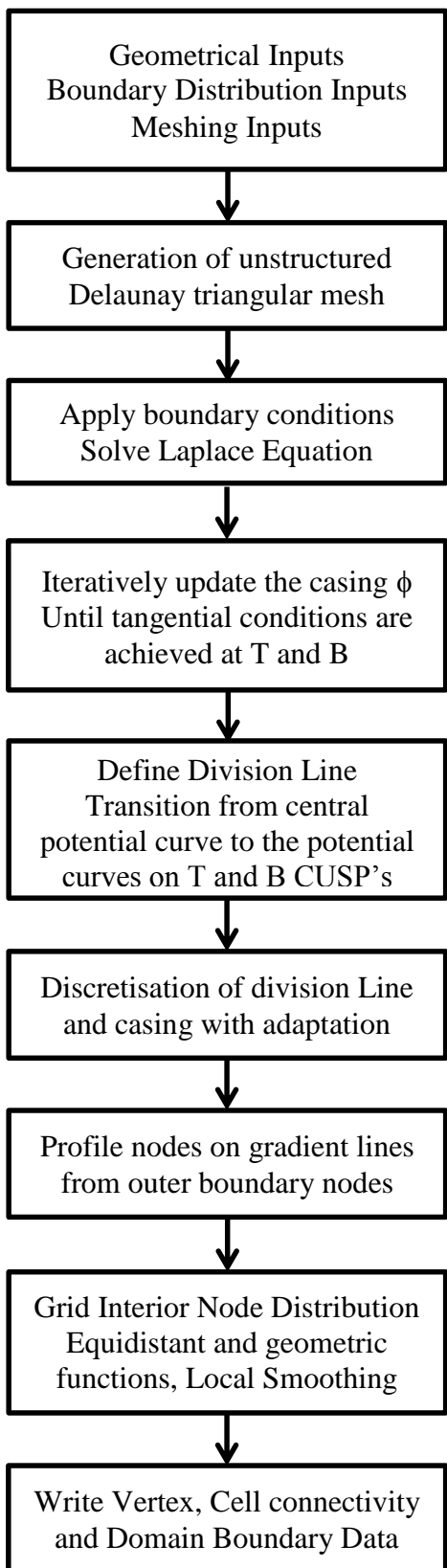


Figure 4.13 Simplified block diagram – Differential rotor grid generation

4.7 Comparison of the two approaches

Table 4.3 presents a comparison between the algebraic and the differential approach applied to screw rotor grid generation. It is seen that each of the approach has its own advantages and limitations.

Table 4.3 Comparison of algebraic and differential approach for screw rotor grids

Criteria	Algebraic Approach (Kovačević et al., 2002)	Hybrid Differential Approach (Vande Voorde et al., 2005)
1 Rotor Domain Decomposition	Analytical rack or Numerical rack. Rack based decomposition is very fast.	Differential division line. Differential division line decomposition is generic in nature.
2 Boundary Distribution	Profile discretisation according to selected adaptation. Rotor projection used with regularity checks for outer boundary Rotor \Rightarrow Outer boundary With Rotor \Rightarrow Outer boundary, the O blocks rotate with the rotor. Grid deformation occurs at the rack interface.	Casing plus Division line distributed first using equidistance and radius of curvature factors. Profile nodes projected of gradient line. Outer boundary \Rightarrow Rotor With Outer boundary \Rightarrow Rotor, the O blocks do not rotate but deform as rotor surface turns.
3 Interface between the two O Blocks	Non-Conformal. Non-Conformal interface is handled by flux balance in the solver, gives more flexibility for adaptation.	Conformal. Conformal interface is desirable for higher solution accuracy. Demanded by some CFD solvers.
4 Control on grid size	Circumferential and radial divisions and rotor angular positions. Fixed number of angular positions constraint the solver time step size for given speed.	Circumferential and radial divisions and rotor angles at every degree position. Intermittent rotor positions obtained by linear interpolation.
5 Control functions	Two variable unidirectional adaptation on the rotor, TFI with tension spline factor, orthogonalisation and smoothing factors. Rotor profile adaptation captures the 3D surface more accurately.	Division line to CUSP transition, local smoothing and geometric spacing in radial direction.

6	Time required for grid generation	<p>For 50 rotor positions, on an i3 processor it takes about 5 sec for boundary distribution and 30 sec for 2D mesh generation.</p> <p>Full set with 750 grids takes about 1 hour.</p>	<p>A representative mesh took about 900 sec for one position on DS20 processor. Full set took about 15hrs.</p> <p>Solution to the initial PDE is iterative and consumes time to get tangential conditions at the CUSP's.</p>
7	Cell structure	<p>In order to retain the CUSP line in 3D, some pyramid or prism cells are introduced by merging nodes at the CUSP.</p>	<p>All cells are purely hexahedral. Near tip of the gate rotors some face Warpage occurs due to grid line alignments.</p>
8	Cell jump	<p>Generally near the CUSP region between the two O blocks.</p>	<p>Generally in the transition region from central division line to casing.</p>
9	Adaptation to variable lead rotors	<p>Directly possible with 3D grid rearrangement.</p>	<p>Directly possible with 3D grid rearrangement.</p>
10	Adaptation to variable profile rotors	<p>Possible with modification in the algorithm to execute 2D generation on each profile and with 3D grid rearrangement.</p>	<p>Practically challenging due to the requirement of potential solution in 3D or on multiple 2D profiles for each position.</p>
11	Advantages	<p>Fast and good control over the node distribution.</p> <p>Rotor profile smoothly captured in the grid.</p> <p>Grid refinement is relatively easy to be achieved.</p>	<p>Very smooth cells.</p> <p>Fully Hexahedral.</p> <p>Conformal interface between O blocks makes the grid suitable for variety of solvers and complexities like Multiphase flows.</p>
12	Difficulties	<p>Due to Non-conformal interface, some solvers do not function with the helical rotor grids.</p>	<p>No functional difficulties except for the computationally expensive generation procedure</p>

From the description of the techniques in the algebraic and differential approach and the comparison of the two, it can be said that a good choice of theories is currently available for extending the grid generation to variable geometry rotors. For variable lead rotors both approaches can be used effectively. For the case of variable profile rotors, the algebraic approach is favourable. Further, on a generic level, if 3D grids have to be directly generated, say for intersecting axis rotors, then the differential approach blends itself favourably because the potential solution used as a base is not dependent on the relative orientation of the rotors.

4.8 Summary

In this chapter the governing equations and strategies of mesh deformation have been reviewed for their applicability to screw machine calculations. For the simplistic case of adiabatic compression and expansion by a piston in a cylinder, the Key-Frame remeshing method gave inconsistent results, with increasing error in pressure and temperature predictions in successive compression cycles, whereas the methods of diffusion smoothing and user defined nodal displacement produced identical results with accurate estimates of pressure and temperature.

Thus for implementing grid generation in variable geometry screw machines, it is necessary to extend the customised grid generation techniques and use a strategy such as user defined nodal displacement, during the ALE calculations. A comparative study between the algebraic and differential approaches has helped in the selection of techniques that can offer feasibility for implementing grids for variable geometry rotors and also for improving the grid quality.

Chapter 5 – Grid Generation for Variable Geometry Screw Machines

5.1 Introduction

The algebraic approach and the differential approach have been employed successfully for grid generation in the deforming rotor domains with available methods and a number of publications have demonstrated the use of these tools. However, there is no commercial grid generation tool that is able to provide a robust solution for variable screw geometries. With this consideration, if any new developments in the fundamental approach of grid generation are to be investigated, or if the grid for any new rotor geometry needs to be generated, then it is best to suitably apply such developments to the existing algebraic or differential framework. The frame work of algebraic approach presented in Section 4.5 and Appendix D and is very adaptable to include variable geometry rotors with parallel axes. From the preliminary investigation in Chapter 4, it appears that grids, thus generated, capture the rotor profile very effectively, because the grid lines run along the helix of the rotors and the rotor profile adaptation functions refine small curved regions. Small clearances are well captured along with the blow-hole area. Also the grids are of suitable quality for major flow solvers like ANSYS CFX, Pumplinx, etc. Hence the development presented in this thesis has been programmed with the algebraic approach. Nonetheless, their formulation is such that these methods could also well be applied to the differential framework, which was presented in Section 4.6 and Appendix E.

The chart, in Figure 5.1, highlights the main features of how the algebraic framework was developed. The two main developments are the 3D rotor grids to capture variable geometry rotors and the 2D cross section grid generation. The work on the 2D grid is given in Section 5.2, with examples of the formulated functions. The grid generation for variable geometry like the lead variation and rotor profile variation is described in Section 5.3. Some examples of variable lead rotors with uniform profile are presented in Section 5.3.4 and an example of a rotor, with uniform lead and a linearly variable rotor profile along the axis, which results in conical rotors, is given in Section 5.3.5. A procedure for generating an inflation layer grid, adjacent to the rotor surfaces, is given in Section 5.4.

The development for variable geometry rotors is designed for working chambers of screw machines with parallel axes and either external or internal meshing of the rotors. It can also include a combination of variable rotor lead and rotor profile. It is not directly suitable for non-parallel axis type machines, like single screw compressors, but by extension of techniques to decompose the working chamber, as described in [Appendix C](#), the variable geometry algorithm can be adapted to globoid types of rotor.

Twin rotor grid generation

3D Grid generation developments	Variable lead rotors	Uniform, linear and stepped lead variation formulated
	Variable profile rotors	Independent profile variation in each rotor section possible
Developments in 2D cross section	Distribution from outer boundary to inner boundary	Achieves fully quadrilateral cells in 2D
	Regularisation by full rotor transformation and skewed sine function	Achieves conformal interface between the rotors for parallel lobed rotors
	Regularisation by background block distribution	Achieves independent grid refinement in the interlobe region
	Inflation layer	Refinement of grid adjacent to rotor surface

Figure 5.1 Grid generation developments for twin screw rotors

5.2 Development of the algebraic approach to improve cross section grid

Motivation for developments in 2D grid generation

There are two features that require attention, with the algebraic approach for 2D grid generation,

- a) The interface between the two O blocks is Non-Conformal

Figure 5.2 shows an example of a non-conformal interface between the two rotor blocks. Such a grid is generated when completely discontinuous O Blocks are constructed. They give flexibility to improve the cell quality in the individual blocks by orthogonalisation and smoothing and at the same time improve the robustness of the control parameters used for profile adaptation and distribution regularisation.

The presence of a non-conformal interface raises concerns about the stability of the solver and quality of the flux balance that will be achieved with any additional physical equations as in the case of oil injection or water cooling. Moreover not all solvers are capable of defining an interface with the high node movements experienced in a helical screw grid.

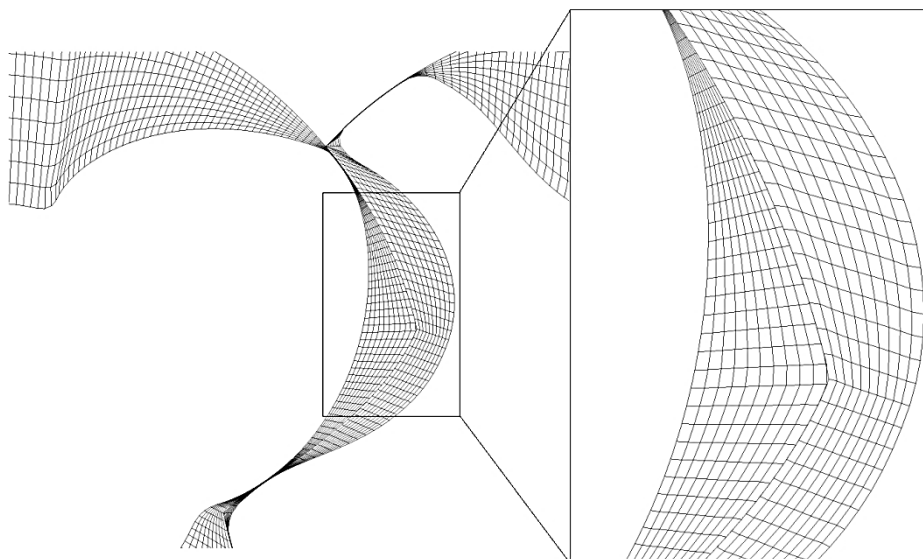


Figure 5.2 Non-conformal interface between the two rotors

- b) At the CUSP points there exist nodes merged with other nodes.

The nodes at the CUSP points need to merge in order to capture a straight line in the axial direction and for accurate estimation of the blow-hole area, as shown in Figure 5.3.

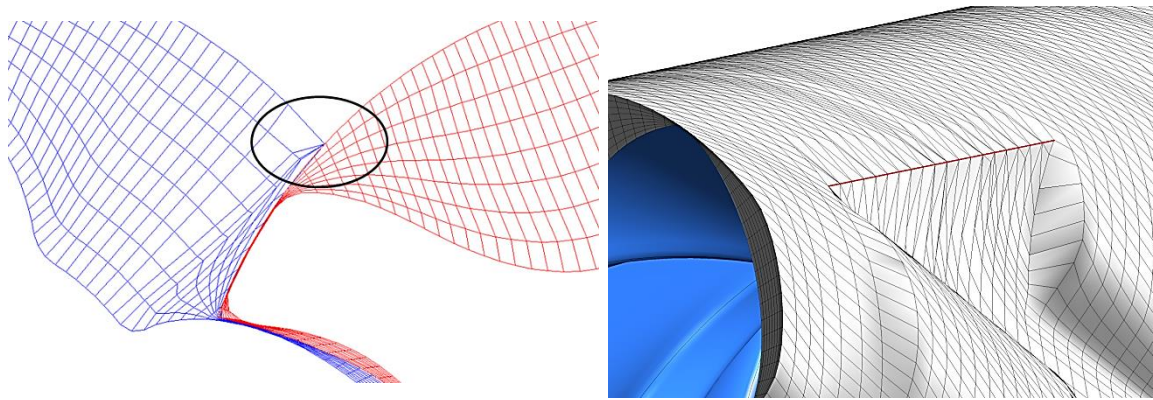


Figure 5.3 Merged nodes at the CUSP point to capture blow-hole

This results in the creation of Pyramid or Prism cell topology at the CUSP's. Although this is not an error, the conservation equations are solved by the solver treating the respective element topologies. However the use of some solvers, when the nodes are merged during the solution progress, can result in degenerated cells.

From the preliminary research of the differential approach, it was found that both of the above attributes are effectively treated if the boundary distribution on the O Blocks is directed from the outer boundary to the rotor profile. This is in contrast to the existing approach of the algebraic method with fixed nodes on the rotor profile and regularisation of distribution on the casing and rack boundary. To address these aspects of the 2D grid, a new distribution function was formulated that maps the boundaries in the required reverse direction. In order to regularise this, two new procedures have been proposed.

The first method uses coordinate transformation of the full rotor region, along with a skewed sine function that is adaptable for a given rotor profile, and has the capability to achieve a conformal interface between the two rotor O blocks when the lobes on the rotor are non-helical.

The second approach for regularisation of distribution is based on the principle of blocking. This generates a new distribution from the outer boundary to inner boundary guided by blocks. This approach independently refines the grid in the interlobe region in order to improve the rotor curvature and leakage gaps. Also a conformal interface between the two rotor O blocks can be achieved.

5.2.1 Distribution from outer boundary to inner boundary

In the algebraic approach presented in Section 4.5, the rotor cross section is first split into two O blocks using analytical or numerical decomposition techniques. The same procedure is used

as the initial step when the distribution is to be directed from the outer boundary to the inner boundary. Once the distribution is obtained the interior nodes are calculated using Transfinite Interpolation (TFI), followed by orthogonalisation and smoothing operations. The main steps in the cross section grid generation are:

1. Split the rotor cross section into two O blocks using rack as the splitting curve. Refer to [Appendix C](#).
2. Define the Outer boundary in each O block as a combination of the rack segment and the casing circle segment. The rack segment runs from bottom CUSP point to the top CUSP point and the casing segment is the remaining part as shown in Figure 5.4.
3. Discretize the rack segment using equidistant distribution. Maintain the same distribution in both the O blocks to get conformal interface. This distribution is not essentially to be equidistant and could also be adapted based on curve functions.
4. Discretize the casing segment in each O block using equidistant distribution. Figure 5.4 shows the distribution obtained on the outer boundaries of the two O blocks that will act as the reference for the rotor profile distribution.
5. Forward coordinate transformation of the outer boundary and the inner boundary from (x, y) to (ξ, η) coordinate system. Fundamentals of transformation are presented in [Appendix B](#).
6. Distribute nodes on the rotor profile with corresponding distribution available on the outer boundary. The initial distribution can be selected as the constant ξ coordinate intersections with the transformed rotor profile to get the η coordinate. But this will produce overlap in the region where lobes twist, especially on the gate rotor profile and has been discussed in [Section 5.2.2](#), Figure 5.7. Hence it is required to regularise this distribution.
7. Regularise the rotor profile distribution. Two methods of regularisation have been proposed here.
 - a. Skewed Sine function.
 - b. Back ground blocking distribution.
8. Reverse coordinate transformation from (ξ, η) to (x, y) domain to get the rotor geometry.
9. Interior node distribution using TFI.
10. Orthogonalisation and Smoothing iterations to improve the cell quality.

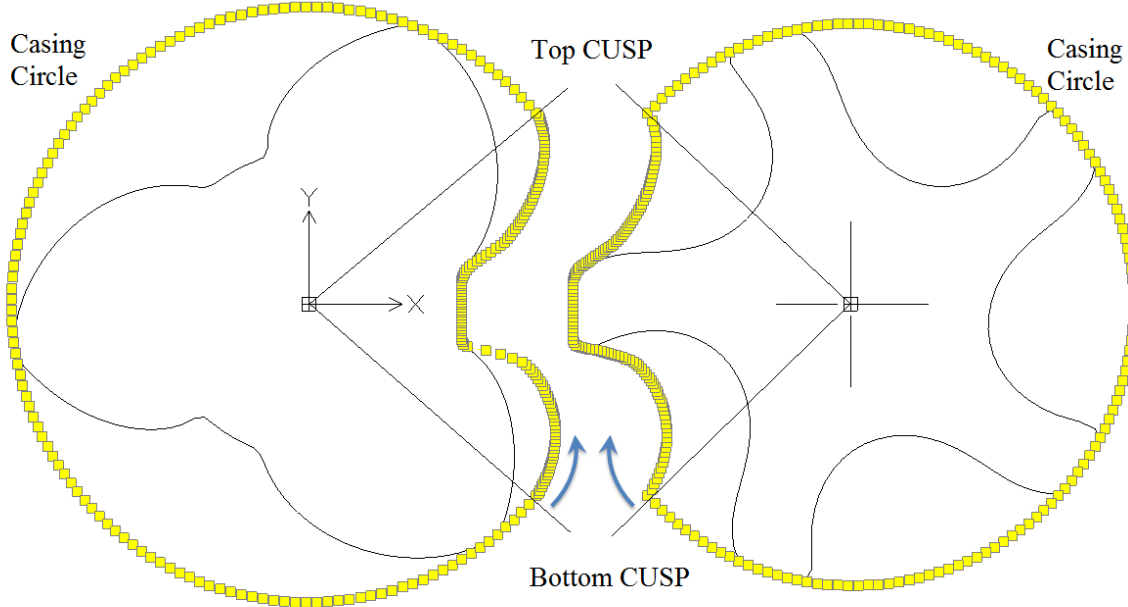


Figure 5.4 Distribution of nodes on the outer boundary

5.2.2 Coordinate transformation of the full rotor region

A mapping function was used to transform the full rotor profile and the rack plus casing onto the (ξ, η) domain, which gives better control of the distribution. In the case of distribution from the rotor profile to the outer boundary this transformation was required only to be in one interlobe space as shown in Figure D.2. The rotor distribution here did not change from one interlobe to the other. But in case of outer to inner distribution each interlobe can have a different number of nodes and also their distribution on the rotor profile can change. Hence a full transformation function is required.

Suppose that the points distributed on the boundaries are represented in index notation with respect to the physical coordinate system as $\mathbf{r}_{i,j}(x, y)$. The points on the inner boundary are $\mathbf{r}_{i,j=0}(x, y)$ and the points on the outer boundary are $\mathbf{r}_{i,j=1}(x, y)$. In addition, an outer circle with a larger diameter than that of the rotor outer diameter is considered and the point distribution on this outer circle is $\mathbf{r}_{i,j'=1}(x, y)$, as shown in Figure 5.5.

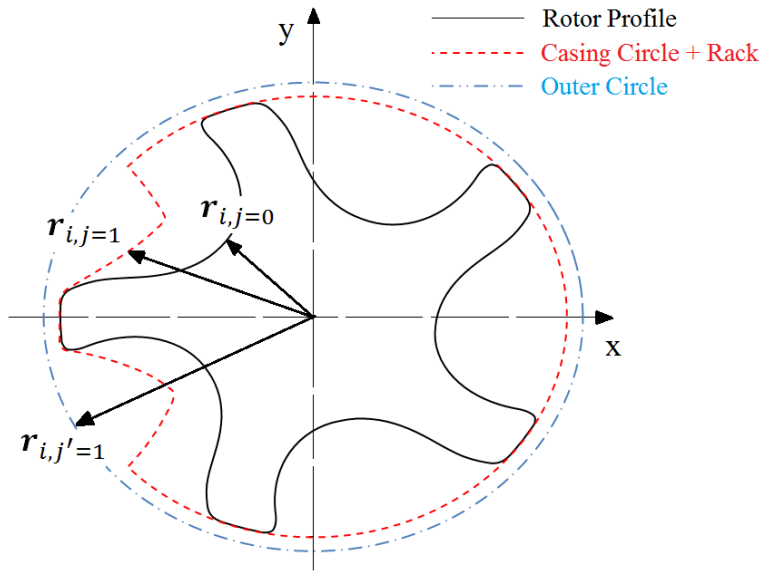


Figure 5.5 Point distribution on inner boundary and outer circle

The node distribution begins at the bottom CUSP with the index $i=0$. Based on equidistant spacing, the distribution on the rack and casing is,

$$\mathbf{r}_{i,j=1}(x,y) = \mathbf{r}_{i-1,j=1}(x,y) + S_i \quad (5.1)$$

S_i is the increment in spacing per node $= \frac{S_I}{I}$. S_I is the length of the boundary and I is the number of nodes on the rack and casing which can be set independently. The transformation from the physical region X^2 onto a computational domain Ξ^2 is such that the outer circular boundary becomes a straight line along the ξ coordinate. The transformation is represented by equation (5.2), below. It is to be noted that in the forward transformation, the rotor profile is a high density point array while in the reverse transform, the rotor profile is a discretised curve with the same number of points as the outer boundary.

For rack plus casing,

$$\begin{aligned} \xi_{i,j=1}(x,y) &= \tan^{-1} \left(\frac{y_{i,j=1}}{x_{i,j=1}} \right) \\ \eta_{i,j=1}(x,y) &= r_o - \sqrt{x_{i,j=1}^2 + y_{i,j=1}^2} \end{aligned} \quad (5.2)$$

For outer circle,

$$\xi_{i,j'=1}(x,y) = \tan^{-1} \left(\frac{y_{i,j'=1}}{x_{i,j'=1}} \right)$$

$$\eta_{i,j'=0}(x, y) = r_o - r_{oc}$$

For Rotor profile

$$\xi_{i,j=0}(x, y) = \tan^{-1} \left(\frac{y_{i,j=0}}{x_{i,j=0}} \right)$$

$$\eta_{i,j=0}(x, y) = r_o - \sqrt{x_{i,j=0}^2 + y_{i,j=0}^2}$$

Where, r_o is the radius of the rotor and r_{oc} is radius of outer circle.

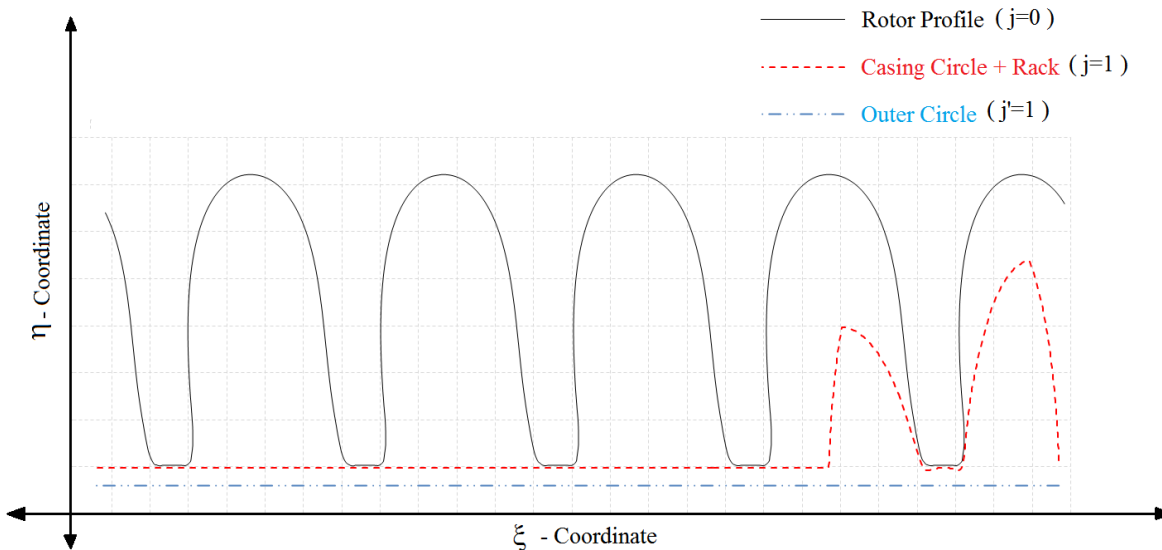


Figure 5.6 Forward transformation of full rotor region to computational domain

The Figure 5.5 shows the physical region X^2 of full rotor space and Figure 5.6 shows the computational coordinate system (ξ, η) with the forward transformed coordinates of the rack, the rotor and the outer circle in full rotor space.

The reverse transformation from computational domain Ξ^2 to physical region X^2 is required for the rotor profile in order to obtain the distribution on the rotor in physical region. This reverse transformation is represented by the following equation (5.3).

$$\begin{aligned} x_{i,j=0}(\xi, \eta) &= \text{abs} [r_0 - \eta_{i,j=0}(x, y)] \cos [\xi_{i,j=0}(x, y)] \\ y_{i,j=0}(\xi, \eta) &= \text{abs} [r_0 - \eta_{i,j=0}(x, y)] \sin [\xi_{i,j=0}(x, y)] \end{aligned} \quad (5.3)$$

Figure 5.7 shows the distribution obtained after the reverse transformation. The distribution on rotor profile has been obtained using equidistant distribution with the transformed rotor profile to get the η coordinate.

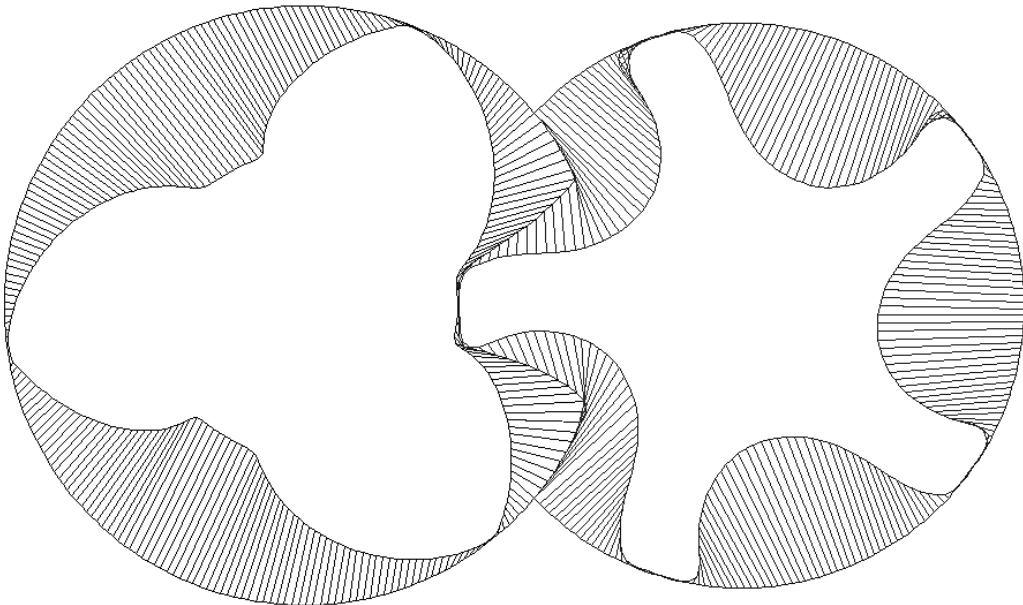


Figure 5.7 Reverse transformation of full rotor region to physical domain

It is seen that there are a lot of irregularities and crossing of the distribution lines takes place. But at the same time a conformal interface has been achieved between the two O blocks and also at the CUSP points there is no necessity to merge the nodes. This is because both CUSPs have the same index i in all the cross sections and the 3D grid line will run as a single edge at the CUSP points. It is necessary to regularise the rotor distribution in the transformed space before reverse transform is carried out to ensure that the distribution is regular.

5.2.3 Regularisation by skewed sine function

In order to achieve a conformal interface between the two rotor blocks, there has to be a one to one correspondence of the nodes on the rack curve. This imposes a constraint that the distribution on the rack curve should not be modified in the transformed space. To regularise the distribution on the profile an additional outer circle is introduced that is offset from the casing circle as shown in Figure 5.6. This outer circle is discretised with the same number of nodes as on the rack and casing circles. Each node on this outer circle is now treated as a controller of the node to be placed on the rotor profiles.

The concept of a lever hinged about the node on the rack and displaced at one end by the node on the outer circle is introduced. This has been presented graphically in Figure 5.8. The intersection of this lever on the rotor profile gives the node corresponding to the node on the rack curve. If the control node on outer circle is made to move to the left, then the intersection point with the rotor profile will move to the right. The magnitude of the leverage will be

controlled by the offset of the outer circle from the rack and the distance between the rack point and the rotor profile point. Thus independent control on each of the points distributed on the rotor profile is achieved by controlling the node movement on the outer circle.

Now a function needs to be formulated that will provide control on the spread or spacing of the nodes on the outer circle and also control the location of the focus point to which these points will attract or repel. Such a control can be achieved by a skewed sine function.

5.2.3.1 Skewed Sine Function

A skewed sine function is one in which the phase of a sine function is controlled to shift the zero crossing point and to advance or retard the peak and valley on the curve. The maximum amplitude and frequency of the function remains unchanged when the phase angle is changed. For the requirement described above, the phase angle should be defined to get a monotonic variation so that the node movement does not happen abruptly. The zero crossing point that acts as a focus point can be controlled by the amplitude of this phase angle function. The amplitude this phase angle is called the skewness of the sine function.

The skewed sine function is defined in equation (5.4).

$$f(t) = A_{sk} - \text{abs} \left\{ A_{sk} \sin \left[2 \pi n_{sk} \frac{t}{t_i} - \sigma_{sk} \text{abs} \left(\sin \left(2 \pi n_{sk} \frac{t}{t_i} \right) \right) \right] \right\} \quad (5.4)$$

Where,

A_{sk} = Amplitude of Sine function [0 to 1.0]

σ_{sk} = Skewness of Sine function [-1 to +1]

n_{sk} = Frequency of Sine function

= 0.5, to get a single focus point in each interlobe

t = time scale = $[i - i_s]$

t_i = Normalization for t = $[i_e - i_s]$

i_s = Starting index of points in current interlobe

i_e = Ending index of points in current interlobe

Points are represented by the index i . Skewness controls the location where the function will change flexure and the amplitude controls the magnitude of the function at a given point. The frequency and time scale factor is normalised such that distance from tip to tip of the

transformed rotor profile along the ξ coordinate matches with one cycle of the sine function and the number of cycles correspond to the number of interlobes as shown in Figure 5.8.

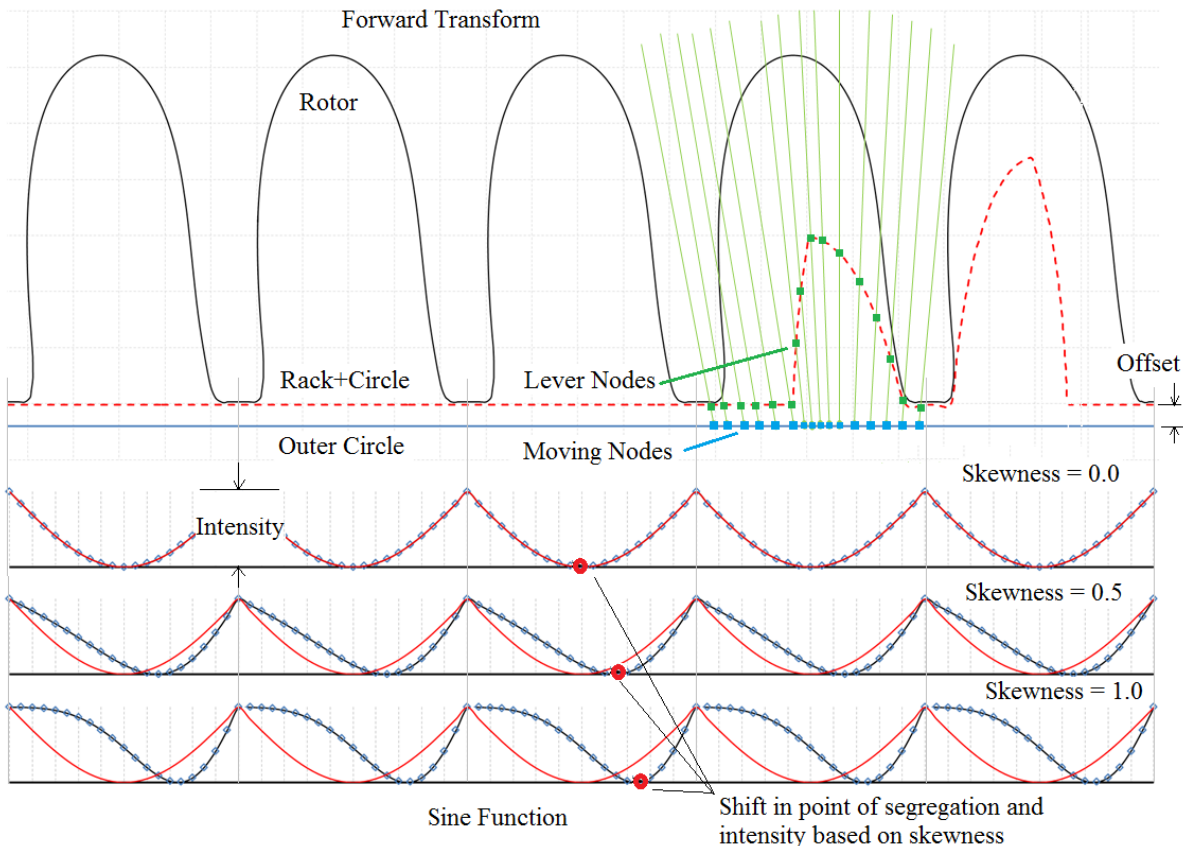


Figure 5.8 Use of skewed sine function to regularise distribution

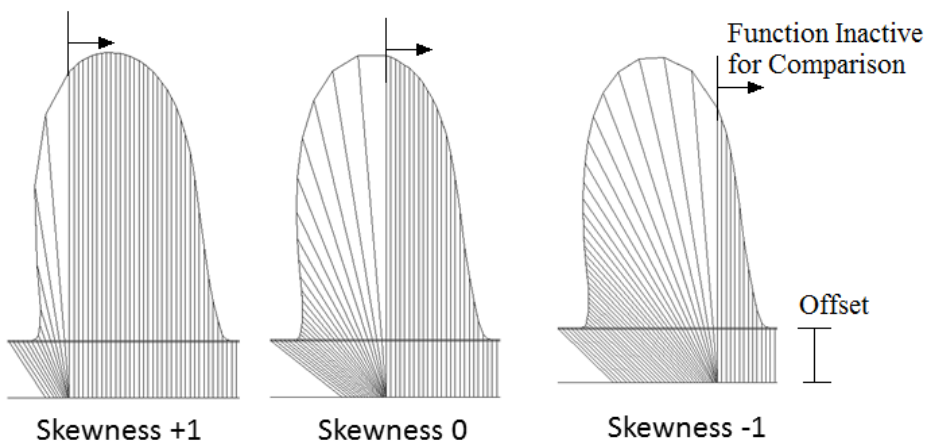


Figure 5.9 Effect of skewness of skewed sine function on distribution

When the skewness is zero, the focal point is at the center of the interlobe space. Figure 5.9 shows the influence of varying the skewness from +1 to -1 for fixed amplitude. The focal point

shifts from left to right as the skewness changes from +1 to -1. The effect has been shown only on the left side for comparison purpose.

When the amplitude is zero, there is no effect of the sine function and node position on rotor profile remains unchanged. It is noticed that in this condition the concave part of the rotor profile has not been captured due to absence of intersections with constant ξ coordinate lines.

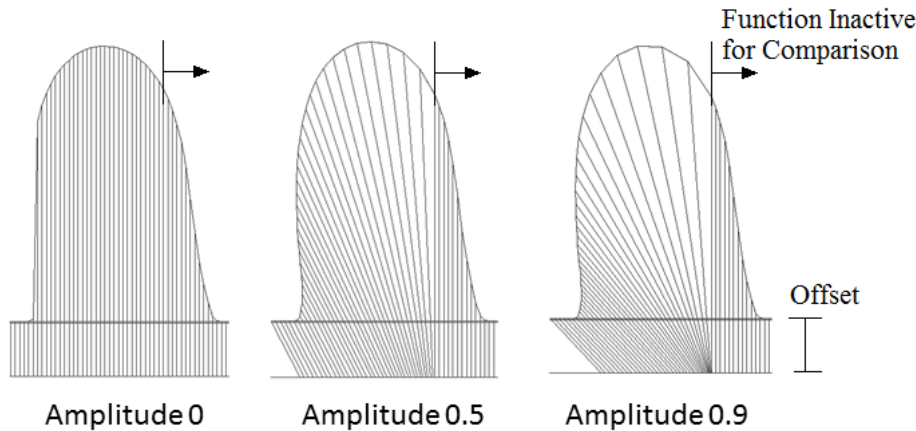


Figure 5.10 Effect of amplitude of skewed sine function on distribution

Figure 5.10 shows the influence of increasing the amplitude from 0 to 0.9. With increase in amplitude for a fixed skewness of -1, the points on the outer circle get attracted more strongly towards the focal point and hence the impact of leverage is strong. The points distributed on the rotor profile start spreading more and more.

Figure 5.11 shows the regularised distribution obtained on the main and gate rotor in the forward transformed space. In the interlobes where the rack curve is present the sine function is made to work only between the start and end points of the rack curve. While the out of rack points are aligned with the starting and ending points to get a smooth distribution.

Equation (5.3) is used for the reverse transformation of this regularised distribution onto the physical space. Figure 5.12 shows the distribution obtained by reverse transformation. The required properties have been achieved on this distribution using the skewed sine function. The interface between the two O blocks has one to one node mapping and there is no merging of nodes at the CUSP points which will produce a fully quadrilateral cell structure in the mesh.

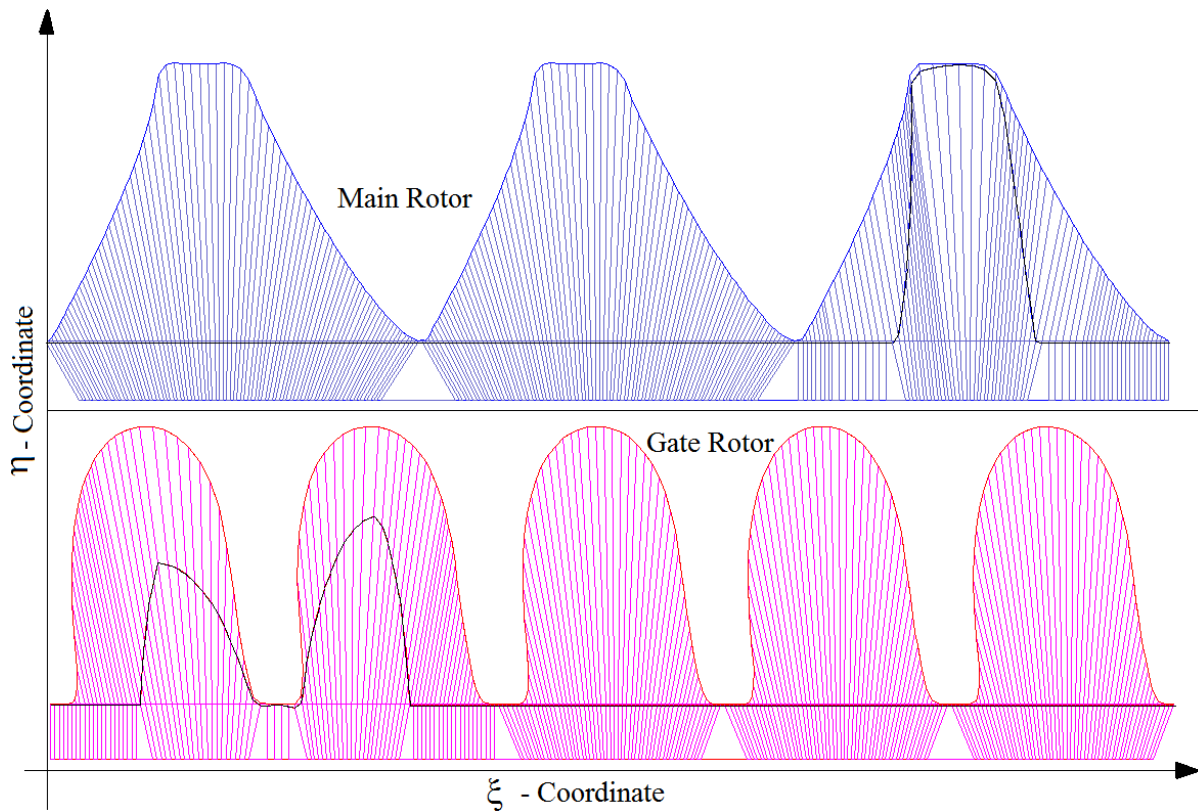


Figure 5.11 Regularised distribution obtained with skewed sine function

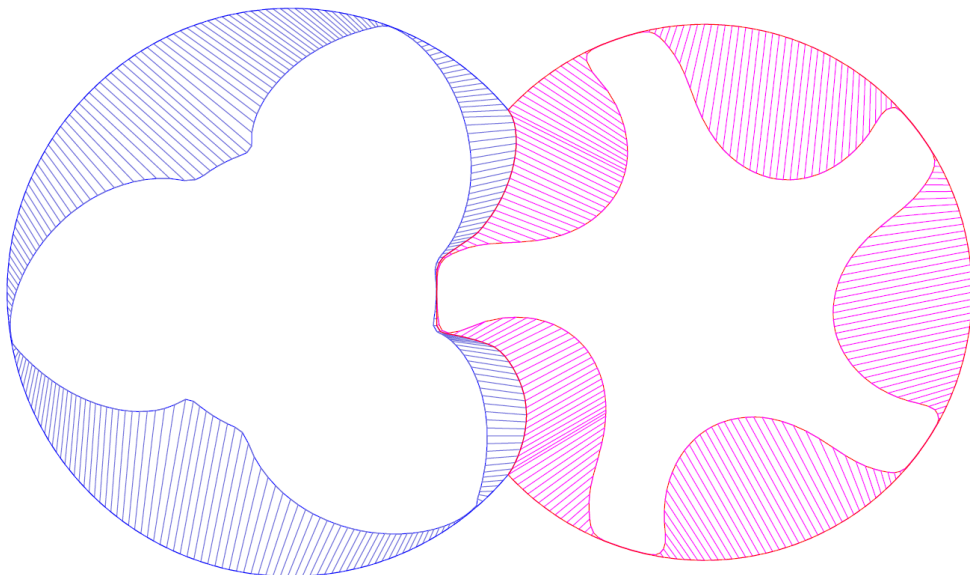


Figure 5.12 Reverse transformation of the regularised distribution

5.2.4 Example of grids with conformal interface

To demonstrate the use of the procedure of distribution from outer boundary to inner boundary and regularisation of the rotor profile by use of the skewed sine function, two types of rotors were considered.

The first example is a symmetric profile for a roots blower type of machine with 3 lobes on each of the main and the gate rotors. The lobes are non-helical and run parallel to the rotor axis. Because of the symmetric profile a small value of skewness is sufficient and also the amplitude of the sine function can be kept low.

The following values of the control parameters were used for the grid generation:

Total Circumferential nodes	230
Circumferential nodes in the interlobe	65
Radial Nodes	8
Angular divisions per interlobe angle	50
For the skewed sine function,	Skewness +0.2 Amplitude 0.15

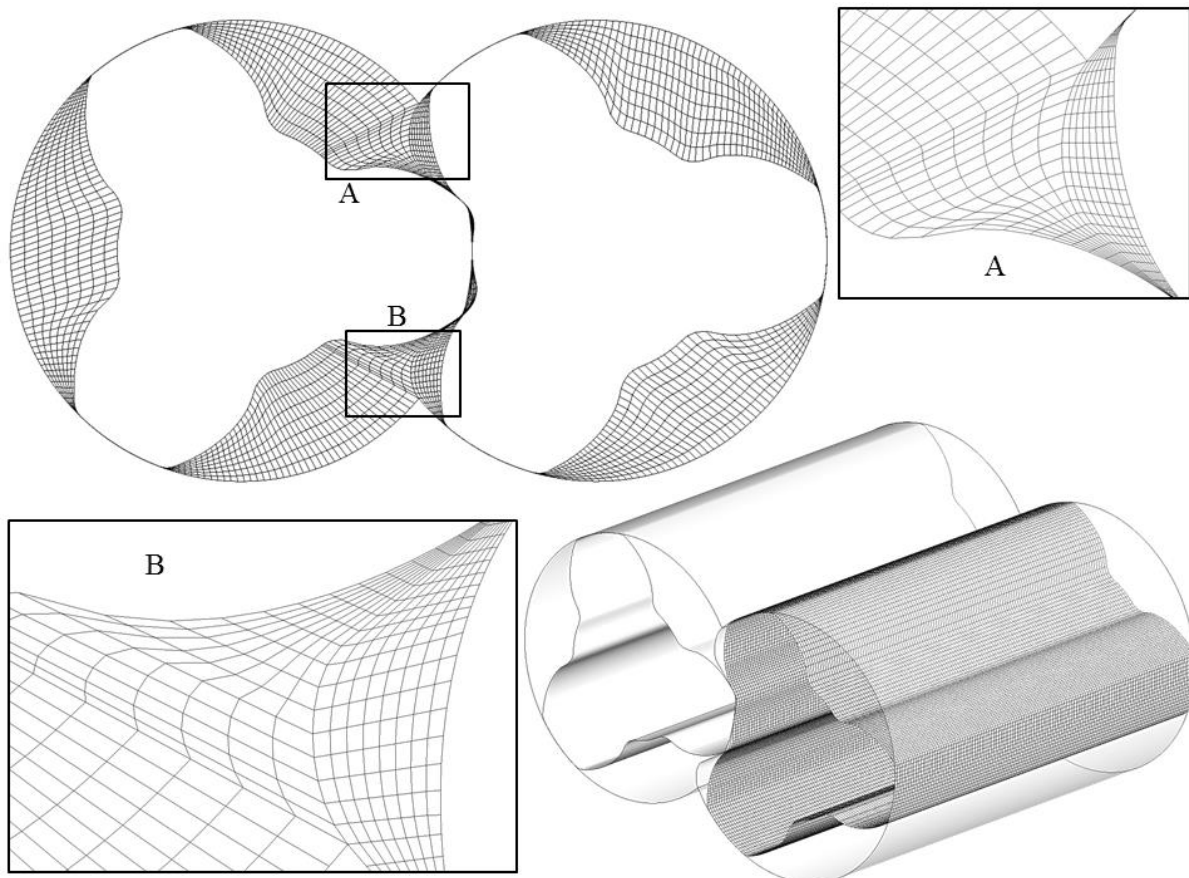


Figure 5.13 Conformal grids generated with sine function in a Roots blower rotor

The grids were successfully generated with all hexahedral cells and one to one mapping between the two rotor blocks at the interface. A cross section mesh with the interface regions highlighted and the three dimensional grid with parallel lobes is shown in Figure 5.13. A jump in cell size is seen at the transition from the rack region to the casing region. The grid in 3D is smooth and captured the rotor surface with highly regular cells.

The second example considered is a screw compressor rotor with an ‘N’ profile. The main rotor has 3 lobes and the gate rotor has 5 lobes. The profiles are deep with small radii at the fillets and also the gate rotor lobes are bent over the main rotor lobes due to the profile being asymmetric. Because of these features a relatively higher skewness and amplitude factor for the sine function were required.

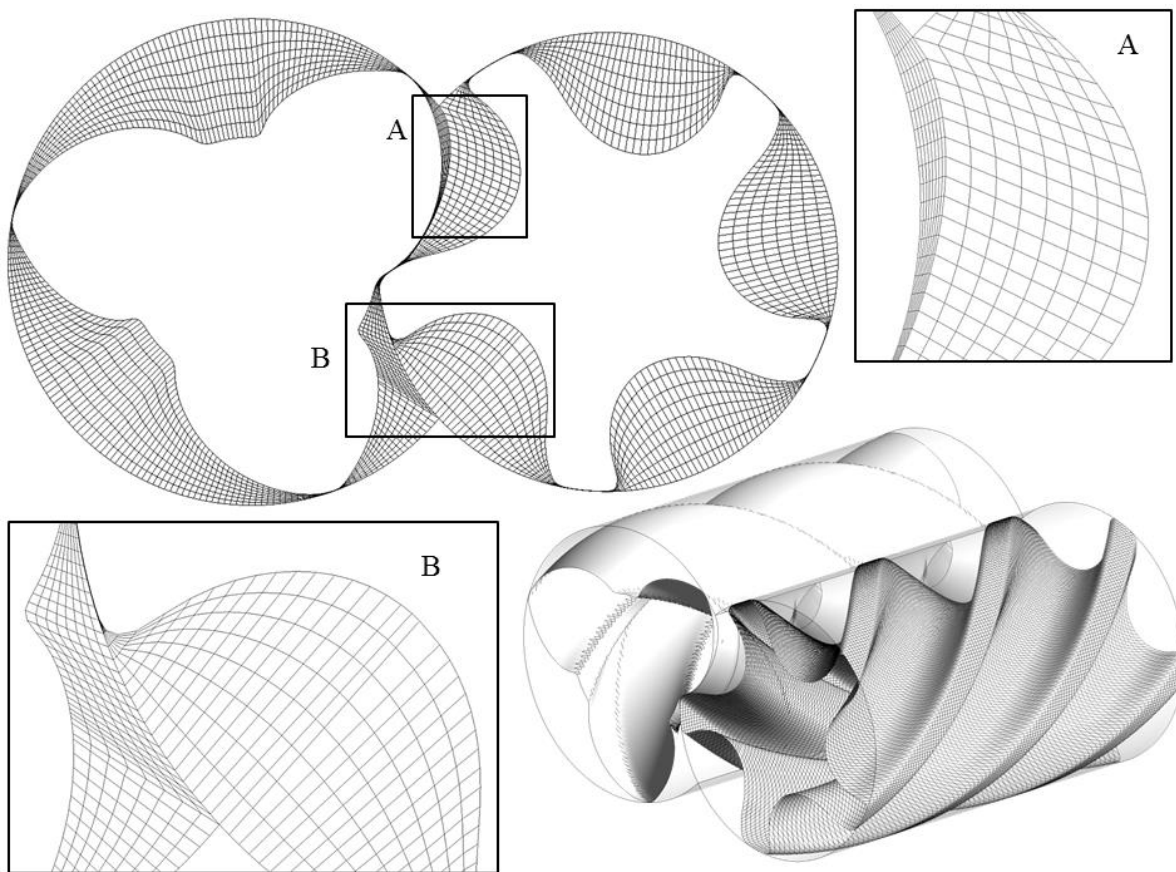


Figure 5.14 Conformal grid generated with sine function in a Screw Compressor rotor

The grids were successfully generated in the cross section with all quadrilateral cells and one to one mapping between the two rotor blocks at the interface. The cross section mesh with interface regions is highlighted and the three dimensional grid with helical lobes is shown in Figure 5.14.

The following values of the control parameters were used for the grid generation:

Total number of circumferential nodes	250
Circumferential nodes in the interlobe	65
Radial Nodes	8
Angular divisions per interlobe angle	50
For the skewed sine function,	
Main Rotor	Skewness +0.2 Amplitude 0.25
Gate Rotor	Skewness -0.5 Amplitude 0.24

Upon generation of a 3D mesh from the 2D mesh, obtained using the skewed sine function, it was found that there are defects on the surface of the rotor. When there is an abrupt change in the node positions between two cross sections, notches were getting created on the rotor profile. Figure 5.15 shows the problem area. This difficulty was not observed for rotors with non-helical lobes. As such, the method of using a skewed sine function for regularisation of rotor profile distribution has been successful for generation of conformal fully hexahedral grids for rotors with non-helical lobes, like the roots blower type, but was not successful for rotors with helical lobes. For helical rotors further improvements in the regularisation function are required in order to control the distribution of nodes on the rotor profile, taking account of the adjacent cross section grids.

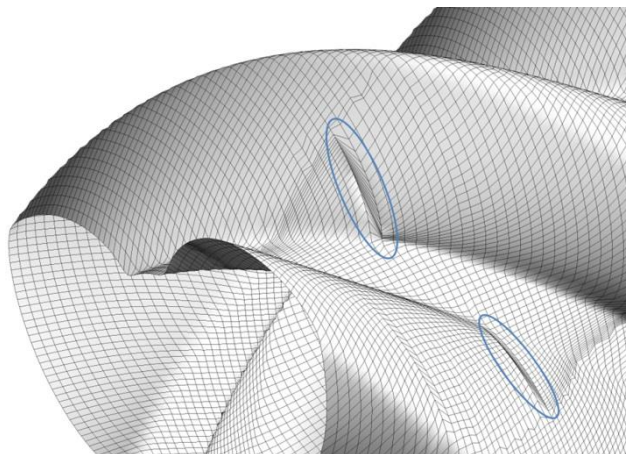


Figure 5.15 Notch defects on the rotor surface in 3D grids

5.2.5 Regularisation by background block distribution

The second approach formulated here for regularisation of distribution of nodes on the rotor profile is based on the principle of blocking used in multi block grid generation techniques (*Thompson, Soni and Weatherill, 1999*). The procedure generates a new distribution from the outer to the inner boundaries, guided by blocking. This approach has the capability of

independently refining the grid in the interlobe region in order to improve the rotor curvature and leakage gaps.

From the implementation of a skewed sine function for regularisation of the rotor profile distribution, it was evident that in case of helical rotors the distribution on the rotor profile needs a reference with respect to adjacent cross sections. Independent movement of nodes on the profile can result in notches on the rotor surface when the difference in position between two adjacent sections is too large. At the same time, with reference to the distribution presented in Section 4.5, which was directed from fixed nodes on the rotor profile to the outer boundary, it was clear that such a distribution, which fixes nodes on the rotor profile, generates a very good quality rotor surface mesh. This feature of the distribution, which is directed from the rotor profile to the outer circle, is used as background blocking to regularise the new distribution on the rotor profile.

5.2.5.1 *Background Blocking*

Background blocking can be considered as a uniform distribution of nodes on the rotor profile and on the outer circle. The outer circle is a full circle and there is no need to consider the rack segment.

Blocking is generated using following steps:

1. Nodes on the rotor profile in each interlobe are distributed, using equidistant distribution. Adaptation can also be applied.
2. On the outer circles an arc-length based distribution is constructed, which needs regularisation.
3. Both the rotor and the outer circle are transformed from physical region X^2 onto a computational domain Ξ^2 such that the outer circular boundary becomes a straight line along the ξ coordinate. The transformation function is represented by the equation (D.9) in Section D.3.
4. The outer circle nodes are regularised and redistributed using the procedure presented in Section D.3 using equation (D.12).
5. This regularised outer circle distribution along with the rotor profile distribution acts as the background blocking as shown in Figure 5.16.

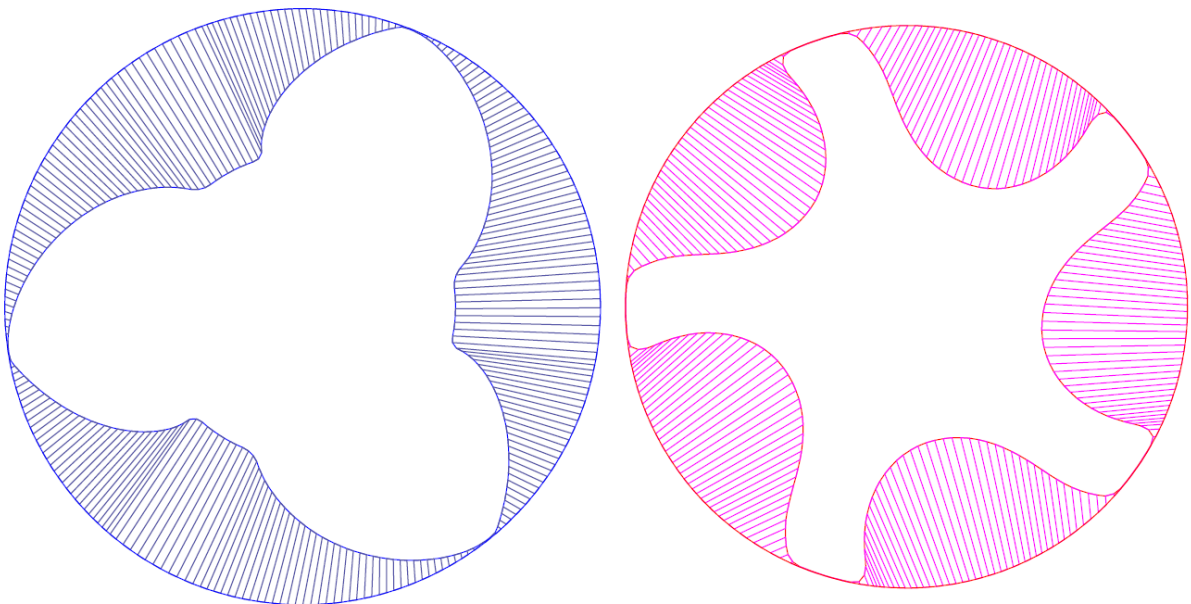


Figure 5.16 Background blocking for the main and gate rotors

The advantage of such blocks is that:

- The blocks do not have to be as refined as the final grid.
- The blocks can be used as reference for refinement in any required regions.
- The blocks have to be calculated only once and simply rotated for various other rotor positions.

5.2.5.2 Using the background blocking

Suppose that the points distributed on the boundaries are represented in index notation with respect to the physical coordinate system as $\mathbf{r}_{i,j}(x, y)$. Points on the rotor profile are $\mathbf{r}_{i,j=0}(x, y)$, points on the outer boundary consisting of casing and rack curve are $\mathbf{r}_{i,j=1}(x, y)$ and the point distribution on outer full circle is $\mathbf{r}_{i,j'=1}(x, y)$. Each of the background blocks is identified by its index \mathbf{B}_i . The points on the inner boundary of the blocks, which are the rotor profile nodes are $\mathbf{rb}_{i,j=0}(x, y)$ and the point distribution on outer full circle is $\mathbf{rb}_{i,j'=1}(x, y)$ as shown in Figure 5.17.

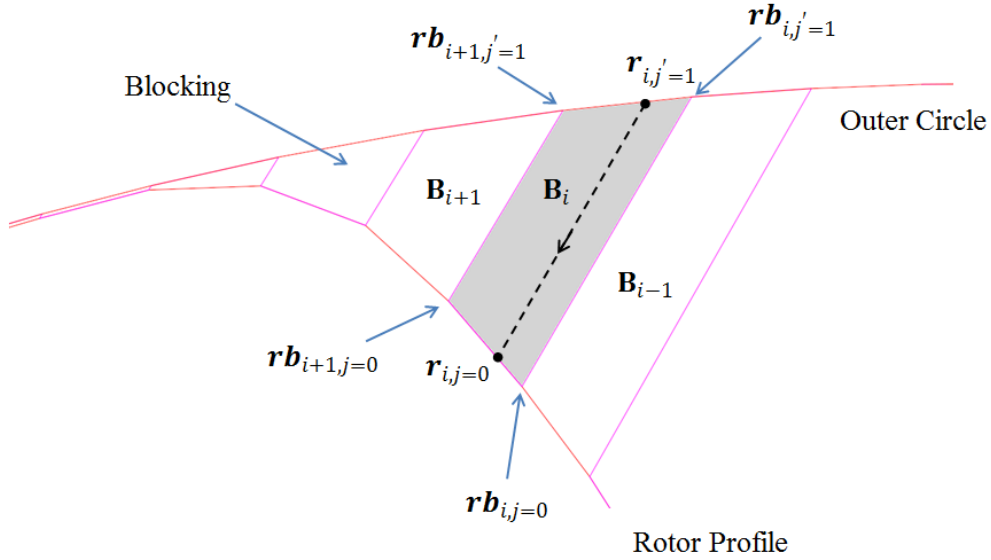


Figure 5.17 Using blocks to get rotor profile distribution

Starting from the bottom CUSP, nodes are distributed on the outer circle covering the rack part with required number of points i_{rack} . The nodes are then distributed on the outer circle covering the casing part with required number of points i_{casing} .

Factors i_{rack} and i_{casing} can be independently chosen for the main and the gate rotor or they can be set such that the sum $i_{rack} + i_{casing}$ is maintained. This will have an effect of coarsening the casing part and refining the rack part as i_{rack} count is increased. At this stage the data are available for $\mathbf{r}_{i,j=0}(x, y)$, $\mathbf{r}_{i,j'=1}(x, y)$ and $\mathbf{r}_{i-1,j'=1}(x, y)$ and it is required to calculate $\mathbf{r}_{i,j=0}(x, y)$ as shown in Figure 5.17.

This node distribution is based on equidistant spacing given in equation (5.5).

$$\mathbf{r}_{i,j'=1}(x, y) = \mathbf{r}_{i-1,j'=1}(x, y) + S_i \quad (5.5)$$

$S_i = \frac{S_I}{I}$, $S_I = \mathbf{r}_{I,j'=1}(x, y) - \mathbf{r}_{i=0,j'=1}(x, y)$, $I = i_{rack}$ on the rack and $I = i_{casing}$ on the casing. A scanning function is introduced that has the information of the background blocking. Starting from the bottom CUSP, the scanning function traces each node $\mathbf{r}_{i,j'=1}(x, y)$ and identifies the block \mathbf{B}_i to which it belongs. There can be situation when a single block has multiple nodes present in it or there can be blocks with no nodes present. This is because the distribution on the rack curve can be refined in comparison to the blocking. Similarly the distribution on the casing can be coarse in comparison with the blocking. Once the nodes

associated with each block are traced by the scanning function, an arc-length based projection is used to determine the nodes $\mathbf{r}_{i,j=0}(x, y)$ to be placed on the rotor profile. At the same time constraint is imposed on the node placement that they have to be bound in the same block \mathbf{B}_i as that of the outer circle nodes $\mathbf{r}_{i,j'=1}(x, y)$.

Figure 5.17 shows the projection of $\mathbf{r}_{i,j'=1}(x, y)$ on the inner boundary of the block in order to get $\mathbf{r}_{i,j=0}(x, y)$. This projection is based on arc length factor given by equation (5.6).

$$\begin{aligned}\mathbf{r}_{i,j=0}(x, y) &= \mathbf{rb}_{i,j=0}(x, y) + (\mathbf{rb}_{i+1,j=0}(x, y) - \mathbf{rb}_{i,j=0}(x, y)) \frac{S_i}{S_I} \\ S_i &= \mathbf{r}_{i,j'=1}(x, y) - \mathbf{rb}_{i,j'=1}(x, y) \\ S_I &= \mathbf{rb}_{i+1,j'=1}(x, y) - \mathbf{rb}_{i,j'=1}(x, y)\end{aligned}\quad (5.6)$$

The calculated positions $\mathbf{r}_{i,j=0}(x, y)$ of nodes ensure that they are guided by a regular rotor profile. Regularised distribution is superimposed onto the rack curve by finding the intersection points of the distribution lines and the rack curve. These intersection points are the new distributions $\mathbf{r}_{i,j=1}(x, y)$ on the rack curve as shown in Figure 5.18.

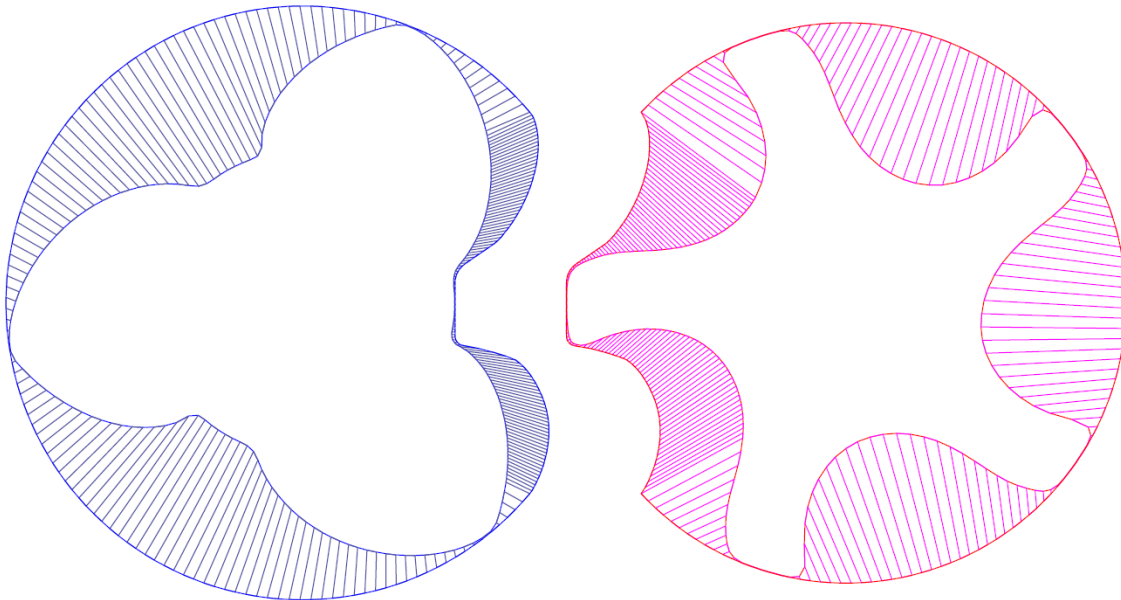


Figure 5.18 Refinement in the rack segment and superimposition of rack curve

Since the blocks on the main rotor side are different from the blocks on the gate rotor side, the intersection points obtained on the common rack curve from the two blocks are not identical. This results in a non-conformal map between the two rotor blocks. But this procedure gives an important feature to the grid to be able to construct refinement in the interlobe region. This

region is important for capturing the rotor profile in the leakage gap and hence has a strong influence on the solution of the leakage flow calculation. Also by setting the same node coordinates on the rack segment for both the blocks of the main and gate rotor a one to one conformal interface can be achieved between the two O blocks as shown in Figure 5.22.

5.2.5.3 Regularised grid with background blocking

To demonstrate the use of the regularisation of rotor profile nodes by use of the background blocking procedure, the same twin screw compressor rotor profiles were considered as those selected for the application of the skewed sine function. The following control parameters values were used for the grid generation:

Blocks per interlobe	Main Rotor	80
	Gate Rotor	50
Total number of circumferential nodes		250
Circumferential nodes in the interlobe		75
Radial Nodes		8
Angular divisions per interlobe angle		50

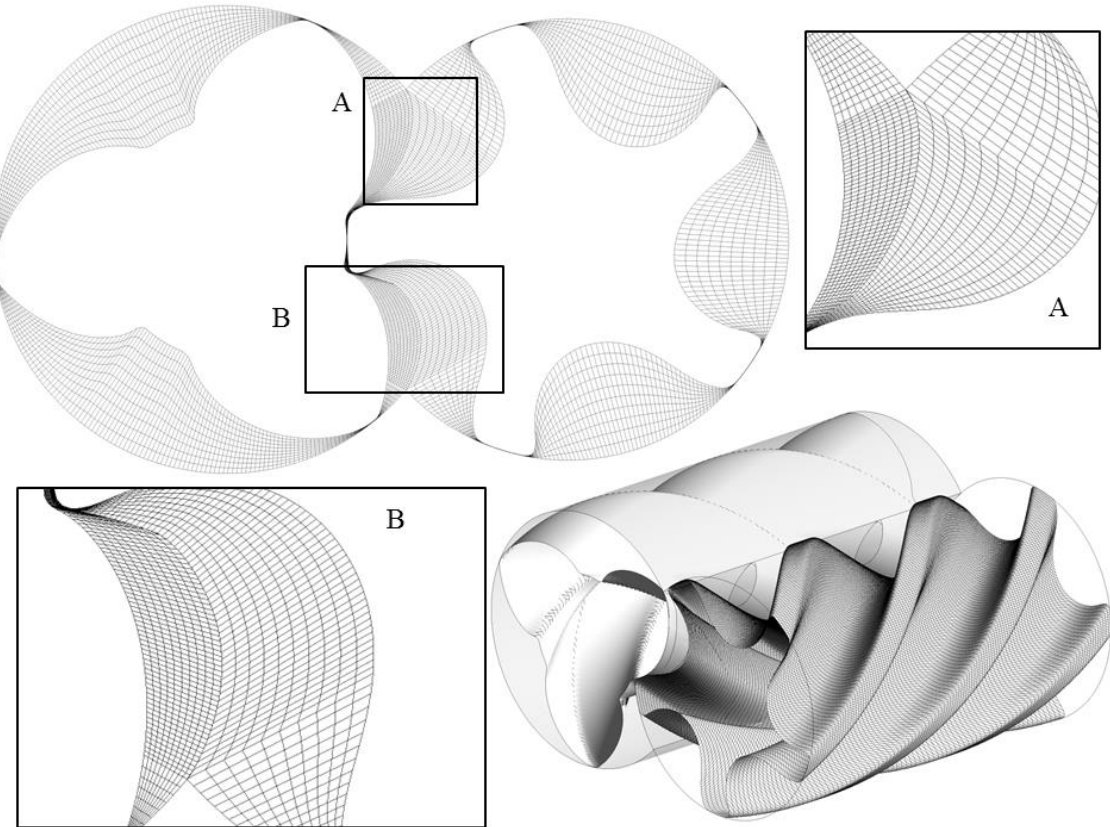


Figure 5.19 Grid generated with background blocking in screw compressor rotor

The cross section mesh with interface regions is highlighted and the three dimensional grid with helical lobes is shown in Figure 5.19. The mesh in the cross sections was successfully generated with all quadrilateral cells and an independent setting could be applied to the number of nodes in the interlobe region.

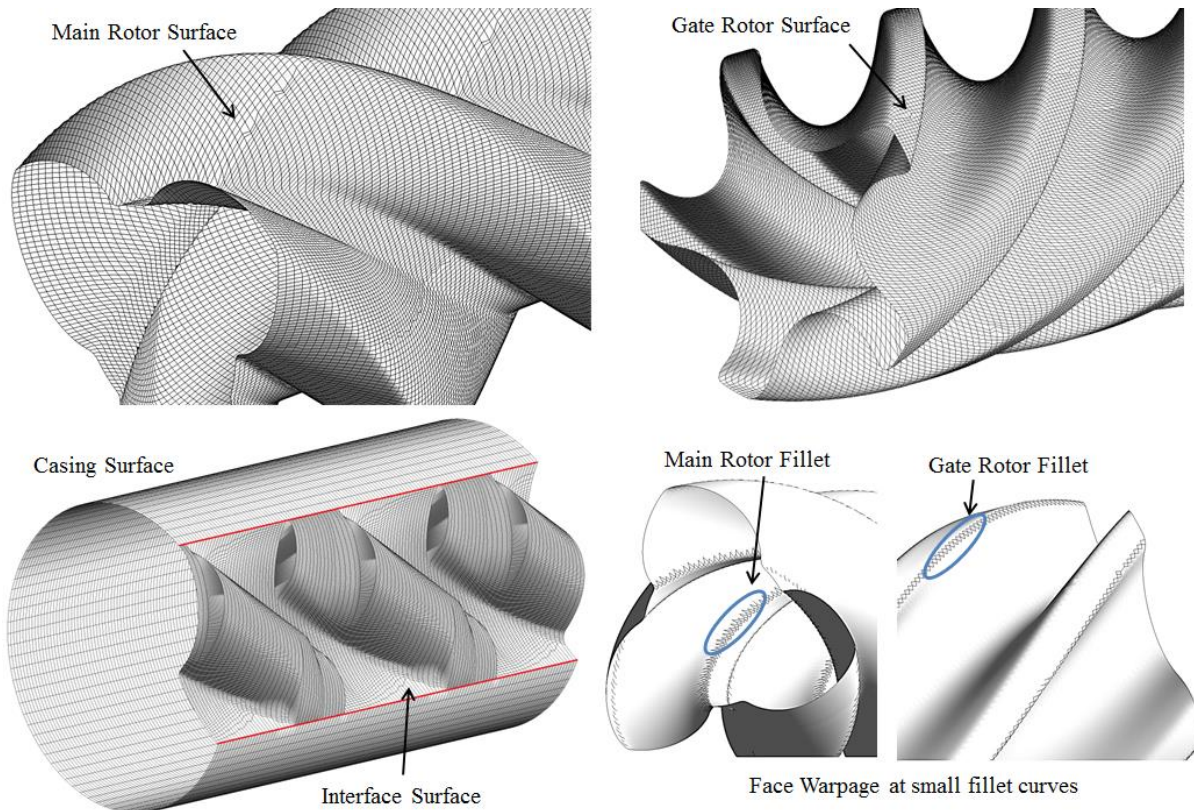


Figure 5.20 Surface mesh on the rotor, casing and the rack interface

Figure 5.20 shows the 3D rotor mesh obtained by the use of background blocking. The skewed sine function had resulted in notches on the surface mesh of these rotors. But with the blocking approach the 3D grid is fully hexahedral and both the main and the gate rotor surfaces are smoothly captured. At the transition point from the interlobe region to the casing region small non-aligned node movements are seen. But these are on the surface of the rotors and do not result in any irregular cells. The casing surface mesh is of the highest quality with very regular quadrilateral cells. The surface mesh on the interlobe interface has axial grid lines that show non-aligned movement, which are cyclically repeated in every set of cross sections near the top and bottom CUSP's. These movements are on the surface of the interface and do not result in any irregular cells. Because the nodes are not mapped one to one on the two sides of the interface there is a difference in the face sizes on the two sides. This needs to be considered by the solver for accurate flux balance. In all the cross sections, the index of the top and bottom

CUSP points is the same and hence a straight line is obtained in the axial direction which captures the blow-hole area accurately.

At the root of the main rotor and at the tip of the gate rotor there are small fillets. When the grid distribution is directed from the rotor profile to the casing, the grid lines, in the axial direction, run along the helix of the rotor and capture these small fillets with good quality. But when the grid distribution is directed from the casing to the rotor profile, the grid lines in the axial direction are the lines connecting the nodes with the same circumferential indices. Hence they do not run along the helix of the rotors. This results in face Warping of the cells that have to come across these small fillet radii in the cross section, as shown in Figure 5.20.

5.2.6 Example of grids with interlobe refinement

From the regularisation of the rotor profile distribution based on the approach of background blocking, it was seen that it is possible to construct the rack distribution by placing a number of nodes independent of those present on the blocking. Also it is possible that the grid density on the rack segment is different, compared to that on the casing segment during redistribution. This feature gives an additional useful property to the grid generated using the distribution directed from outer boundary to the rotor profile, that the interlobe region can be refined by placing a higher number of nodes on the rack segment. Figure 5.21 shows an example of successively increased refinement in the interlobe region. The sum of $i_{rack} + i_{casing}$ is maintained constant in these examples. This has the effect of coarsening the casing part and refining the rack part as the i_{rack} count is increased from 75 to 200, but the total mesh count remains constant.

Even with large differences between the number of nodes on the casing and the number of nodes on the rack segment, a smooth rotor surface is captured. This is because background blocking ensures that the nodes are always placed within the constraints guide by the rotor profile. With higher refinement, the rotor curvature in the interlobe region is captured more accurately and this will result in better prediction of the interlobe leakage flow. There is a large cell volume change observed at the transition from the rack to the casing region and a gradual redistribution on the casing nodes can be applied to get a smooth transition.

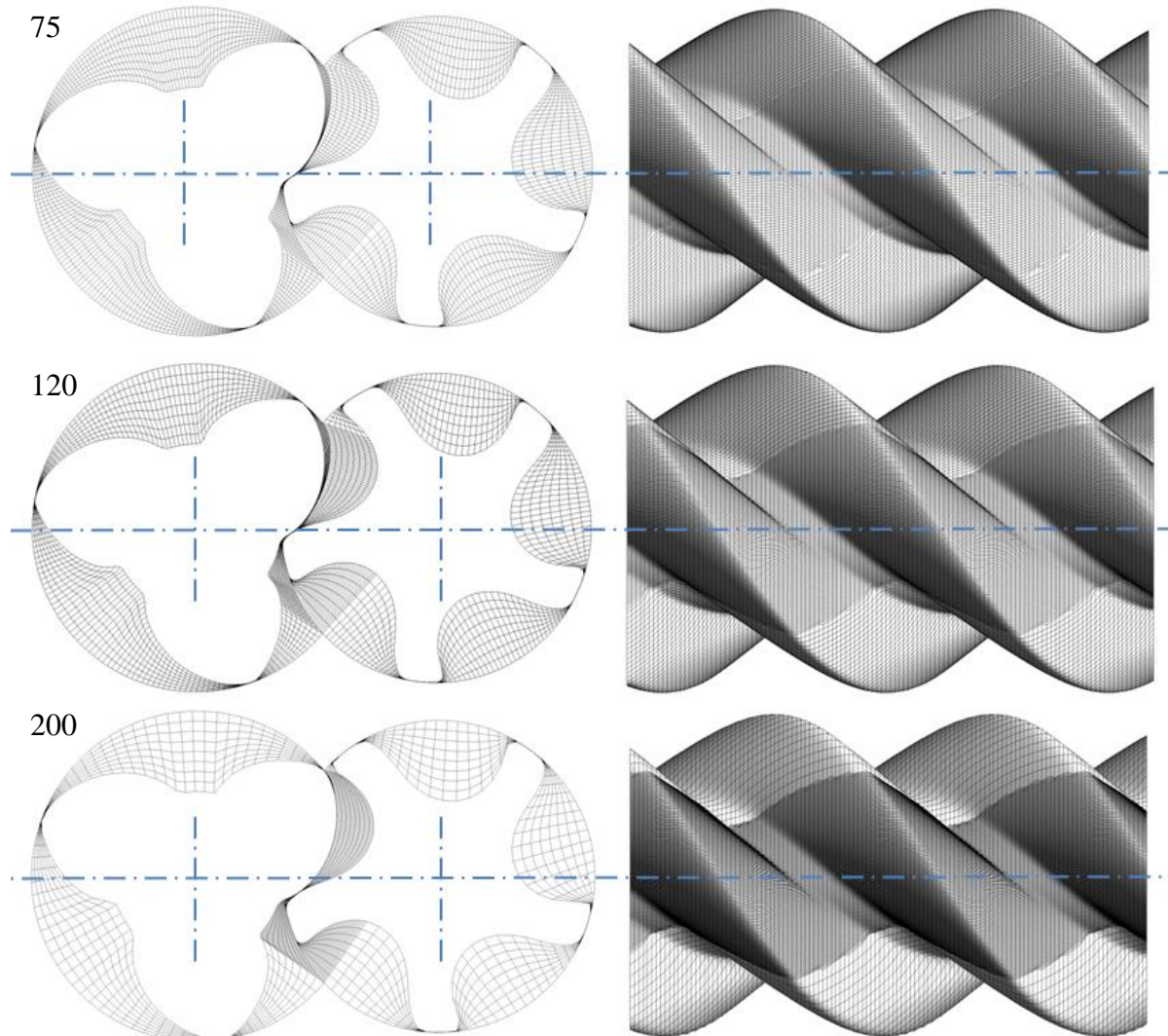


Figure 5.21 Examples of grids with interlobe refinement

5.2.7 Example of grid with one to one connected interface

Figure 5.22 shows an example of grid cross section with one to one connected interface between the two O blocks. From the regularisation of the rotor profile distribution based on the approach of background blocking, it was possible to construct identical rack distribution by placing the same nodes in the interlobe region.

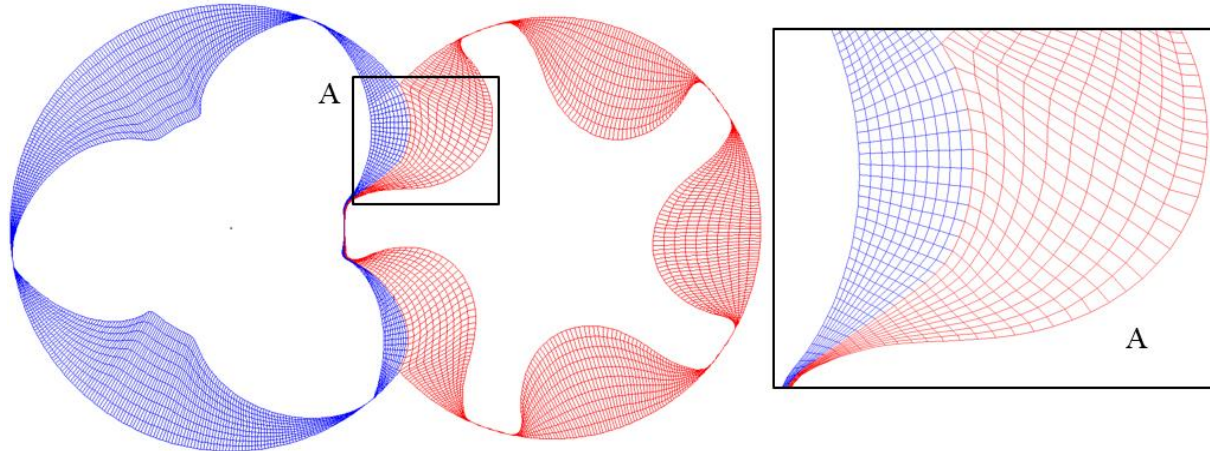


Figure 5.22 Example of grids with one to one connected interface

5.2.8 Comparison of grid quality parameters

It is important that the grids generated are acceptable by the flow solver, have regular cells and should capture the geometry at boundaries as accurately as possible. There are possibilities that if there are large numbers of cells with poor quality then the error induced in numerical calculations is large resulting in inaccurate or false predictions from the CFD models. At the same time large number of poor quality cells can lead to solver instability and convergence difficulty particularly at higher operating pressure ratio when the leakage flow rates are high. Some of the important quality criteria are considered below and a comparison of quality parameters between the algebraic grids has been presented.

Two types of grids have been analysed:

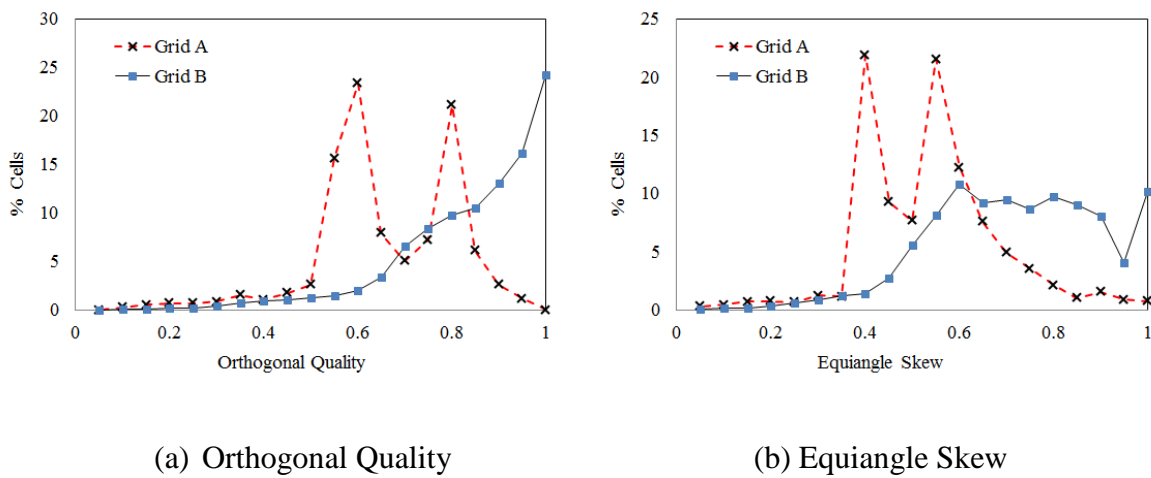
Grid A – This grid is generated using the approach of directing the distribution from rotor profile to the casing and rack segment and has been well validated as acceptable for flow solutions using the ANSYS CFX solver (*Kovačević et al., 2007*).

Grid B – This grid is generated using the newly formulated approach of directing the distribution from the casing and rack segment to the rotor profile. The procedure of regularisation using background blocking has been adopted.

The total grid size and spacing in circumferential, radial and axial direction has been maintained in both the grids. The quality factors used for analysis are Orthogonality, Equi-angle Skew, Aspect Ratio, Determinant and Max Warp angle.

5.2.8.1 Orthogonality Quality

The orthogonal quality is cosine of the angle between the vector normal to the cell face and the vector from the cell centroid to the centroid of the adjacent cell or the vector from the cell centroid to its face. The smaller of the two values is selected. A value of 1 represents a perfect hexahedral cube and a value of 0 is a degenerated hexahedron. Grid A showed an average orthogonal quality of 0.63, while Grid B showed an improved average orthogonal quality of 0.82. From Figure 5.23a, Grid A has about 43% cells with orthogonal quality higher than 0.7 while Grid B has about 88% cells with orthogonal quality higher than 0.7. An orthogonal quality factor greater than 0.3 is recommended by ANSYS CFX solver and is in the same range for most of the flow solvers. An improvement in orthogonal quality in Grid B is because the grid lines in the axial direction run normal to the cross section faces as opposed to those running along the helix of the rotors in case of Grid A.



(a) Orthogonal Quality

(b) Equiangle Skew

Figure 5.23 Comparison of Grid A and Grid B - % cells vs Quality factor

5.2.8.2 Equi-angle Skew

Equi-angle Skew quality computes the deviation of the cell with respect to a perfect cubic hexahedron as given by equation (5.7). A value of 1 represents a perfect hexahedral cube and a value of 0 is a degenerated hexahedron.

$$\text{Equiangle Skew} = 1.0 - \text{Max} \left(\frac{(Q_{\max} - Q_e)}{(180 - Q_e)}, \frac{(Q_e - Q_{\min})}{Q_e} \right) \quad (5.7)$$

Where,

Q_{\max} and Q_{\min} = largest and smallest angle in the element

$$Q_e = 90^\circ, \text{ angle of an equiangular element}$$

Grid A showed an average equi-angle skew factor of 0.49 while Grid B showed an improved average equi-angle skew factor of 0.66. Grid A has a minimum equi-angle skew of zero in some cells because of the nodes merged at the top and bottom CUSP's as shown in Figure 5.3. From Figure 5.23b, Grid A has about 1.4% cells with equi-angle skew less than 0.15 while Grid B has about 0.35% cells with equi-angle skew less than 0.15. These cell locations are represented graphically in Figure 5.24 which shows that these cells are mostly in the interlobe region.

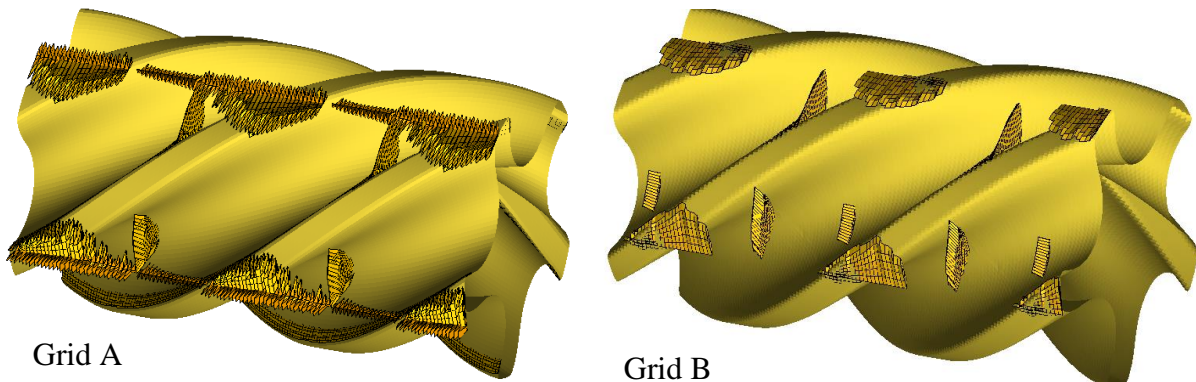


Figure 5.24 Comparison of cells with Equi-angle Skew factor < 0.15

5.2.8.3 Aspect Ratio

The Aspect Ratio is an indicator of the degree of stretching on the cells. For an individual hexahedral cell it is defined as the ratio of its maximum face area to its minimum face area. For the entire grid the largest ratio is considered as the maximum aspect ratio. In Grid A the aspect ratio was found to be 230 in the main rotor and 280 in the gate rotor in less than 0.1% cells. In Grid B the aspect ratio was found to be 443 in the main rotor and 348 in the gate rotor in less than 0.1% cells. Maximum Aspect ratio recommended by ANSYS CFX solver is less than 100. But for double precision it can be as high as 1000 in limited number of cells. Cell locations with aspect ratio exceeding 200 are represented graphically in Figure 5.25 which clearly shows that these high aspect ratio cells are present in the radial and interlobe leakage gaps.

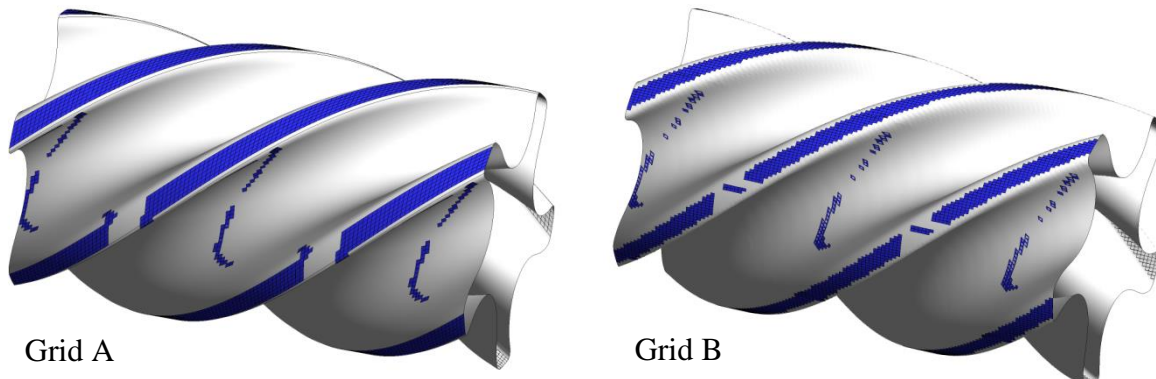


Figure 5.25 Comparison of regions with aspect ratio > 200

5.2.8.4 Determinant

Determinant quality check computes the deformation of the cell with respect to a perfect hexahedron cube. A value of 1 represents a perfect cube and a value of 0 is a degenerated hexahedron. Negative values indicate inverted elements with negative volume.

$$\text{Determinant Quality} = \frac{\text{Min } |J|}{\text{Max } |J|} \quad (5.8)$$

$|J|$ = Determinant of the Jacobian Matrix calculated at each node of the cell

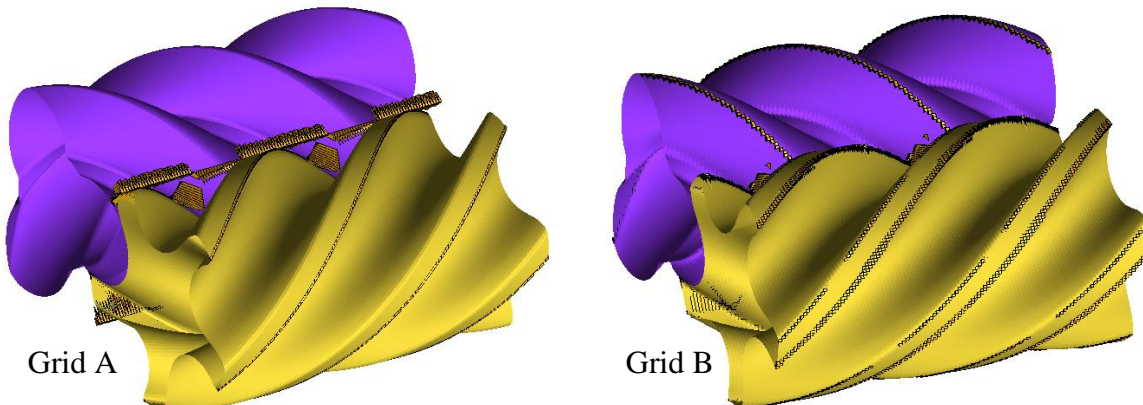


Figure 5.26 Comparison of cells with Determinant < 0.1

Figure 5.26 highlights the cells in the grid with a determinant value less than 0.1. In Grid A these cells are concentrated near the CUSP points where the nodes are merged and are about 1.4%, while in Grid B they are present on the tip of the rotors and are about 2%. Mean value of determinant was found to be 0.78 in the Grid A, while it was 0.75 in the Grid B.

5.2.8.5 MaxWarp

The warping factor indicates the level of element distortion. The nodes forming a face that are in-plane with one another will produce a cell with small warping. The maximum warp of a hexahedron is the maximum warp of its faces. A value of 0° represents a perfect hexahedron and a value of 90° is a degenerated hexahedron. Grid A showed an average MaxWarp factor of 4.9° while Grid B showed an increase in average MaxWrap factor to 7.0° . Figure 5.27 highlights the cells in the main rotor domain with Max Warp factor greater than 50. It is seen that in Grid B cells with higher warping are at the root fillet of the profile as the grid lines in axial direction do not run aligned with the helix of the rotor. This has decreased the Max Warp quality of the cells as compared with those in Grid A. In Grid A, 96% of cells have a good Max Warp factor in the range $0^\circ – 10^\circ$ while in Grid B this number has reduced to 75%.

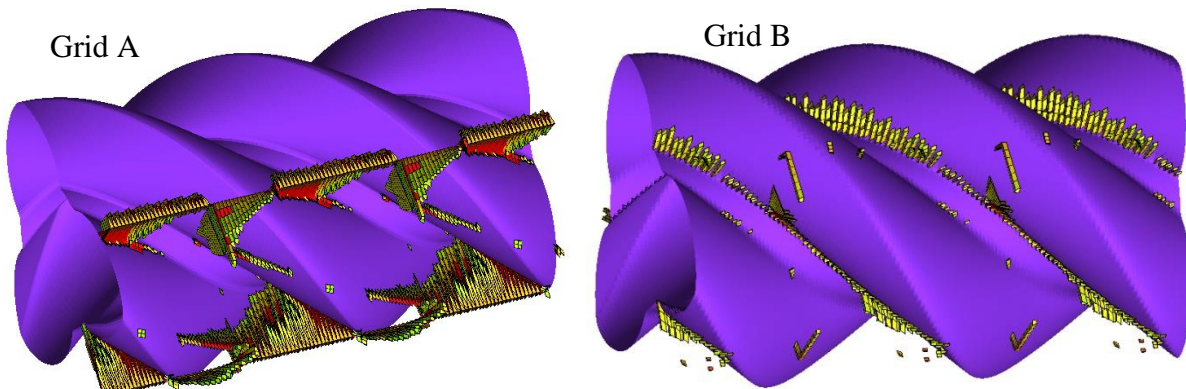


Figure 5.27 Comparison of cells with MaxWarp factor > 50

From these quality parameters it is seen that the grid with new distribution have acceptable quality for the solver. There has been an improvement in the orthogonality and equi-angle skew factors, but there has been a decrement in the maximum aspect ratio and maximum warp factors. The determinant factor was found to be in the same range in the two grids.

To summarise, the new approach to grid generation is acceptable for performing calculations on twin screw machines and has the additional capability to refine the interlobe region without increasing the total mesh count drastically. For non-helical rotors a one to one map at the interface can also be achieved by using the sine function approach of regularisation.

5.3 Grid generation for variable pitch and variable profile screw rotors

Motivation for developments

The most common type of twin screw machines are twin screw compressors. These normally contain rotors of uniform pitch and profile along the rotor length. However, in some cases such as in twin screw vacuum pumps with very large pressure ratios, variable pitch rotors are often used to improve their efficiency. Such variable lead and profile rotors are slowly being investigated for screw compressor and expander applications, as pointed out in Section 2.1. The limited use of rotors with variable pitch and/or section profile has been mainly due to manufacturing constraints. In order to analyse the performance of such machines by means of Computational Fluid Dynamics, it is necessary to produce a numerical mesh capable of calculating 3D transient fluid flows within their working domains. The methods of grid generation currently used for deforming rotor domains have been developed for uniform rotor geometry and parallel axis alignment and it was required to develop additional procedures to make them suitable for rotors with variable geometry.

In this section an algebraic grid generation algorithm for variable pitch and variable profile screw machines has been proposed. The lead variation on the rotors is achieved by defining functions that vary the axial spacing of the grid cross sections and achieve the required lead function. For the case of variable profile rotors the task is difficult, due to changes in the cross section profiles of the rotors. In order to solve this, the algebraic framework has been extended to work as a sequential process over the rotor cross sections independently. A new 3D data structure has been formulated that allows the grid to be assembled from data generated in 2D cross sections. Continuous variation in the rotor profile can then be effectively taken into account by the proposed algorithm.

5.3.1 Integration of 2D grid sections into a 3D mesh

Variable rotor geometries demand that the grid generation procedures be modified in 3D. Hence it is essential to have a well-defined structure for integration of 2D grid sections into a 3D mesh.

With reference to Figure 5.28, one interlobe angle is defined as the angle covered in a cross section from one lobe to the other and on the male rotor it is equal to $\frac{360^\circ}{z_1}$. On the female rotor it is related by the gear ratio. After rotating for one interlobe angle, the rotors, in a given section, come in a geometrically identical position to that at their starting position. Hence grid vertex

positions can be reset to the starting position, while maintaining the node indexing required for progressive rotor rotation. The angular rotation of the rotor covering one interlobe angle is discretised into j_a divisions and each increment is equal to $\Delta\alpha$ given by equation (5.9).

$$\Delta\alpha = \frac{360^\circ}{j_a z_1} \quad (5.9)$$

This angular increment is also the governing factor for the time step size in the transient simulation. 2D grids are generated using the functionality shown in the flow chart given in Figure 4.12 for each of the positions of the rotor, starting from zero degrees to $\frac{360^\circ}{z_1}$ degrees and stored as vertex coordinates.

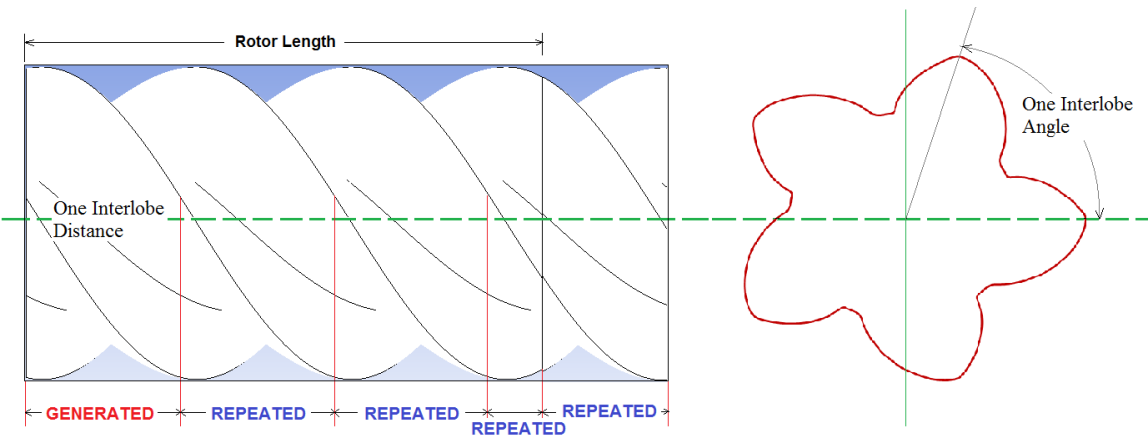


Figure 5.28 Grid generation for rotors with uniform lead

Along the axial direction, there is a proportional angular twist to the rotor lobes because of the helix. The lead of the rotor gives the geometrical relation between the axial distance and the angular rotation of the lobes. This angular rotation can be made identical to the angular increment $\Delta\alpha$ by discretizing the axial length of one pitch into same number of divisions – j_a . As shown in Figure 5.28, one interlobe distance is the axial rotor length corresponding to one pitch distance. If discretisation is done in this fashion, the rotor position in one cross section which is at an angular increment of $\Delta\alpha$ from the reference position becomes the starting position for the adjacent cross section and the sequence follows along the length of the rotor. Hence the 3D data structure consists of a repetition of blocks of data, generated only once for one interlobe angular space, simultaneously representing one interlobe distance.

The GENERATED length, shown in Figure 5.28, covers an interlobe distance i.e. from starting point on one lobe's helix to corresponding point on adjacent lobe's helix. The GENERATED, or calculated, length is then repeated to cover the actual length of the rotor during mesh

assembly. During this stage, cell connectivity data are also established in order to generate hexahedral elements using 4 nodes from one section and 4 nodes from neighbouring section for each cell.

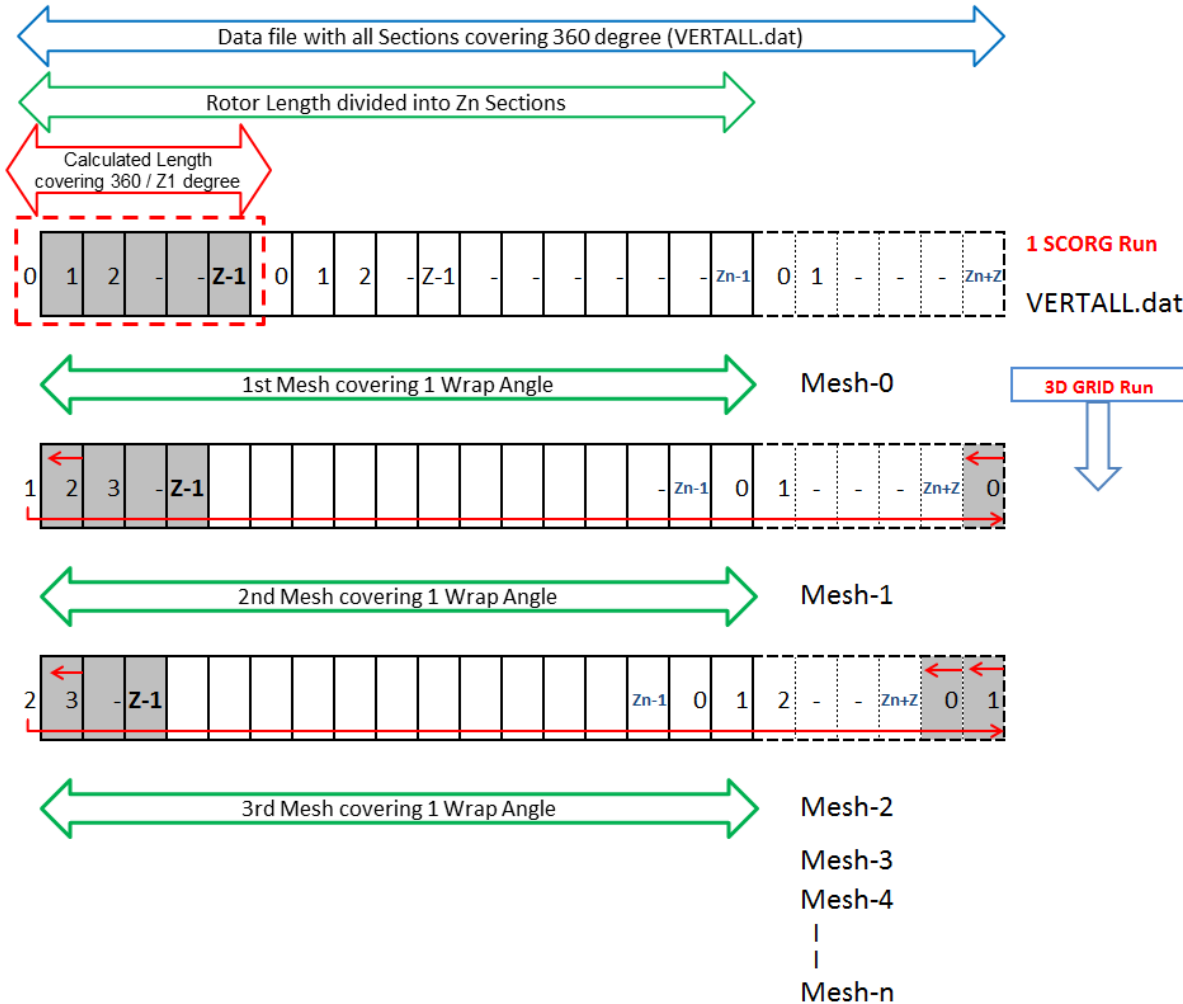


Figure 5.29 Grid assemblies in 3D from data of 2D sections

All axial grid sections are equally spaced from each other and the rotor length is divided into Z_n sections governed by the wrap angle ϕ_w of the male rotor, as given in equation (5.10).

$$Z_n = \text{int} \left(\frac{\phi_w}{\Delta\alpha} \right) \quad (5.10)$$

The simulation process used in the solver requires that an external mesh, representing the deformed domain at every time step, should be made available. Hence it is necessary to write grid files for each time step. This process is represented by a block diagram in Figure 5.29. The mesh, representing the initial position, is written with data from the Z_n sections. In the next time step the grid data should be such that the rotor rotation and meshing of male and female rotors is represented correctly. This is achieved by stacking the data with an increment of

angular increment $\Delta\alpha$ in every section relative to its previous time step position. In another way this is achieved by re-indexing the nodes from first section to the last, second to the first and cyclically repeating over Z_n sections.

Since there is a fixed angular increment of $\Delta\alpha$ from one mesh to the next, this imitates the rotation of rotors with a constant r.p.m over time. The simulation time step size for a given main rotor speed, in rpm, is then given by equation (5.11).

$$\Delta t = \frac{60.0}{r.p.m j_a z_1} \text{ sec} \quad (5.11)$$

For uniform pitch rotors, there is a fixed relation between the axial distance travelled and the angle turned by the rotor over the entire length of the rotor. This also remains unchanged from one interlobe space to the next. The advantage of this from grid generation perspective is that, the grid for one interlobe space can be generated and then the whole data block can be reused in consecutive interlobes covering the length of the rotor as shown in Figure 5.28. However, when the rotors have a continuously variable pitch, even though there exists a geometric relation between the axial distance travelled and the angle turned by the rotor, this relation varies continuously from one interlobe space to the next. For example at one end of the rotor, for a unit axial distance, the angular displacement is say 0.5° but at the other end it can be 3.0° .

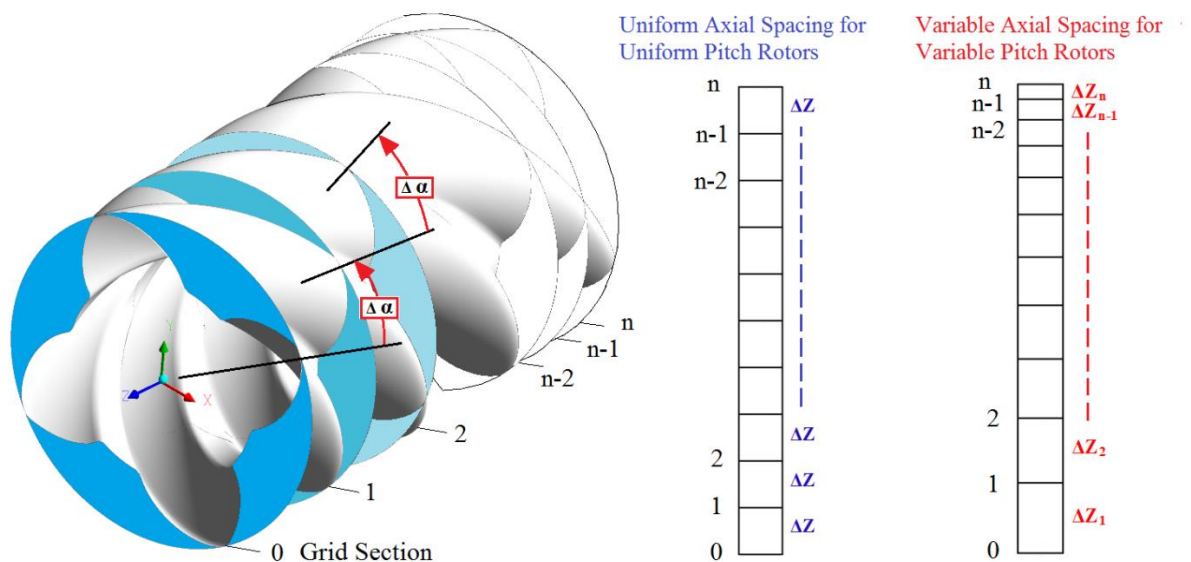


Figure 5.30 Axial spacing difference between uniform pitch and variable pitch grids

Hence if the first interlobe data block is reused, the same angular or axial orientation will not remain valid. This is shown in Figure 5.30, where the right hand side stacking of cross sections is with uniform pitch and for a constant angular displacement of $\Delta\alpha$, from one section to the

other, there is a constant axial displacement of Δz . The left side stacking of sections is with variable pitch and, for a constant angular displacement $\Delta\alpha$, from one section to the other, there are variable axial displacements of $\Delta z_1, \Delta z_2, \Delta z_3, \dots, \Delta z_n$ which depend on the pitch variation specified for the rotors.

When the rotors have a variable section profile, the situation becomes more complex and not only the data structure changes, but also the grid distribution varies from one section to the other. In order to incorporate these variations into grid generation, it is necessary to modify some of the functionality and reorder the data structure to be adaptable for pitch or profile variations.

Also in the case of variable pitch rotors, as the twist of the rotor changes along the rotor length, it is required to refine or coarsen the axial spacing of the sections in order to maintain the grid quality within limits, and this refinement can be independent of the geometric relations. In the present implementation, grid spacing in the axial direction conforms only to the geometric relations and provision for independent stretching has not been made available due to its complexity.

Accordingly the existing structure of 3D grid generation in the algebraic grid generation tool SCORG (**Screw Compressor Rotor Grid Generator**) Program was reformulated to be adaptable for variable pitch and variable profile screw rotors. Figure 5.31 shows the top level blocks of the program. The main program is branched with a direction for variable pitch rotors and this stream is further branched into uniform profile or variable profile. Uniform pitch and Uniform section is the existing functionality. Variable Pitch and Uniform Section is a mid-way level of complexity. The combination of variable profile and variable pitch rotor is the most complex and computationally the most expensive.

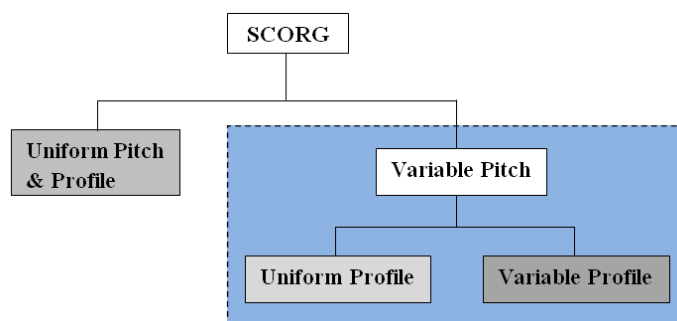


Figure 5.31 SCORG structure for variable pitch and variable profile rotors

5.3.2 Grid generation for variable lead rotors

The procedure presented in the flow chart of the algebraic grid generation Figure 4.12 does not change and is used to generate the cross section grids. The difference is that the generated data are arranged in a suitable manner in order to satisfy the pitch variation function.

5.3.2.1 Variable pitch functions

It is desired to vary the pitch as a constant, linear or a step function. Depending on the rotor design, different variations can be incorporated. The pitch functions currently implemented are *Constant* and *Linear*. If required, *Step*, *Quadratic* or a *Constant-Quadratic* combination can be added. The expressions for pitch function can be in the form of equations (5.12, 5.13, 5.14) and are defined on the main rotor.

Constant Lead

$$p = \text{constant} \quad (5.12)$$

Linear Lead

$$p = \left(\frac{p_e - p_s}{L} \right) Z + p_s \quad (5.13)$$

Quadratic Lead

$$p = \left(\frac{p_e - p_s}{L^2} \right) Z^2 + p_s \quad (5.14)$$

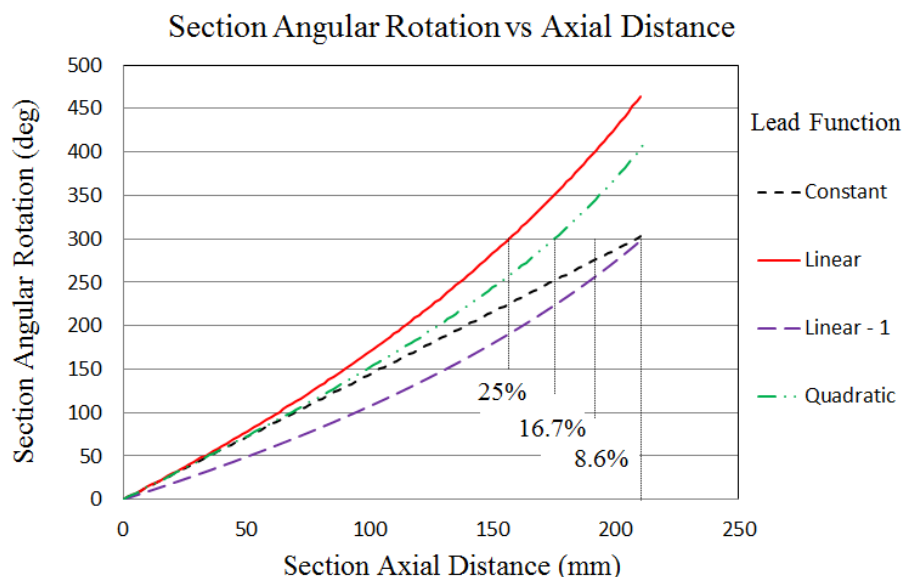
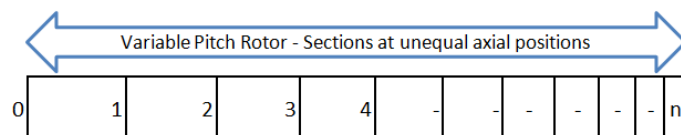


Figure 5.32 Section angular rotation with axial distance for different Pitch Functions

Figure 5.32 shows the section angular rotation with axial distance for different types of Pitch functions. As seen, for a given rotor length the wrap angle can be altered by varying the lead. In this example a rotor has been considered with uniform pitch of 50.46 mm for which the wrap angle is 300°. For the same rotor a linear variation from an initial pitch of 50.46mm to a final pitch of 20.00mm will increase the wrap angle to 461° while a quadratic variation will increase it to 402°. If the wrap angle is kept constant at 300°, the rotor length with linear pitch variation will be 25% shorter than that with constant pitch. For a quadratic function this change will be smaller. This reduction in rotor length could be an advantage in screw machine designs such that for the same wrap angle, the compression process caused by the steeper reduction of volume will be faster and the discharge port opening can be positioned earlier, thus increasing the discharge port area. This could reduce throttling losses in the discharge port. Curve Linear-1 in Figure 5.32 is a function that maintains the rotor length and wrap angle the same as that for uniform lead. The function is achieved by setting $\left(\frac{p_s+p_i}{2}\right) = \text{constant}$ in equation (5.17).

The pitch function specified for the rotors is used to derive a relation between the fixed angular increments of $\Delta\alpha$, from one section to the other and the required variable axial displacements $\Delta z_1, \Delta z_2, \Delta z_3, \dots, \Delta z_n$ for each cross section of the rotor. So the grid vertex data generated for one interlobe angle are reused but positioned in the axial direction with variable Δz , such that the pitch variation function gets applied.

An example of an axial displacement function for linear pitch variation is shown below. The objective is to find the axial position of the current rotor section, such that it is offset by a fixed angular rotation of $\Delta\alpha$ from the previous section.



$$\text{Current section angle} = \alpha_i \quad \text{deg}$$

$$\text{Axial position} = z_i \quad \text{m}$$

$$\text{Adjacent section angle} = \alpha_{i-1} \quad \text{deg}$$

$$\text{Axial position} = z_{i-1} \quad \text{m}$$

The fixed angular offset from one section to the other is given by equation (5.15).

$$(\alpha_i - \alpha_{i-1}) = \Delta\alpha = \frac{360^\circ}{j_a z_1} \quad (5.15)$$

If p_{st} and p_{en} are starting and ending pitch values and z_1 is number of lobes on male rotor, then for the current section, linear lead variation, as given by equation (5.13), will give the local lead as a function of axial position by the equation (5.16).

$$p_i = \left[\frac{(p_{en} - p_{st}) z_1}{L} \right] z_i + p_{st} z_1 \quad (5.16)$$

$$p_s = p_{st} z_1 \text{ and } p_e = p_{en} z_1$$

By definition of rotor lead, locally angle per unit length will be $\frac{d\alpha}{dl} = \frac{360}{p_i}$, therefore for the current section, angular position will be as given by equation (5.17).

$$\alpha_i = \alpha_{i-1} + \frac{360}{p_i} (Z_i - Z_{i-1}) \quad (5.17)$$

$$(\alpha_i - \alpha_{i-1}) = (Z_i - Z_{i-1}) \frac{360}{p_i}$$

From equation (5.16),

$$Z_i = Z_{i-1} + \frac{\left(\frac{(p_{en} - p_{st}) z_1}{L} \right) (\alpha_i - \alpha_{i-1})}{360} Z_i + \frac{p_{st} z_1 (\alpha_i - \alpha_{i-1})}{360}$$

$$Z_i \left[1 - \frac{\left(\frac{(p_{en} - p_{st}) z_1}{L} \right) (\alpha_i - \alpha_{i-1})}{360} \right] = Z_{i-1} + \left[\frac{p_{st} z_1 (\alpha_i - \alpha_{i-1})}{360} \right]$$

$$Z_i = \frac{Z_{i-1} + \left[\frac{p_{st} z_1 (\alpha_i - \alpha_{i-1})}{360} \right]}{\left[1 - \frac{\left(\frac{(p_{en} - p_{st}) z_1}{L} \right) (\alpha_i - \alpha_{i-1})}{360} \right]} \quad (5.18)$$

Equation (5.18) gives the relation between the specified starting and ending pitch of the rotor and the axial position of the cross section for a specified angular increment between successive cross sections. This equation is used to find out the axial position of each of the sections over the rotor length.

In this approach, the additional computational effort required is only to calculate the axial function once, compared to that of a uniform pitch rotor grid generation calculation. The assembly of the grid from a 2D to a 3D structure remains the same as shown in Figure 5.29.

5.3.3 Grid generation for variable profile rotors

The approach presented in Section 5.3.2 is limited to rotors with uniform profile. Because as shown in Figure 5.28, the GENERATED block of cross section grids is reused over the length of the rotors. But when the rotors have a variable profile the GENERATED block cannot be used. Hence a new approach to the grid generation has been proposed here, that can be used for a combination of variable profile as well as variable pitch rotor geometries.

The grid generation algorithm is represented as a block diagram in Figure 5.33. This approach is based on the assumption that every cross section of the rotor is a conjugate screw rotor pair. Therefore each cross section can be handled independently and the grid generation process which uses an analytical or numerical rack to divide the working domain in two subdomains for the male and female rotors, can be repeated over each cross section independently.

Procedure:

- The process starts with the division of the rotor length into n cross sections and proceeds with the generation of 2D vertex data (nodal x and y coordinates) in the first cross section. This involves boundary discretisation and adaptation. Interior nodes at this section are calculated using TFI and the vertex data are recorded after grid orthogonalisation and smoothing operations. This step is labelled as ‘Subroutine Run – 1’ in the block diagram. Angular increment α_0 to α_z covers one interlobe angular rotation of the rotor.
- The process is repeated over the second cross section and additionally this section will receive its axial position (nodal z-coordinate) from the pitch variation function.
- The 2D grid generation is repeated n times until all cross sections along the z axis are calculated. Calculated vertex coordinates are generated first for the α_0 angular position and then the process is repeated for up to the α_z position.
- Blocks of vertices representing first rotor position in each cross section are collected to construct the 3D assembly for the first time step. Figure 5.34 shows the block diagram of the mesh assembly algorithm. Particular attention is given to the correct z coordinate position of each cross section from the Pitch variation function. This initial mesh is

called Mesh-0. The second mesh called Mesh-1 is constructed from the corresponding data from each cross section for the second time step and the process is repeated until meshes for all the required time steps are generated.

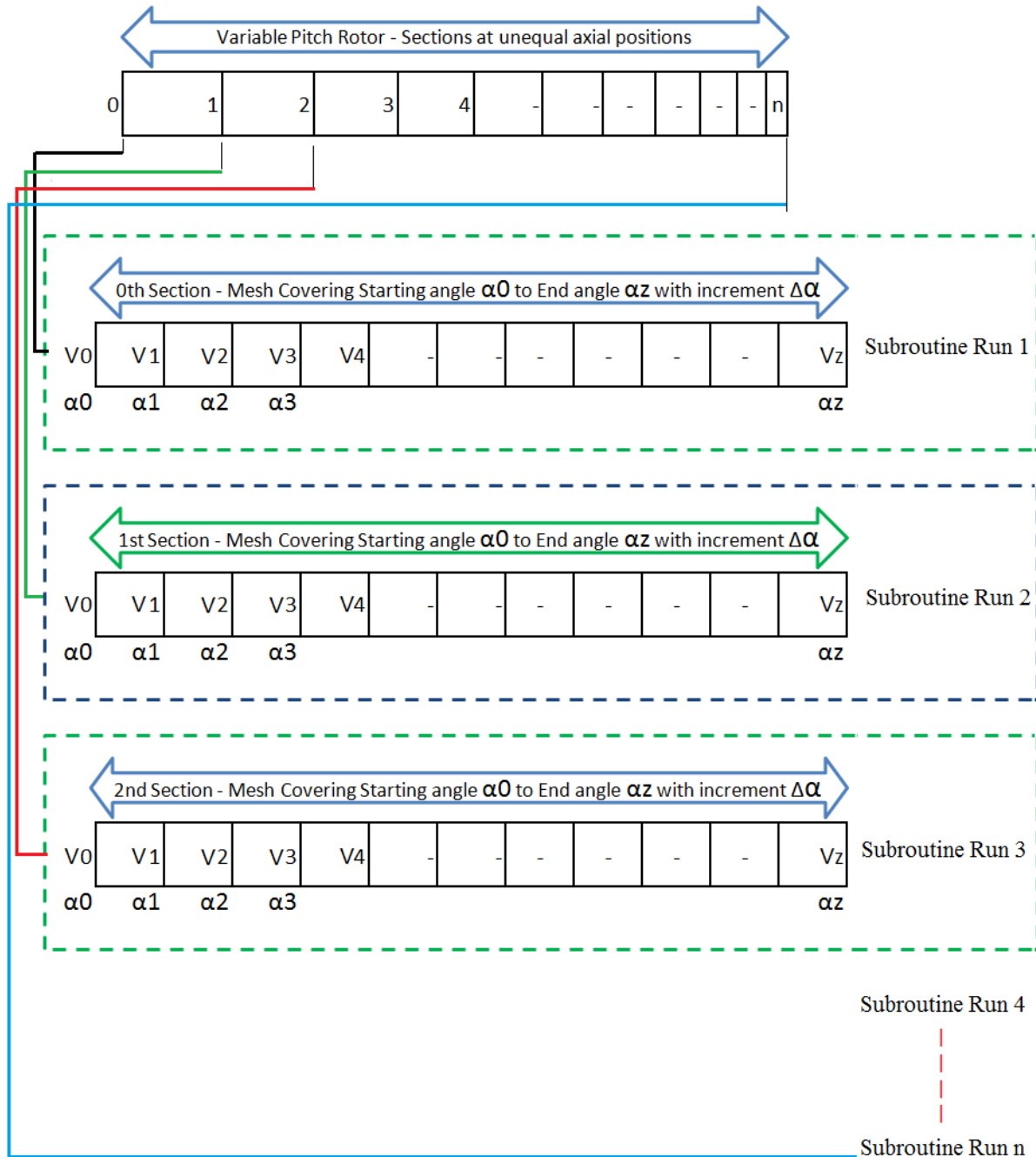


Figure 5.33 Variable pitch and variable profile grid generation

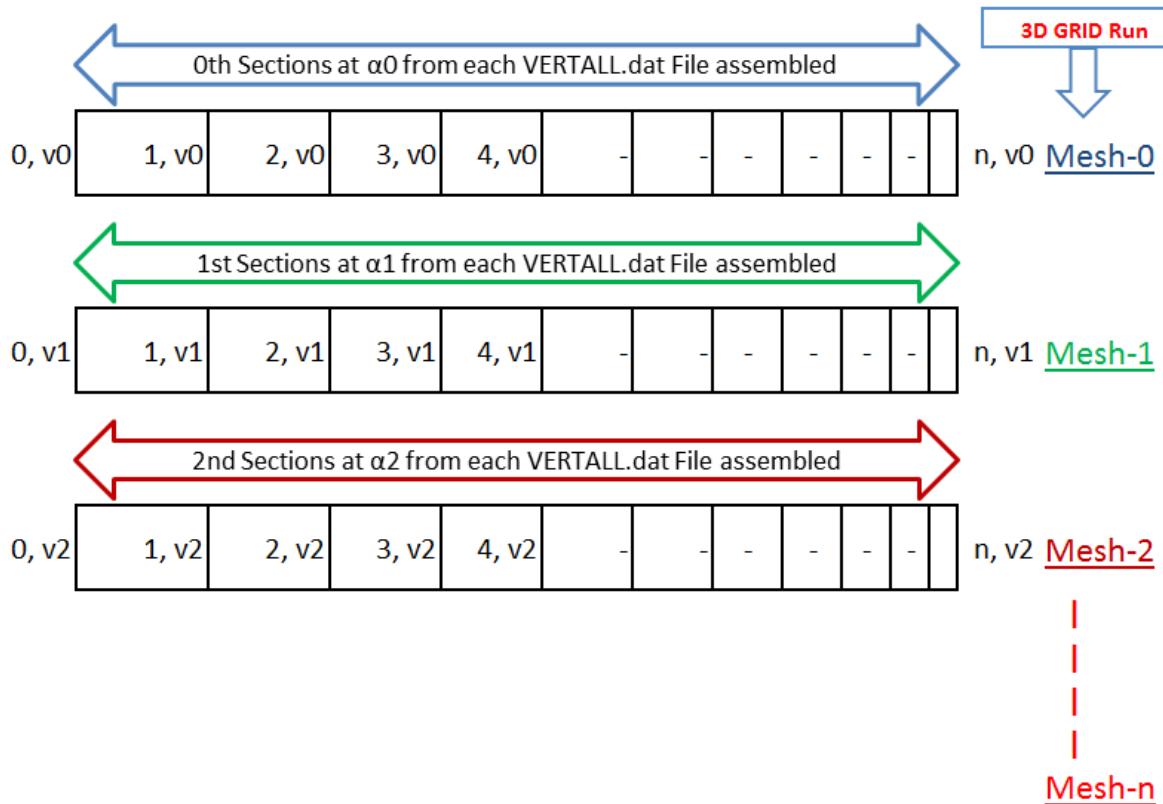


Figure 5.34 Grid assembly in 3D for variable pitch and variable profile rotors

After one interlobe angle, the rotors return to the geometrically identical position as at the starting position. So again, the first vertex coordinate data blocks from every section are collected and when building the 3D mesh care is taken to re-index the nodes correctly such that the rotor position gets an increment of *One Interlobe Angle + $\Delta\alpha$* angle and does not return to the starting position instead. After one complete cycle of rotor intermeshing, which is given by $(j_a z_1 z_2)$ meshes, the grid truly returns to its original position.

In his approach the additional computational effort required is to calculate the 2D grid data in every cross section as compared to that of a uniform pitch rotor grid generation calculation. The assembly of the grid from 2D to 3D structure is completely redesigned in order to provide flexibility to generate grids for variable geometry rotors.

The inputs for the geometry of the rotor can be provided as a set of profile coordinate files for the main and gate rotors in each cross section. These data points can be extracted from CAD models. In the case of profiles such as the 'N' profile which are defined by a generating rack, a set of rack coordinate files for each of the rotor cross section could be provided.

5.3.4 Examples of grids with variable pitch and uniform profile

As an example of grid generation with variable pitch and uniform section, a 5/6 lobe combination compressor with 'N' rotor profiles was generated. The original rotor design was with an L/D ratio of 1.65, wrap angle of 300° and rotor length of 210.25 mm.

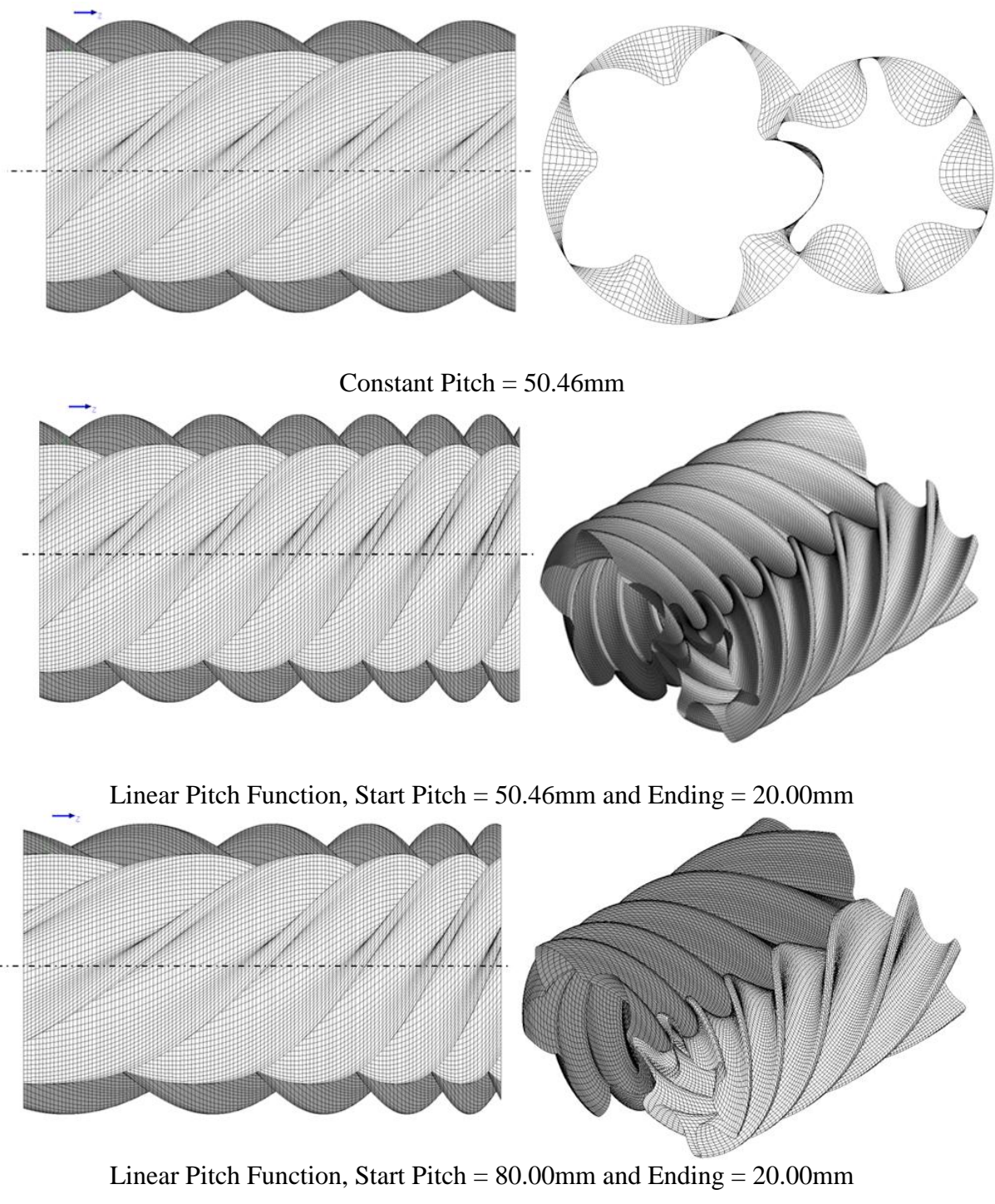


Figure 5.35 Examples of variable pitch grid with uniform profile on 5/6 'N' rotors

The approach described in Section 5.3.2 for variable pitch, was used and three sets of grids were generated as shown in Figure 5.35. In all of these grids, the node density was circumferential, while the radial and axial direction was maintained the same. The first grid is with a constant pitch, the second one is with a linear pitch variation such that the starting pitch is the same as that of the uniform rotors but it ends with a low pitch of 20.00 mm. This variation results in an increased wrap angle of 425°. The third example is where the initial pitch is high at 80.00 mm and the final pitch is low at 20.00 mm. This variation gives a wrap angle of 340°, which is near that of the uniform pitch rotors. The examples shown for variable pitch in Figure 5.35 are to demonstrate the grid generation capability; as such these high levels of variation may not be ideal compressor designs.

5.3.5 Examples of grid with uniform pitch and variable profile

As an example of grid generation with uniform pitch and variable section, a 3/5 lobe compressor with ‘N’ profiles was generated as shown in Figure 5.36. The original rotor design was with an L/D ratio of 1.7, wrap angle of 306° and a rotor length of 230.70 mm.

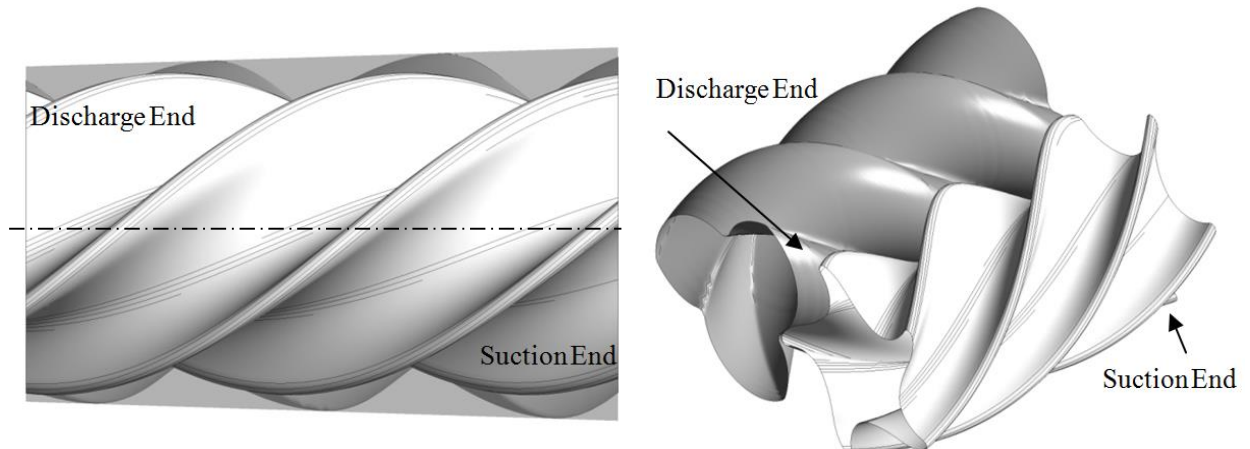


Figure 5.36 Example of variable geometry rotor grid with uniform pitch

In all the grid sections, the node density in the circumferential, radial and axial directions was maintained the same. The rotor cross section profile changes continuously from the one end of the rotor to the other. This set of rotors with parallel axes has a fixed centre distance so that the rotors are tapered. Thus, the outer diameter of the main rotor is reduced from the suction to the discharge end while the inner diameter remains constant. On the gate rotor, the inner diameter changes while the outer diameter is constant. Figure 5.37 shows the 2D cross sections grids for variable rotor ‘N’ profile at the suction end, middle of the rotors and the discharge end.

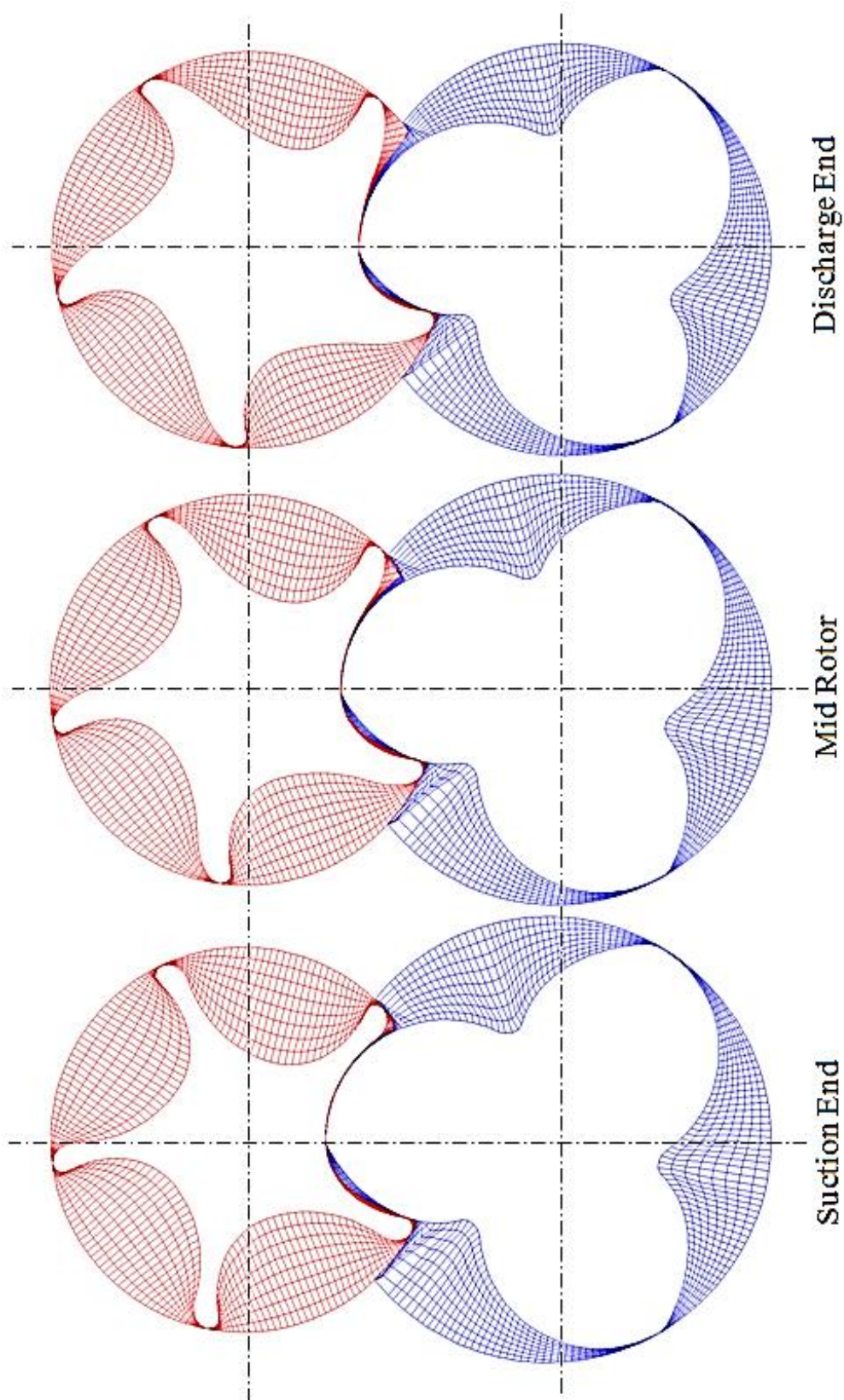


Figure 5.37 Grid sections of variable geometry rotor, 3/5 'Rotor generated N' profile

5.3.6 Example of grid for internal conical rotary compressor

Another example of grid generation with uniform pitch and variable section but with internal meshing is the Vertrotor (2011). A 3/4 lobe combination compressor with cycloidal profiles was generated as shown in Figure 5.38 using the procedure described in Section 5.3. The main specification of the configuration is:

Internal rotor outer diameter	=	37.50 mm
External rotor outer diameter	=	58.92 mm
Rotor length	=	224.00 mm
Axis offset at the suction side	=	3.58 mm

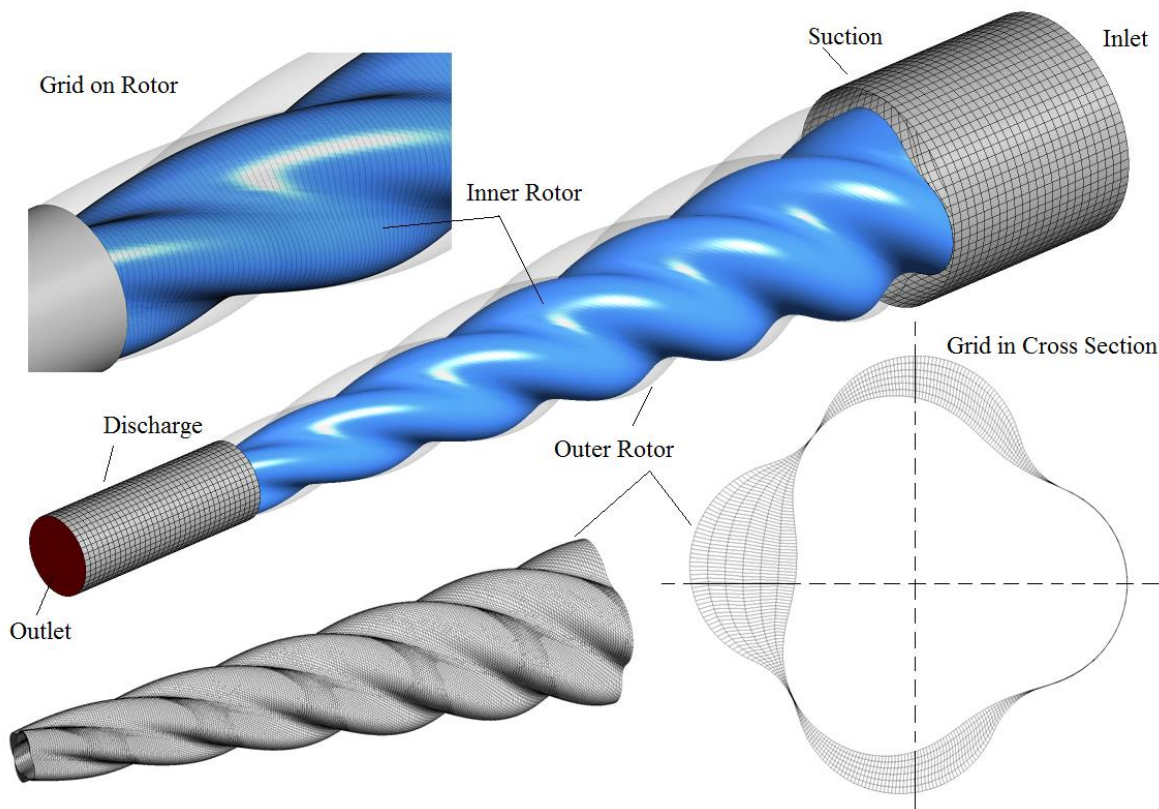


Figure 5.38 Grid of the working chamber for conical internal screw rotors

In operation, the outer rotor is positioned on a central axis while the inner rotor rotates about an eccentric axis with varying centre distance from the suction to the discharge ends. Both axes are stationary in space. In the CFD model, for ease of setting up the grid deformation, the inner rotor is positioned on the central axis while the outer rotor is positioned on the eccentric axis. Momentum imparted to the gas due to boundary motion is a function of the motion of the inner and outer rotor surfaces and this change in kinetic energy due to switching of the rotation axis is very small compared with the increase in internal energy due to compression.

5.4 Development of inflation layer grid

In order to apply a wall function approach with the SST k-omega turbulence model in the numerical solver, it is desirable to build a grid that gives y^+ such that the first grid point normal to the wall falls close to the end of laminar sub-layer and hence the Log-law of the wall can be applied instead of resolving the laminar sub-layer. On the other hand if a near wall modelling approach is used than even the sub-layer needs to be resolved and the magnitude of y^+ to be attained is much below 1.0. This requirement increases the number of meshes to an unreasonably high value. In industrial flows, like those in screw machines, it is desirable to use the wall function approach to limit the cell count in grids. With this approach the number of nodes that should be placed in the boundary layer normal to the wall is about 10 (ANSYS, 2011).

On the rotor surface, the inflation layer can be produced in the form of an O grid as shown in Figure 5.39. The approach used here is a simplified procedure that acts after the TFI distribution of interior nodes has been successfully completed in the rotor cross sections. This approach provides robustness to the generation of refined cells close to the rotor surface and also constraints the divisions to fall in the first cell produced by TFI.

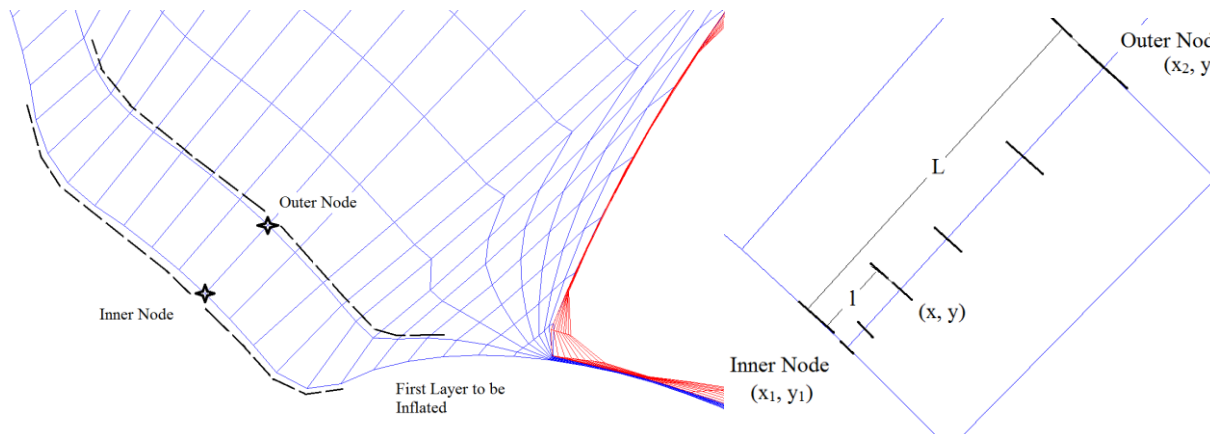


Figure 5.39 Construction of inflation layer adjacent to rotor surface

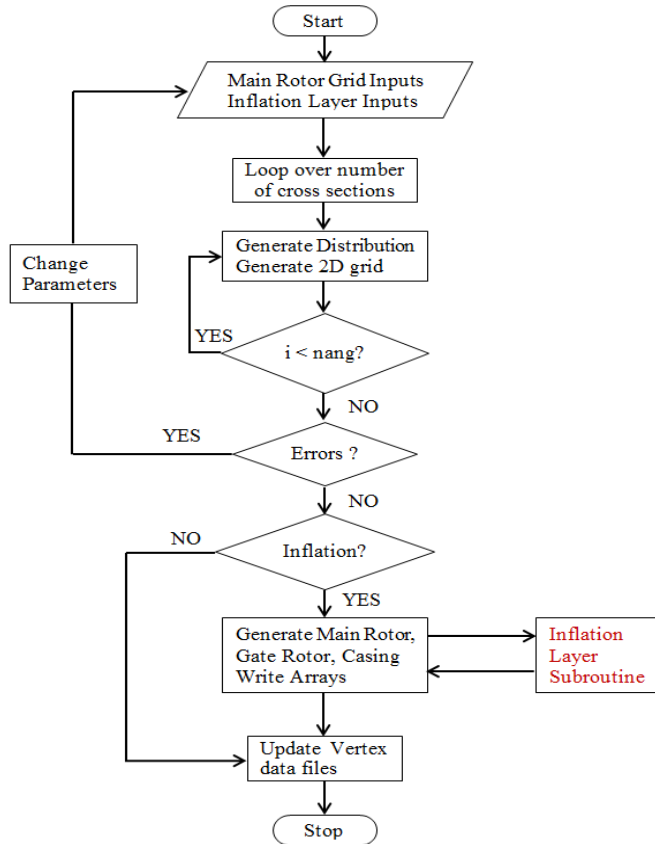


Figure 5.40 Inflation layer subroutine with the main grid generation

As shown in the flow chart of Figure 5.40, the Inflation layer subroutine is executed after the cross section grid is successfully generated with all regular cells. Cells in the first layer adjacent to the rotor are used as reference for further discretisation in the wall normal direction.

5.4.1 Calculation of the node spacing

The inputs required for node spacing calculation are the number of layers (*nlayers*) and the growth rate (*gr*) between adjacent layers.

The equation of a line joining the inner and outer node shown in Figure 5.39 can be stated as:

$$y = m(x - x_1) + y_1 \quad (5.19)$$

The coordinates of the inner node are (x_1, y_1) , the coordinates of the outer node are (x_2, y_2) and the coordinates of the splitting node are (x, y) . Slope $m = \frac{(y_2 - y_1)}{(x_2 - x_1)}$.

The length L of the edge of initial coarse cell is split into *nlayers* resulting in the quadratic equation (5.20).

$$(1 + m^2) \cdot x^2 - (2 \cdot x_1 + 2 \cdot m^2 \cdot x_1) \cdot x + [(1 + m^2) \cdot x_1^2 - l^2] = 0 \quad (5.20)$$

Where,

$$L = \sqrt{(x_2 - x_1)^2 + (y_2 - y_1)^2}$$

$$l = \frac{L}{n_{layers} \cdot gr}$$

$$l^2 = (x - x_1)^2 + (y - y_1)^2$$

Solution of equation (5.20) gives the x coordinate and equation (5.19) gives the y coordinate of splitting node. Figure 5.41 shows an example grid generated with 8 layers and a growth rate of 1.2. Equation (5.20) can possibly have two roots. In such situations a comparison of the two roots has to be made and the logical real coordinate that falls between inner and outer reference nodes has to be selected.

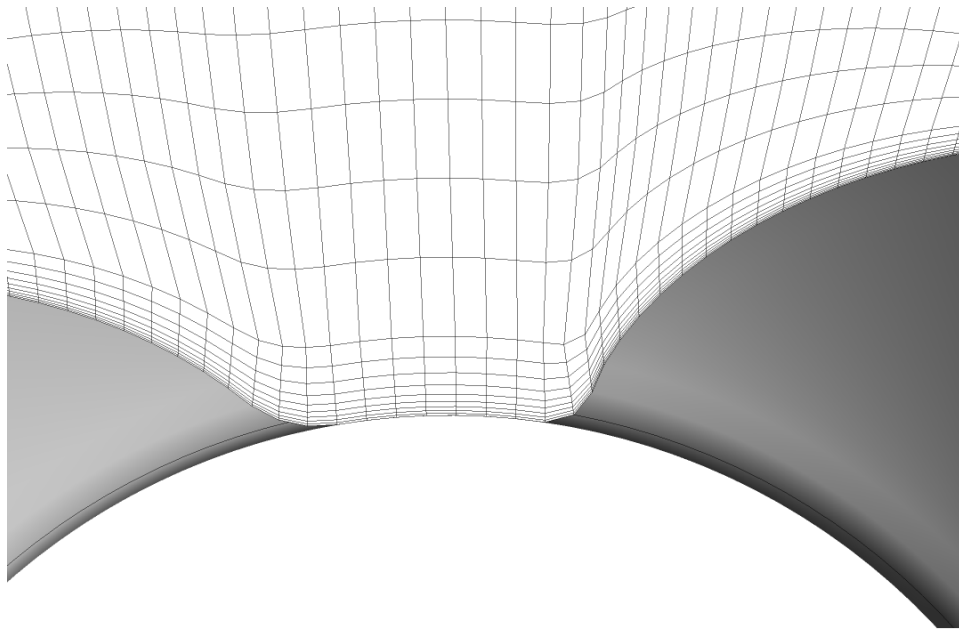


Figure 5.41 Example inflation layer with 8 divisions and growth rate 1.2

The inflation layer grid generation procedure presented here is independent of the approach used for boundary distribution and cross section mesh generation and hence can be used even when the distribution approach presented in Section 5.2 is used. Case studies presented in Chapter 6, in Section 6.3.5 and 6.2.8 present the results obtained with the calculations on a grid with inflation layers.

5.5 Summary

In this chapter developments that were carried out for grid generation of screw machines have been presented. Proposed techniques were directed towards the objective of the research to improve grid quality features and to develop new procedures for variable geometry screw machines. In this direction two categories of developments were presented.

I. *Development of deforming grid generation techniques*

- A variant of algebraic grid generation in which the deforming rotor blocks are generated from the outer boundary (casing) to the inner boundary (rotor profile) was developed.
- For non-helical rotors like the Roots blower type, regularisation based on a skewed sine function with full domain transformation has been formulated that allows not only generation of full hexahedral mesh but also achieves a conformal interface between the two rotor blocks.
- For helical rotors, a regularisation method has been formulated that uses a background blocking technique. This method provides an independent refinement in the interlobe clearance zone and also achieves a conformal interface between the two rotor blocks.
- A sample grid generated using the new distribution technique has been analysed using selected quality criteria. It was found that the grid has acceptable quality for the solver with an improvement in the orthogonality and equiangle skew factors but with a decrement in the maximum aspect ratio and max warp factors.
- A procedure has been formulated to refine the grid adjacent to the rotor surfaces producing an inflation layer with specified divisions and growth rate.

II. *Extending the algebraic grid generation algorithms to variable geometry screw rotors*

- In order to generate grid for rotors with variable lead, the algebraic grid generation procedures have been extended with variable cross section spacing. Functions for uniform, linear or a stepped type of lead variation have been formulated.
- The same algorithm has also been extended to generate grids for rotors with variable profiles. This grid generation has the capability to accommodate continuously variable rotor geometry, making it possible to solve flow in domains with conical rotors.

The proposed techniques have been implemented in the customised grid generation tool SCORG.

Chapter 6 - Case Studies and Discussion

6.1 Introduction

The grid generation development presented in the previous chapter has been installed in the customised grid generation tool SCORG and is available to be coupled as a deforming grid with solvers such as ANSYS CFX and Pumplinx. In this chapter three case studies are presented, utilizing grids generated by the methods described, to validate the grid generation procedures, and to compare performance predictions made with them with experimental measurements.

The aim of the first case study was to evaluate the influence of the differences in solver formulation used for the ALE calculations. Two commonly used commercial CFD solvers were used to predict flow in a dry air twin screw compressor at various operating conditions. The results obtained from the two solvers have been compared both with each other and with measurements. Differences in the predicted results and their probable causes are discussed. Additionally the approach of grid generation with local interlobe region refinement was used in a set of successive studies. The results from these calculations have been compared with the base grid, and the influence of interlobe refinement has been evaluated. At one of the operating conditions, an inflation layer adjacent to the rotor surface has been included and its effect on the grid was evaluated.

The second case study is an analysis of a twin screw dry air expander. The analysis is presented in two stages. The first stage evaluates the results from the numerical models for various modelling parameters such as clearance gap sizes, pressure boundary condition, turbulence models and high pressure end clearance. These results have been compared with experimental data of pressure variation in the expansion chamber, indicated power and mass flow rate. A set of modelling parameters has been identified that gives the best comparison. In the second stage of analysis the numerical model is set with these parameters and a full performance map is calculated at three discharge pressures and various rotor speeds. The full performance map has been compared with experimental measurements and important conclusions have been drawn. At a few operating conditions, grids with inflation layers adjacent to the rotor surface have been analysed and compared with the base grid and the results have been compared to see their influence.

The third case study is a demonstration of 3D grid generation for variable geometry screw rotors in an oil free air compressor. Three types of rotor geometry have been studied and their performance has been compared. The first design is the standard rotor with uniform pitch and profile. The second rotor is of same size as that of the uniform rotor but has a linearly variable lead from the suction end to the discharge end. The third rotor is slightly smaller in size because the rotor profile is continuously varied from the suction end to the discharge end. A variable profile produces conical rotors with parallel axes. Performance prediction and flow characteristics from the numerical analysis have been compared in the study. An attempt was made to manufacture the variable lead rotors for experimentation but it was not successful due to inaccuracies in the profile contours and lead errors.

In all the three case studies the working fluid was dry air with the following thermodynamic properties.

Density	<i>Ideal gas law</i>
Molar mass	28.96 $\frac{\text{kg}}{\text{kmol}}$
Specific heat capacity	1004.4 $\frac{\text{J}}{\text{kg K}}$
Dynamic viscosity	$1.831 \times 10^{-5} \frac{\text{kg}}{\text{m s}}$
Thermal conductivity	$2.61 \times 10^{-2} \frac{\text{W}}{\text{m K}}$

Numerical grids for all time steps were generated in advance of the CFD calculation and were passed to the solver initially in the model setup. At each time step, the mesh, for the appropriate position of the rotors, is updated in the solver by use of an external subroutine. The solver is set with a higher order advection scheme (blend of 1st and 2nd order) and the second order backward Euler temporal discretisation is used.

The convergence criteria for all conservation equations were set to 1.0×10^{-3} applying up to 20 iterations for every time step. During solution, r.m.s residuals for all time steps achieved values between 1.0×10^{-3} and 5.0×10^{-3} for the momentum equation, while the values for the continuity and energy equations were always less than 1.0×10^{-3} . The calculations were allowed to run for a sufficient number of time steps in order to ensure that cyclic repetition of the flow and pressure values was achieved. The integral quantities were calculated as cycle averages from the data of the time history and using equations listed in [Appendix A](#).

6.2 Analysis of a 3/5 synchronised Dry Air Compressor

6.2.1 Case description

The factors that influence flow predictions are not only related to computational grids but also to the approach which numerical solvers use to calculate the solutions of conservation equations. A case study of an expander analysis in *Kovačević and Rane* (2013) showed that CFD predictions align to measurements better at higher speeds than at lower speeds. Similarly higher deviations were reported at higher pressure ratios. Some other recent studies, not yet published, have also reported differences between CFD predictions and measurements. It was therefore necessary to investigate the influence of CFD model parameters, and the different solver formulations currently available for solving flows in screw machines. In this case study, two commonly used solvers in commercial CFD software are compared. The same deforming rotor grid generated by SCORG is used for performance calculation with both solvers. The performance was also measured on a test compressor in the test rig at City University London. Performance predictions obtained from CFD models are compared with measurement results. The compared performance indicators include pressure variation in the compressor chamber, mass flow rate, indicated power and the volumetric efficiency. The first solver is a coupled vertex-centre based solver which is implemented in ANSYS CFX (2011) and has been commonly used for screw compressor analysis. The second solver is a segregated cell-centre based solver used in PumpLinx (2014). Both are pressure based finite volume solvers. The later segregated solver has been frequently used for modelling flow and cavitation in pumps and piston and scroll compressors. Recent developments of the solver allow it to be used for modelling of twin screw compressors. *Jiang et al.*, (2007) have reported the analysis of crescent oil pumps using this solver. *Wang et al.*, (2012) have modelled a vane oil pump using the segregated solver. The newly proposed grid generation in Section 5.2 with interlobe region refinement and inflation layer adjacent to rotors presented in Section 5.4 has also been evaluated here to compare the results with base grids (described in Appendix D) and analyse their influence on performance prediction.

Figure 6.1b shows the 3D CAD model of the compressor and the extracted fluid volumes. The suction and discharge ports are extended by circular pipes connected to the domains by interfaces. A reduced uniform clearances of 60 micro meters in the interlobe and radial gaps with no end gaps is considered. Grid refinement has been selected based on grid independence study presented in Section 6.2.7 and time step dependency has not been considered.

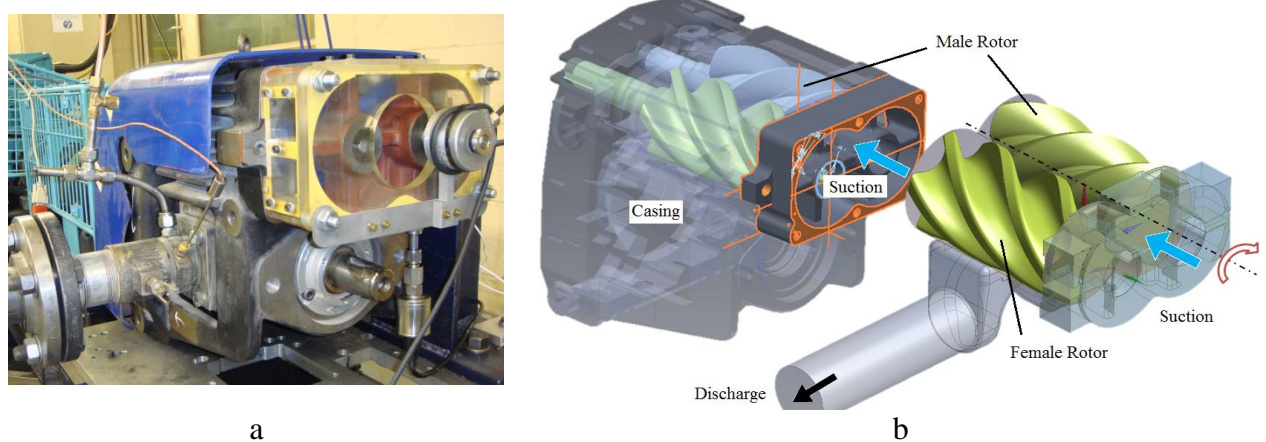


Figure 6.1 Screw compressor – a) The machine and b) Extracted flow model

6.2.2 Pressure based coupled solver

The pressure based coupled solver (ANSYS CFX) has been referenced here as Solver-1 and the segregated solver used in PumpLinx has been referenced as Solver-2. Solver-1 uses an Element-based finite volume method. Figure 6.2a presents a flow chart with an overview of the solution process used by a generic coupled solver whereas Figure 6.2b is a 2D illustration of the Element-based construction of the control volume.

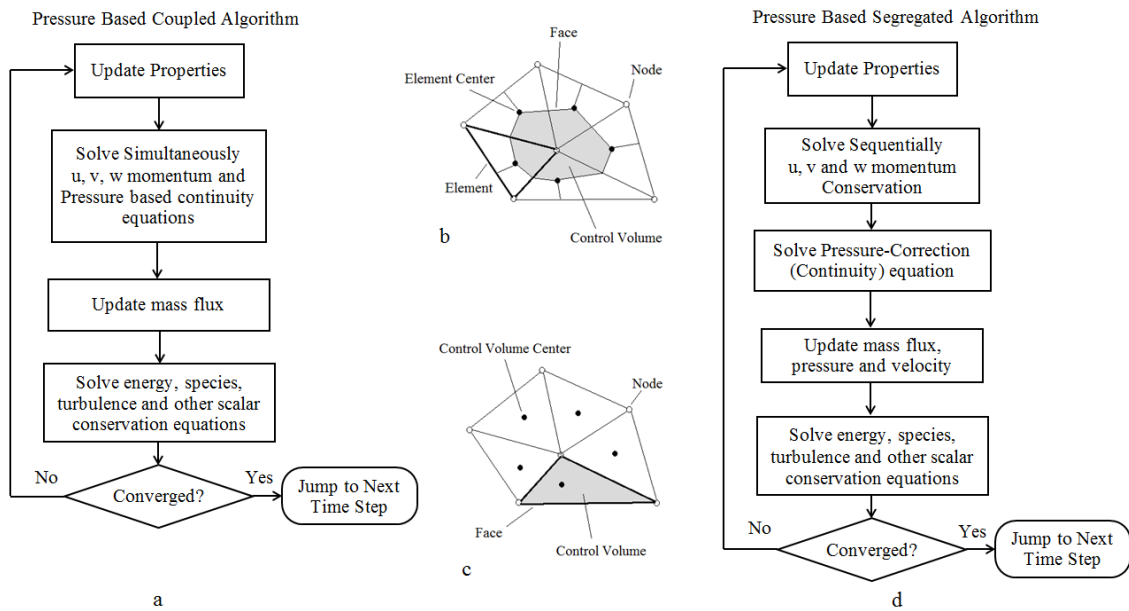


Figure 6.2 Overview of the pressure based solver

- a) Coupled approach, b) Element-based control volume, c) Cell centred control volume and
- d) Segregated Approach

Table 6.1 Solver-1 modelling parameters (used by ANSYS CFX)

Criteria	Selection	Remark	
Mesh in rotor	Hexahedral + Pyramid	Generated by customised grid generator	
Mesh deformation	User defined	Via junction box routines	Conservative
Mesh in ports	Tetrahedral with boundary layer refinements	Generated by Solver-1 pre-processor	Represented in Figure 6.3
Turbulence model	SST – k Omega	Flow regime is Turbulent	
Inlet boundary condition	Opening	Specified total pressure and temperature	Allows for flow to go in and out of the domain
Outlet boundary condition	Opening	Static pressure For backflow; total pressure and temperature	Allows for flow to go in and out of the domain
Control volume gradients	Gauss divergence theorem	Shape functions used to interpolate ϕ	
Advection scheme	Upwind	High resolution	Blend of 1 st and 2 nd order
Pressure-Velocity coupling	Co-located layout	Rhie and Chow 4 th order	
Turbulence scheme	First order upwind		
Transient scheme	Second order	Backward Euler	Fully implicit
Transient inner loop coefficients	Up to 20 iterations per time step		
Convergence criteria	1e-03	r.m.s residual level	
Relaxation parameters	Solver relaxation fluids	0.1 or lower	For stability

In the Element-based method of Solver-1, the spatial domain is firstly discretised into a mesh by using an external grid generator like SCORG. This mesh is then used to construct virtual control volumes within the solver. All solution variables and fluid properties are stored at the nodes. A coupled system of equations comprising the momentum equations and the pressure-based continuity equation is solved in one step. The remaining equations, such as energy and turbulence, are solved in a decoupled fashion. The rate of convergence is expected to improve with this approach but the memory requirement increases 1.5–2 times compared with a segregated solver since the momentum and pressure-based continuity equations need to be

stored in the memory at the same time. Table 6.1 summarizes the important selections of Solver-1 parameters for the screw compressor analysis. Turbulence scheme is selected as first order upwind for stability reasons but a second order formulation could also be selected.

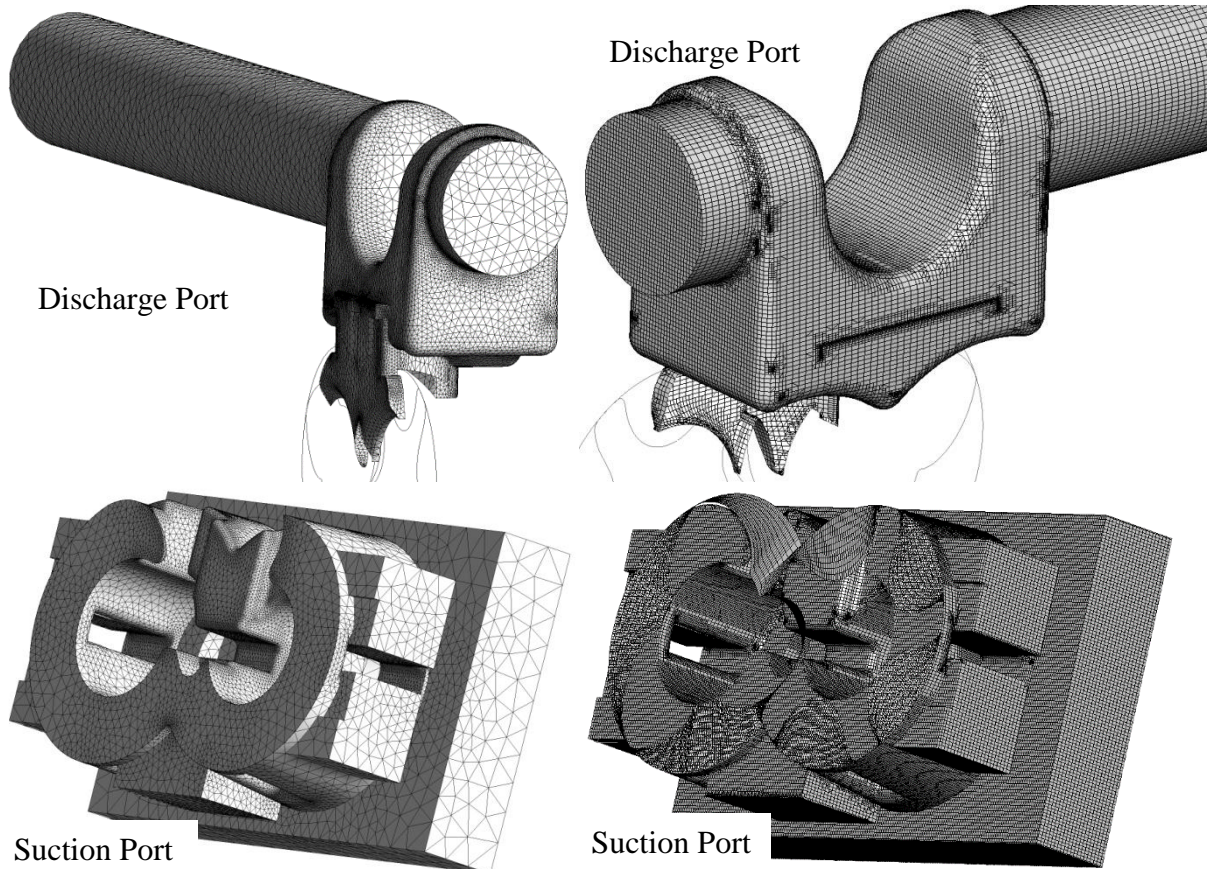


Figure 6.3 Tetrahedral mesh in Solver-1

Figure 6.4 Body-fitted binary tree mesh in
Solver-2

6.2.3 Pressure based segregated solver

The pressure based segregated Solver-2 uses a cell-centred finite volume approach. Figure 6.2c is a 2D illustration of the cell centre based construction of the control volume. The cell-centre approach directly uses the mesh generated by the external grid generator to form control volumes. Figure 6.2d presents a flow chart with an overview of the solution process used by a generic segregated solver. The governing equations are solved separately for each variable. Firstly, the momentum equations are solved using the updated values of pressure and face mass fluxes. This is followed by the pressure correction equation. Face mass fluxes, pressure, and the velocity field are then corrected using the pressure correction obtained from a pressure-velocity coupling solution. The solution is then obtained iteratively until the convergence

criteria are met. An important step in the segregated approach is the pressure-velocity coupling algorithm. Many algorithms, Simple, SimpleC, PISO, SimpleS etc., have been developed over years to improve the robustness of this approach. The segregated algorithm is memory-efficient, since the discretised equations need only to be stored in the memory one at a time. Table 6.2 summarizes the important Solver-2 parameters and their selections for the screw compressor analysis. Turbulence and transient scheme is selected as first order upwind due to the formulation available in the solver.

Table 6.2 Solver-2 modelling parameters (used by PumpLinx)

Criteria	Selection	Remark	
Mesh in rotor	Hexahedral + Pyramid	Generated by customised grid generator	
Mesh deformation	Screw compressor template	Conservative	
Mesh in ports	Body-fitted binary tree	Generated by Solver-2 pre-processor	Represented in Figure 6.4
Turbulence model	k-epsilon RNG	Flow regime is turbulent	
Inlet boundary condition	Pressure inlet or total pressure	Specified static/ total pressure and static/ total temperature	
Outlet boundary condition	Pressure outlet	Specified static pressure and temperature	
Advection scheme	Upwind	First/second Order	
Pressure-velocity coupling	Co-located layout	SIMPLE S	Simerics proprietary
Turbulence scheme	First order upwind		
Transient scheme	First order	Backward Euler	Fully implicit
Transient inner loop coefficients	Up to 25 iterations per time step		
Convergence criteria	1e-02	r.m.s residual level	
Relaxation parameters	Pressure	0.5	For stability

6.2.4 Experimental measurement

Experimental investigation of the compressor performance was carried out in the air compressor test rig at City University London. Figure 6.5 presents the layout of the measurement setup with the main components and measurement points. The compressor is

driven by a variable speed 75kW motor and has an internal synchronising gear box with the gear ratio 7.197:1. The speed of the motor is adjusted using a variable frequency drive. The torque meter is installed on the motor shaft while the digital encoder for the speed measurement is mounted on the male rotor shaft. Figure 6.1a shows the compressor in the test rig.

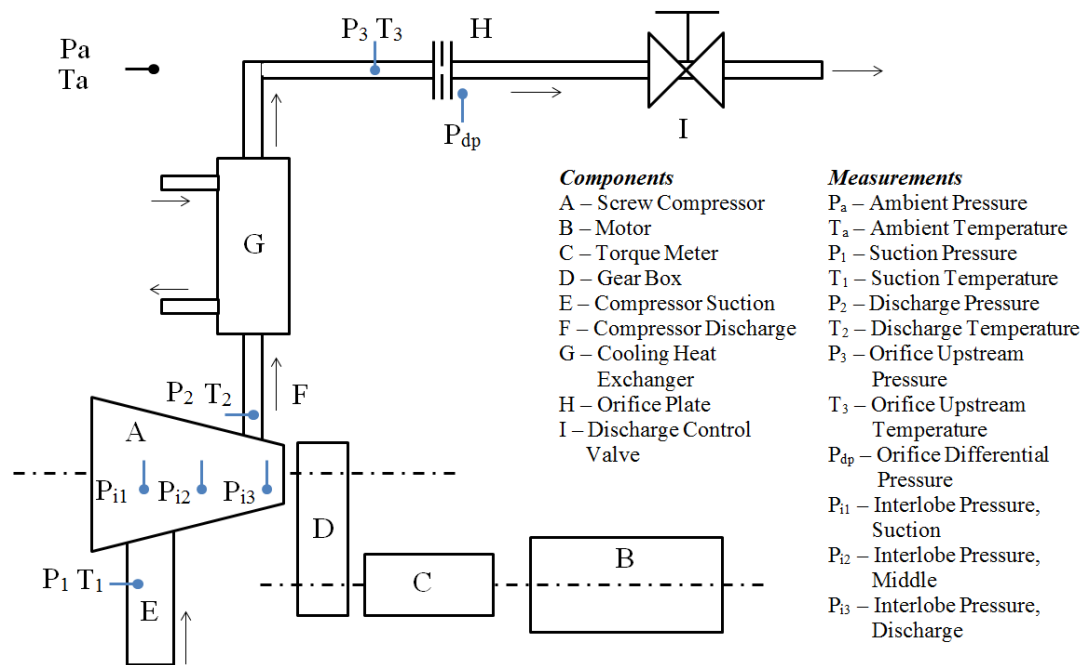


Figure 6.5 Experimental setup for performance measurement

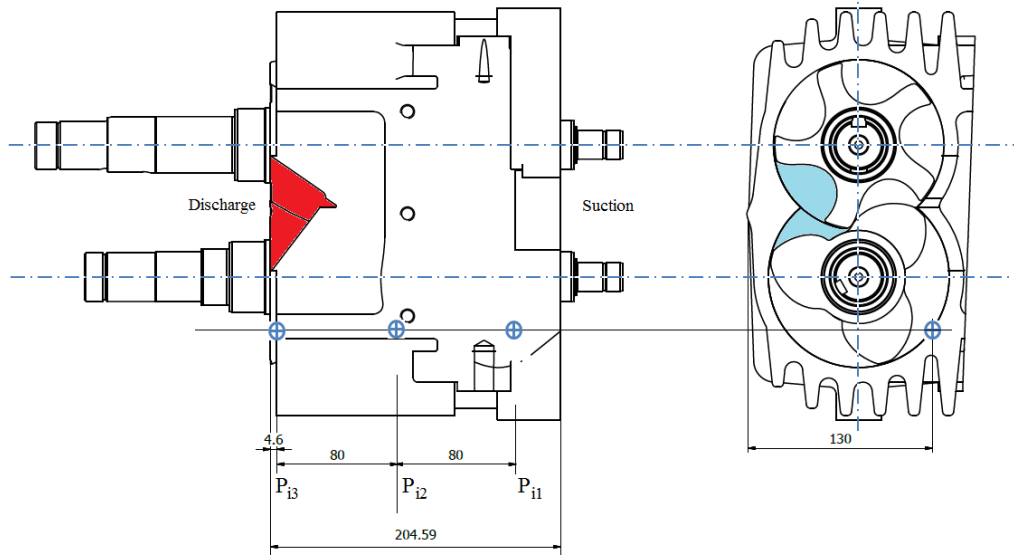


Figure 6.6 Location of interlobe pressure transducers on the compressor

The pressure and temperature of the gas are measured at the inlet, the discharge and upstream of the orifice plate. In addition, three pressure transducers are used for recording the interlobe

pressures and are located in the working chamber through the compressor casing on the male rotor side. Figure 6.6 shows the location of the dynamic interlobe pressure transducers in the compressor housing.

The flow through the compressor is measured by use of an orifice plate installed in the discharge line of the system. The discharge line contains a control valve for regulation of the discharge pressure. Table 6.3 provides information on the transducers used for the measurements. The data acquisition is carried out using CompactRIO (CRI0-9022) from National Instruments and Labview. The measurements were taken for discharge pressures up to 2.5bar and speeds from 6000 to 8000rpm.

Table 6.3 Test rig instrumentation details

Measured Parameter	Transducer	Specifications
Compressor Speed, N	Shaft Encoder (BHG 16.25W.3600-B2-5)	360 TTL pulses per revolution Accuracy= $\pm 10\%$
Compressor Torque, T	TRP-500Torque meter (strain gauge transducer)	Max capacity: 500Nm, Calibration level: 335Nm Range = 0 - 6000 rpm, Supply volt=10v dc, Accuracy= 0.25 % of max capacity
Inlet pressure, P₁	PDCR 110/w -Pressure Transducer	Operating range = 3.5bar(abs) Excite voltage=10V dc, Accuracy =0.6%,
Outlet pressure, P₂	PDCR 922-Pressure transducer	Operating range =15 bar (abs) Excite voltage=10V dc, Output voltage= 100 mV Accuracy =0.6%
Orifice plate differential pressure, P_{dp}	PDCR 2120- Pressure transducer	Pressure diff= 0.35 bar, Excitation Voltage=10V dc, Accuracy= 0.6%,
Orifice plate inlet press, P₃	PDCR 922-Pressure transducer	Operating range =15 bar (abs) Excite voltage=10V dc, Output voltage= 100 mV Accuracy =0.6%
Interlobe Pressure, P_{i1}, P_{i2}, P_{i3}	XTME 190 M Series – Pressure transducer Inorganically Bonded Piezoresistive Sensor	Operating range =35 bar g Excite voltage=10V dc, Output voltage= 75 mV Sensitivity =2.14 mV/bar g Range= -55 ⁰ C to 235 ⁰ C
Inlet temperature , T₁ Outlet temperature, T₂ Orifice plate inlet Temperature, T₃	Platinum Resistance Thermometer	Range= -75 ⁰ C to 350 ⁰ C, Accuracy= $\pm 0.5^{\circ}\text{C}$
Water Temp at the inlet and outlet of the cooler	K- type thermocouple (based on Ni/Cr-Ni/Al alloy)	Range= -200 ⁰ C to 1300 ⁰ C, Accuracy= $\pm 2.2^{\circ}\text{C}$ sensitivity = 41 $\mu\text{V}/^{\circ}\text{C}$

6.2.5 Results and discussion

The results obtained from CFD modelling are compared with the experimental results. The equations presented in [Appendix A](#) have been used for the calculations.

6.2.5.1 Pressure-Angle diagram

Figure 6.7 shows the variation of the chamber pressure with the angle of rotation of the male rotor at two speeds, 6000 and 8000rpm. The results from CFD calculation are compared with experimental data.

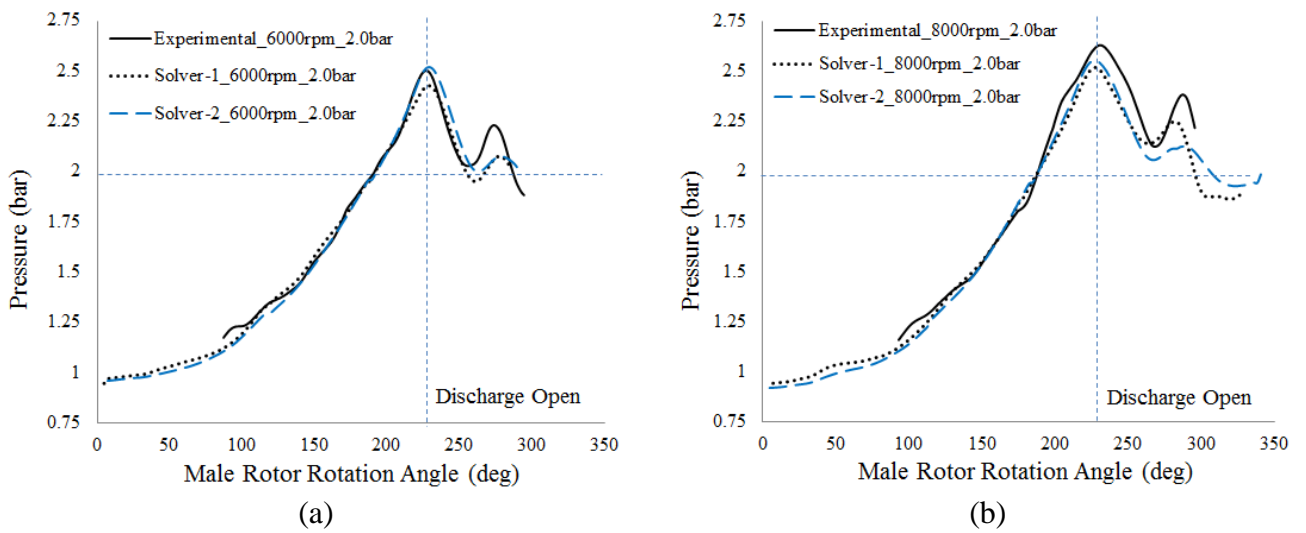


Figure 6.7 Pressure-Angle diagram a) 6000 rpm, b) 8000 rpm

The internal pressure calculated by both solvers is agreeing well with the measured pressure curve at both speeds. Some differences between predictions and measurements are noticed near the peak pressure at the moment of opening of the discharge port. Solver 2 shows slightly better agreement with measured data.

6.2.5.2 Mass flow rate

Figure 6.8a shows the comparison of the flow predictions from the CFD calculations with experimental data and Figure 6.9a shows the comparison between the two solvers over the full range of speeds and pressures. Solver-2 predicts higher mass flow rate than Solver-1 and this is closer to the experimental results. The predicted mass flow rate depends on the assumption of clearances. A smaller clearance would result in higher flow rates and vice versa. The assumed clearance gap was 60 micrometres. In order to determine the sensitivity of the results to the clearances, another calculation was performed with Solver-2 with a clearance of 120 micrometres. As shown in Figure 6.8a, this resulted in a flow rate lower than that measured.

This indicates that the average physical clearance is between 60 and 120 micrometres, probably around 100 micrometres in this case. It is known that the clearances in the rotor domain are varying non-uniformly with operating conditions and the assumption of average clearances may introduce inaccuracy.

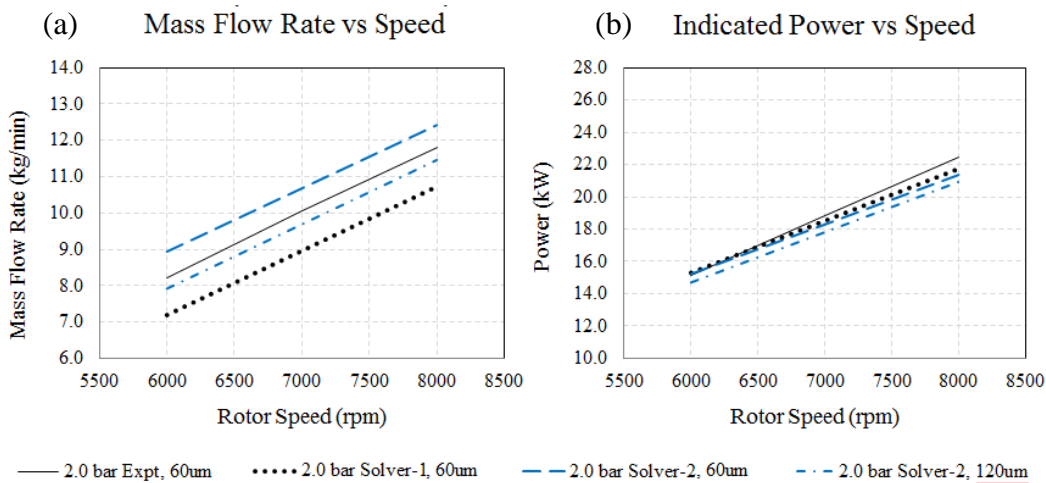


Figure 6.8 Comparison of mass flow rate and indicated power

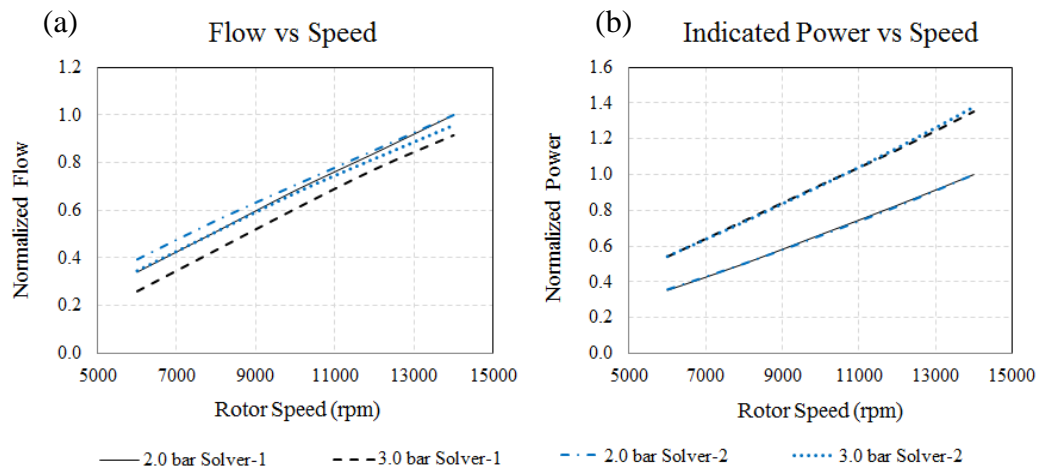


Figure 6.9 Comparison of full range mass flow rate and indicated power

6.2.5.3 *Indicated power*

In the experiment, the power was measured on the motor shaft and a constant mechanical efficiency of 95% was assumed for the integral gearbox at all speeds. Figure 6.8b shows a comparison of the indicated power prediction from CFD calculations with experimental data and Figure 6.9b shows a comparison between the two solvers over the full range. Both solvers are predicting similar indicated power which is very close to the experimental results. The assumption of the constant mechanical efficiency of the gearbox is not the most accurate since

the efficiency of the gearbox changes with speed. Despite this, the agreement in power prediction is good.

6.2.5.4 Specific power and volumetric efficiency

Specific power is the ratio of the indicated power to the flow through the compressor. A lower specific power indicates a better machine. Figure 6.10a compares the specific power, prediction from the CFD calculations, with the experimental data and Figure 6.11a shows a comparison between the two solvers over the full range. Solver-1 is predicting higher specific power than the experiment while Solver-2 is predicting lower specific power than the experiment. This directly correlates to the lower and higher flow predictions from both the solvers with respect to the measurement. The trend is same at both the speeds but the results obtained from Solver-2 are closer to the experimental results and could be further improved by specifying clearances closer to the real values. The difference between the specific power from both the solvers is gradually reducing and at the highest speed both the solvers are predicting same specific power.

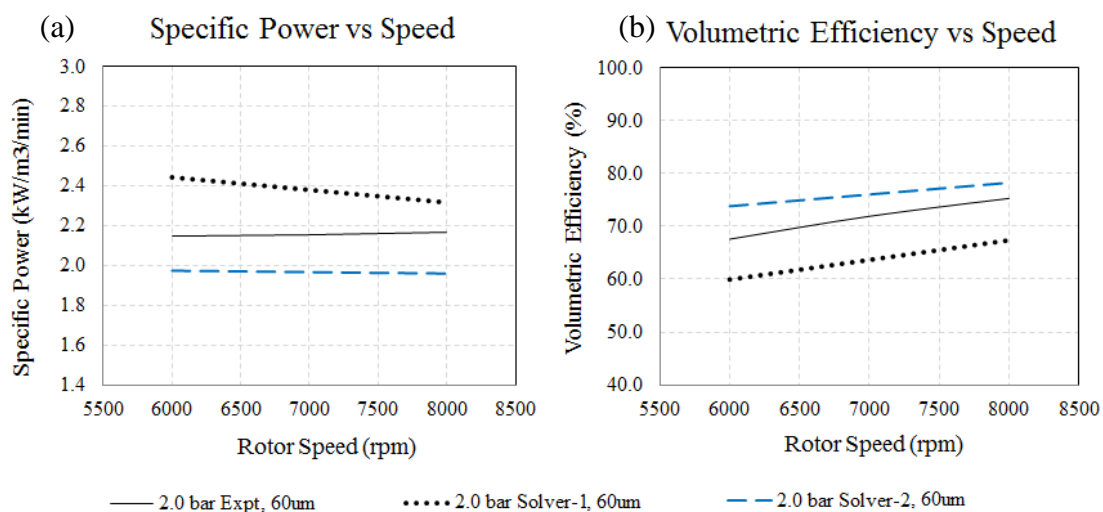


Figure 6.10 Comparison of specific power and volumetric efficiency

Figure 6.10b compares the volumetric efficiency prediction from the CFD calculations with the experimental data and Figure 6.11b shows the comparison between the solvers over the full range. Efficiencies obtained from Solver-2 are closer to the experimental results and could be further improved by specifying accurate clearances. As the compressor speed increases the volumetric efficiency increases. Both solvers predict the same trend in volumetric efficiency and at speeds beyond 11000rpm there is only a small gain in efficiency. The offset in efficiency prediction from the solver continues to remain throughout the speed range but reduces at higher speed and 2.0bar discharge, as compared to lower speed at 3.0bar discharge pressure.

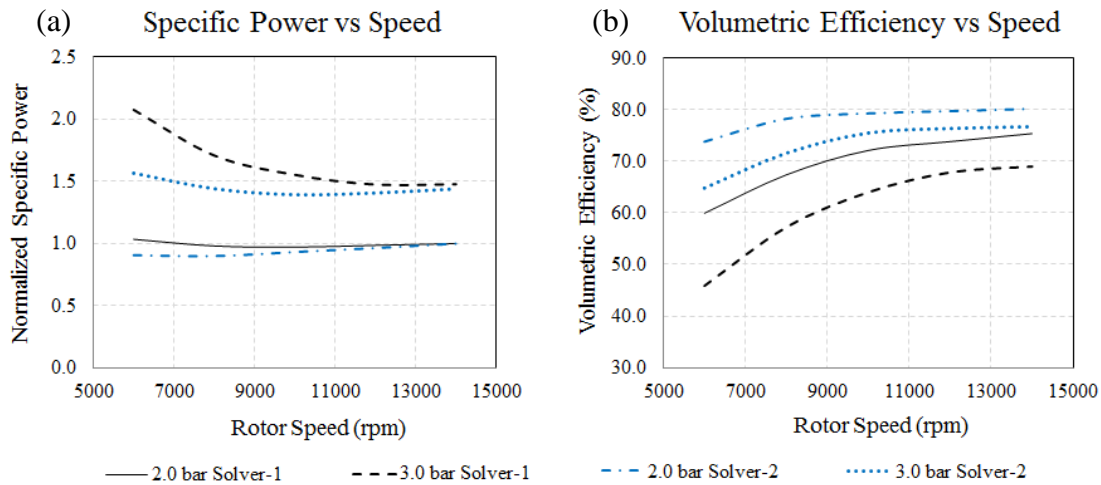


Figure 6.11 Comparison of full range specific power and volumetric efficiency

The study revealed differences in mass flow rate predictions between the two CFD solvers and also deviations compared with the experimental results. The leakage flow through the compressor is dependent on the grid used for the deforming rotor domain. In these two solvers the same grid was used. Cross section of the grid is shown as level Fine in Figure 6.48 and was found to give grid independence with Solver-1 with 2.0 bar discharge pressure at 8000rpm. Hence this level of refinement was chosen for the comparison of solvers. But as seen from the mass flow results, same grids produce different leakage flow rates with the two solvers. The main reasons for this have been assumed to be as follows:

- Treatment of the physical mesh.*

Solver-1 with a vertex centred computational cells generates a different topology of the physical mesh as seen in Figure 6.2b. On the other hand Solver-2 with cell centred computational cells uses the physical cell without alteration as seen in Figure 6.2c. It is anticipated that, due to internal conversion of the cell structures into polyhedral, grid coarsening is being experienced by solver-1 and hence there is some loss in curvature of the rotor profiles. It has been ruled out that any difference in the port grid cell structure influences the leakage flow because of the non-conformal interface with the rotor domain and, a separate test with an identical port mesh in both solvers produced the same differences in leakage flow.

- Solver formulation*

Solver-1, with a pressure based coupled approach solves the mass and momentum conservation equation as one set while Solver-2 with pressure based segregated approach

solves the mass and momentum conservation equations in sequential fashion, with each equation successively becoming converged in the coefficient loop. Even though the mass imbalance between the suction flow and discharge flow of the compressor was found to be of the same order from both the solvers, it is anticipated that a sequential solution leads to higher velocities but lower density in the leakage gaps and hence lower leakage flow is being predicted by Solver-2.

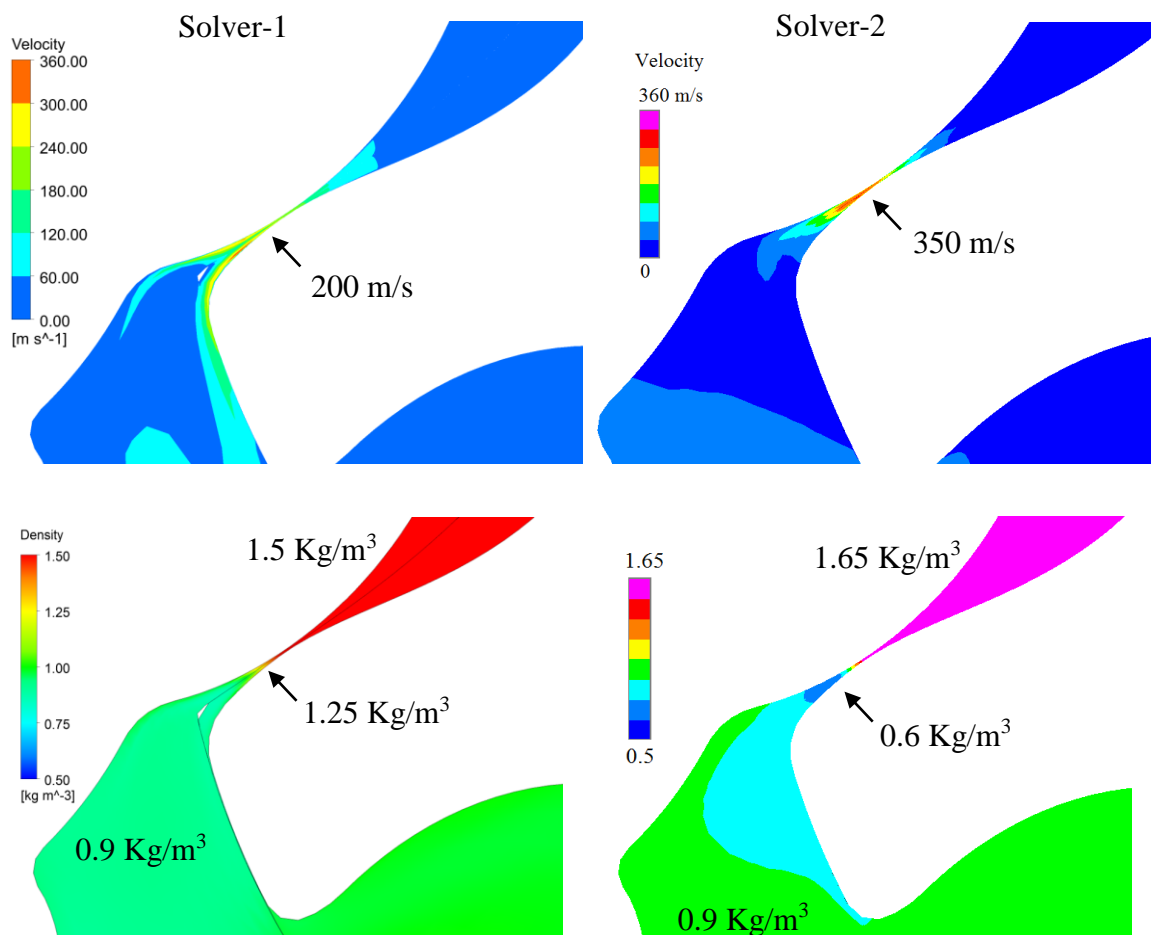


Figure 6.12 Comparison of velocity and density in leakage gaps

Figure 6.12 shows a comparison of leakage velocity magnitudes and density variation in the leakage gap predicted by the two solvers. In the case of Solver-1, the leakage velocity is nearly 200m/s and the density in these gaps is about 1.25 Kg/m^3 . This results in an approximate leakage flow of 250 Kg/s per unit area of leakage. Similarly with Solver-2 in the same leakage zone, the velocity is much higher in the range of 350m/s while the density is much lower in the range of 0.6 Kg/m^3 . This results in an approximate leakage flow of 180 Kg/s per unit leakage area which is 16% lower than in case of Solver-1.

Below samples at 8000rpm and 2.0bar discharge pressure present the level of conservation achieved with the two solvers between suction and discharge mass flow rates averaged over a few number of cycles. Imbalance in mass with both the solvers is of the same order.

	Suction (Kg/sec)	Discharge (Kg/sec)	Imbalance (%)
Solver-1	0.179	0.178	0.40
Solver-2	0.203	0.202	0.45

3. Numerical schemes

In the case of Solver-1 the turbulence model selected was SST k-Omega. This choice was based on the author's experience of getting better solver stability with this model. In the case of Solver-2, the turbulence model was selected as k-epsilon. This choice was based on the availability of the model in the solver. It was anticipated that a difference in the type of turbulence model employed would influence the leakage flow. However, this hypothesis needs to be validated with further extensive analysis of the model and the solvers, because a separate test with Laminar flow i.e. no turbulence model employed, predicted the same level of difference in mass flow rates in the results from both the solvers while the internal pressure distribution remained identical.

6.2.6 Inference from comparison of solvers

Flow in a twin screw compressor was modelled using two different CFD solvers which have different approaches to discretisation and solution of the governing equations. Performance predictions were obtained over a range of speed and pressure ratios. These performance parameters were also measured on a test rig. The following conclusions can be derived from comparison of the results in this study:

- Differences exist between the two solvers in the prediction of flow rates through the compressor. Comparison with experimental data suggests that Solver-2 gives more accurate estimates of flow rates for the expected clearances.
- In the future, it will be necessary to carry out further studies in order to establish the reason for under prediction of the flow by the coupled solver used in Solver-1.
- Both solvers predict indicated power close to the experimental value.
- Operational clearances change due to temperature variation under different operating conditions. In order to obtain accurate predictions, this change should be accounted for

in the CFD models in future. This may require employment of fluid solid interaction modelling.

- The time required for the segregated cell-centre Solver-2 to reach a cyclic solution is about one third of the coupled Solver-1; it is less memory intensive and resulted in flow predictions closer to the experimental values.

This study provides a good basis for further consideration of the application of variable leakage gaps based on empirical or analytical correlations and also in improvement of the differencing schemes and other settings required for specific CFD solvers. The availability of extended data from the experimental measurements will be beneficial for comparison over a wider range of operating conditions and will help improve the CFD models.

6.2.7 Influence of interlobe grid refinement on performance prediction

During operation, the rotors are subjected to thermal deformation which changes the clearance gap size. The CFD models used in the study do not take such changes into consideration. Therefore, it is estimated that the clearances will reduce with the increase in temperature. Therefore the grids for CFD are generated with reduced uniform clearances of 60 micro metres in the interlobe and radial gaps in order to compensate for thermal distortion. The axial end clearances are not included in the CFD model. Figure 6.13 shows the CFD model domain, boundaries and the sample grid in the cross section of the rotor domain. A uniform pressure of 1.0 bar was specified at the suction while the discharge pressure is 2.0bar. The main rotor speed was 6000rpm and 8000rpm. The high resolution scheme was used in the ANSYS CFX solver and the cycle average mass balance between the rotor suction and discharge was achieved within 1% in all cases.

Table 6.4 Grid levels and number of divisions.

Level	Circumference	Radial	Angular	Interlobe	Outer Circle	Mesh Size in Rotors
Base Grid	70	10	50		260	913682
Grid – 1	72	10	50	120	240	942480
Grid – 2	80	10	50	150	250	1049818
Grid – 3	90	10	50	200	250	1178100
Grid – 4	120	10	50	350	250	1570800

Four levels of interlobe refinement have been generated with the new grid such that the first level has a refinement comparable to that of the base grid. The refinement is only on the profile in the interlobe space (Section 5.2.6) and on the casing side the number of divisions has been maintained equivalent to that of the base grid. Table 6.4 shows the different grid levels used for calculations and cross section mesh is shown in Figure 6.13. The results obtained have been compared with experimental measurements.

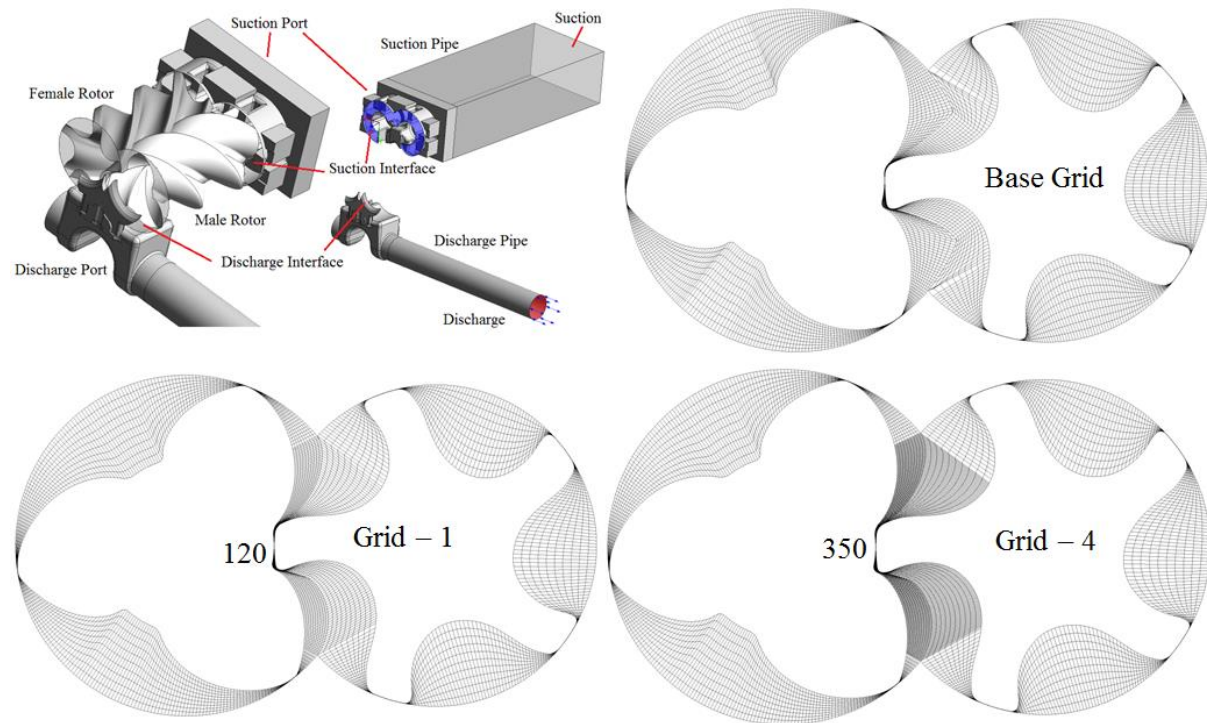


Figure 6.13 CFD Model Domain and Grid refinements in the interlobe clearance

6.2.7.1 Results and Discussion

The results from the analysis have been presented as a comparison of the internal pressure rise, indicated power (P_{ind}), flow rate, volumetric efficiency (η_v) and specific indicated power (P_{sind}) between the Base grid case and the various refinement levels of the new grid. Figure 6.14 is a plot of the pressure contour on the rotor surface with the two different grids at 8000rpm. The surface of the rotor with Base grid is much regular as compared with the new grid but the pressure contour shows similar variation in both the cases.

6.2.7.2 Pressure – Angle variation

Figure 6.15 shows the variation of pressure in the compression chamber at 6000rpm and 8000rpm. Plots from the base and new grids are compared with experimental measurements. The internal pressure increase predicted by the base grid and new grids are close to each other.

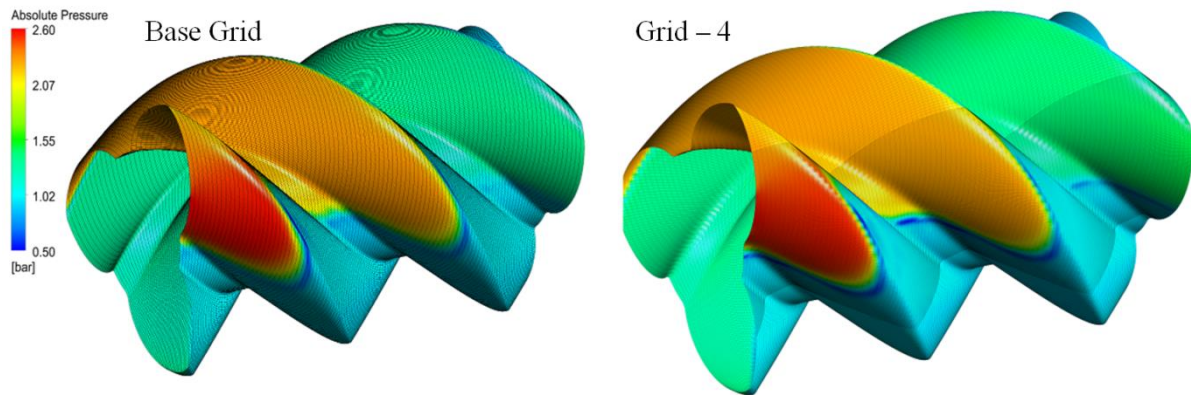


Figure 6.14 Pressure contours on the rotor surface with Base grid and Grid – 4

A small increase in the compression rate is observed with new Grid – 4. The pressure curves obtained from the CFD are close to the experimentally obtained pressures, but the peak pressures from the CFD models are slightly lower than the experimental peak pressures at both 8000rpm and 6000rpm. Since the difference between CFD and experimental peak pressures increases with speed it is concluded that the thermal deformation of rotors and casing affects the leakage gaps and further account of this on clearance will be necessary for better predictions. At a discharge pressure of 2.0bar and the current size of the discharge port, over-compression is observed with pulsations in the discharge port which are being predicted accurately by CFD.

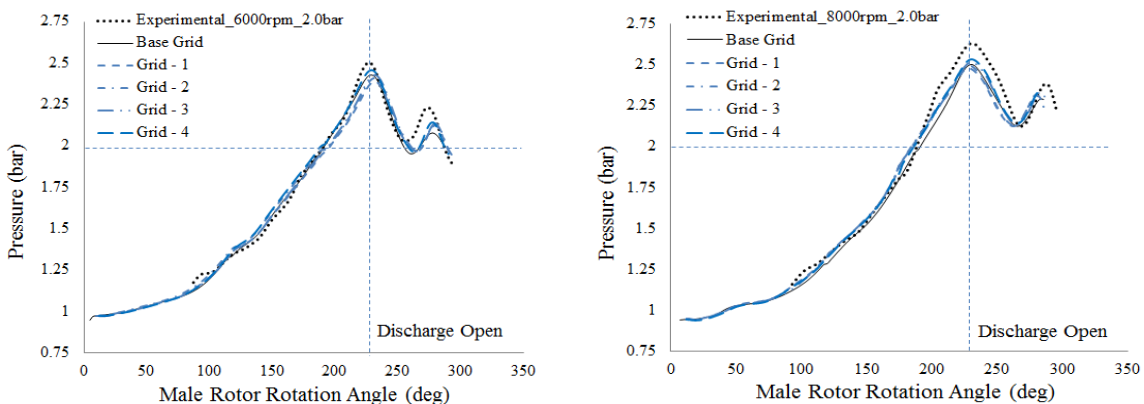


Figure 6.15 Pressure variation in the chamber with at 6000 and 8000rpm

6.2.7.3 Indicated Power

Figure 6.16 shows the variation of P_{ind} with speed for different grid refinements. Predicted values of P_{ind} have been normalised with respect to the experimental measurements. A constant mechanical efficiency (η_{mech}) of 95% has been assumed for the experimental

measurements. It is seen that the difference in P_{ind} between CFD prediction and experiment is about -2.7% at 6000rpm and about -6.6% at 8000rpm with the base grid. With the new grid, P_{ind} has increased at both the speeds and also with grid refinement from Grid – 1 to Grid – 4. The difference between CFD and experiment is about $+1.4\%$ at 6000rpm and about -2.8% at 8000rpm with Grid – 4. It should be noted that η_{mech} will change with speed.

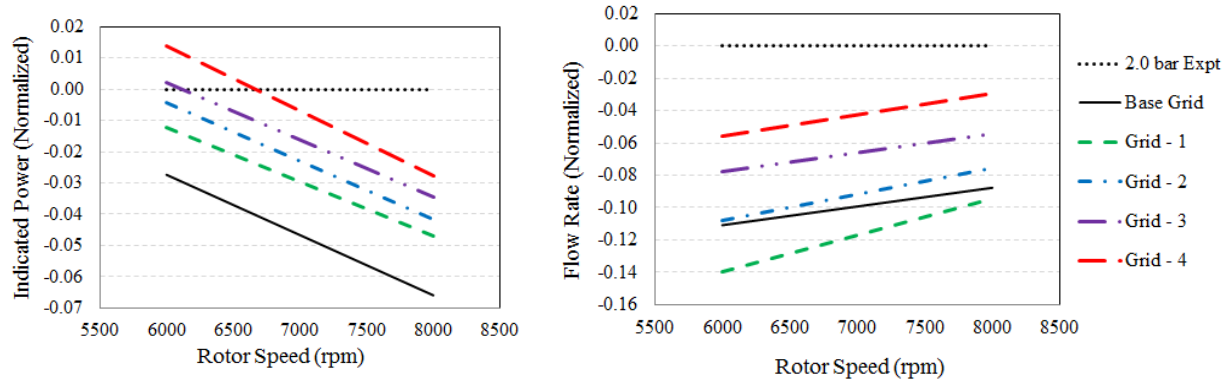


Figure 6.16 Comparison of Indicated power and Flow rate

6.2.7.4 Flow rate

Figure 6.16 shows the variation of Flow rate with speed for different grid refinements. The predicted Flow rates have been normalised with respect to the experimental measurements. As can be seen, interlobe grid refinement greatly influences the flow rate. With the Base grid the difference between CFD prediction and experiment was about -11% at 6000rpm and -8.7% at 8000rpm. But this difference has been reduced with Grid – 4 to -5.5% at 6000rpm and -2.9% at 8000rpm. The increase in flow rate also correlates with the increase in P_{ind} from Grid – 1 to Grid – 4.

The difference in flow rate prediction was reduced with interlobe refinement but it is still present. This is because the clearance gap of 60 micro meters has been assumed in the CFD model as the operating gap size. Due to thermal deformation and other operating uncertainties, the gap size is expected to vary. A few more iterations with reduced gap size could help to improve the model predictions.

6.2.7.5 Volumetric efficiency

Figure 6.17 shows the variation of volumetric efficiency with speed for different grid refinements. η_v predicted from the Base grid is about 7% lower than the experiment. With the new grid the difference is higher with Grid – 1 but reduces with further interlobe refinement.

With Grid – 4 the difference in η_v from the experiment is just about 3%. In line with the flow prediction, the difference is smaller at 8000rm than at 6000rpm.

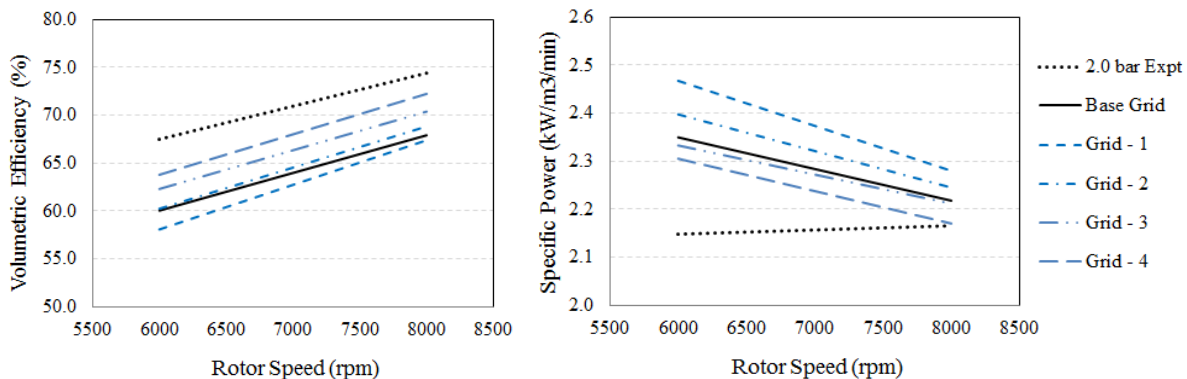


Figure 6.17 Comparison of Volumetric efficiency and Indicated Specific power

6.2.7.6 *Indicated Specific Power*

Figure 6.17 also shows the variation of indicated specific power with speed for different grid refinements. P_{sind} is influenced by both the calculation of indicated power and the mass flow rate. The Base grid specific power prediction is higher than that of the experiment at both speeds. The same trend is seen with the new grids because of the slight increase in indicated power as seen in Figure 8. From the level of Grid – 1 to Grid – 4, however, this difference goes on reducing. At 6000rpm the difference between calculated and experimental P_{sind} is about 0.2 kW/m³/min with Base grid and is reduced to 0.15 kW/m³/min with Grid – 4. At 8000rpm, the predicted specific power with Grid – 4 matches with the experiment.

6.2.7.7 *Inferences from results with interlobe grid refinement*

- The non-conformal interface between the rotors was better resolved because of interlobe grid refinement.
- The results of pressure showed that there was a very small difference between the base grid and the new grids and the internal pressure rise curve followed well with the experimental measurement.
- The indicated power increased by a small amount from Grid – 1 to Grid – 4 and was close to the experimental value at both speeds.
- There was a big influence of interlobe grid refinement on the predicted mass flow rate and hence the leakage flows. From Base grid to the Grid – 4 the difference between the experimental measurement of flow rate and CFD flow rate reduced at both speeds.

- A difference between CFD calculations and experimental measurement still exists. This can be attributed to the choice of operational clearance gaps in the CFD model.

In order to obtain higher accuracy in CFD predictions, change in leakage gap sizes due to thermal deformation need to be accounted in the CFD models. This requires employment of fluid solid interaction modelling or using experimental data. The new grid generation approach however provides the flexibility to improve the resolution of the rotor geometry and thereby to some extent reduces the inaccuracy in leakage flow calculations.

6.2.8 Influence of inflation layer on the performance prediction

Nouri et al. (2006) presented measurements of velocity profiles in the working chamber of a twin screw compressor using LDV and *Kethidi et al.* (2011) compared their statistically averaged data with computational results from selective RANS turbulence models. In these studies it was seen that though the mean profiles tend to agree with the experimental data, there is a vast difference in the local velocity magnitudes and directions. The need to refine the rotor domain grids locally, close to the walls and capture leakage more accurately was highlighted.

A test case was solved for the dry air compressor. Results were compared with solution on a grid having 8 layers in the inflation with a linear growth rate of 1.2. Cross section of the grid is shown in Figure 6.18 and Table 6.5 gives the size of the grids. The simulation was for an operating condition of 2.0 bar discharge pressure and 8000 rpm male rotor speed. The suction pressure was 1.0 bar and temperature 300K.

Table 6.5 Grid size comparison with inflation layers

	Nodes	Elements
No Inflation	838378	1526355
With Inflation	1316282	2000243

The results of interest from the calculations can be classified into two broad categories. One set is the comparison of flow features like velocity, Boundary Layer y^+ , Wall Shear, and the other set is a comparison of the integrated performance quantities like power, mass flow rate and internal pressure variation in the chambers during the cycle.

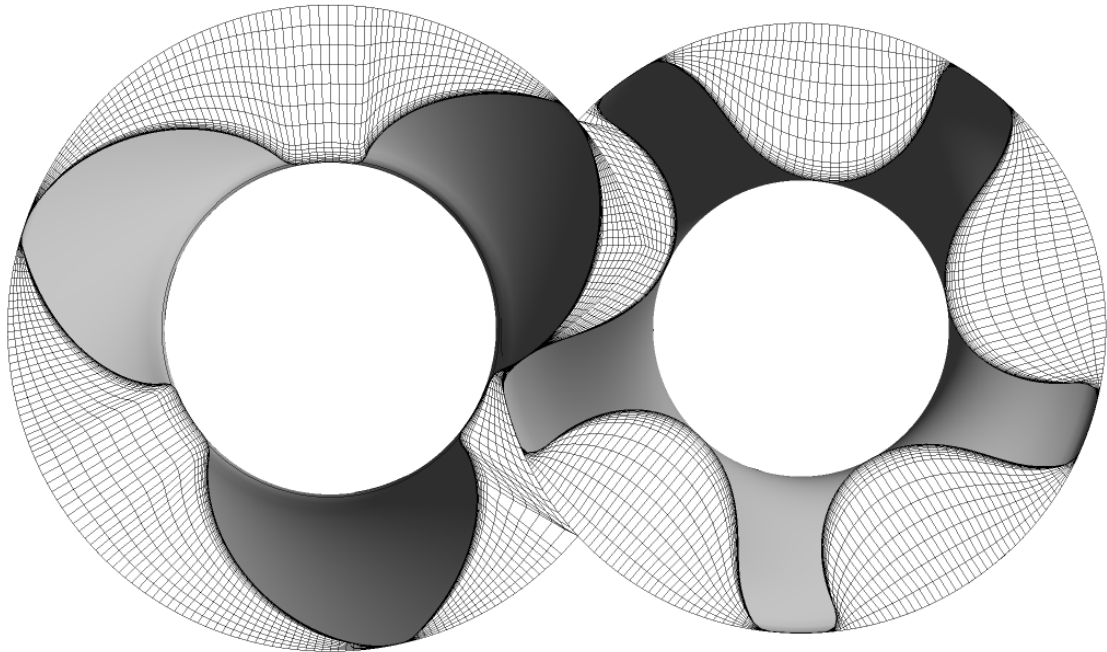


Figure 6.18 Example of Inflation layer grid on the two rotors

6.2.8.1 Flow features

i. Local Velocity Profile

Figure 6.19 shows the comparison of local instantaneous velocity profiles in the compression chamber near the discharge port. Two sampling lines from the root of the male and female rotor are constructed in the y direction towards the casing. The lines are 0.5 mm distance upstream from the axial discharge face. Approximately 450 velocity magnitude samples were extracted on these lines from the local field data. From the velocity profiles it is seen that close to the rotor surface the grid with inflation layer is resolving the velocity gradients and grid without inflation layer is resulting in a very coarse profile.

Table 6.6 Rotor tangential velocity at root diameter

Units [m/sec]	$V_t = r\omega$	No Inflation	With Inflation
Male 8000rpm	27.486	20.063	26.317
Female 4800rpm	14.626	22.036	14.508

Also Table 6.6 presents the rotor tangential velocities at the root diameter. The tangential velocity is the dominant direction of wall motion and hence gas velocity at the rotor surface under no slip conditions should be close to this wall velocity. It is seen that the grid with

inflation layers closely matches the root diameter tangential velocities on both the male and gate rotors. On the other hand the root tangential velocities derived from the grid without the inflation layer deviate significantly. On the male rotor they are under estimated and on the gate rotor they are over estimated. This could be due to the clockwise and anticlockwise rotation of these two rotors and the relative flow direction into the discharge port.

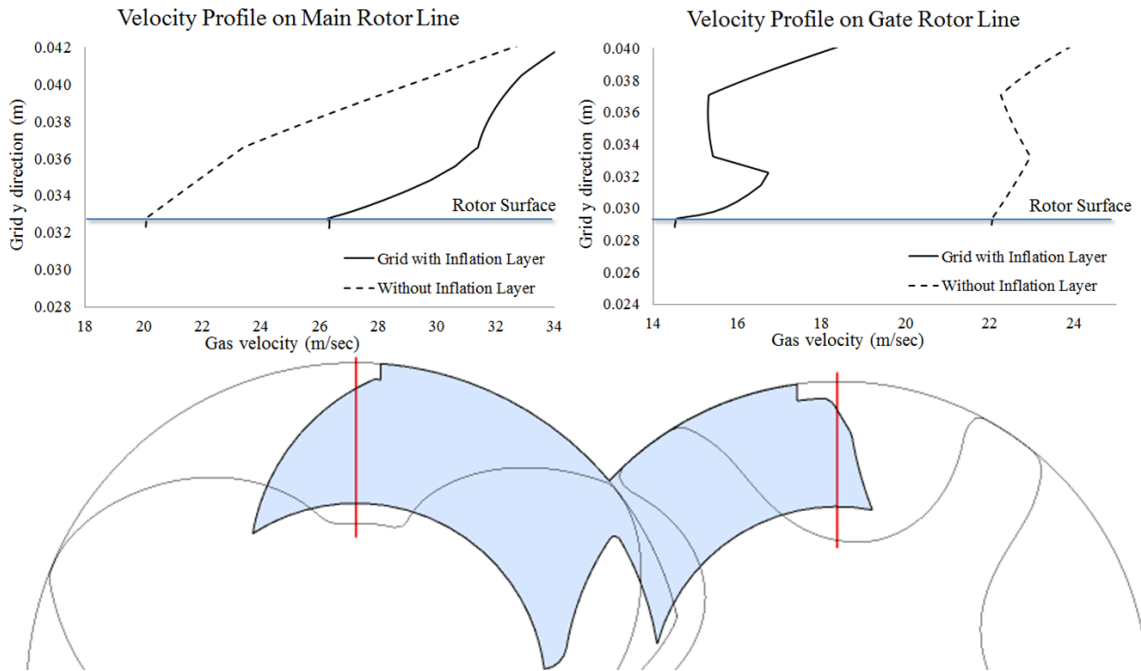


Figure 6.19 Comparison of velocity profile close to discharge port

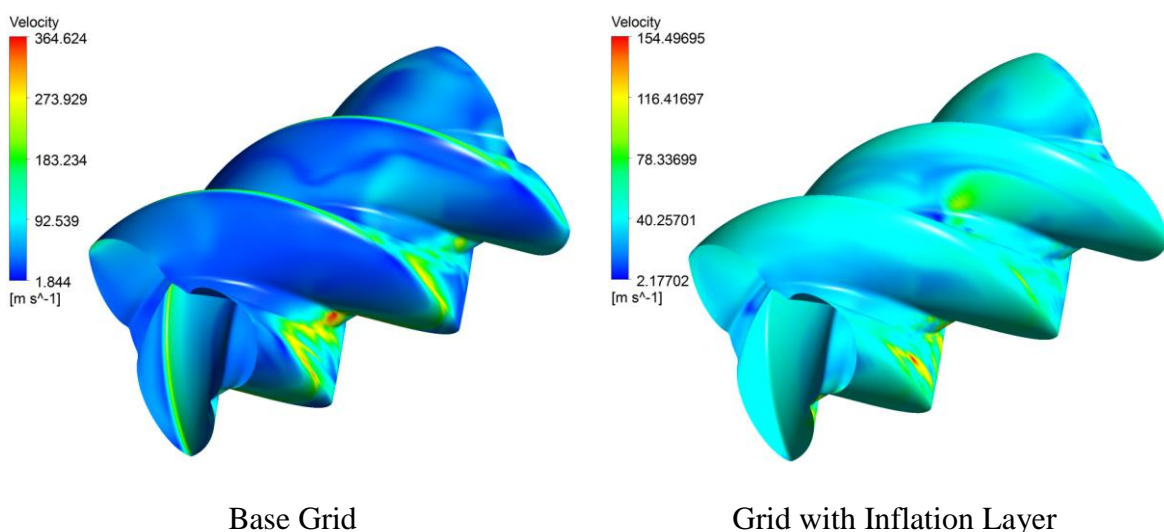


Figure 6.20 Comparison of gas velocity adjacent to Male Rotor

As seen in Figure 6.20 the gas velocity variation near the male rotor surface is significantly different in the two cases. The maximum velocity location is in similar leakage zones in both cases but the peak local velocity magnitude in the case without the inflation grid is 364.6m/s giving a Mach number of about 1. In the case with inflation it is about 154.5m/s, which is almost 40% lower, giving a Mach number of about 0.4. The machine tip speed is 53.4 m/s at 8000rpm.

ii. y^+ Variation

Wall y^+ is the normalised distance perpendicular to the wall and gives an indication of the resolution of the boundary layer zone. In order to apply the wall function approach with the SST k-omega turbulence model in the numerical solver, it is desirable to build a grid that gives y^+ such a value that the first grid point normal to wall falls close to the end of the laminar sub-layer and hence the Log-law of the wall can be applied instead of resolving the laminar sub-layer. On the other hand if the near wall modelling approach is used, then even the sub-layer needs to be resolved and the magnitude of y^+ to be attained is much below 1.0.

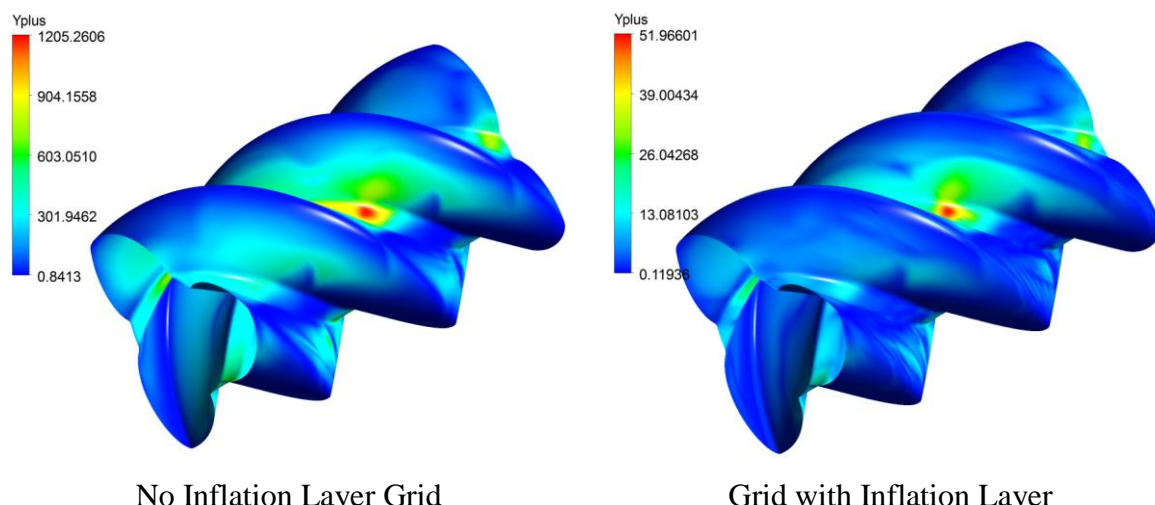


Figure 6.21 Comparison of y^+ based on first grid point coordinate from the Male Rotor

In industrial flows like those of screw machines it is desirable to use the wall function approach to limit the cell count in grids. With this approach number of nodes that should be placed in the boundary layer normal to the wall is about 10 (ANSYS, 2011). Figure 6.21 shows the variation of y^+ on the male rotor with and without inflation layer grid. Wall normal distance of the first grid point is used in the calculation of this y^+ . Clearly the y^+ with the inflation layer grid is improved with about a maximum of 52 in the core region of the domain. The maximum surface is covered by y^+ of about 10 whereas in the grid without inflation the maximum surface

is covered by y^+ more than 100. This will result in inaccurate velocity gradients and wall shear calculations.

iii. Wall Shear

Wall shear indicates the magnitude of the viscous resistance to the gas motion close to the wall and is directly influenced by the resolution of the velocity gradients normal to the wall. If wall shear is under or over predicted, it can result in inaccuracies in the calculation of leakage flows. Figure 6.22 compares the wall shear on male rotors with and without inflation layer grids. The grid with the inflation layer shows a value of about 1460 N/m^2 maximum wall shear in the leakages. The grid without inflation shows a maximum wall shear in the same zones but the magnitude is almost 50% lower.

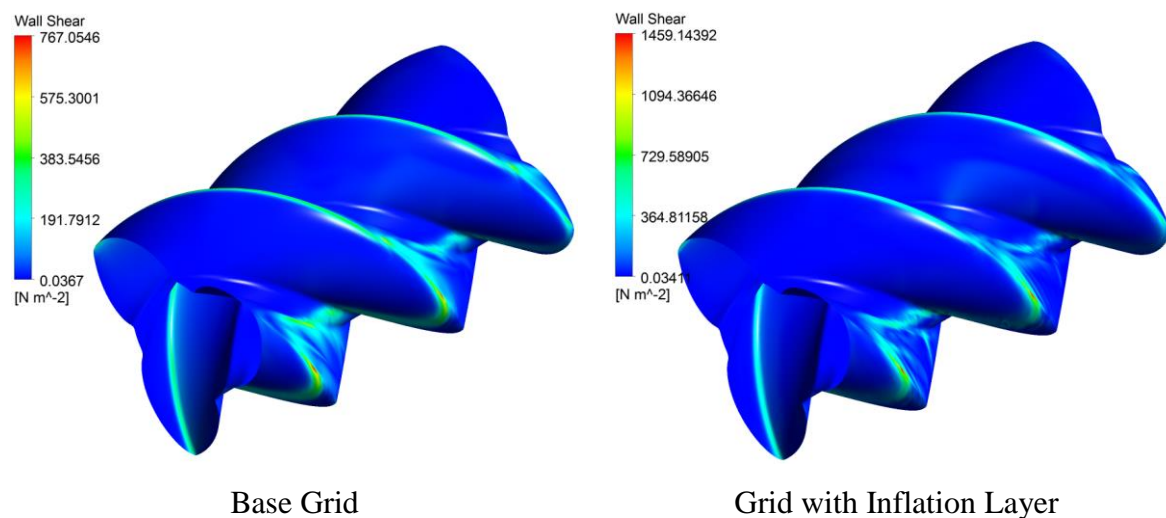


Figure 6.22 Comparison of Wall Shear proximate to the Male Rotor

6.2.8.2 Integrated performance quantities

i. Pressure – Angle variation

Figure 6.23 shows a comparison of the compression chamber pressure with the rotation of the male rotor from grids with and without inflation layer. The results agree closely with each other and there is no difference between the two. This indicates that the chamber pressure rise is not influenced by the grid resolution close to the rotor surface.

ii. Power and Mass flow

Table 6.7 presents a comparison of cycle average mass flow rate, power and specific power and, in addition, the peak pressure in the pressure curve. There is no indication that grid refinement close to the rotor surface influences these quantities. A small increase of only 2%

in the mass flow rate was observed with the inflation layer grid. This could be due to better capture of the wall shear. Since the rotor curvature refinement remained unchanged between these cases, the bulk leakage flow remained unchanged, but the specific power was reduced by 1.7% with the inflation layer grid.

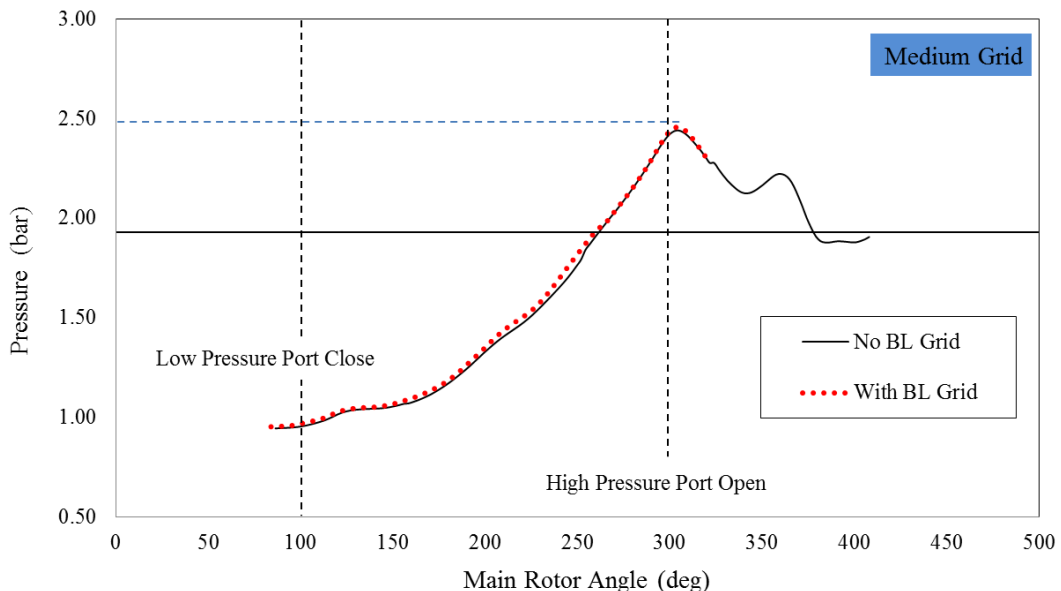


Figure 6.23 Pressure Angle diagram with Inflation layer grid

Table 6.7 Comparison of results with inflation layer grid

Case	Mass Flow (Kg/sec)	Peak Pressure (bar)	Power (kW)	Specific Power (kW/Kg/sec)
No Inflation	0.16396	2.44	21.457	130.87
With Inflation	0.16731	2.46	21.528	128.67

6.2.8.3 Inference from results with inflation layer grids

Results presented here and from Section 6.4.3, show that flow in positive displacement screw machines is highly influenced by circumferential and axial grid refinement and not as significantly by wall normal refinement of the rotor domain. However, as seen from the results, inflation layers give better predictions of the local flow features that are desirable for computational flow models. These conclusions are specific to the SST k-omega turbulence model in CFX solver and for the reported levels of grid refinement.

6.3 Analysis of a 3/5 synchronised Dry Air Expander

GL-51.2 is a dry running, synchronised twin screw machine designed at TU Dortmund. It has been tested for use as an oil free expander of high pressure air at various operating conditions. The experimental data, obtained from these tests, has been used in the present study to compare the results of 3D transient CFD calculations. Experimental data and expander design data, with CAD models, rotor profiles and operating conditions were provided for the study by TU Dortmund. At a few operating conditions, grids were constructed with inflation layer refinement using the procedure described in Section 5.4 and its influence on performance prediction was analysed and compared with those derived from the base grid.

In a compressor, the rotation of rotors displaces the gas from the low pressure port to the high pressure port with gradual decrease in the contained volume. Expander screw rotors rotate in the opposite direction to compressor rotors in such a way that the gas is displaced from the high pressure port to the low pressure port with gradual increase in volume. Since these two processes more or less mirror each other, the same CFD analysis calculation procedures used for screw compressors, can be applied to expanders. The expander fluid domain is decomposed into four main regions namely, the male rotor flow domain, the female rotor flow domain, the high pressure flow domain and the discharge flow domain. The rotor flow domains were mapped in SCORG (rotor to casing type of distribution) and the numerical grids of the port domains were generated by commercial software ANSYS. This was followed by the simulation setup which comprises importing the integral numerical grid in the CFD solver and definition of the operating parameters and solution schemes.

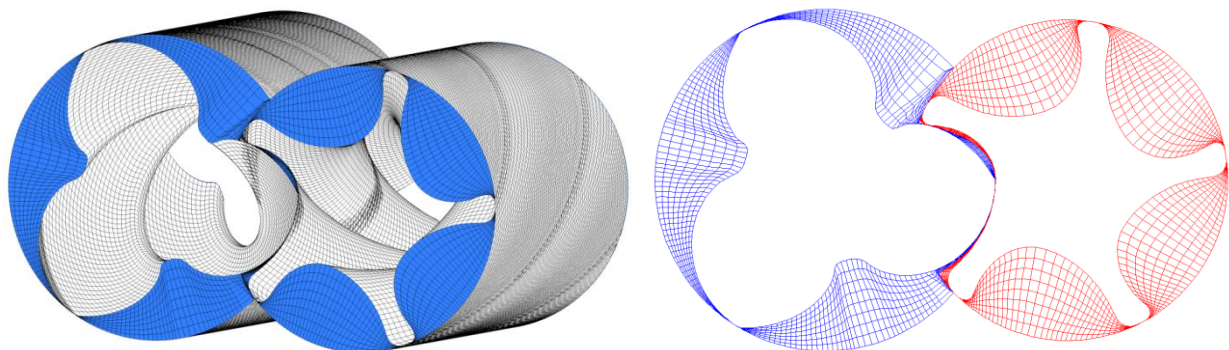


Figure 6.24 Numerical grid of the GL-51.2 screw expander rotors

6.3.1 Case description

GL 51.2 is a twin screw expander with a 3/5 lobe rotor combination. The outer diameters of the male and female rotors are 71.847mm and 67.494mm respectively. The L/D ratio is 1.406 and the centre distance between the rotors is 51.22mm. The male rotor wrap angle $\Phi_w = 200^\circ$. SCORG was used to generate a hexahedral grid in the rotor domain. The grid of the rotors used in this research is comprised of 40x8x40 divisions in the circumferential, radial and axial direction per interlobe respectively in the male and female fluid zones. The complete rotor grid for one of the cross section is shown in Figure 6.24.

The mesh in the high and low pressure ports is tetrahedral and generated by use of the ANSYS grid generator. The three domains were assembled together in the solver through non-conformal conservative interfaces. The connecting pipes were meshed by a hexahedral grid. Figure 6.25 shows the complete model of the analysed expander with all sub domains.

Initially, the end clearance leakage area was not included in the calculation but after preliminary evaluation it was noticed that this leakage area plays an important role in the performance of the machine. Therefore a hexahedral numerical grid with 5 cells across its thickness was introduced in the model to account for the high pressure end leakage gap.

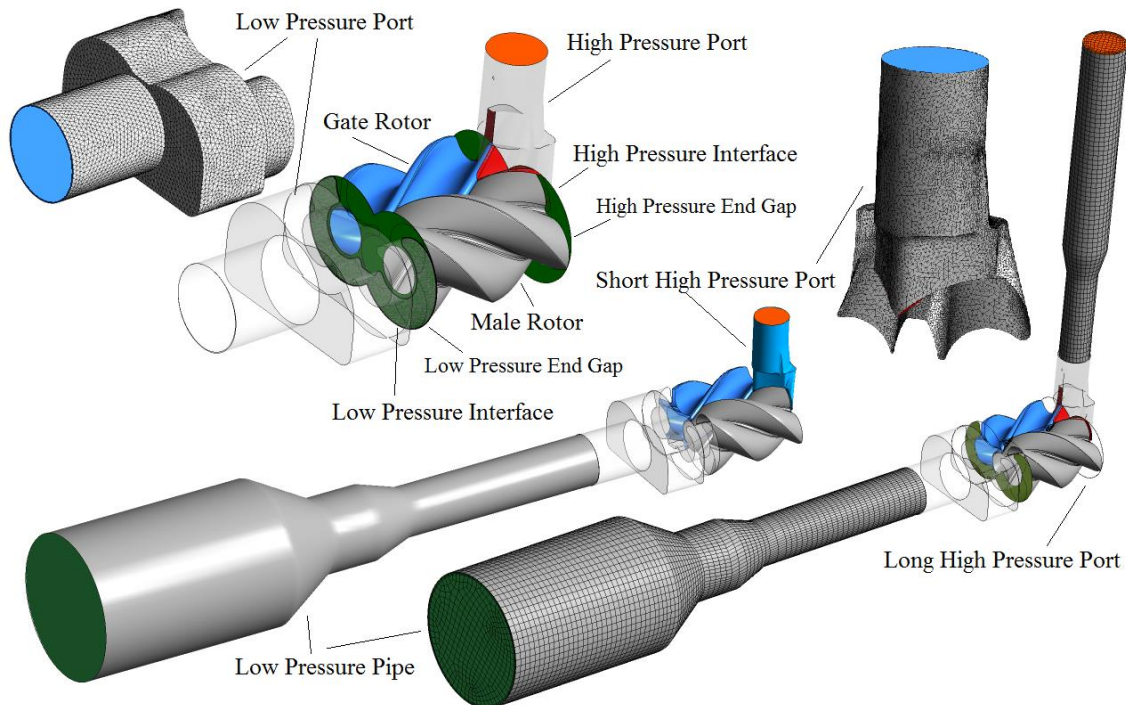


Figure 6.25 Flow domains for analysis of the twin screw expander

The numerical grid for the screw compressor rotors was comprised of 213328 cells. The numerical grid for the short ports accounted for 574813 cells while for the long ports it was

585761 cells. The overall number of computational numerical cells with short ports was 788141 while with the long ports it was 799089.

6.3.2 Simulation

The analysis was carried out in two stages. The aim of the first stage was to identify the modelling parameters that influence the predicted results from the CFD calculations and select those parameters that provide the best results, when compared with experimental data. The main aim of the second stage was to calculate the machine performance, using a selected set of modelling parameters, obtained from the first stage, which best coincided with measured test results. A few operating conditions were calculated with grids constructed with inflation layer refinement and its influence on performance prediction was analysed.

6.3.2.1 *Stage I: Selection of modelling parameters*

The accuracy of performance predictions with a CFD model depends on many factors which are dependent on the level of assumptions introduced in the setup. The first phase in analysing this screw expander was to determine the influence of the following modelling parameters:

- i) Size of clearance gaps,

Clearance gaps have a significant effect on the performance of screw machines. It was noticed in previous studies (*Kovačević et al.*, 2007) that they affect the fluid flow much more significantly than the pressure distribution in the working domain. Three different clearance gaps were evaluated namely the interlobe, radial and end face. The design clearances of this machine were defined as 50-80 µm in the interlobes, 80 µm radially, 100 µm at the high pressure end and 250 µm at the low pressure end. Due to thermal deformation and bearing clearances, these gaps change during the operation of the machine. In order to evaluate the effects of individual gaps on the performance, a number of different values for each of these gaps were compared.

- ii) Location of the domain boundary,

Figure 6.25 shows a model of the screw expander with short and long domains on the suction and discharge ends of the machine. It was expected that the length of the ports and location of boundaries might affect the solution.

- iii) Type of boundary condition,

Due to the cyclic variation of pressure, temperature and other values of the flow in the compressor ports, it is difficult to define fixed conditions at the boundaries of the flow domain.

Usually it is possible to define an “opening” boundary with a specified non-reflecting pressure head at the boundary location. This type of boundary permits the flow to enter and leave the computational domain but affects the solution, depending on the location of the boundary relative to the source of the pulsations. An alternative approach, proposed by *Kovačević et al.*(2002), is to define a computational domain at the end of the machine flow domains which will account for a mass and energy source or sink to simulate constant conditions in the machine reservoirs. Such a source domain adds to or removes mass and energy from the gas so that pressure oscillations in the ports are damped and maintained at a given level.

iv) Flow regime, Laminar or Turbulent simulation,

Flow calculations assuming both laminar flow and the Spalart-Allmaras turbulence model were checked in various test cases to evaluate their influence on the results. The Spalart-Allmaras turbulence model is a one-equation model that solves transport equation for the kinematic eddy (turbulent) viscosity. It will be shown that the turbulence modelling influences the mass flow through the expander.

Table 6.8 Cases evaluated for the analysis in *Stage I*

Case No	High Pressure Port	Male Rotor Speed		High Pressure Boundary	Turbulence	Clearance (um)			
		rpm	rpm			Interlobe	Radial	HP End	LP End
1	Short	4000	10000	Opening Pressure	Spalart-Allmaras	50	80	400	0
2	Short	4000	10000	Opening Pressure	Spalart-Allmaras	50	80	100	0
3	Short	4000	10000	Opening Pressure	Spalart-Allmaras	50	80	100	250
4	Short	4000	10000	Opening Pressure	Spalart-Allmaras	10	10	0	0
5	Long	4000	10000	Opening Pressure	Spalart-Allmaras	50	80	100	0
6	Short	4000	10000	Opening Pressure	Laminar	50	80	100	0
7	Long	4000	10000	Source Domain	Spalart-Allmaras	50	80	100	0

The designed operating speed range of the expander was from 2000 to 16000 rpm. Hence two points at 4000 and 10000 rpm were selected for *Stage I* calculations. Similarly the high end port pressure can range from 1.5 to 3.0 bar; hence a Pressure of 2.0 bar was selected. The results obtained were compared with the measured pressure variation inside the working chamber presented in a Pressure – Angle diagram. Details of the cases analysed are given in Table 6.8.

6.3.2.2 Stage II: Performance evaluation

In the second stage, the CFD models, with setup conditions selected from Stage I, were analysed to evaluate the performance of the expander over a wide range of operating

conditions. Experimental values of flow and power, together with the corresponding pressure history inside the machine, as obtained from the TU Dortmund expander test rig are given by *Hutker and Bruemmer* (2013). The relevant test results obtained are presented in Table 6.9.

Table 6.9 Experimental test results for Expander GL 51.2

Speed	2000 rpm		5000 rpm		10000 rpm	
Pressure	Flow rate [kg/s]	Power [W]	Flow rate [kg/s]	Power [W]	Flow rate [kg/s]	Power [W]
1.6 bar	0.0292	511.93	0.0451	1318.84	0.0615	1748.06
2.0 bar	0.0327	758.50	0.0511	1817.65	0.0786	3444.82
3.0 bar	0.0409	1492.35	0.0737	3589.64	0.1179	7148.29

All measured points were taken at a high pressure air filling temperature of 350° K.

6.3.3 Results and Discussion

6.3.3.1 Pressure – Angle Diagram

A specimen Pressure – Angle diagram, presented in Figure 6.26, shows the phases in the expansion process. The working cycle starts with filling, which is characterised by an increase in the volume formed between the rotors exposed to the high pressure port. This part of the process is characterised by pressure fluctuations resulting from the moving rotor and gas interaction.

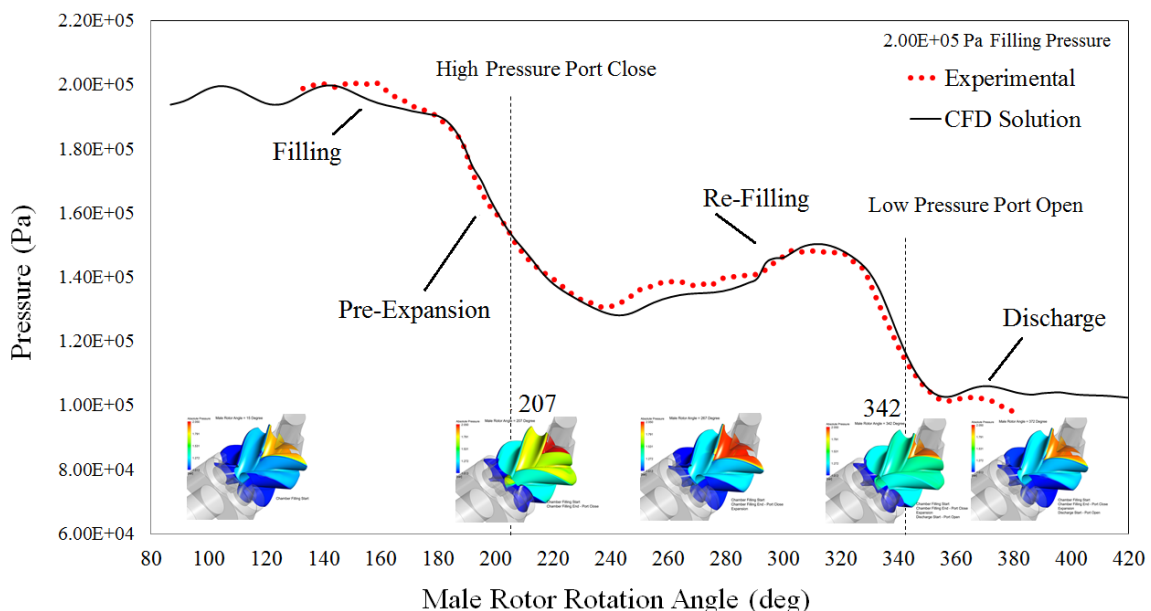


Figure 6.26 Variation of pressure in a twin screw expander

The inlet port of the machine has a relatively small area which results in throttling losses and a pressure drop in the expander inlet. The inlet area initially increases but it then decreases sharply, causing a further pressure reduction in the suction process which is defined as pre-expansion in the diagram. Pre-expansion reduces the pressure and hence the generated power. Useful work is produced during the expansion of the gas trapped in the enlarging working chamber. As expansion proceeds, the mass in the working chamber increases due to leakage flow from adjacent chambers which are at higher pressure. If the leakage paths are sufficiently large, this gain in mass can induce a pressure rise in the working chamber, despite its increasing volume. This process is referred to as re-filling and affects the expander power output. The final phase of the process is discharge. Ideally, this should start with the pressure in the working domain near the pressure downstream of the machine.

6.3.3.2 Influence of the clearance size on the performance of the expander

Figure 6.27 shows the P-Angle diagram for an inlet pressure of 2.0 bar and an expander speed of 4000 rpm, with various sizes of clearance gaps. It is shown that the size of the clearance gaps does not significantly affect the pressure during the filling, pre-expansion and discharge phases. However, it has a significant effect on the re-filling process. The nominal clearances specified in the design of this machine are: Interlobe 50 μm , Radial 80 μm and Axial 100 μm . To evaluate their influence on the performance, the following cases were calculated. In Case 1, both the interlobe and the radial clearances were assumed to have their design value, but the axial clearance on the high pressure side was assumed to be 400 μm . This case, with deliberately over-specified clearances, produced a P-Angle diagram close to that of the experiment, but resulted in a very high mass flow rate and a very low indicated specific power. The small clearances assumed in Case 4 inhibited the leakage and thus reduced the mass flow through the expander, thereby increasing the specific power output. The design values were assumed for interlobe, radial and high pressure axial clearances in Case 2 and zero axial clearance was taken for the low pressure end. This predicted the mass flow rate and specific power well but underpredicted the pressure in the re-filling phase. Case 3 with the same interlobe and radial gaps as in Case 2, but with a 250 μm axial low pressure clearance gap also predicted a similar re-filling pressure, with a nearly equal mass flow rate.

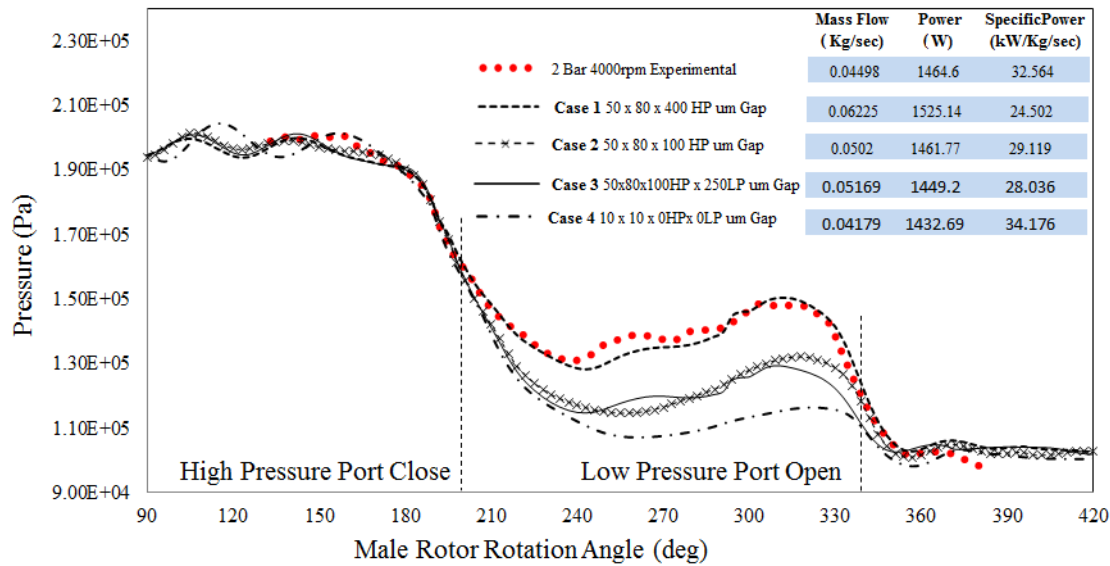


Figure 6.27 Influence of clearance variation on P-Angle at 4000rpm

These cases and several others, not presented here, in order to maintain clarity, confirmed that the axial clearance on the high pressure end makes a significant contribution to the direct leakage which increases the mass flow rate through the machine. The axial clearance on the low pressure end, although contributing to the internal leakage, does not affect the mass flow rate through the machine.

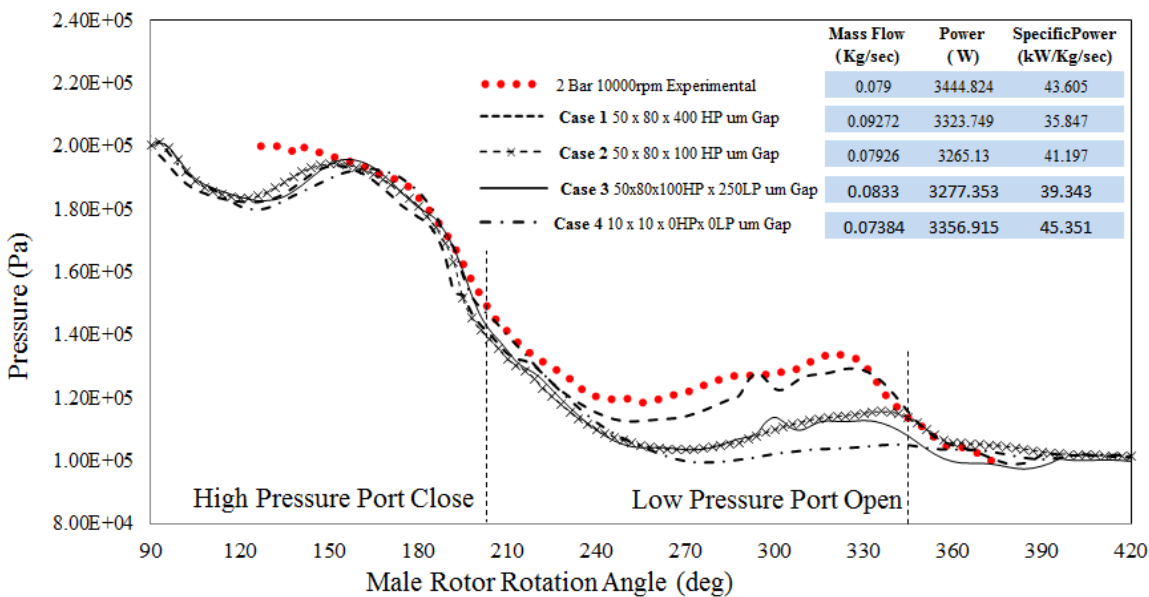


Figure 6.28 Influence of clearance variation on P-Angle at 10000rpm

The diagram for 2.0 bar filling pressure and 10000 rpm is shown in Figure 6.28. It is clear from this that the influence of the clearance gaps is larger at lower speeds but it was also noticed that

the increase in the interlobe and radial leakage gaps significantly increases mass flow rate through the machine. The design clearance gaps in Case 2 were selected for further analysis of the machine performance in stage II since they gave the best agreement with the test results in terms of predicting mass flow rate, indicated power and the P-Angle diagram at both speeds.

The area under the pressure-volume diagram gives the indicated power, which has been compared with experiment. Although the measured and estimated mass flow rates and indicated powers in Case 2 agree well, the measured refilling pressure is higher at both speeds. This can be explained by the dominant influence of the high pressure region on the indicated power due to the steep change in trapped volume and high pressure level. Therefore it appears to be vital to select operating clearances which will result in an accurately predicted mass flow rate rather than to closely match the pressure curve in the refilling process. It appears that these clearances coincide with the design clearances. However, during the operation of the machine, these clearances will certainly change and will result in different machine performance. It is thought that some of the clearance gaps change in such a way that the refilling process does not affect the main mass flow, since it occurs after the high pressure port is closed. Further investigation by use of Fluid-Solid Interaction studies may be useful to validate this theory.

6.3.3.3 Influence of the length of high pressure ports on performance

The P-Angle diagrams shown in Figure 6.29 are obtained with different lengths of high pressure ports for the 4000 and 10000 rpm studies.

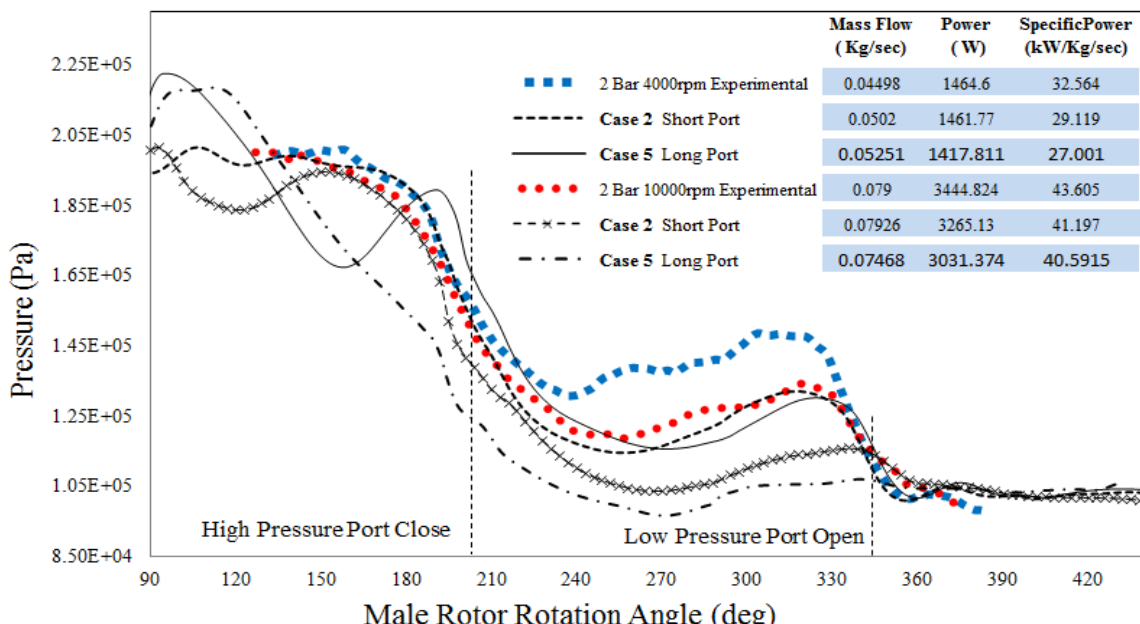


Figure 6.29 Influence of the location of high pressure boundary on P-Angle

The arrangements for the long and the short ports are shown in Figure 6.25. The long ports place the boundary condition far upstream of the inlet to the rotor filling. This produces pressure fluctuations in the filling process. These fluctuations are not noticeable in the experimental results. On the other hand, the short ports in which the boundary is placed much closer to the expansion chamber provides better predictions of the filling and pre-expansion phase and this result in a much closer match with the test results. Hence the short high pressure ports were selected for *Stage II* calculations.

6.3.3.4 Setting boundary conditions for the high pressure inlet

Kovačević (2002) described the use of a boundary domain for providing quick and stable calculation of the performance of screw compressors. A similar approach was applied to evaluate the expander performance and was compared with non-reflecting pressure boundary conditions at the high pressure opening. Figure 6.30 shows a comparison between the estimated P-Angle diagrams and the test results, with two different types of boundary conditions at the high pressure inlet side. The introduction of a source domain caused damping of the pressure fluctuations in the filling stage. Since non-reflecting pressure boundary conditions at the short port openings gave better predictions of both power and mass flow, these were selected for all further performance calculations.

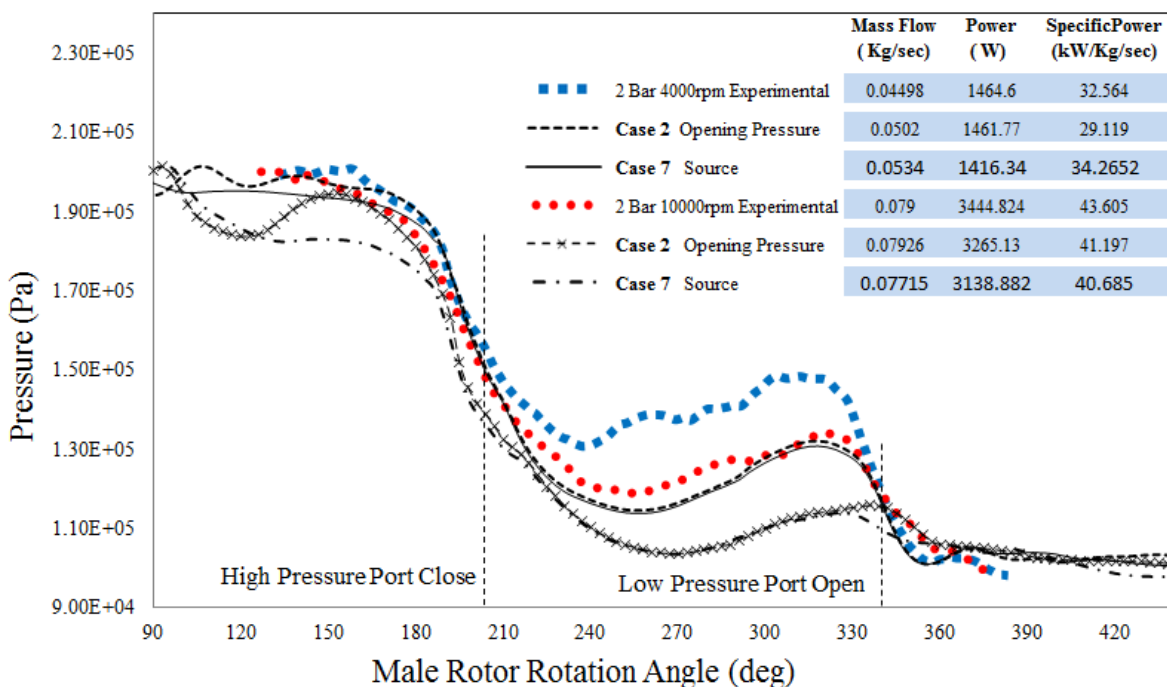


Figure 6.30 Influence of high pressure boundary condition on P-Angle

6.3.3.5 Influence of the turbulence model

Figure 6.31 shows P-Angle diagrams of predicted performance at 4000 and 10000 rpm for both laminar flow and turbulent flow, compared with test results. The inclusion of turbulence reduces the leakage flows and increases the power, thus indicating that it plays a role in clearance flows. Based on the values of power and flow, also given in Figure 6.31, the Spalart-Allmaras turbulence model was used for all further calculations. Comparing the results in Figure 6.31 with those in Figure 6.27, it can be seen that leakage flow and power output are far more sensitive to the size of the clearance gaps than to turbulence effects since the Pressure-Angle diagram is significantly affected by clearance gap changes but only slightly by the inclusion of turbulence.

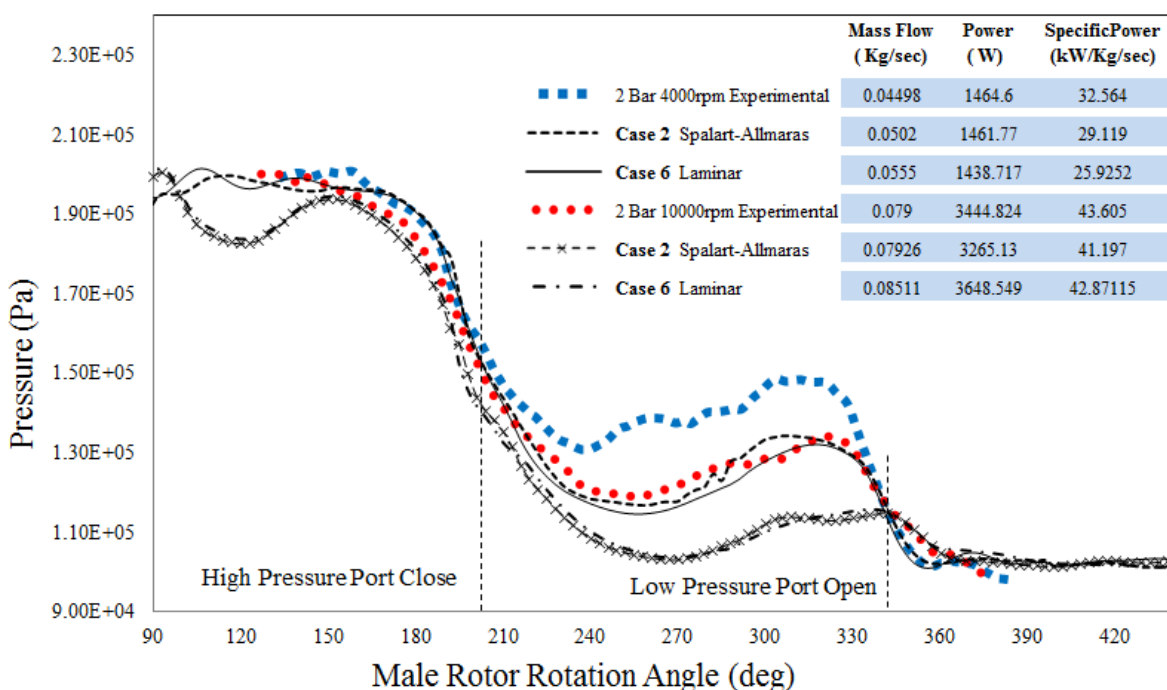


Figure 6.31 Influence of laminar and turbulence model on P-Angle

6.3.3.6 Mass flow rate and Indicated power

Estimated mass flow rates and indicated power (calculated using equation A.6) outputs for the cases studied, compared with measured values, are shown in Figure 6.32 and Figure 6.33 respectively. These were obtained with the selected modelling conditions i.e. short high pressure port, opening pressure boundary condition, the Spalart-Allmaras turbulence model and a clearance distribution of 50 μm interlobe, 80 μm radial and 100 μm axial clearance on the high pressure side and no axial gap on the low pressure side. These show good agreement for

Case 2 studies at 4000rpm and 10000rpm. These selected modelling parameters were used for further performance evaluation carried out at operating conditions listed in Table 6.9.

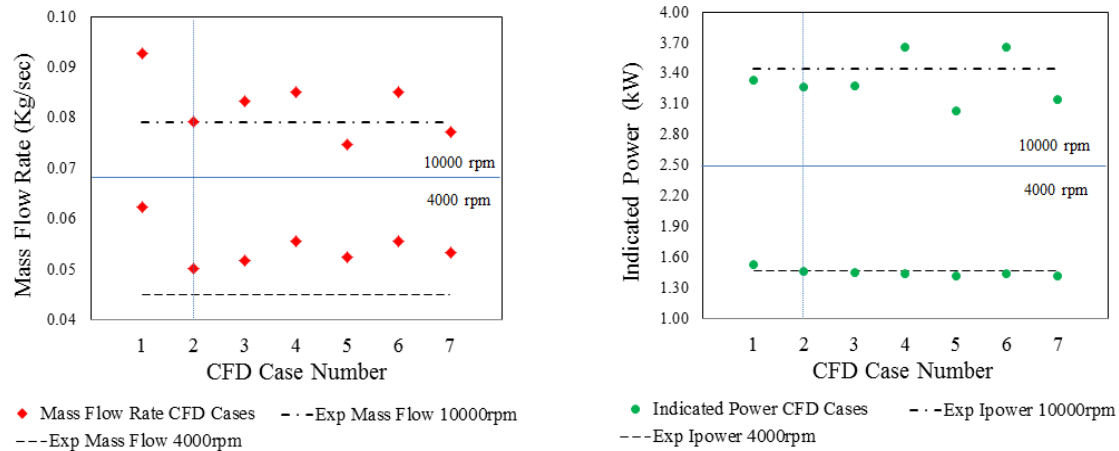


Figure 6.32 Mass flow rate Vs CFD case variants

Figure 6.33 Indicated power Vs CFD case variants

6.3.4 Evaluation of overall performance characteristics

The performance of the expander can be evaluated by comparing the indicated power and mass flow rate with test results at the operating speeds and operating pressures given in Table 6.9. The results obtained from *Stage II* CFD calculations are presented in Table 6.10 for the respective operating conditions.

Table 6.10 CFD model performance prediction of GL 51.2

Speed	2000 rpm		5000 rpm		10000 rpm	
	Pressure	Flow rate [kg/s]	Power [W]	Flow rate [kg/s]	Power [W]	Flow rate [kg/s]
1.6 bar	0.0297	435.531	0.0425	993.606	0.0621	1690.72
2.0 bar	0.0395	759.192	0.0551	1793.303	0.0794	3265.13
3.0 bar	0.0622	1594.74	0.0852	3877.391	0.1215	7361.67

All calculated points assume the high pressure air temperature to be 350° K.

The estimated performance characteristics of the expander in terms of indicated power and mass flow rate versus male rotor speed at different filling pressures are shown in Figure 6.34 and Figure 6.35 respectively. The trends obtained by CFD modelling vary progressively and follow those of the experimental results.

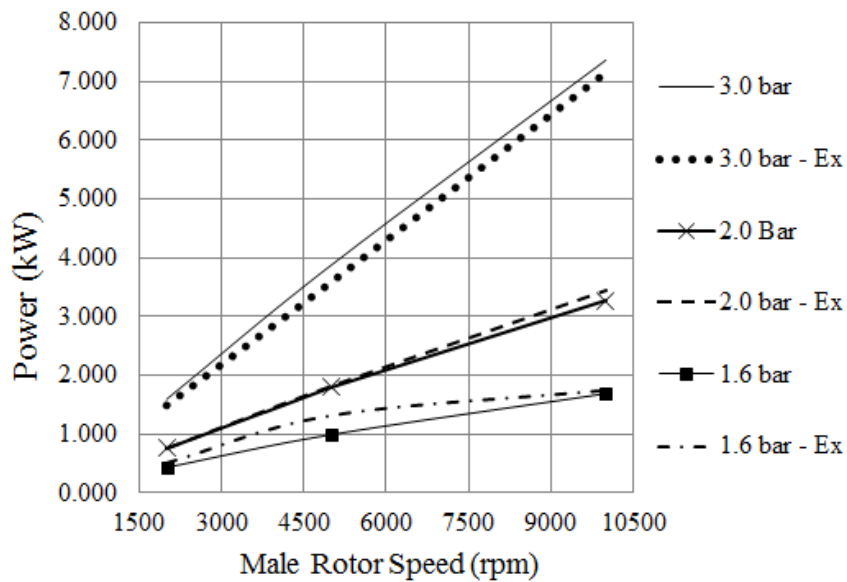


Figure 6.34 Power vs. Speed at different filling pressures

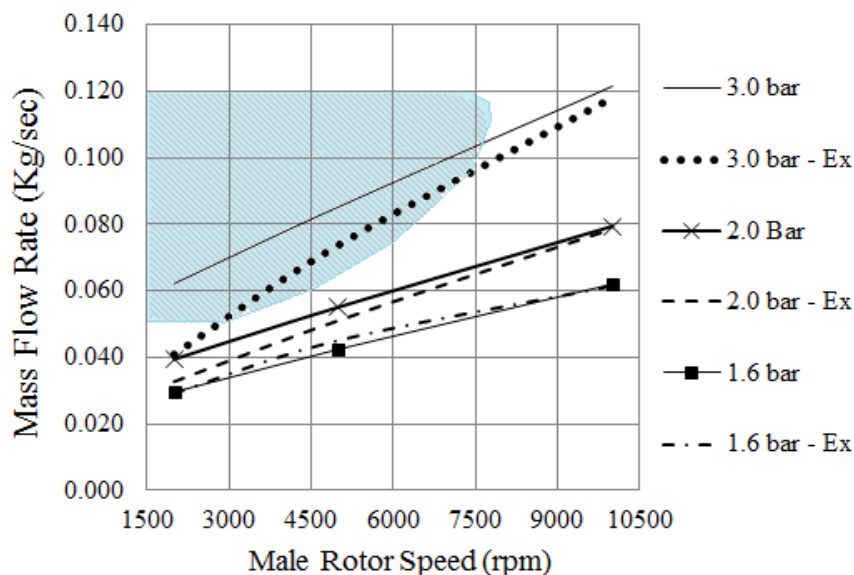


Figure 6.35 Mass flow rate vs. Speed at different filling pressures

These characteristics represent the following:

- The indicated Power increases with both higher rotor speeds and filling pressures. Also the Specific Power increases at higher pressures. The CFD Model predictions of power are relatively over estimated at higher pressure.
- The Mass flow rate increases with both higher speeds and filling pressures, due to the higher gas density in the filling port. The CFD Model mass flow rate predictions are very accurate at low pressure but are over estimated at high pressures and Low Speed

conditions, where the influence of leakage is higher. This region is highlighted in Figure 6.35 and further investigation of the CFD models, including clearance variation is required to get better results in this regime.

6.3.5 Influence of inflation layer grid on performance

The inclusion of refined grid adjacent to the walls is recommended for capturing gradients accurately and this is expected to influence the results of flow and pressure drop especially in the leakage gaps. In order to analyse the influence of inflation layer grid the operating points at 2.0 bar filling pressure were analysed. Grid generation with the inflation layer procedure described in Section 5.4 has been used to generate layers adjacent to the main and gate rotors. Figure 6.36 shows a cross section grid with 8 layers and a growth rate of 1.2. This makes the total radial divisions from the rotor to the casing equal to 16.

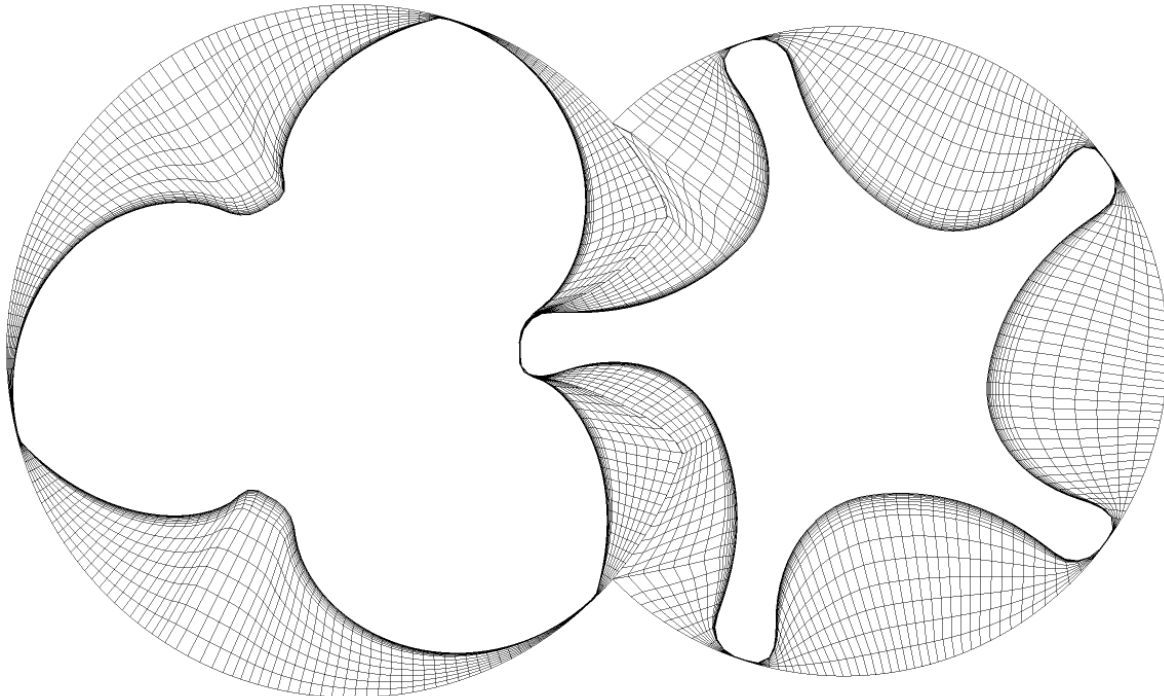


Figure 6.36 Cross section grid of the expander with inflation layer on the rotors

The comparison of mesh count with and without inflation is shown in Table 6.11 for the rotors.

Table 6.11 Rotor grid size comparison with inflation

	Nodes	Elements
Base Grid	243576	213328
With Inflation	453322	420288

6.3.5.1 Local Velocity Profile

Figure 6.37 shows a comparison of local instantaneous velocity profiles in the high pressure port close to the axial opening. Two sampling lines from the root of the male and female rotor were constructed in the y direction up to the casing. The lines are 1.0 mm distance apart from the axial face. Velocity magnitude samples were extracted on these lines from the local field data. From the velocity profiles it is seen that, close to the rotor surface, the grid with the inflation layer resolves the velocity variation.

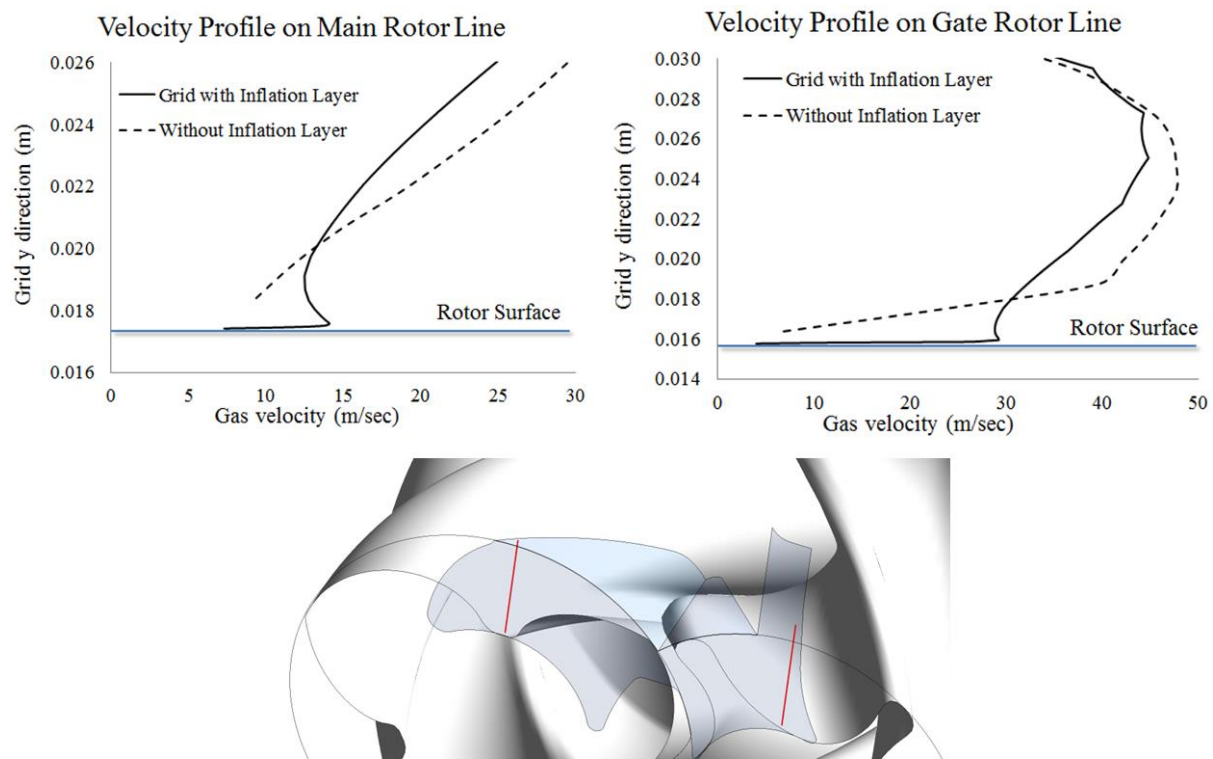


Figure 6.37 Comparison of velocity profile close to high pressure port

Table 6.12 presents the rotor tangential velocities at the root diameter. The tangential wall velocity is dominant in the direction of the wall motion and hence the gas velocity at the rotor surface under no slip conditions should be close to this wall velocity. It is seen that the grid with inflation layers matches the root diameter tangential velocities on both male and gate rotors very closely, but the tangential velocities derived from the grid without the inflation layer deviate from the root tangential velocities. On both the male and gate rotors they are over estimated. This could be due to the relative gas flow direction into the high pressure port. It is necessary to take more samples in different rotor positions and different spatial locations to get a map of the overall flow field.

Table 6.12 Rotor tangential velocity at root diameter

Units [m/sec]	$V_t = r\omega$	Base Grid	Grid with Inflation
Male 4000rpm	7.317	9.363	7.302
Female 2400rpm	3.838	6.831	3.976

The machine tip speed is 15.06 m/s at 4000rpm. As seen in Figure 6.38 maximum gas velocity location is in the similar zones near the tip leakage in both cases. The peak of local velocity magnitude in case without inflation grid is 264.27m/s whereas in case with inflation layers it is almost 84% low of about 42m/s.

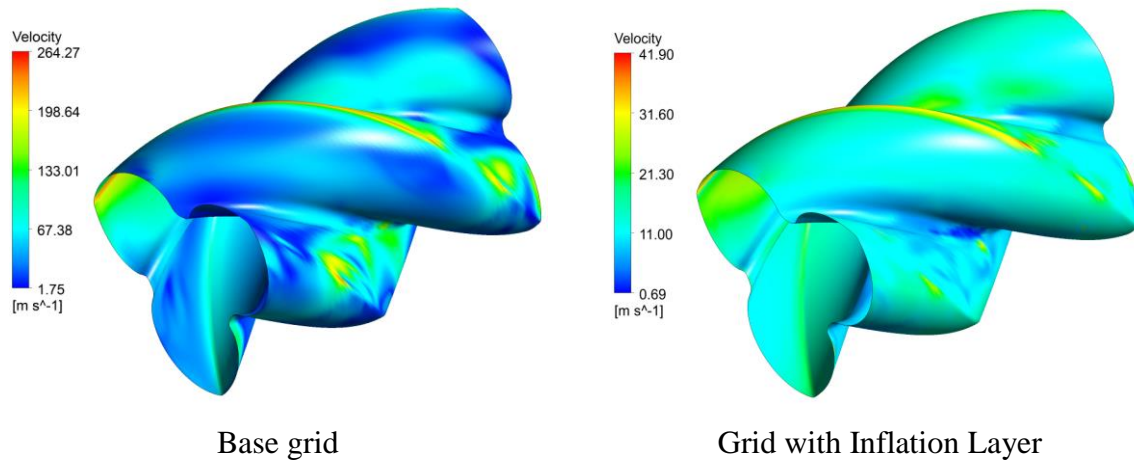


Figure 6.38 Comparison of gas velocity adjacent to Male Rotor

6.3.5.2 Pressure – Angle variation

Figure 6.39 shows a comparison of Pressure – Angle variation at 4000rpm and 2.0bar filling pressure. The results from grids with and without inflation layer closely follow each other and there is no difference between the two. This indicates that chamber pressure rise has not been influenced by the grid resolution close to the rotor surface.

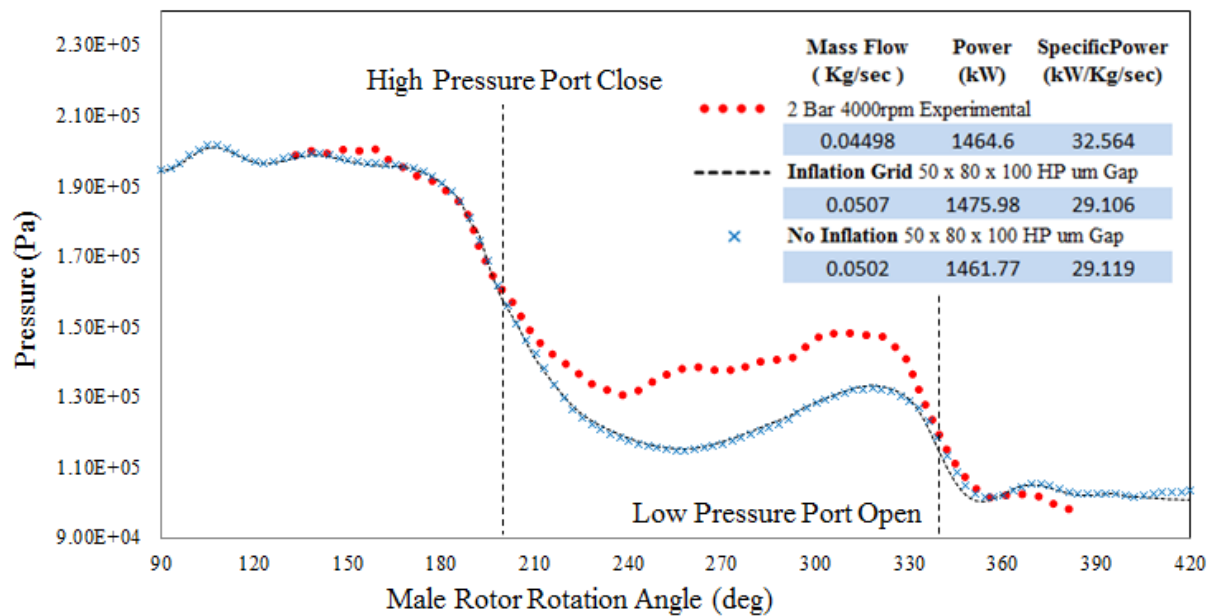


Figure 6.39 Comparison of Pressure Angle diagram with Inflation layer grid

6.3.5.3 Power and Mass flow

Table 6.13 presents a comparison of cycle average mass flow rate, power and specific power at 4000 rpm. Also the peak pressure during refilling in the pressure curve is reported. No influence of grid refinement close to the rotor surface is seen on these quantities. Only a small increase of 1% in the mass flow rate and power was observed with inflation layer grid. Since the rotor curvature refinement remained unchanged between these grids, the bulk leakage flow remained unchanged even with refinement adjacent to the rotor wall.

Table 6.13 Comparison of results with inflation layer grid

Case	Mass Flow (Kg/sec)	Refilling Pressure (bar)	Power (W)	Specific Power (kW/Kg/sec)
Base Grid	0.0502	1.321	1461.77	29.119
Grid with Inflation	0.0507	1.334	1475.98	29.107

Figure 6.40 shows a comparison of power and mass flow rate at different speeds and 2.0 bar filling pressure. It is seen that both the power and mass flow rates are similar in cases with and without inflation layer grid.

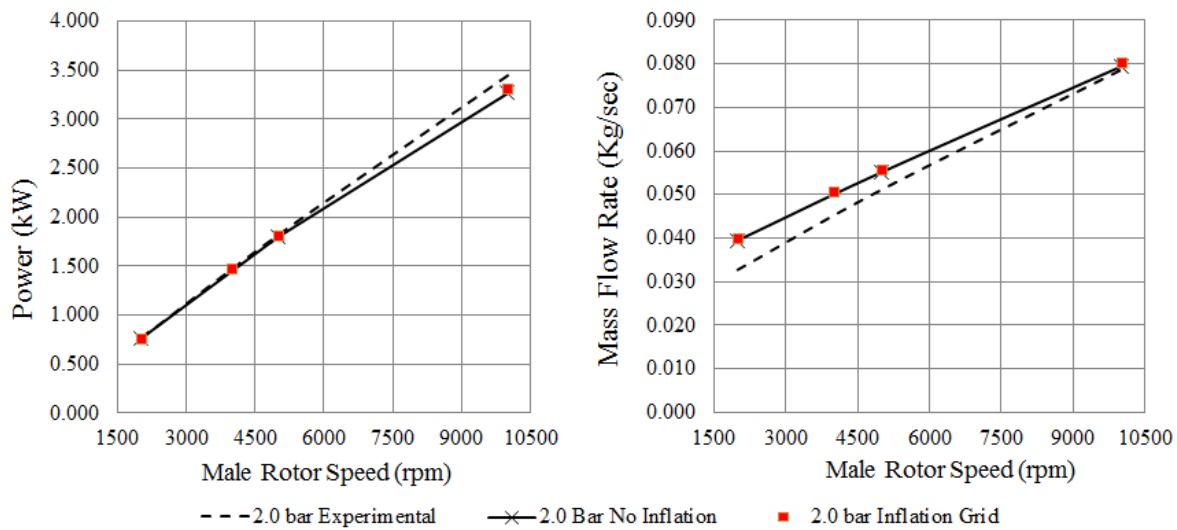


Figure 6.40 Comparison of power and mass flow rate with inflation layer grid

These results show that inflation layers give better predictions of local flow features like gas velocities but do not influence the prediction of integrated quantities. These conclusions are specific to the Spalart-Allmaras turbulence model in CFX solver and for reported levels of grid refinement. It will be necessary to study other turbulence models, other refinement levels and wall modelling approaches for better flow characteristic prediction.

6.3.6 Inference

In this study, experimental Pressure-Angle diagrams were used as a guideline for the selection of appropriate modelling parameters for CFD calculations. In the performance stage, a set of different pressure ratios, over a range of operating speeds at fixed inlet gas temperature was used to compare the results from the CFD model. A few operating conditions were calculated with grids constructed with inflation layer refinement and its influence on performance prediction were analysed.

The following conclusions can be made from the study:

- It is important to define the appropriate geometry and position of the pressure boundary of the high pressure port. This has a strong influence on the pressure fluctuations and throttling in the port. Further investigation is necessary in order to generalise this procedure to be able to set the location of the boundary for a given operating condition.
- The inclusion of turbulence modelling in CFD calculations does not affect the pressure history within the machine, but it does influence the gap flows and hence the predicted mass flow rate and specific power. The Spalart-Allmaras turbulence model was used in

this study but further investigation will need to be performed in order to determine the best turbulence model for screw expanders.

- Clearance distribution in interlobe, radial and axial gaps has a strong influence on the performance of the expander. It is difficult to predict their exact operating values. These were obtained by iterative trials in this case but a comprehensive Fluid-Solid interaction study would lead to better understand of their dynamic behaviour.
- An Inflation layer grid gave better predictions of local flow features like gas velocities but had no influence on the prediction of integrated quantities like mass flow rate and indicated power for the selected turbulence models and grid refinement.

This case study presents the process of selection of modelling parameters for CFD analysis and has highlighted the operating region of the machine where large deviations between flow predicted from the numerical model and the experimental measurements would be expected.

6.4 Analysis of Variable Geometry Dry Air Screw Compressor

The case study, reported here, is a numerical analysis, carried out with the aim of validating the new grid generation procedures presented in Section 5.3 and to study the flow behaviour in variable geometry screw compressors. The test case **DRUM XK 18** is an oil free twin screw compressor. The male rotor, with 3 lobes, has 127.45 mm outer diameter, L/D ratio of 1.6 and a wrap angle Φ_w of 285°. The female rotor is with 5 lobes and the rotor to rotor centre distance is 93mm. Rotors have rack generated ‘N’ profiles. The compressor speed was 8000 rpm with pressure ratio of 2.0 and 3.0. Figure 6.41 shows the CAD model of the compressor and the rotors in position are with variable lead. Figure 6.42 shows the CFD model domain. The compressor has an axial suction and a combined axial and radial discharge port.

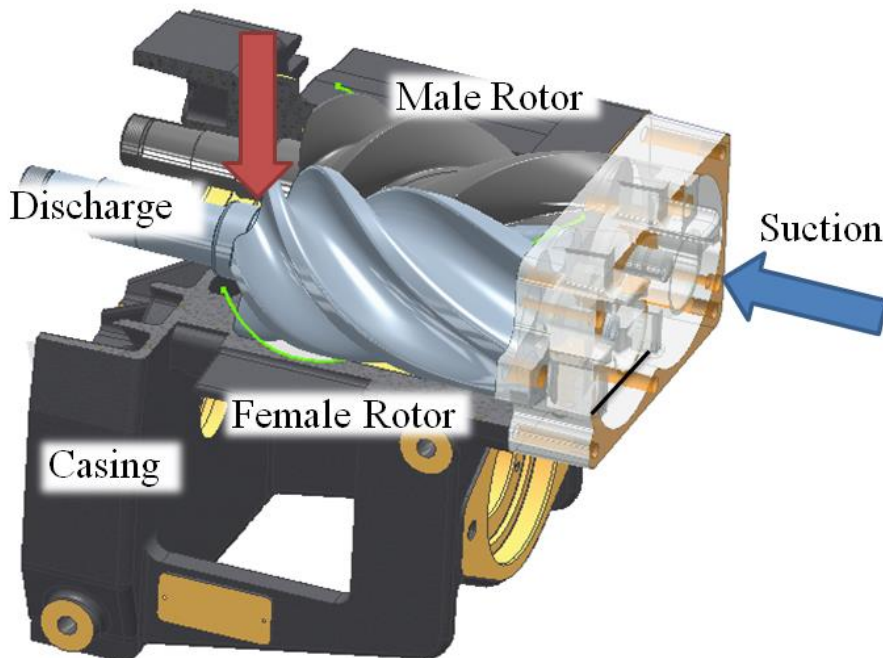


Figure 6.41 Twin screw compressor and its working chamber

Three designs of the rotor geometry were studied and their performance has been compared. The first design is the standard rotor with uniform pitch and profile. The second rotor is of the same size as that of the uniform rotor but has a linearly variable lead from suction end to the discharge end. The third rotor is slightly smaller in size because the rotor profile is continuously varied from the suction end to the discharge end. The variable profile produces conical rotors with parallel axes.

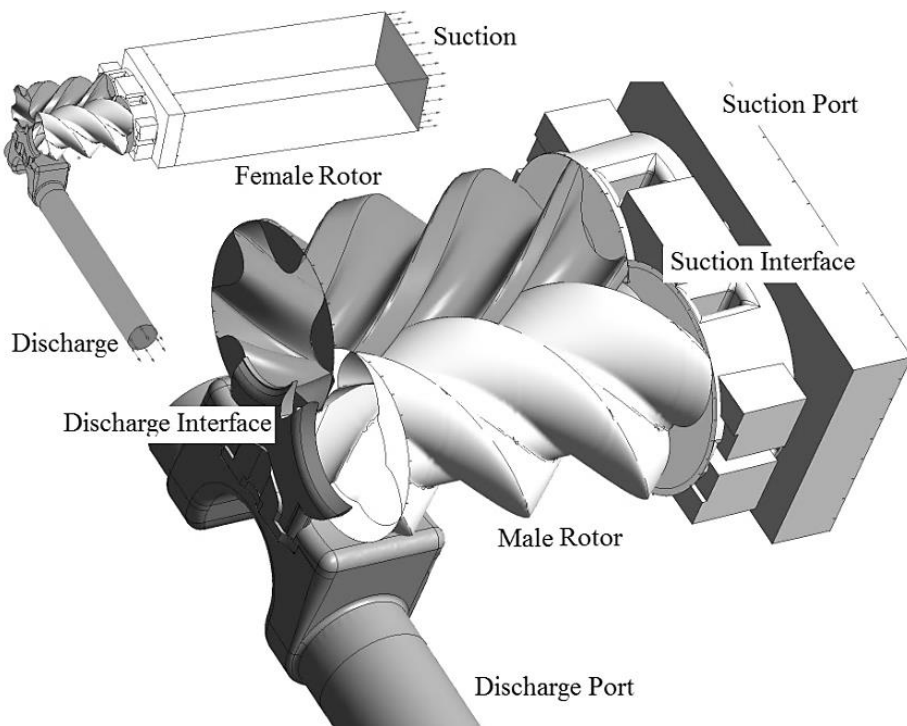


Figure 6.42 CFD model – flow domain of the twin screw compressor

6.4.1 Case description

Four cases were calculated. Figure 6.43 shows twin screw rotors with uniform pitch whereas Figure 6.44 shows twin screw rotors of the same size but with variable pitch. It has been shown in literature that for the same rotor lengths, diameter, wrap angles and lobe profiles, variable pitch rotors can be designed to provide higher pressure ratios and larger discharge port opening areas with reduced throttling losses when compared to constant pitch rotors (*Gardner, 1969*).

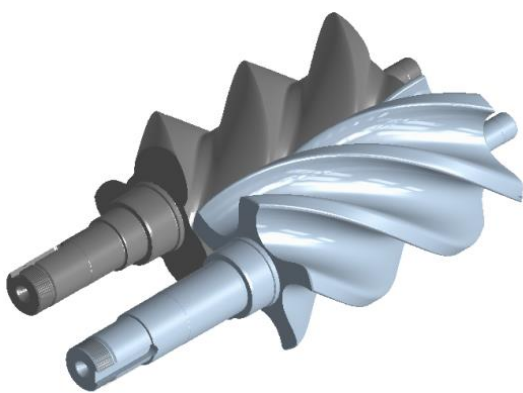


Figure 6.43 Meshing of Uniform Pitch Twin
Screw Rotors

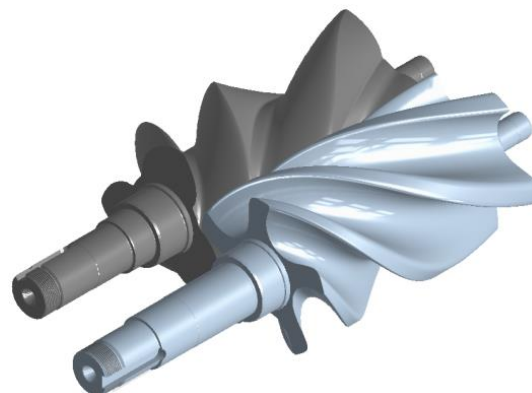


Figure 6.44 Meshing of Variable Pitch
Twin Screw Rotors

- Case 1.** Uniform pitch and uniform profile rotors with built in volume index V_i of 1.8. Rotors are shown in Figure 6.43.
- Case 2.** Uniform Pitch and Profile rotors with a reduced discharge port opening area to give a built in volume index V_i of 2.2. In this case, the compression chamber is exposed to the discharge pressure relatively late in the cycle as shown in Figure 6.45 and allows for further pressure build up in the chambers.

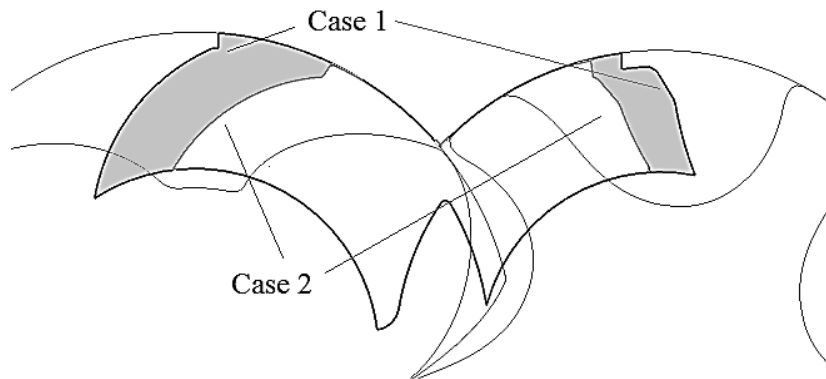


Figure 6.45 Reduced discharge port area in *Case 2* compared with *Case 1*

- Case 3.** Variable pitch with uniform profile rotors and built in volume index $V_i > 1.8$. The Suction side pitch was 130mm and Discharge side pitch was 40mm. The wrap angle of Φ_w 285° was maintained as shown in Figure 6.46.

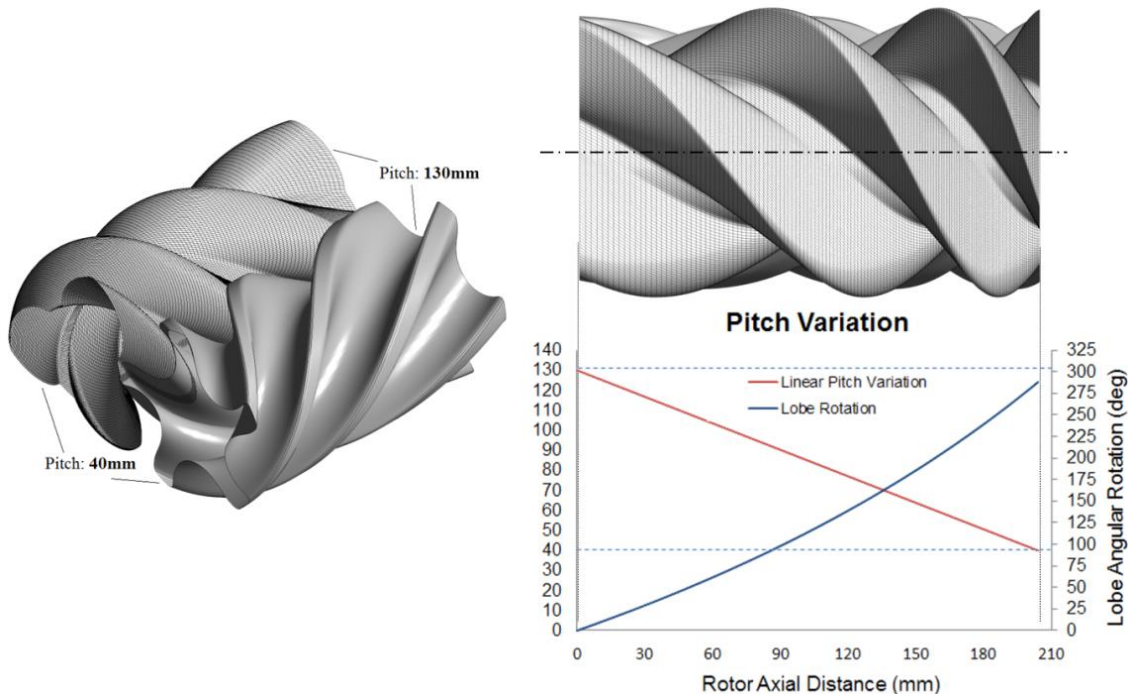


Figure 6.46 Variable pitch grid – 3/5 ‘N’ rotors

Case 4. Variable profile and uniform pitch rotors. The rotor profile in successive sections is generated using rack generation procedure by variation of addendum on the defining racks (*Stošić*, 1998). Addendum on the suction end of the rotors was 33mm while on the discharge side it was reduced to 21mm. The addendum on the uniform profile rotors had constant value 28.848mm. Due to the variation of addendum the outer diameter of the male rotor changes while the inner diameter remains constant and vice versa for the female rotor, as shown in Figure 6.47. The displacement of these rotors is smaller than for the uniform profile rotors.

Each rotor configuration was analysed with five levels of successive grid refinements. Table 6.14 shows the number of computational nodes in each case. Stationary compressor ports were meshed by use of the commercial grid generator. Figure 6.42 shows the different parts of the numerical model and the grid refinement is shown in Figure 6.48. The numerical solver used for the study was ANSYS CFX (2011), which uses a vertex-based Finite Volume Method and iteratively solves for momentum and continuity in a pressure coupled algorithm. All the generated grids are passed to the solver in the model setup and during solution the rotor domain grids were updated for every time step using external subroutines. The space conservation law is retained during this grid motion by modifications to the governing equation as described by *Ferziger and Perić* (1996).

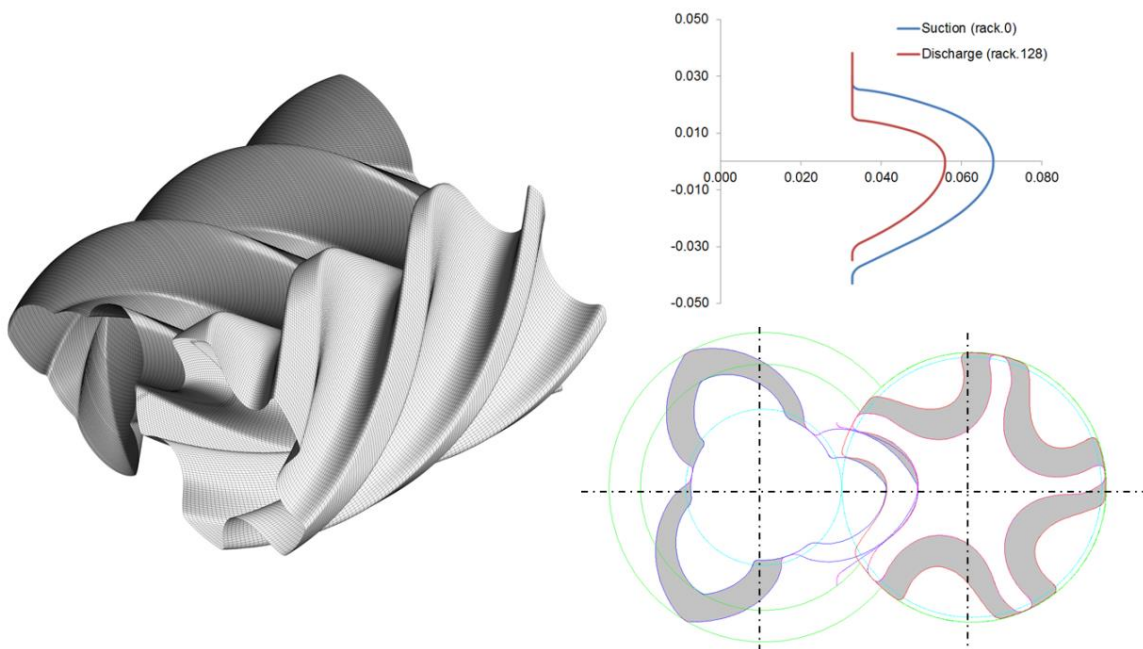


Figure 6.47 Variable profile grid – 3/5 ‘N’ rotors

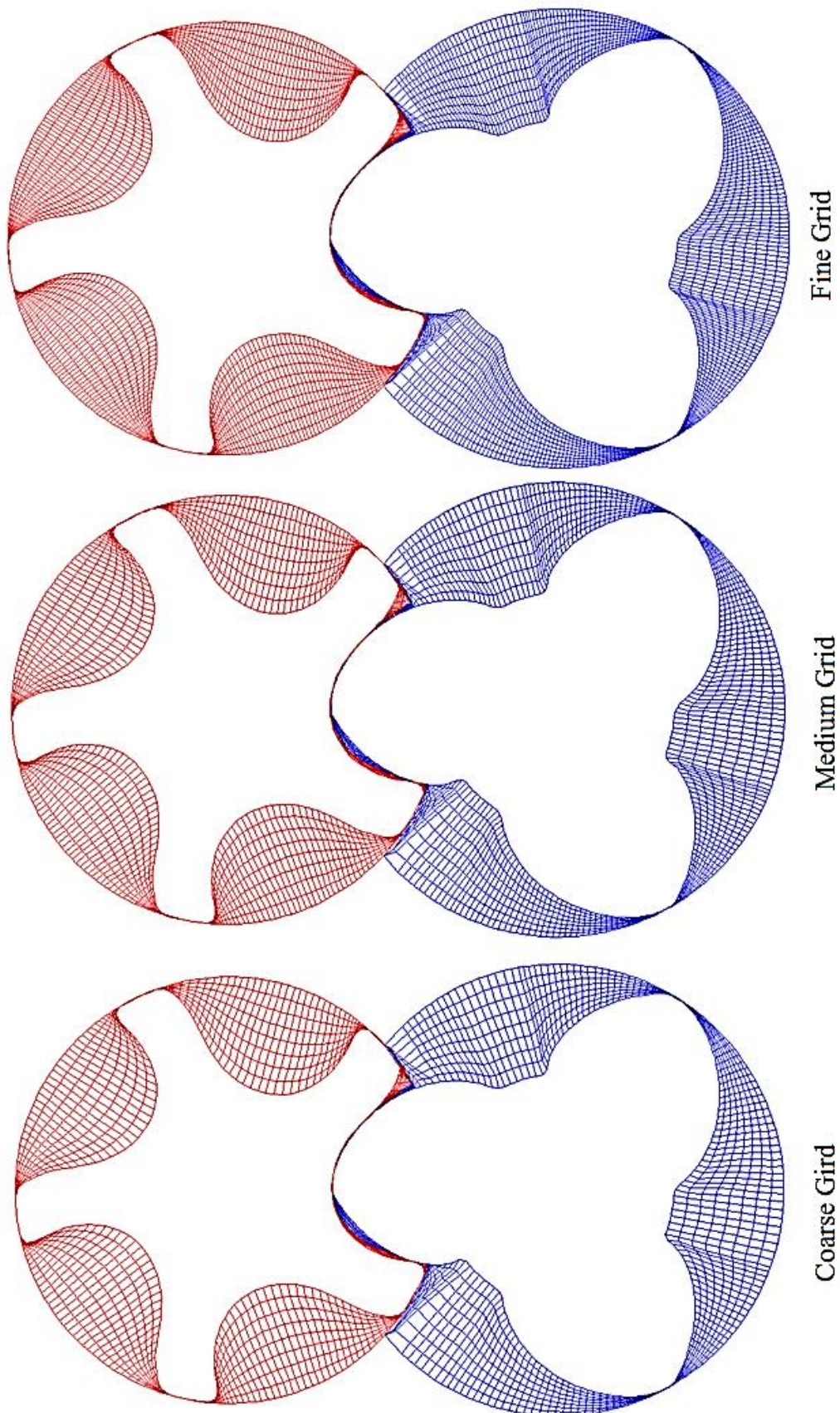


Figure 6.48 Three levels of grid refinements shown for one section

Table 6.14 Grid refinement as number of computational nodes

Case	Uniform	Variable Pitch	Variable Profile
Coarse	648190	691174	675918
Medium	838378	847414	889794
Fine	1214418	1229774	1297434
Fine1	1478836	1498636	1351872
Fine2	1871536	1897936	1700172

6.4.2 Simulation

The boundary conditions at the suction and discharge of the compressor are highly unsteady and therefore difficult to specify. To provide good boundary conditions, the ports were reasonably extended to get good convergence of the flow and reduce the numerical discrepancies arising from pressure pulses in the flow. Each case was calculated with both Laminar and SST k-Omega Turbulence model.

6.4.3 Results and Discussion

6.4.3.1 *Compression characteristics*

Figure 6.49 shows the variation of pressure in the case of variable pitch rotors. Figure 6.50 shows the compression characteristic of cases 1, 3 and 4 for one full cycle with fine grids with a discharge pressure of 2.0 bar. With uniform rotors the maximum pressure goes up to 2.5 bar and with variable geometry rotors the maximum pressure goes up to 3.0bar. **Case 3** with the variable rotor pitch and **Case 4** with variable rotor profile have a steeper rise in internal pressure than **Case 1**, which has constant rotor geometry. The highest peak pressure is achieved with the variable pitch rotors. For a discharge pressure of 2.0 bar this internal pressure rise is due to over-compression.

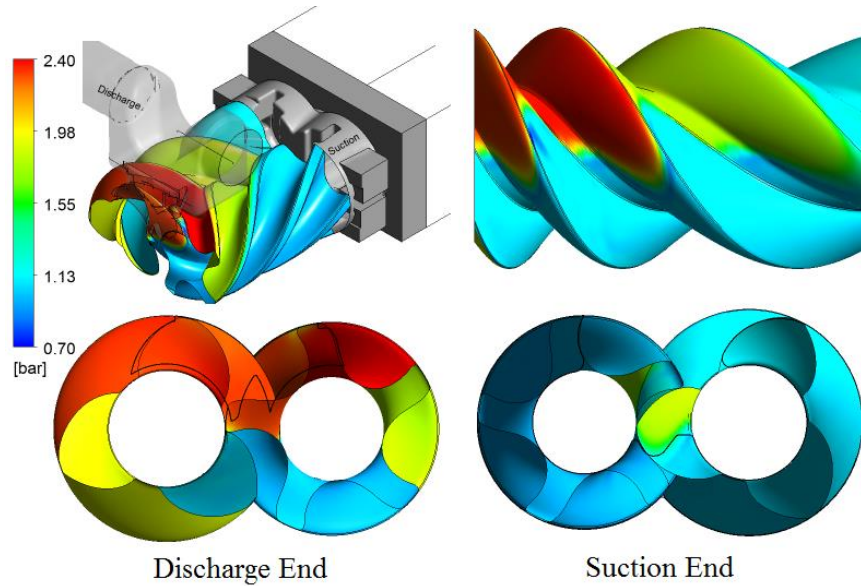


Figure 6.49 Pressure variation on variable pitch rotor with discharge at 2.0bar.

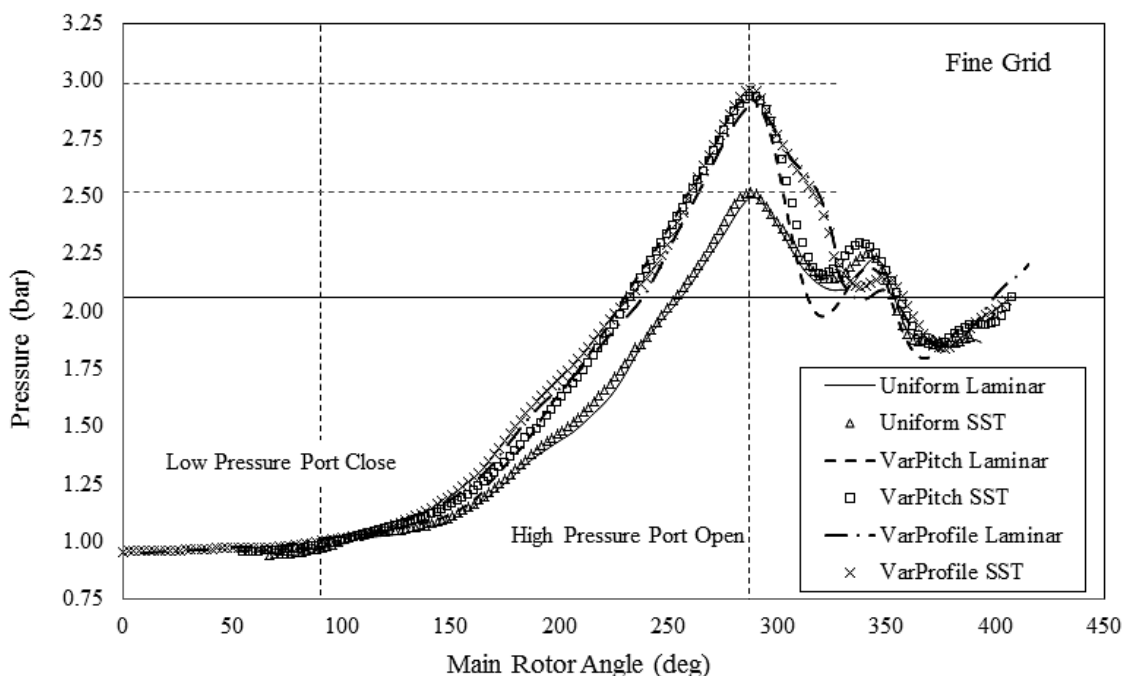


Figure 6.50 Indicator diagram for cases calculated on fine grid with discharge at 2.0 bar.

Figure 6.51 shows the compression characteristic of the four cases on fine grids with discharge pressures of 2.0bar and 3.0bar and SST k-omega turbulence models. Uniform rotors show high under compression and the maximum pressure goes up to 3.4bar. High pressure port opens at the same angle for all the cases because the rotor wrap angle has been maintained constant except for the uniform rotor case with V_i 2.2 when the discharge port opens after 10-12 degree rotation.

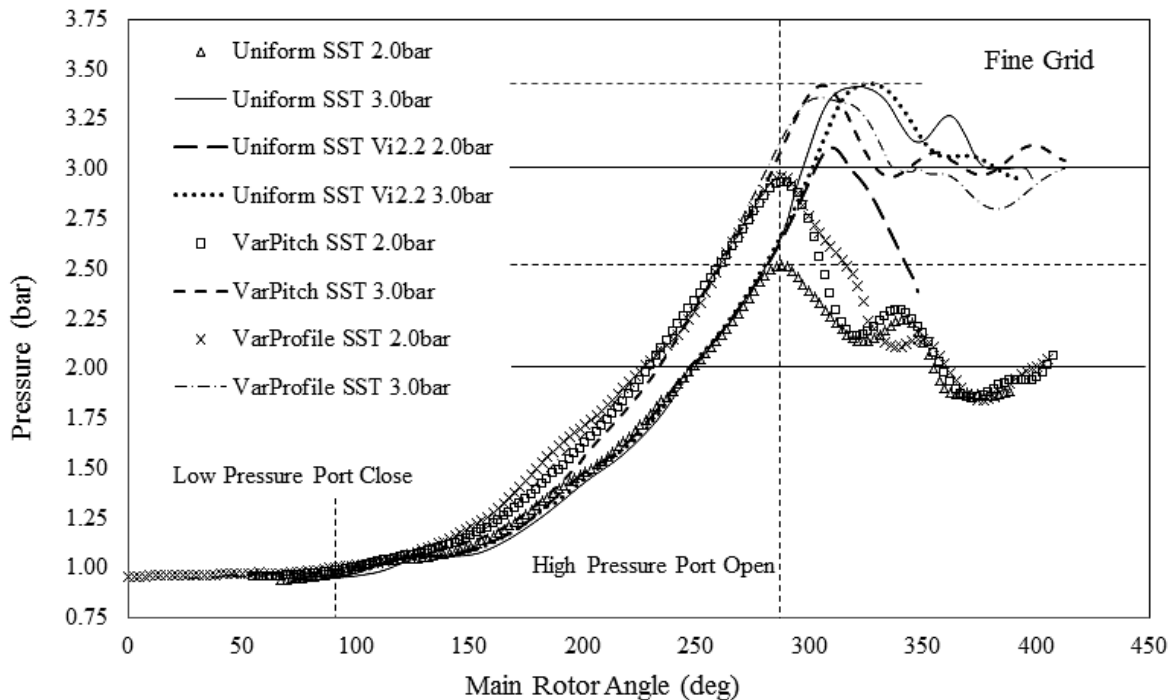


Figure 6.51 Indicator diagram for cases calculated on fine grid with turbulence models.

6.4.3.2 Discharge port area

Figure 6.45 shows a decrease in the discharge port area with the V_i increased to 2.2. In **Case 2**, with uniform pitch and a reduced discharge port opening area, the internal pressure rise was about 3.1bar before exposure to a discharge pressure of 2.0bar as seen in Figure 6.51. This pressure rise was close to that of the variable geometry rotors of about 3.0 bar, for which the opening area was 22% higher. The increment in the discharge area for comparable pressure rise is favourable to the reduction of throttling losses in the variable geometry compressor if it were to operate at 3.0 bar discharge pressure.

6.4.3.3 Influence of grid refinement

Figure 6.52 shows the effect of grid refinement on the predicted integral quantities, such as the mass flow rate and specific power for cases 1, 3 and 4. The cases presented in the figure are with 2.0 bar discharge pressure and mass flow rate and specific Power of the uniform rotors. The SST Turbulence model on Fine 2 grid level has been used for normalisation. The mass flow rate showed an increase with grid refinement. The difference between consecutive grid refinements is around 10% between Coarse and Medium level but with further grid refinements of level Fine1 and level Fine2 the change is mass flow rate is less than 3%.

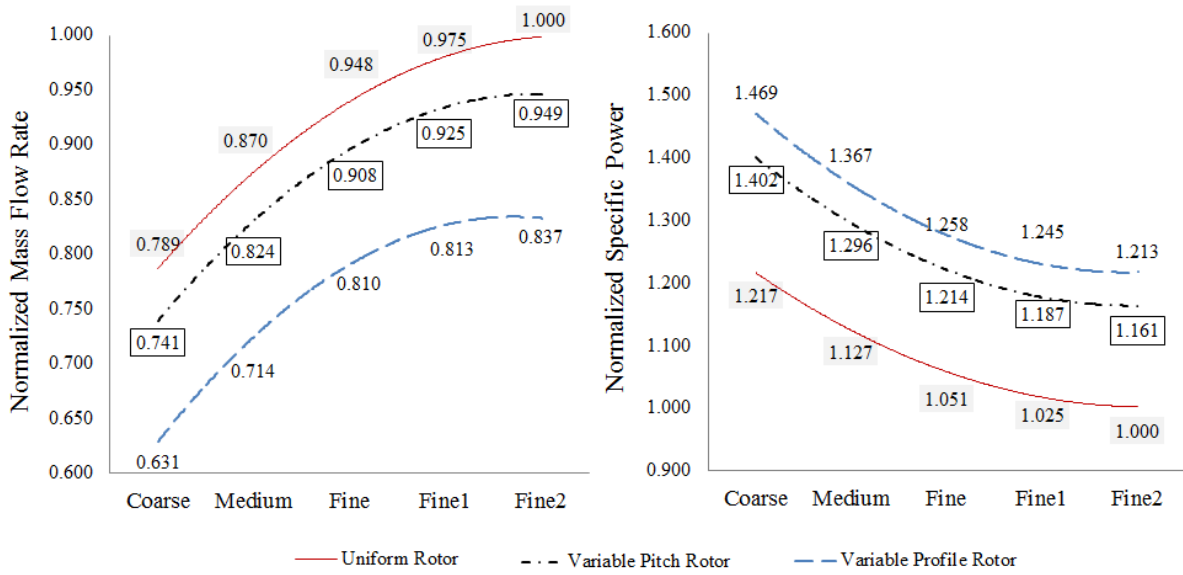


Figure 6.52 Effect of grid refinement on integral parameters

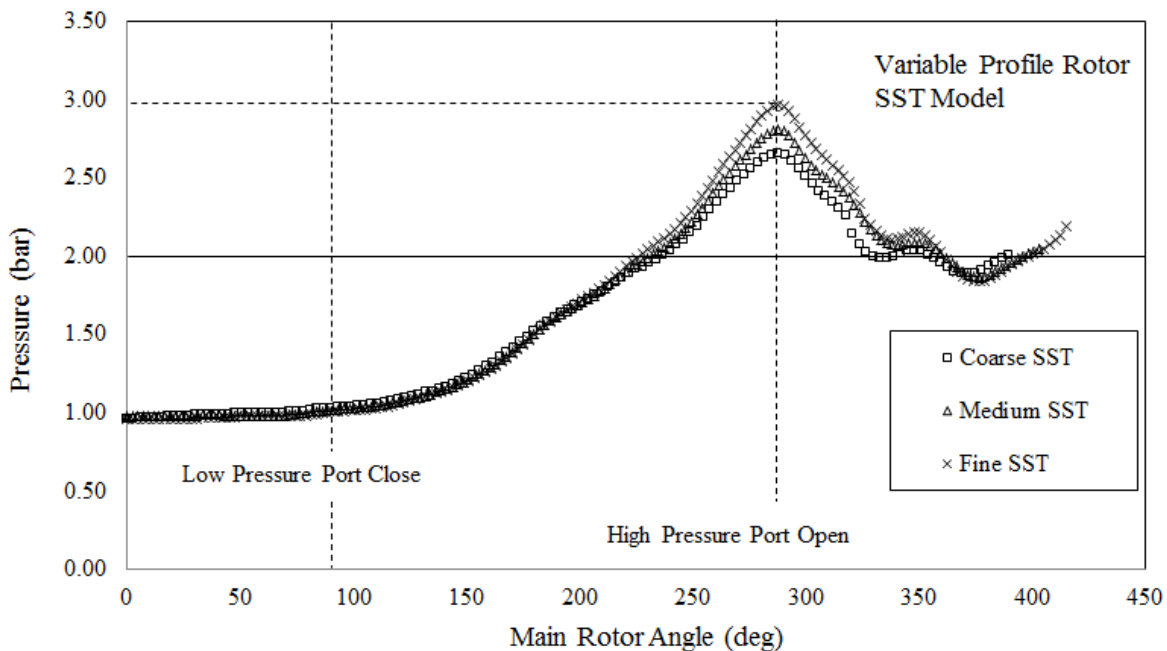


Figure 6.53 Effect of grid refinement on pressure diagram

This indicates that the rotor geometry is captured better with finer grids, which results in reduction of leakages. Similarly, the indicated power increases by 2-5% when the grid is refined from Coarse to Medium level but with further grid refinements the change in indicated power is less than 0.8%. The increase in the chamber pressure with grid refinement is shown in Figure 6.53 for **Case 4** with variable profile rotors as an example.

With a Fine level of grid refinement, acceptable grid independence has been achieved and the computational resources demanded with level Fine1 and level Fine2 refinements were much higher. Hence further performance calculations at 3.0bar pressure were undertaken with only the Fine level grids.

6.4.3.4 Influence of turbulence model

As shown in Figure 6.54, higher mass flow rates are achieved when the turbulence model is applied. The indicated power also increases. However, the specific power is reduced for all turbulent cases indicating that the influence of turbulence models on mass flow rate prediction is higher than that on indicator diagram and power prediction.

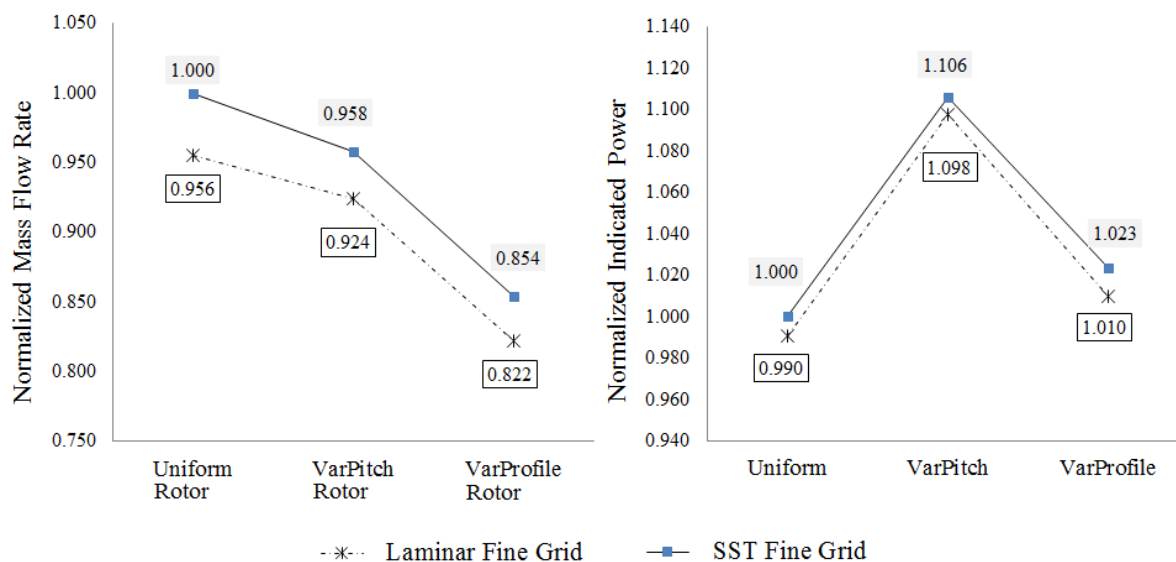


Figure 6.54 Influence of turbulence models on performance parameters

6.4.3.5 Sealing line length

The interlobe sealing line is the line of closest proximity between the two rotors. Leakage of gas takes place through this gap and is proportional to the length of the sealing line and clearance normal to it (Hanjalić and Stošić, 1997). Contours of pressure distribution on the rotors can be established from numerical calculations and the dividing line between high and low pressure levels can be considered as the sealing line. The maximum pressure gradient is present across this division and is the driving force for leakage.

Table 6.15 Comparison of Interlobe Sealing Line Length [mm]

Interlobe No	Uniform	Variable Pitch	Difference	Variable Profile	Difference
1	145.8	175.9	-30.1	158.4	-12.6
2	170.3	164.0	+6.4	162.2	+08.1
3 (part)	069.1	056.8	+12.2	068.4	+00.6
Total	385.2	396.6	-11.5	389.1	-03.9

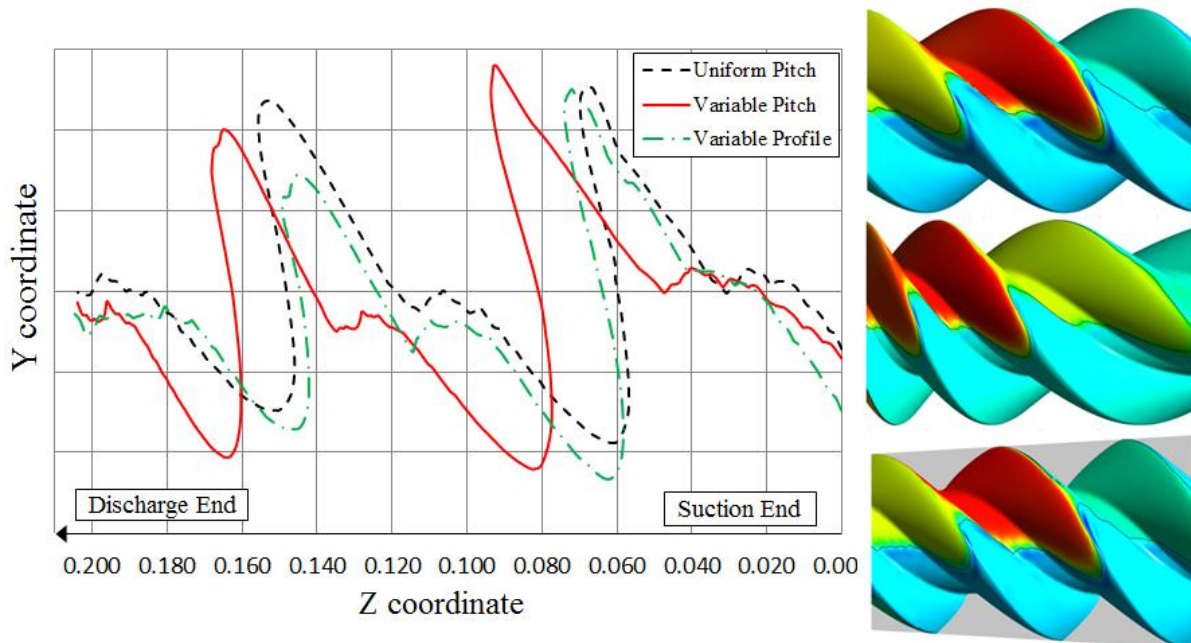


Figure 6.55 Comparison of interlobe sealing line lengths

Figure 6.55 shows the sealing lines obtained for the uniform pitch rotors (**Case 1**) and variable geometry rotors (**Case 3** and **Case 4**). The projection of the sealing line on the rotor normal plane shows the difference more clearly. The sealing line on the uniform pitch rotor is of the same length for each interlobe space along the rotor. However, on the variable pitch rotors, the sealing line is longer at the suction end. It decreases towards the discharge end of the rotor. Table 6.15 presents the variation in the sealing line lengths between the uniform and variable geometry cases at one of the rotor positions, indicating the magnitude of change along the rotors. At the suction end the sealing line on the variable pitch rotor is 30mm longer but at the discharge end it is 12mm shorter. This helps to reduce leakage as the largest pressure difference across the sealing line is at the discharge. Additionally, the total length of the sealing line is

reduced by 11mm in the variable pitch rotors. In **Case 4**, with variable profile, the suction end is longer by 12mm but at the discharge end, is only slightly different to that of the uniform profile. There is no overall gain in sealing line length because of the increased gate lobe thickness near the discharge end of the rotors.

6.4.3.6 Blow-hole area

The blow-hole area is the leakage area formed between the male and female rotors and the casing at the rotor cusp as shown in Figure 6.56. The blow-hole area on the high pressure side is important for leakage due to the pressure difference between adjacent compression chambers. A smaller blow-hole area is desired for improved performance of the machine. Table 6.16 shows the blow-hole areas measured on the medium size grid for different calculated cases at three positions on the rotor.

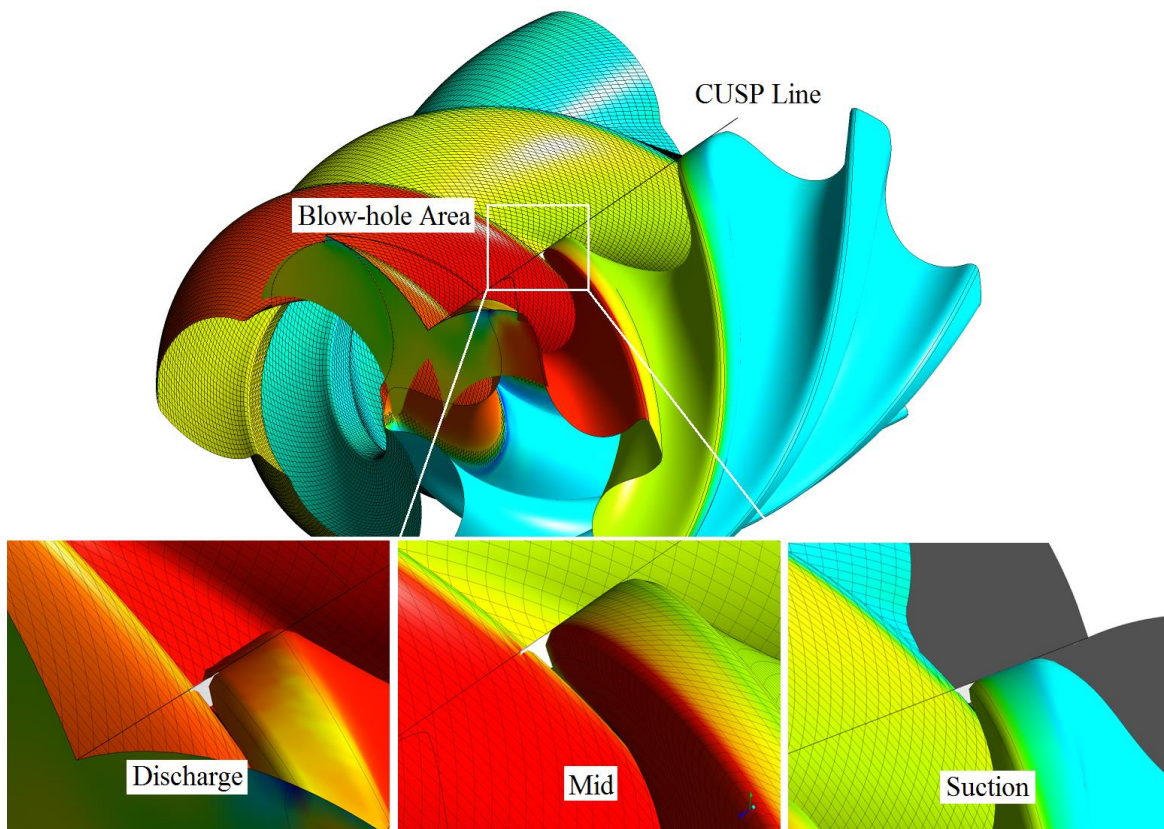


Figure 6.56 Comparison of Blow-hole area

Table 6.16 Comparison of Blow-hole area [mm²]

Position	Uniform	Var. Pitch	Diff %	Var. Profile	Diff %
Suction	9.817	12.49	+27.2	9.83	+0.15
Mid	9.908	9.263	-6.51	9.35	-5.64
Discharge	9.701	6.562	-32.3	9.19	-5.29

The blow-hole area for the uniform rotors remains constant along the length of the rotors. In the variable pitch rotors, the suction side blow-hole area is larger than in the uniform rotors but the discharge side blow-hole area is smaller than that of the uniform rotors. In the variable profile rotors, the suction side blow-hole area is nearly the same as that of the uniform rotors but the discharge blow-hole area is smaller than for the uniform rotors. Proportionally, the reduction of blow-hole area towards the discharge side rotors is most pronounced in the case of variable pitch rotors.

6.4.3.7 Overall performance

The influence of the discharge pressure on the compressor performance for the cases 1, 3 and 4 is shown in Figure 6.57. Mass flow rate and specific Power of the uniform rotors with SST Turbulence model on Fine grids has been used for normalisation. The uniform rotors have the highest flow rate and the lowest specific power for both pressures. However the difference in the specific power between the uniform and variable geometry rotors is much reduced at higher pressures. Table 6.17 shows a comparison of predicted volumetric and adiabatic efficiencies.

Table 6.17 Comparison of variable geometry rotor efficiencies

		Volumetric Efficiency %		Adiabatic Efficiency %	
		2.0 bar	3.0 bar	2.0 bar	3.0 bar
Uniform	V_i 1.8	75.30	56.70	54.13	51.73
Uniform	V_i 2.2	64.00	55.66	44.06	49.91
Variable Pitch	$V_i > 1.8$	66.20	57.60	46.88	50.99
Variable Profile	$V_i > 1.8$	62.80	55.04	45.16	51.01

Equations presented in [Appendix A](#) have been used for the calculations.

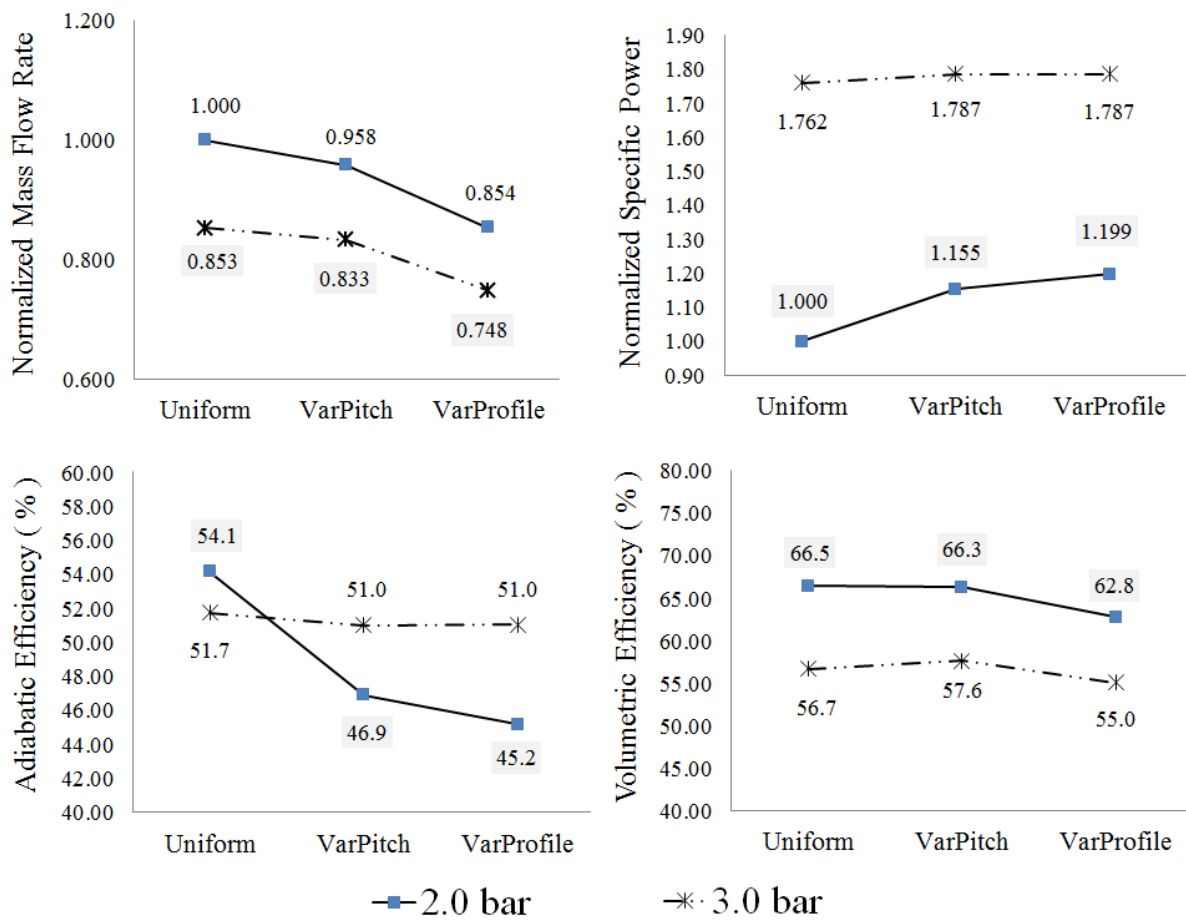


Figure 6.57 Comparison of performance parameters

Uniform rotors show highest volumetric efficiency at 2.0 bar. But with $V_i = 2.2$ the efficiency is lower than that of the variable pitch rotors due to comparable internal pressure rise and comparatively shorter sealing line length. An improvement of 2.2% at 2.0 bar and 2.0% at 3.0 bar has been observed with variable lead rotor. There is not much gain in η_v with variable profile rotor at 3.0bar due to there being no significant reduction in the sealing line length. A 1.2% reduction is observed at 2.0 bar due to smaller capacity of the machine and higher internal pressure rise with over-compression.

The uniform rotors show the highest adiabatic efficiency at 2.0 bar. But with $V_i = 2.2$ the efficiency is lower than that of the variable geometry rotors. At 3.0 bar, the uniform rotors have reduced adiabatic efficiency (still 0.7% higher than variable geometry rotors) but both variable pitch and variable profile rotors show an increment in adiabatic efficiency due to a balanced internal pressure rise. An improvement of 2.8% at 2.0 bar and 1.0% at 3.0 bar with variable lead and 1.1% at both pressures with variable profile has been observed. This further supports that the variable geometry rotors are more suitable for high pressure applications.

6.4.4 Inference

3D CFD grid generation for twin screw compressors with variable pitch and variable profile rotors was formulated and implemented in Section 5.3. The case study presented in this chapter verified the use of these grids and the flow characteristics in the machines could be understood better.

- From numerical analysis, the advantages identified with variable pitch rotors were evaluated. The analysis showed that by varying the rotor lead continuously from the suction to the discharge end it is possible to achieve a steeper internal pressure build up.
- The analysis also showed that varying the rotor lead allows a larger discharge port area, thereby reducing throttling losses, and increases the volumetric efficiency by reducing the sealing line length in the high pressure zone.
- Analysis of variable profile rotors also showed a steeper internal pressure rise but there was no gain in sealing line length and blow-hole area with this size of the rotors.
- The increase in root diameter of the female rotors with variable profile certainly helps to produce stiff rotors for high pressure applications.

The CFD results presented here enabled a comparison to be made between different types of variable geometry rotor machines.

6.5 Closure

In this chapter three case studies have been presented utilizing the grids generated using the proposed methods and the aim was to verify the grid generation method, compare the predicted performance and validate the results by comparison with experimental measurements.

In the **first case study** two CFD solvers have been compared for prediction of flow in a dry air twin screw compressor. Performance predictions from the solvers have been compared with measurements. Differences in predicted results and probable causes have been discussed. This investigation showed that for the same grid, the performance prediction from the numerical model is influenced by the approach used for solving the conservation equations. The grids with interlobe region refinement and inflation layer were generated using the procedures proposed in Section 5.2 and Section 5.4. Results showed that flow was highly influenced by circumferential and axial grid refinement and not as significantly by wall normal refinement of the rotor domain. However, inflation layers give better predictions of the local flow features that are desirable from computational flow models.

The **second case study** was an analysis of a twin screw dry air expander. A set of modelling parameters were identified that give the best comparison with experimental data. A full performance map was calculated at various operating conditions and compared with experimental measurements. Rotor clearance and its effect on leakage prediction has been evaluated. Deviation between flow predictions from the numerical model and the experimental data has also been highlighted. Inflation layer grids were generated using the procedure proposed in Section 5.4 giving better predictions of the local velocity close to the rotor, but did not influence the integral expander performance parameters.

In the **third case study**, three types of rotor geometry were studied and their performance has been compared. The first type was a standard rotor, the second type rotor had a linearly variable lead and the third type of rotor had a variable rotor profile. Grids were generated for them, using the procedures proposed in Section 5.3. The flow and dynamics of such working chambers has not been analysed previously due to lack of grid generation procedure and developments in this thesis have extended the role played by computational methods in innovative screw machine designs.

Chapter 7 – Conclusions and Recommendation for Future Work

Interest in 3D numerical analysis of flow in screw machines with variable geometry rotors is increasing. The developments of grid generation for such machines and some of the key factors of numerical analysis have been presented. A summary of the research and recommendations for future work are proposed here.

7.1 Summary of the research

This research focused on the grid generation technology and numerical analysis of flow in positive displacement screw machines with variable geometry.

In this respect the current methods of flow calculation and grid deformation were explored and reviewed. Algebraic methods applied to grid generation for twin screw machines which are used with Arbitrary Lagrangian-Eulerian solver formulations were studied and their applicability for further extension to variable geometry rotors was evaluated. Similarly the differential grid generation methods used with Arbitrary Lagrangian-Eulerian formulations were reviewed in detail. Desirable features from each of these approaches were identified. The relatively new approach of Key-Frame remeshing used in commercial solvers was also evaluated for its accuracy and applicability to screw machines by solving a reversible adiabatic compression and expansion process. It proved to be inaccurate due to lack of space conservation.

Developments that were carried out for grid generation of screw machines with variable geometry fall in two categories:

Development of deforming grid generation techniques

- A variant of the algebraic grid generation in which the deforming rotor blocks are generated from the outer boundary (casing) to the inner boundary (rotor profile) has been developed.
- For non-helical rotors like the Roots blower, regularisation based on a skewed sine function with full domain transformation has been formulated that allows not only

generation of a full hexahedral mesh but also achieves a conformal interface between the two rotor blocks.

- For helical rotors, a regularisation method has been formulated that uses a background blocking technique for the redistribution of nodes on the rotor profile. This grid generation method provides an independent refinement in the interlobe clearance zone and also improves the orthogonality quality of the cells. Additionally this procedure also achieves a conformal interface between the two rotor blocks.
- A function has been formulated that can be used to generate a fine inflation layer adjacent to the rotors for a prescribed number of layers and growth rate.

These developments of deforming grid have been evaluated in two case studies. One on a twin screw compressor and other on a screw expander.

Extending the algebraic grid generation algorithms to variable geometry screw rotors

- In order to generate a grid for rotors with variable lead, the algebraic grid generation procedures have been extended with variable cross section spacing. Functions for uniform, linear or a stepped type of lead variation can be prescribed.
- A new algorithm has been developed to generate grids for rotors with variable profiles. This grid generation has the capability to accommodate continuously variable rotor geometry and makes it possible to solve flow in domains with conical rotors.

To validate the grids generated using the developed methods a detailed case study has been presented that investigates the relative performance of a twin screw dry air compressor with three rotor designs; one with uniform lead and profile, one with linearly variable lead and one with uniform lead but linearly variable profile i.e. conical main and gate rotors.

7.2 Conclusions

Chapter 4, Chapter 5 and the three case studies in Chapter 6 have presented inferences from the various grid generation developments and numerical analysis. Important conclusions that can be drawn from the overall research are

1. User Defined Nodal Displacement with ALE formulations is the preferred approach for flow calculation in screw machines.
2. A new approach of algebraic grid distribution to distribute boundary points on the rotors from the fixed points on the rack and casing has been implemented. This technique

provides a capability to refine the interlobe region without radically increasing the total mesh count. A fully conformal interface could be achieved between the two rotor domains. The orthogonality and equiangle skew quality factors were improved while the face warp quality factor was degraded with this new approach.

3. Deforming grid generation for twin screw machines with variable pitch and variable profile rotors was formulated and implemented using an algebraic approach.
4. A simplified function to generate inflation layer grid adjacent to rotor surface has been implemented.
5. **Case Study I** on the twin screw compressor showed that two different solver formulations predicted an indicated power very close to the experiment but showed differences in the prediction of mass flow rates and hence the leakage flows. A cell centred, pressure based segregated solver gave more accurate estimation of the flow rates for the expected clearance gap sizes as compared to a vertex centred, pressure based coupled solver. Operational clearances are strongly influenced by the change in temperature for different operating conditions. In order to obtain more accurate predictions, this change in clearance should be accounted for in the CFD models. Grids with successive interlobe refinement were generated using the new techniques. The results showed a strong influence on the prediction of leakage flows and improvement in comparison with experimental results with higher refinement in the interlobe. Presence of the inflation layer influenced the local flow features but not the integral performance parameters.
6. **Case Study II** on the twin screw expander showed that it is important to define the appropriate geometry and position of the pressure boundary of the high pressure port. The inclusion of turbulence modelling in CFD calculations did not affect the pressure distribution within the machine, but it influenced the leakage flows and hence the predicted mass flow rate and specific power. Clearance distribution in the interlobe, radial and axial gaps had a strong influence on the performance prediction. It is difficult to predict exact operating clearance values and comprehensive Fluid-Solid interaction study would help to better understand the dynamic behaviour. Presence of the inflation layer grid influenced the local gas velocities but had no influence on the integral performance parameters.
7. **Case study III** verified feasibility of using the developed procedure for variable geometry rotors so that the flow characteristics in the machines could be better

understood. The analysis showed that by varying the rotor lead continuously from the suction to the discharge ends, it is possible to achieve steeper internal pressure build up. The analysis also showed that varying the rotor lead allows a larger discharge port area, thereby reducing throttling losses, and provides increase in volumetric efficiency by reducing the sealing line length in the high pressure zone. Analysis of variable profile rotors showed the steeper internal pressure rise but there was no reduction of the sealing line length and blow-hole area for the same size of the rotors. The increase in root diameter of the female rotors with variable profile certainly helps in producing stiffer rotors for high pressure applications.

7.3 Recommendations for future work

In order to fully utilize the potential of 3D numerical analysis it will be important, in future, to develop procedures to better account for complex physical processes in the numerical model to achieve more accurate and reliable results. Some of the influential factors are:

- Leakage Gaps and Clearances.

Design clearances on the rotor and casing change due to thermal deformation and pressure forces during operation of the machine. It is necessary to have a full scale model with Fluid-Structure interaction that will accurately predict the changes in the leakage gaps. This will help in improving the prediction of the leakage flow and volumetric efficiency of the machines increasing the reliability of numerical models.

- Oil Injection.

Screw machines are most commonly used in the oil injection mode. Such machines are designed for higher pressure differences with lower clearances and lower rotor tip speeds than oil free compressors. Under these operating conditions it is of a high importance to consider the cooling and sealing effect of oil injection. This can be achieved in the numerical model by development of suitable multiphase flow models which are robust for high level of grid deformation experienced within the screw machine chambers.

Alternatively a suitable mechanism to mimic the effect of oil injection by mass, momentum and energy source and sink terms in the conservation equations may be formulated. Such models can be calibrated to get reliable results from the numerical analysis. Availability of extended data from the experimental measurements will be beneficial for comparison over a wider range of operating conditions and will help improve the CFD models.

- Grid generation for Single screw and Non-parallel axis Compressors.

The developments in this research verified the use of algebraic grid generation for variable profile rotors with parallel axis. However in the case of machines with non-parallel axis such as single screw compressors, this method needs to be extended. The proposed techniques in Chapter 5 will be directly applicable for such geometric variations if the rotor domain could be split using the analytical, numerical or differential rack approach. Hence new methods of grid decomposition and generation need to be formulated that will make it possible to generate grids for such arrangements.

The possibilities of exploration and developments in screw machine numerical analysis are virtually limitless. The author anticipates that the ideas and developments proposed in this thesis will contribute positively towards such improvements in future.

References

- Amosov P. E.**, 1977. Vintovie kompresornie mashinii - Spravochnik (Screw Compression Machines - Handbook), Mashinstroenie, Leningrad.
- Andreev P. A.**, 1961. Vintovie kompressornie mashinii (Screw Compression Machines), SUDPROM, Leningrad.
- ANSYS CFX®, 2011. User guide. R13.0.0: ANSYS Inc.
- Arbon I. M.**, 1994. The Design and Application of Rotary Twin-shaft Compressors in the Oil and Gas Process Industry, MEP London.
- Arina R.**, 1986. Orthogonal grids with adaptive control, Numerical grid generation in computational field simulations (B. K. Soni, J. F. Thompson, J. Hauser, P. Eiseman, eds.) NSF engineering research centre for computational field simulation, Mississippi state university, pp 113-124.
- Arjeneh M., Kovačević A., Gavaises M., Rane S.**, 2014. Study of Multiphase Flow at the Suction of Screw Compressor, *Proc. Int. Compressor Conf. at Purdue*, Paper 1353.
- Bein T. W., Hamilton J. F.**, 1982. Computer Modelling of an Oil Flooded Single Screw Air Compressor. *Proc. Int. Compressor Conf. at Purdue*, Paper 383.
- Boblitt W. W., Moore J.**, 1984. Computer Modeling of Single -Screw Oil Flooded Refrigerant Compressors, *Proc. Int. Compressor Conf. at Purdue*, Paper 506.
- Brackbill J. U., Saltzman J.**, 1980. An adaptive computation mesh for the solution of singular perturbation problems, Numerical grid generation techniques, NASA conference publication 2166, pp. 193-196.
- Brackbill J. U., Saltzman J.**, 1982. Adaptive zoning for singular problems in two directions, *J. Comput. Phys.* 46, pp. 342-368.
- Brummer A., Hütter J.**, 2009. Influence of geometric parameters on inlet-losses during the filling process of screw-type motors. *Developments in mechanical engineering*, vol. 4, pp. 105-121.
- CFX Berlin, 2014. TwinMesh for positive displacement machines. <http://www.cfx-berlin.de/software/stroemungsmechanik/twinmesh-fuer-verdraengermaschinen.html>

- Chawner J. R., Anderson D. A.**, 1991. Development of an Algebraic Grid Generation Method with Orthogonality and Clustering Control, *Conference on Numerical Grid Generation in CFD and Related Fields* at Barcelona, 107.
- Crowley W. P.**, 1962. An equipotential zoner on a quadrilateral mesh. Memo, Lawrence Livermore national Lab.
- Dagang X., Xion Z., Yu Y.**, 1986. The Computer Simulation of Oil Flooded Refrigeration Twin-Screw Compressor, *Proc. Int. Compressor Conf. at Purdue*, Paper 345.
- Date W. A.**, 2005. Introduction to computational fluid dynamics. Cambridge university press. ISBN-10 0-521-85326-5.
- David W.**, 1993. Turbulence Modeling for CFD, ISBN 0-9636051-0-0, DCW Industries Inc.
- Demirdžić I., Muzaferija S.**, 1995. Numerical Method for Coupled Fluid Flow, Heat Transfer and Stress Analysis Using Unstructured Moving Mesh with Cells of Arbitrary Topology, *Comp. Methods Appl. Mech. Eng.*, Vol.125, pp. 235-255.
- Demirdžić I., Perić M.**, 1990. Finite Volume Method for Prediction of Fluid flow in Arbitrary Shaped Domains with Moving Boundaries, *Int. J. Numerical Methods in Fluids* Vol.10, p. 771.
- Demirdžić I., Issa I. R., Lilek Z.**, 1990. Solution Methods for Viscous Flows at all Speeds in Complex Domains, in P. Wesseling (ed.), Notes on Numerical Fluid Mechanics, Vol 29, Vieweg, Braunschweig.
- Eiseman P. R.**, 1982. Orthogonal grid generation, Numerical grid generation (J. F. Thompson, ed), Elsevier, New York, pp. 193-230.
- Eiseman P. R.**, 1987. Adaptive grid generation. *Comput. Methods. Appl. Mech. Eng.* 64, 321-376.
- Eiseman P.R.**, 1992. Control Point Grid Generation, *Computers Mathematical Applications*, Vol.24, No.5/6, 57-67.
- Eiseman P.R., Hauser J., Thompson J.F., Weatherill N.P.**, (Ed.), 1994. Numerical Grid Generation in Computational Field Simulation and Related Fields, *Proceedings of the 4th International Conference*, Pineridge Press, Swansea, Wales, UK.
- Farrashkhhalvat M., Miles P. J.**, 2003. Basic structured grid generation with an introduction to unstructured grid generation. BH publication Oxford. ISBN 0 7506 5058 3.

- Ferziger J. H. and Perić M.**, 1996. *Computational Methods for Fluid Dynamics*, ISBN 978-3-540-42074-3, Springer, Berlin, Germany.
- Fleming J. S., Tang Y.**, 1994. The Analysis of Leakage in a Twin Screw Compressor and its Application to Performance Improvement, Proceedings of IMechE, Journal of Process Mechanical Engineering, Vol209, 125
- Fleming J. S., Tang Y., Cook G.**, 1998. The Twin Helical Screw Compressor, Part 1: Development, Applications and Competitive Position, Part 2: A Mathematical Model of the Working process, *IMechE, Journal of Mechanical Engineering Science*, Vol. 212, p. 369.
- Fost C.**, 2006. Geometrical Variations at the Inlet of Screw–Type Engines. *International screw compressor conference*, VDI-Berichte Nr. 1932, TU Dortmund.
- Fujiwara M., Mori H., Suwama T.**, 1974. Prediction of the Oil Free Screw Compressor Performance Using Digital Computer, *Proc. Int. Compressor Conf. at Purdue*, Paper 186.
- Fujiwara, M., Kasuya, K., Matsunaga, T. and Watanabe, M.**, 1984. Computer Modeling for Performance Analysis of Rotary Screw Compressor. *Proc. Int. Compressor Conf. at Purdue*, Paper 503.
- Fujiwara M., Osada Y.**, 1990. Performance Analysis of Oil-Injected Screw Compressors and its Applications. *Proc. Int. Compressor Conf. at Purdue*, Paper 689.
- Fukazawa Y., Ozawa U.**, 1980. Small Screw Compressors for Automobile Air Conditioning Systems. *Proc. Int. Compressor Conf. at Purdue*, Paper 351.
- Gardner J. W.**, 1969. US Patent No 3,424,373 – Variable Lead Compressor. Patented 1969.
- Godunov S. K., Prokopov G. P.**, 1972. On utilisation of moving grids in gas dynamics computations. *J. Vychisl. Matem. Phys.* 12, 429-440 (Russian). English translation: USSR Comput. Math. and Math. Phys. 12, 182-195.
- Goldfarb V.I., Voznyuk R.V.**, 1998. Development of a CAD Tool for Enveloping Modelling, *Mechanics in Design, Proceedings of the International Conference*, Nottingham, UK, p.471-478.
- Goldfarb V.I., Lunin S.V., Trubchev E.S.**, 2004. Direct Digital Simulations for Gears - Volume 1, Izhevsk, ISBN 5-7526-0196-7, Published in Russia. English translation available at <http://www.stepanlunin.com/book1.html>

- Gordon W.J., Hall C.A.,** 1973. Construction of Curvilinear Coordinate Systems and Applications to Mesh Generation, *Int. J. Numer. Meth. Engineering*, Vol.7, 461-477.
- Gosman D.A., Watkins P.A.,** 1977. A computer prediction method for turbulent flow and heat transfer in piston/cylinder assemblies, Proceeding of 1st Symposium on Turbulent Shear Flows, The Pennsylvania State University, Pennsylvania, p.523.
- Gosman D.A., Johnson J.R.,** 1978. Development of a predictive tool for in-cylinder gas motion in engines' SAE Paper 780315.
- Gosman D.A.,** 1984. Prediction of in-cylinder processes in reciprocating internal combustion engines, in Glowinski and Lions edition of Computing Methods in Applied Science and Engineering, Elsevier, Amsterdam, 604-629.
- Grieb M, Brümmer A.,** 2014. Design and examination of a small-scale screw expander for waste heat recovery, International Screw Compressor Conference, TU Dortmund.
- Hanjalić K., Stošić N.,** 1997. Development and Optimisation of Screw machines with a simulation Model – Part II: Thermodynamic Performance Simulation and Design Optimisation. *Journal of Fluid Engineering. Transactions of the ASME*, Vol. 119, 664-670.
- Hanjalić K. and Launder B.,** 2011. Modelling Turbulence in Engineering and the Environment: Second-Moment Routes to Closure, Cambridge University Press, ISBN 978-0-521-84575-5.
- Hauser J. and Beinert M.,** 2013. CFD analysis of pressure pulsation in screw compressors - combine theory with practice. 8th Int conf on compressors and their systems, p. 625.
- Hesse J., Spille-Kohoff A., Hauser J., Schulze-Beckinghausen P.,** 2014. Structured meshes and reliable CFD simulations: TwinMesh for positive displacement machines. *International screw compressor conference*, TU Dortmund.
- Holmes C. S.,** 1990. A Study of Screw Compressor Rotor Geometry Leading to a Method for Inter-Lobe Clearance Measurement, PhD Thesis, School of Engineering, Huddersfield Polytechnic, UK.
- Hutker J., Brummer A.,** 2012. Thermodynamic Design of Screw Motors for Constant Heat Flow at Medium Temperature Level. Proc. *Int. Compressor Conf. at Purdue*, pp. 1478.
- Hütker J., Brümmer A.,** 2013. Physics of a dry running unsynchronised twin screw expander, *International Conference on Compressors and their Systems*, City University London.

- Janicki M.**, 2007. Modellierung und Simulation von Rotationsverdrängermaschinen. PhD Dissertation, TU Dortmund.
- Jiang Y., Furmanczyk M., Lowry S., Zhang D., and Perng Chin-Yuan**, 2007. A Three-Dimensional Design tool for Crescent Oil Pumps. SAE p. 2008-01-0003.
- Jianhua Wu and Guangxi Jin**, 1988. The Computer Simulation of Oil-Flooded Single Screw Compressors, *Proc. Int. Compressor Conf. at Purdue*, Paper 646.
- Jensen D.**, 1998. A New Single Screw Compressor Design that Enables a New Manufacturing Process. International Compressor Engineering Conference. Paper 1306.
- Kauder K., Fost C.**, 2002. Investigations about the improvement of the Filling process of a Screw-Type Engine, Part III. VDI-Berichte Report, TU Dortmund.
- Kauder K., Rau B.**, 1994. Auslegungsverfahren fur Schraubenkompressoren. (Design Procedure for screw compressors), VDI Berichte 1135, S. 31-44, Düsseldorf: vdiVerlag.
- Kethidi M., Kovačević A., Stošić N., Smith I. K.**, 2011. Evaluation of various turbulence models in predicting screw compressor flow processes by CFD. *7th Int conf on compressors and their systems*, p. 347.
- Kethidi M., Kovačević A., Stošić N., Rane S.**, 2012. Modelling of turbulence in screw compressor flows, *Proc. Turbulence, Heat and Mass Transfer* 7, E308.
- Kim J. H., Thompson J.F**, 1990. 3-Dimensional Adaptive Grid generation on a Composite-Bloch Grid, *AIAA Journal*, Vol.28, Part.3, 470-477.
- Konka K. H.**, 1988. Schraubenkompressoren (Screw Compressors) VDI-Verlag, Duesseldorf.
- Kovačević A., Stošić N., Smith I. K.**, 1999. Development of CAD-CFD Interface for Screw Compressor Design, *International Conference on Compressors and Their Systems, London, IMechE Proceedings*, Paper C542-075, 757-767.
- Kovačević A., Stošić N., Smith I. K.**, 2000. Grid Aspects of Screw Compressor Flow Calculations, *ASME Congress*, Orlando FL, Vol. 40, pp. 83.
- Kovačević A.**, 2002. Three-Dimensional Numerical Analysis for Flow Prediction in Positive Displacement Screw Machines, Ph.D. Thesis, School of Engineering and Mathematical Sciences, City University London.

- Kovačević A., Stošić N., Smith I. K.**, 2002a. Numerical Simulation of Fluid Flow and Solid Structure in Screw Compressors, *Proceedings of ASME Congress*, New Orleans, IMECE2002-33367.
- Kovačević A., Stošić N., Smith I. K.**, 2002b. Influence of Rotor Deflection upon the Screw Compressor Process, *Schrauben compressor tagung*, Dortmund.
- Kovačević A., Stošić N., Smith I. K.**, 2003. 3-D Numerical Analysis of Screw Compressor Performance. *Journal of Computational Methods in Sciences and Engineering* 3: 259-284.
- Kovačević A.**, 2005. Boundary Adaptation in Grid Generation for CFD Analysis of Screw Compressors, *Int. J. Numer. Methods Eng.*, Vol. 64: 401-426.
- Kovačević A., Stošić N., Smith I. K.**, 2006. Numerical simulation of combined screw compressor-expander machines for use in high pressure refrigeration systems, *Simulation Modeling Practice and Theory*, Volume 14, Issue 8, Pages 1143–1150.
- Kovačević A., Stošić N. and Smith I. K.**, 2007. *Screw compressors - Three dimensional computational fluid dynamics and solid fluid interaction*, ISBN 3-540-36302-5, Springer-Verlag Berlin Heidelberg New York.
- Kovačević A., Stošić N., Mujić E. and Smith I. K.**, 2007. CFD integrated design of screw compressors, *Engineering Applications of Computational Fluid Mechanics* Vol. 1 – 2. p. 96–108.
- Kovačević A., Stošić N., Smith I. K., Mujić E. and Guerrato D.**, 2009. Extending the role of computational fluid dynamics in screw machines, *6th Int conf on compressors and their systems*, p. 41.
- Kovačević A. and Rane S.**, 2013. 3D CFD analysis of a twin screw expander, 8th International conference on compressors and their systems, London, p. 417.
- Kovačević A., Rane S. and Stošić N.**, 2013. Grid generation for screw compressors with variable geometry rotors, *Int Journal of Aerospace and Lightweight Structures*, Vol. 3, No. 2, p. 191–206.
- Kovačević A., Rane S., Stošić N., Jiang Y., Furmanczyk M. and Lowry S.**, 2014. Influence of approaches in CFD Solvers on Performance Prediction in Screw Compressors, *Proc. Int. Compressor Conf. at Purdue*, Paper 1124.

- Lehtimaki R.**, 2000. An Algebraic Boundary Orthogonalisation Procedure for Structured Grids, *Int Journal Numerical Methods in Fluids*, Vol. 32, 605-618.
- Li Hong Qi and Jin Li Wen**, 2004. Design Optimisation of an Oil-Flooded Refrigeration Single Screw Compressor, *Proc. Int. Compressor Conf. at Purdue*, Paper 1715.
- Liseikin V.D.**, 1998. Algebraic Adaptation Based on Stretching Functions, *Russian Journal for Numerical and Analytical Mathematical Modeling*, Vol.13, No.4, 307-324
- Liseikin V. D.**, 1999. Grid Generation Methods, Springer-Verlag.
- Litvin F. L.**, 1956. Teoria zubchatiih zaceplenii (Theory of Gearing), Nauka Moscow, second edition 1968, also Gear Geometry and Applied Theory Prentice-Hill, Englewood Cliffs, NJ 1994.
- Lundberg A. and Glanvall R.**, 1978. A Comparison of SRM and Globoid Type Screw Compressors at Full Load, *Proc. Int. Compressor Conf. at Purdue*, Paper 288.
- Mujić E., Kovačević A., Stošić N., and Smith I. K.**, 2008. The influence of port shape on gas pulsations in a screw compressor discharge chamber, *Proceedings of IMechE, Vol. 222 Part E: Journal of Process Mechanical Engineering*.
- Nikolov A., Huck C., Brummer A.**, 2012. Influence of Thermal Deformation on the Characteristics Diagram of a Screw Expander in Automotive Application of Exhaust Heat Recovery. *Proc. Int. Compressor Conf. at Purdue*, pp. 1447.
- Nilsson H. R.**, 1949. US Patent No 2,481,527 – Rotary Multiple Helical Rotor Machine.
- Nouri J. M., Guerrato D., Stošić N., Kovačević A., and Arcoumanis, C.**, 2006, Cycle-resolved velocity measurements within a screw compressor. *Proc. Int. Compressor Conf. at Purdue*, Paper 1810.
- O'Neill P. A.**, 1993. Industrial Compressors, Theory and Equipment, Butterworth-Heinemann, Oxford.
- Papes, I., Degroote, J., Vierendeels, J.**, 2013, 3D CFD analysis of an oil injected twin screw expander. Proceedings of the ASME 2013 International Mechanical Engineering Congress and Exposition, San Diego, USA: ASME IMECE 2013.
- Papes, I., Degroote, J., Vierendeels, J.**, 2014. 3D CFD analysis of a twin screw expander for small scale ORC systems. Proceedings of the 11th World Congress on Computational Mechanics. pp. 7207–7217.

- Pascu M., Kovačević A. and Udo N.**, 2012. Performance Optimisation of Screw Compressors Based on Numerical Investigation of the Flow Behaviour in the Discharge Chamber. *Proc. Int. Compressor Conf. at Purdue*. Paper 1145.
- Patankar V. S.**, 1980. Numerical Heat Transfer and Fluid Flow. Taylor and Francis. ISBN 0891165223.
- PumpLinx 3.2.2, 2014, User guide. Simerics Inc.
- Perić M.**, 1985. A Finite Volume Method for the Prediction of Three Dimensional Fluid Flow in Complex Ducts, *PhD Thesis, Imperial College of Science, Technology & Medicine*, London
- Powel G, Weathers B and Sauls J**, 2006. Transient Thermal Analysis of Screw Compressors, Part III- Transient Thermal Analysis of a screw Compressor to determine Rotor-to-Rotor Clearances. *Proc. Int. Compressor Conf. at Purdue*, Paper 1813.
- Prasad, B. G. Shiva**, 2004. CFD for Positive Displacement Compressors, *Proc. Int. Compressor Conf. at Purdue*. Paper 1689.
- Perna V.**, 2003. Equipment with mutually interacting spiral teeth. US Patent 2003/0012675 A1.
- Rane S., Kovačević A. and Kethidi M.**, 2012. CFD Modeling in Screw Compressors with complex multi rotor configurations. *Proc. Int. Compressor Conf. at Purdue*. Paper 1576.
- Rane S., Kovačević A., Stošić N. and Kethidi M.**, 2013. Grid Deformation Strategies for CFD Analysis of Screw Compressors, *Int Journal of Refrigeration*, **36**, 7, p. 1883-1893.
- Rane S., Kovačević A., Stošić N. and Kethidi M.**, 2013. CFD grid generation and analysis of screw compressor with variable geometry rotors, *8th Int conf on compressors and their systems*, C1390, p. 601.
- Rane S., Kovačević A., Stošić N. and Kethidi M.**, 2014. Deforming grid generation and CFD analysis of variable geometry screw compressors, *Computers and Fluids*, **99**, p. 124–141.
- Read M., Stošić N., Smith I. K.**, 2014. Optimisation of Screw Expanders for Power Recovery from Low-Grade Heat Sources. *Energy Technology and Policy*.
- Riemslagh K., Vierendeels J., Dick E.**, 1998. Two-dimensional incompressible Navier-Stokes calculations in complex-shaped moving domains, *J. Eng. Math.*, 34(1-2):57-73.

- Riemslagh K., Vierendeels J., Dick E.**, 2000. An arbitrary Lagrangian-Eulerian finite-volume method for the simulation of rotary displacement pump flow. *Applied Numerical Mathematics*, 32:419-433.
- Rinder L.**, 1979. Schraubenverdichter (Screw Compressors), Springer Verlag, New York.
- Rinder L.**, 1984. Schraubenverdichterläufer mit Evolventenflanken (Screw Compressor Rotor with Inolute Lobes), Proc. VDI Tagung "Schraubenmaschinen 84" VDI Berichte Nr. 521 Düsseldorf.
- Rinder L.**, 1985. Screw rotor profile and method for generating, Patent 4643654.
- Sakun I.A.**, 1960. Vintovie kompresorii (Screw Compressors), Mashinostroenie Leningrad.
- Samareh J. A.**, 1987. Topology and grid adaptation for high-speed flow computations. PhD Thesis. Mechanical Engineering, Old Dominion University. USA.
- Samareh A. J., Smith R.E.**, 1992. A Practical Approach to Algebraic Grid Adaptation, *Computers Mathematical Applications*, Vol.24, No.5/6, 69-81.
- Sangfors B.**, 1982. Analytical Modeling of Helical Screw Machine for Analysis and Performance Prediction, *Proc. Int. Compressor Conf. at Purdue*, 144.
- Sangfors B.**, 1984. Computer Simulation of the Oil Injected Twin Screw Compressor, *Proc. Int. Compressor Conf. at Purdue*, 528.
- Sauls J. and Branch S.**, 2013. Use of CFD to develop improved one-dimensional thermodynamic analysis of refrigerant screw compressors. *8th Int conf on compressors and their systems*, p. 591.
- Sauls J, Powel G and Weathers B**, 2006. Transient Thermal Analysis of Screw Compressors, Part I- Use of Thermodynamic Simulation to determine Boundary Conditions for Finite Element Analysis. *Proc. Int. Compressor Conf. at Purdue*, Paper 1811.
- Schulze-Beckinghausen P., Hauser J., Beinert M., Herleemann S.**, 2014. Advanced analysis of twin screw compressors with variable rotor pitch using one-dimensional thermodynamic simulation, *International screw compressor conference*, TU Dortmund.
- Sharpe H., Anderson D. A.**, 1991. Orthogonal adaptive grid generation with fixed internal boundaries for oil reservoir simulation, Numerical grid generation in computational field simulation and related fields (A. S. Arcilla, J. Hauser, P. R. Eiseman and J. F. Thompson, eds), North Holland, New York, pp. 405-417.

- Shih T. I. P., Bailey R. T., Nguyen H. L., Roelke R. J.**, 1991. Algebraic Grid Generation for Complex Geometries, *International Journal for Numerical Methods in Fluids*, Vol. 13, 1-31.
- Shyue-Cheng Yang**, 2006. Profile generation and analysis for a pp-type single-screw compressor. *International Journal of Advanced Manufacturing Technology* 30: 789–796.
- Singh P. J., Onuschak A. D.**, 1984. A Comprehensive Computerised Method for Twin Screw Rotor Profile Generation and Analysis, *Proc. Int. Compressor Conf. at Purdue*.
- Singh P. J., Patel G. C.**, 1984. A Generalised Performance Computer Program for Oil Flooded Twin -Screw Compressors, *Proc. Int. Compressor Conf. at Purdue*, Paper 544.
- Singh P. J., Schwartz J. R.**, 1990. Exact Analytical Representation of Screw Compressor Rotor Geometry, *Proc. Int. Compressor Conf. at Purdue*, Paper 925.
- Smith I.K, Stošić N, Aldis C A**, 1996. Development of the trilateral flash cycle system, Part3: design of high-efficiency two phase screw expanders, *Proceedings of IMechE, Part A: Journal of Power and Energy*, Volume 210.
- Smith I.K, Stošić N, Kovačević A**, 2004. An Improved System for Power Recovery from High Enthalpy Liquid Dominated Field, *GRC Annual Meeting*, Indian Wells, California.
- Sorenson R. L., Steger J. L.**, 1977. Simplified clustering of nonorthogonal grids generated by elliptic partial differential equations. Ames research centre, Moffett field, California, NASA Technical Memorandum 73252.
- Sorenson, R. L.**, 1980. A Computer Program to Generate Two-Dimensional Grids about Air foils and Other Shapes by the use of Poisson's equation, NASA Technical Memorandum 81198.
- Sorenson R. L., Steger J. L.**, 1983. Grid generation in three dimensions by Poisson equations with control of cell size and skewness at boundary surfaces, Advances in grid generation (K. N. Ghia and U. Ghia, eds.), FED-vol. 5, ASME Applied Mechanics, Bioengineering and fluids engineering conference, Houston, Texas.
- Soni B.K**, 1992. Grid Generation for Internal Flow Configurations, *Computers Mathematical Applications*, Vol.24, No.5/6, 191-201.
- Steger J. L., Sorenson R. L.**, 1979. Automatic mesh-point clustering near a boundary in grid generation with elliptic partial differential equations. *J. Comput. Phys.* 33, 405-410.

- Steinþorsson E., Shih T. I. P., Roelke R. J.**, 1992. Enhancing Control of Grid Distribution In Algebraic Grid Generation, *International Journal for Numerical Methods in Fluids*, Vol. 15, 297-311
- Stošić, N., Hanjalić, K.**, 1977. Contribution towards modelling of two-stage reciprocating compressors, *International Journal of mechanical Science*, Vol. 19, p.439- 445.
- Stošić N., Hanjalić K., Kovačević A., Milutinovic Lj,** 1988. Mathematical Modeling of the Influence of Oil on the Working Cycle of Screw Compressors. *Proc. Int. Compressor Conf. at Purdue*, Paper 645.
- Stošić N., Milutinovic Lj., Hanjalić K., Kovačević A.,** 1992. Investigation of the influence of oil injection upon the screw compressor working process. *Int. J. Refrig.* vol. 15(4), pp. 206-220.
- Stošić N, Smith I.K, Zagorac S**, 1996. CFD Studies of Flow in Screw and Scroll Compressors. *Proc. Int. Compressor Conf. at Purdue*. Paper 1103.
- Stošić N., Hanjalić K.,** 1997. Development and Optimisation of Screw machines with a simulation Model – Part I: Profile Generation. *Journal of Fluid Engineering. Transactions of the ASME*, Vol. 119, 659-663.
- Stošić N., Hanjalić K.,** 1994. Development and optimisation of screw engine rotor pairs on the basis of computer modelling, *Proc. Int. Compressor Conf. at Purdue*. Paper 55.
- Stošić N.,** 1997. Plural screw positive displacement machines, Patent US 6296461 B1.
- Stošić N.,** 1998. On Gearing of Helical Screw Compressor Rotors, Proceeding of IMechE, *J. Mech. Eng. Science*, Vol.212, and pp. 587.
- Stošić N., Smith I. K., Kovačević A,** 2002. A Twin Screw Combined Compressor and Expander for CO₂ Refrigeration Systems. *Proc. Int. Compressor Conf. at Purdue*, pp. C21-2.
- Stošić N., Smith I.K. and Kovačević A.,** 2005a. *Screw Compressors: Mathematical Modeling and Performance Calculation*, Monograph, Springer Verlag, Berlin, June 2005, ISBN: 3-540-24275-9.
- Stošić N., Smith I. K. and Kovačević A.,** 2005b. Numerical Investigation of Heat Transfer on Screw Compressor Rotors. *8th Argentinian Congress on Computational Mechanics*, Buenos Aires, Argentina.

- Stošić N., Mujić E., Smith I. K., Kovačević A.**, 2008. Profiling of Screw Compressor Rotors by Use of Direct Digital Simulation. *Int. Compressor Eng. Conf. Purdue*. Paper 1860.
- Tang Y.**, 1995. Computer aided design of twin screw compressors. PhD Thesis, Department of Mechanical Engineering, University of Strathclyde. UK.
- Tannehill J. C., Anderson D. A., Pletcher H. R.**, 1997. Computational Fluid Mechanics and Heat Transfer. Taylor and Francis, Second Edition. ISBN 1-56032-046X.
- Thomas P., Lombard C.**, 1979. Geometric conservation law and its application to flow computations on moving grids, *AIAA Journal*, 17, 1030–1037.
- Thomas P. D., Middlecoff J. F.**, 1980. Direct control of the grid point distribution in meshes generated by elliptic equations. *AIAA Journal*, 18(6), 652-656.
- Thomas W. Bein, James F Hamilton**, 1982. Computer modeling of an oil flooded Single Screw Compressor. *Proc. Int. Compressor Conf. at Purdue*, Paper 383.
- Thompson J. F., Thames F. C., Mastin C. W.**, 1974. Automatic Numerical Generation of Body-Fitted curvilinear coordinate system for field containing any number of arbitrary two-dimensional bodies. *J. Comput. Phys.*, vol. 15, pp. 299-319.
- Thompson J. F.**, 1984. Grid Generation Techniques in Computational fluid Dynamics, *AIAA Journal*, Vol.22, No.11, 1505-1523.
- Thompson J. F.**, 1985. A survey of dynamically-adaptive grids in the numerical solution of partial differential equations. *Appl. Numer. Math.* 1, 3-27.
- Thompson J. F.**, 1996. A Reflection on Grid Generation in the 90's: Trends, Needs and Influences, Numerical grid Generation in computational field simulations (B. K. Soni, J. F. Thompson, J. Hauser and P. Eiseman, eds.), NSF engineering research centre for computational field simulation, Mississippi State University, Vol.1, 1029-1110.
- Thompson J. F., Soni B and Weatherill N. P.**, 1999. Handbook of Grid Generation, CRC Press.
- Trulio G.J., Trigger R.K.**, 1961. Numerical solution of the one-dimensional hydrodynamic equations in an arbitrary time-dependent coordinate system, University of California Lawrence Radiation Laboratory Report, UCLR-6522.
- Ushakova O. V.**, 2007. Advances in Grid Generation, Nova Science Publishers Inc., ISBN: 1-59454-273-2.

- Utri M., Brümmer A.**, 2014. A comparative examination of the potential of screw expanders with variable rotor pitch, *International screw compressor conference*, TU Dortmund.
- Versteeg K.H., Malalasekera W.**, 1995. An Introduction to computational Fluid Dynamics – The Finite Volume Method, Longman Scientific & Technology, UK.
- Vertrotors**, 2011. <http://vertrotors.com/>
- Vimmr J.**, 2005. Turbulent compressible fluid flow computation in a male rotor-housing gap of screw compressors. *Proc. Appl. Math. Mech.* 5, 567–568.
- Vande Voorde J., Vierendeels J., Dick E.**, 2004. A Grid Generator for flow calculations in Rotary Volumetric Compressors, European Congress on Computational Methods in Applied Sciences and Engineering.
- Vande Voorde J., Vierendeels J.**, 2005. A grid manipulation algorithm for ALE calculations in screw compressors. 17th AIAA Computational Fluid Dynamics Conference, Canada, AIAA 2005-4701.
- Vande Voorde J.**, 2005. Numerical flow calculations in rotary positive-displacement machines. PhD dissertation. Ghent University.
- Wang D., Ding H., Jiang Y. and Xian X.**, 2012. Numerical modeling of vane oil pump with variable displacement. SAE Paper 2012-01-0637.
- Wei-feng WU, Quan-ke FENG**, 2008. Leakage Paths of Two Type of Meshing Pairs in Single Screw Compressors, *Proc. Int. Compressor Conf. at Purdue*, Paper 1864.
- Weathers B., Sauls J and Powel G**, 2006. Transient Thermal Analysis of Screw Compressors, Part II - Transient Thermal Analysis of a screw Compressor to determine Rotor-to-housing Clearances. *Proc. Int. Compressor Conf. at Purdue*, Paper 1812.
- Winslow A.**, 1964. Numerical calculation of static magnetic fields in an irregular triangle mesh. Lawrence Radiation Laboratory (Livermore, California) Report, UCRL-7784.
- Winslow A.**, 1966. Numerical solution of the quasilinear poisson equation in a nonuniform triangle mesh. *J. Comput. Physics*, 1:149-172.
- Xing Z.**, 2000. Screw Compressors: Theory, Design and Application, China Machine Press, Beijing (In Chinese).

Xing Z., Peng X., and Shu, P., 2000. Development and Application of a Software Package for the Design of Twin Screw Compressors, *Proc. Int. Compressor Conf. at Purdue*, Paper 1492.

Zimmern B., 1984. From Water to Refrigerant: Twenty Years to Develop the Oil Injection-Free Single Screw Compressor. *Proc. Int. Compressor Conf. at Purdue*, Paper 500.

Zimmern B., Patel G., 1972. Design and Operating Characteristics of the Zimmern Single Screw Compressor, *Proc. Int. Compressor Conf. at Purdue*, Paper 16.

Appendices

Appendix A. Screw compressor performance parameters

The design of screw machines is greatly influenced by the dynamics of the working chamber, the suction and the discharge.

Geometrical features of screw rotors and their influence on the compressor design have been presented in details in texts such as *Stošić et al.* (2005a). Briefly they have been listed here:

- Built in volume ratio V_i and internal pressure ratio.
 - Under compression, optimum compression and over compression.
 - Timing of the discharge port.
- Rotor tip speed.
- Number of lobes and lobe combinations.
- Wrap angle.
- L/D Ratio.
- Rotor profiles.
- Clearances in the radial, interlobe and end gaps.
- Sealing line length.
 - Radial.
 - Interlobe.
- Blow-hole area.

Integral quantities of importance for a screw compressor performance are the compressor mass flow rate, the indicated power, specific indicated power, volumetric efficiency, adiabatic efficiency and isothermal efficiency. These quantities are obtained as theoretical estimates or as measurements.

Mass flow rate

Mass flow rate is the mass of gas delivered per unit time. It is obtained from the mass trapped in the chamber per cycle and the rotational speed of the main rotor.

$$\dot{m} = m z_1 \frac{n}{60} [Kg/sec] \quad (A.1)$$

Volumetric Efficiency

Volumetric efficiency is a comparison of flow actually obtained from the machine with the theoretical capacity of the machine.

$$\eta_v = \frac{\dot{V}}{\dot{V}_t} \quad (\text{A.2})$$

The volumetric delivery is referenced to the suction condition.

$$\dot{V} = \frac{60 \dot{m}}{\rho_0} \quad [\text{m}^3/\text{min}] \quad (\text{A.3})$$

The theoretical volumetric delivery is obtained from the geometry of the rotors. It is possible to estimate \dot{V}_t directly from the CAD model of the compressor rotors at a position when the suction port is just cut-off from the compression chamber and does not include leakage flows.

Indicated power

Indicated work transferred to the screw rotors during the compression is the area under the pressure-volume diagram.

$$W_{ind} = \int_{cycle} p dV = \int_{cycle} V dp \quad [\text{J}] \quad (\text{A.4})$$

Indicated power is given by,

$$P_{ind} = \frac{W_{ind} z_1 n}{60} \quad [\text{W}] \quad (\text{A.5})$$

From the numerical model if the torque on the rotor shafts is available then the indicated power can be calculated as

$$P_{ind} = \frac{2 \pi n \left(T_{main} + \frac{z_1}{z_2} T_{gate} \right)}{60} \quad [\text{W}] \quad (\text{A.6})$$

Specific indicated power

Specific indicated power is the quantity of energy consumed to deliver a unit quantity of mass of the gas. It is calculated as the ratio of indicated power and mass flow rate.

$$P_{sind} = \frac{P_{ind}}{\dot{m} 1000} \quad [\text{kW/Kg/sec}] \quad (\text{A.7})$$

Theoretical isothermal power

If the compression process was under isothermal conditions, then the theoretical power required for the given pressure rise from P_1 to P_2 is

$$P_{iso} = R T_1 \ln \frac{P_2}{P_1} \dot{m} \quad [\text{W}] \quad (\text{A.8})$$

Theoretical adiabatic power

If the compression process was under adiabatic conditions, then the theoretical power required for the given pressure rise from P_1 to P_2 is

$$\begin{aligned} P_{ad} &= \frac{\gamma}{\gamma - 1} R (T_2 - T_1) \dot{m} [W] \\ &= \frac{\gamma P_1 \dot{V}}{\gamma - 1} \left[\left(\frac{P_2}{P_1} \right)^{\frac{\gamma-1}{\gamma}} - 1 \right] [W] \end{aligned} \quad (\text{A.9})$$

Isothermal efficiency

Isothermal efficiency is the comparison of actual indicated power and theoretical isothermal power for the compression.

$$\eta_{iso} = \frac{P_{iso}}{P_{ind}} \quad (\text{A.10})$$

Adiabatic efficiency

Adiabatic efficiency is the comparison of actual indicated power and theoretical adiabatic power for the compression.

$$\eta_{ad} = \frac{P_{ad}}{P_{ind}} \quad (\text{A.11})$$

Integral quantities as defined here are used for the performance comparison of the machines.

Appendix B. Fundamentals of Grid Generation Approaches

B.1 Algebraic grid generation

An algebraic grid generation starts with the boundary node distribution in 2D and then some coordinate transformation as suited by the bounding curve is performed to convert the physical space into computation space that allows for better control over distribution. Once the grid has been distributed in the computation space a reverse transformation is employed to bring the grid definition in physical space. The result is that complex physical boundaries can be mapped onto simple computational building blocks irrespective of the dimensions and analytical functions can be used to get the grid distribution. Most commonly transfinite interpolation schemes (*Gordon and Hall, 1973*) are used for the coordinate transformations along with blending functions and stretching functions. The boundary grid points are generally available as a set of data points and tension splines can be used to approximate these data (*Eiseman, 1992*). Advantage of algebraic methods is that the grids are calculated with very less computational effort, hence are generated very fast. Control on spacing and boundary orthogonality is achieved via selection of coefficients in transfinite interpolation (*Chawner and Anderson, 1991*). However with these methods smoothness in the interior grid is not assured directly and discontinuities on the boundaries get propagated into the interior. No control over the Jacobian of transformation is maintained when TFI is used. Hence grid crossing can happen with complex boundaries. The methods are therefore used generally in domains with smooth boundaries. They can provide a good starting mesh for differential or variational methods though.

B.2 Coordinate transformation

Consider an elementary example of curved area bounded by r and θ in two dimensional polar coordinates as shown in Figure B.1.

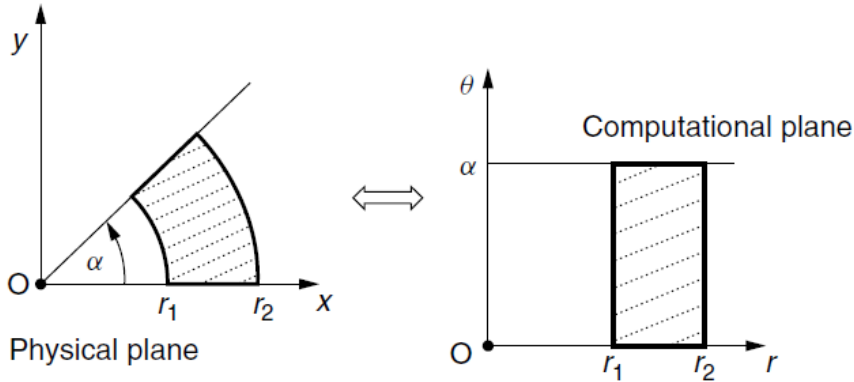


Figure B.1 Mapping of a curved physical region onto a rectangle

Points (x, y) represent the physical space with bounds given by r and θ .

$$r_1 \leq r \leq r_2 \text{ and } 0 \leq \theta \leq \alpha$$

The mapping in equation (B.1) gives a one to one correspondence between the points (r, θ) in a rectangular computational region in which r and θ are treated like Cartesian co-ordinates and points (x, y) in physical space of Figure B.1.

$$x = r \cos\theta, \quad y = r \sin\theta \quad (\text{B.1})$$

The inverse mapping in equation (B.2) represents a reverse transformation from the rectangular computational space (r, θ) to a curved physical space (x, y) .

$$r = \sqrt{x^2 + y^2}, \quad \theta = \tan^{-1}(y/x) \quad (\text{B.2})$$

The mapping equation (B.1) can be normalised by a further transformation of coordinates from (r, θ) to (ξ, η) where,

$$\xi = \frac{r - r_1}{r_2 - r_1}, \quad \eta = \frac{\theta}{\alpha}, \quad (\text{B.3})$$

These now maps the rectangle into a unit square in the (ξ, η) plane with bounds

$$0 \leq \xi \leq 1, \quad 0 \leq \eta \leq 1$$

Then the equation (B.1) becomes

$$\begin{aligned} x &= [(r_2 - r_1)\xi + r_1] \cos(\alpha\eta), \\ y &= [(r_2 - r_1)\xi + r_1] \sin(\alpha\eta), \end{aligned} \quad (\text{B.4})$$

Equation (B.4) now maps a unit square in the new computational space onto the original curved physical region. A uniform rectangular grid in the unit square, where increments in ξ and η

along the grid lines between adjacent grid-points are constant, maps to a grid in the physical region where increments in r and θ along grid lines $\theta = \text{const.}$ and grid curves $r = \text{const.}$ respectively, are constant. This method of generating a grid in the physical region, using a simple analytical transformation equation (B.1) or a combination of transformations (B.3) and (B.4) may be regarded as basic method of algebraic grid generation (*Farrashkhhalvat and Miles, 2003*).

The determinant of first derivatives of the mapping function is the so called Jacobian of transformation. A necessary condition for a one to one transformation to exist is that the Jacobian of transformation should be nonzero. In physical space this ensures that there is no folding or overlapping of grid lines which is essential for any discretisation.

$$J = \begin{vmatrix} \frac{d\xi}{dx} & \frac{d\xi}{dy} \\ \frac{d\eta}{dx} & \frac{d\eta}{dy} \end{vmatrix} \quad (\text{B.5})$$

A simple example violating this condition is the mapping of rectangle $0 \leq x \leq 1, -1 \leq y \leq 1$ onto a square $0 \leq \xi \leq 1, 0 \leq \eta \leq 1$, with the transformation

$$\xi = x, \quad \eta = y^2$$

The Jacobian $J_{y=0} = 0$ produces a fold along the x-axis in this formulation.

Once a mapping of boundary curves in physical region onto coordinate curves in the computational region are available, simple interpolation functions can be utilised to get the interior grid points which can then be inverse mapped into the physical region to get the computational grid. A basic Lagrange polynomial and Hermite polynomial is presented here. Interpolation can be unidirectional or multidirectional.

Unidirectional interpolation

Unidirectional interpolation is essentially a curve fitting operation.

B.3 Lagrange basis polynomial interpolation

Consider a finite number of $(n + 1)$ points available as Cartesian coordinates

$$(x_0, y_0), (x_1, y_1), (x_2, y_2), \dots, (x_n, y_n)$$

The set of data can be represented in terms of function as $y = f(x)$ in order to perform interpolation or other operations. Lagrange basis polynomial gives a unique polynomial of degree n that passes through the given points.

$$L_i(x) = \frac{(x - x_0)(x - x_1) \dots (x - x_{i-1})(x - x_{i+1})(x - x_n)}{(x_i - x_0)(x_i - x_1) \dots (x_i - x_{i-1})(x_i - x_{i+1})(x_i - x_n)} \quad (B.6)$$

$$i = 0, 1, 2, \dots, n$$

These functions may be written in compact form as,

$$L_i(x) = \prod_{\substack{j=0 \\ j \neq i}}^n \frac{(x - x_j)}{(x_i - x_j)}$$

These polynomial have the property that $L_i(x_j) = 0$ for $j \neq i$ and $L_i(x_i) = 1$. The polynomial of degree n which passes through the given points is then

$$p(x) = \sum_{i=0}^n y_i L_i(x) \quad (B.7)$$

Lagrange interpolation polynomials match the function values provided at given $(n + 1)$ data points.

B.4 Hermite interpolation polynomial

It is possible to match function values as well as first derivative values at given data points by using Hermite interpolation polynomials. Consider $n + 1$ points available as Cartesian coordinates along with the $n + 1$ corresponding values of derivatives of y with respect to x at these points.

$$(x_0, y_0), (x_1, y_1), (x_2, y_2), \dots, (x_n, y_n) \text{ and } y'_0, y'_1, y'_2, \dots, y'_n,$$

The required polynomial of degree $2n + 1$ can be represented as

$$p(x) = \sum_{i=0}^n y_i H_i(x) + \sum_{i=0}^n y'_i \tilde{H}_i(x) \quad (B.8)$$

Where $H_i(x)$ and $\tilde{H}_i(x)$ are polynomials of degree $2n + 1$ satisfying,

$$H_i(x_j) = \delta_{ij}, \quad H'_i(x_j) = 0, \quad \tilde{H}_i(x_j) = 0, \quad \tilde{H}'_i(x_j) = \delta_{ij}, \quad (B.9)$$

The most commonly used form of Hermite interpolation makes use of the cubic Hermite polynomials for which $n = 1$.

$$\begin{aligned} H_0(x) &= 2x^3 - 3x^2 + 1, \\ H_1(x) &= 3x^2 - 2x^3, \\ \tilde{H}_0(x) &= x^3 - 2x^2 + x, \\ \tilde{H}_1(x) &= x^3 - x^2, \end{aligned} \tag{B.10}$$

Multidirectional Interpolation and TFI

Consider a transformation

$$x = x(\xi, \eta), \quad y = y(\xi, \eta) \tag{B.11}$$

which maps a unit square $0 \leq \xi \leq 1, 0 \leq \eta \leq 1$, onto the interior of the region ABDC in x-y plane as shown in Figure B.2.

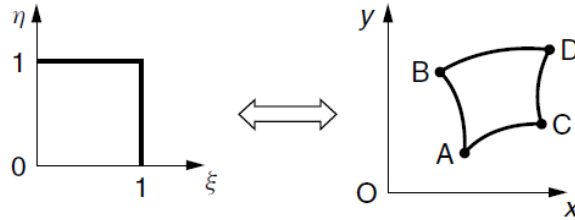


Figure B.2 Mapping of a unit square onto a curved four sided region

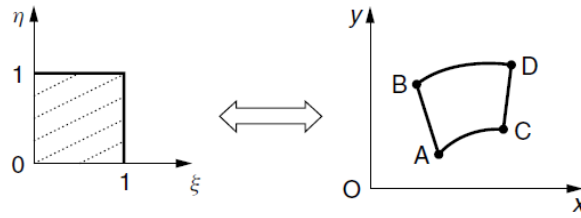
The edges $\xi = 0, 1$ maps to boundaries AB, CD respectively which can be formulated as position vectors $\mathbf{r}(0, \eta)$ and $\mathbf{r}(1, \eta)$. Similarly boundaries AC, BD can be formulated as position vectors $\mathbf{r}(\xi, 0)$ and $\mathbf{r}(\xi, 1)$.

A projector \mathbf{P}_η is a new transformation that maps points in computational space to points (position vectors) in the physical space considering linear Lagrange basis functions.

$$\mathbf{P}_\eta(\xi, \eta) = (1 - \eta) \mathbf{r}(\xi, 0) + (\eta) \mathbf{r}(\xi, 1) \tag{B.12}$$

This transformation maps the unit square in the plane (ξ, η) onto the region ABDC in which the boundaries AB, DC are replaced by straight lines as shown in Figure B.3. Furthermore

coordinates of constant η are mapped into straight lines rather than coordinate curves in the physical region.



Reproduced from: *Farrashkhalvat and Miles (2003)*

Figure B.3 Mapping of a unit square by projector \mathbf{P}_η

Similarly projector \mathbf{P}_ξ can be defined that maps the unit square onto a region which preserves the boundaries AB, CD but replaces the boundaries AC, BD with straight lines.

$$\mathbf{P}_\xi(\xi, \eta) = (1 - \xi) \mathbf{r}(0, \eta) + (\xi) \mathbf{r}(1, \eta) \quad (\text{B.13})$$

A composite mapping of \mathbf{P}_ξ and \mathbf{P}_η can be defined such that,

$$\begin{aligned} \mathbf{P}_\xi(\mathbf{P}_\eta(\xi, \eta)) &= \mathbf{P}_\xi[(1 - \eta) \mathbf{r}(\xi, 0) + (\eta) \mathbf{r}(\xi, 1)] \\ &= (1 - \xi) [(1 - \eta) \mathbf{r}(\xi, 0) + (\eta) \mathbf{r}(\xi, 1)] \\ &\quad + (\xi) [(1 - \eta) \mathbf{r}(\xi, 0) + (\eta) \mathbf{r}(\xi, 1)] \quad (\text{B.14}) \\ &= (1 - \xi)(1 - \eta) \mathbf{r}(0, 0) + (1 - \xi)(\eta) \mathbf{r}(0, 1) \\ &\quad + (\xi)(1 - \eta) \mathbf{r}(1, 0) + (\xi)(\eta) \mathbf{r}(1, 1) \end{aligned}$$

This bilinear transformation has the property that the four vertices A, B, C and D are preserved, but the boundaries are all replaced by straight lines. i.e. the unit square is mapped onto a quadrilateral ABDC.

Another composite mapping $\mathbf{P}_\xi(\mathbf{P}_\xi(\xi, \eta))$ gives $\mathbf{P}_\xi \mathbf{P}_\xi = \mathbf{P}_\xi$.

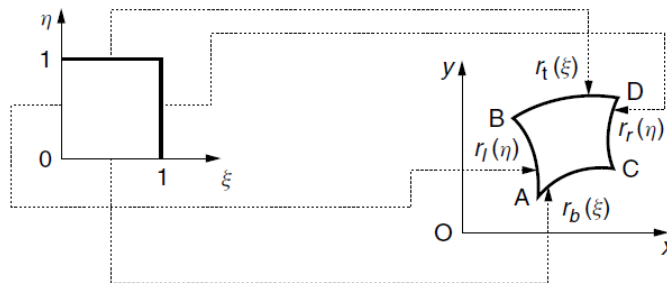
But the composite mapping $\mathbf{P}_\xi + \mathbf{P}_\eta - \mathbf{P}_\xi \mathbf{P}_\eta$ is a transformation which maps the entire boundary of the unit square onto the entire curved boundary ABDC. This map is called the Boolean Sum of the transformation \mathbf{P}_ξ and \mathbf{P}_η and is denoted by $\mathbf{P}_\xi \oplus \mathbf{P}_\eta$. The mapping has been represented in Figure B.4.

$$\mathbf{P}_\xi \oplus \mathbf{P}_\eta = \mathbf{P}_\xi + \mathbf{P}_\eta - \mathbf{P}_\xi \mathbf{P}_\eta \quad (\text{B.15})$$

$$\begin{aligned}
(\mathbf{P}_\xi \oplus \mathbf{P}_\eta)(\xi, \eta) &= \mathbf{P}_\xi(\xi, \eta) + \mathbf{P}_\eta(\xi, \eta) - \mathbf{P}_\xi \mathbf{P}_\eta(\xi, \eta) \\
&= (1 - \xi) \mathbf{r}(0, \eta) + (\xi) \mathbf{r}(1, \eta) \\
&\quad + (1 - \eta) \mathbf{r}(\xi, 0) + (\eta) \mathbf{r}(\xi, 1) \\
&\quad - (1 - \xi)(1 - \eta) \mathbf{r}(0, 0) - (1 - \xi)(\eta) \mathbf{r}(0, 1) \\
&\quad - (\xi)(1 - \eta) \mathbf{r}(1, 0) - (\xi)(\eta) \mathbf{r}(1, 1)
\end{aligned}$$

This transformation is the basis of Transfinite Interpolation in two dimensions. A grid will be generated by taking discrete values of ξ and η with

$$\begin{aligned}
0 \leq \xi_i &= \frac{i-1}{\tilde{\iota}-1} \leq 1, \quad i = 1, 2, 3, \dots, \tilde{\iota} \\
0 \leq \eta_j &= \frac{j-1}{\tilde{j}-1} \leq 1, \quad j = 1, 2, 3, \dots, \tilde{j}
\end{aligned} \tag{B.16}$$



Reproduced from: *Farrashkhalvat and Miles (2003)*

Figure B.4 TFI mapping of a unit square by composite projector $\mathbf{P}_\xi \oplus \mathbf{P}_\eta$

TFI is the most commonly used approach in algebraic grid generation. *Kovačević* (2002) has successfully used TFI with boundary adaptation for screw machine grid generation in the rotor domain as well as for theoretical suction and discharge ports.

B.5 Differential grid generation

In structured grid generation, techniques based on solutions of Partial Differential Equations to define coordinate transformation are widely used. The idea of using elliptic PDE like Laplace equation or Poisson equation is based on the work of *Crowley* (1962) and *Winslow* (1964, 1966). *Thompson* (1985), *Thompson et al.* (1974, 1999) have worked extensively on using elliptic PDE's to generate block structured grids. Elliptic PDE's have certain beneficial properties in their solution that make them preferable for body fitted curvilinear grids:

Extremum principle – It is possible to formulate PDE's such that the extrema of their analytical solutions cannot be within the domain. Hence there are fewer tendencies for folding of mesh lines i.e. a monotonic solution.

Inherent smoothness – The resulting coordinate curves in the interior are smooth and some discontinuities over the boundaries do not get propagated into the interior of the domains.

Boundary – The coordinate points on physical boundaries can be exactly specified as boundary conditions in the computational space.

But the numerical solution of such systems is computationally expensive and generally an initial grid based on algebraic methods needs to be prescribed in order to get the required derivatives for solution of PDE's.

Liseikin (1999) has shown that with a Laplacian system, the generated grid lines are attracted towards the concave part of the boundaries and repelled near the convex part of the boundaries.

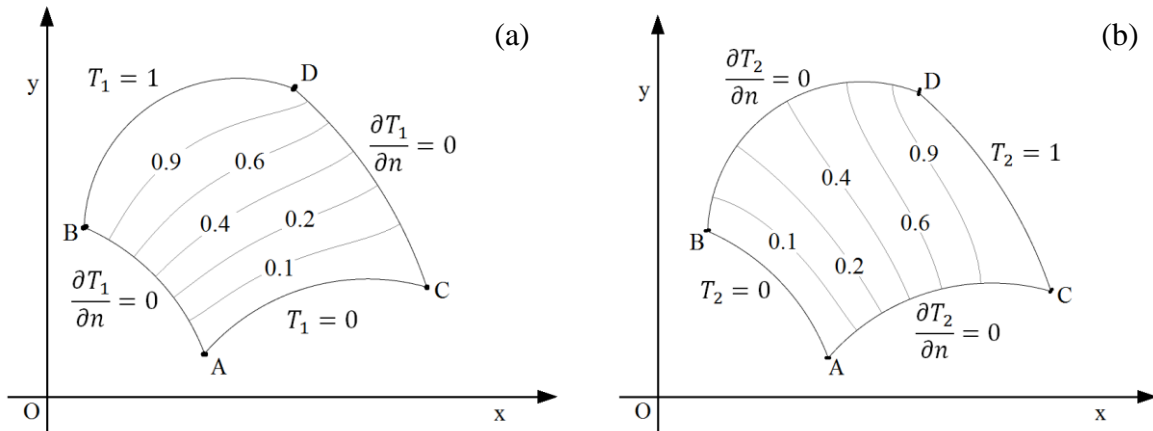


Figure B.5 Differential construction of a 2D curvilinear grid

Hence the Poisson system provides a better control on the properties of the grid compared to Laplace system via the stretching functions (*Godunov and Prokopov*, 1972). *Steger and Sorenson* (1979) developed an extension to the Poisson system to achieve grid clustering at the boundary by specifying first spacing and forcing grid lines to be nearly orthogonal at the boundaries. Their formulation was implemented in the code GRAPE (1980) for aerofoil class of problems. *Thomas and Middlecoff* (1980) have developed a method that provides approximate control of the point spacing by evaluating stretching functions according the desired point distribution on the boundaries. Many developments in differential methods have

been presented in the work by *Eiseman* (1982), *Sharp and Anderson* (1991), *Arina* (1986) and *Thompson* (1996).

Consider a 2D domain as shown in Figure B.5.

The region is bounded by four curves AB, BD, CD and AC. If we consider a heat conduction equation in the domain with two sets of boundary conditions as in Figure B.5 a and b.

For domain (a)

$$\frac{\partial^2 T_1}{\partial x^2} + \frac{\partial^2 T_1}{\partial y^2} = \frac{q''_1}{k},$$

$$T_1 = 0, \text{ at } AC \text{ and } T_1 = 1, \text{ at } BD \quad (\text{B.17})$$

$$\frac{\partial T_1}{\partial n} = 0, \quad AB \text{ and } CD$$

where n is the Normal to the boundary

Similarly for domain (b)

$$\frac{\partial^2 T_2}{\partial x^2} + \frac{\partial^2 T_2}{\partial y^2} = \frac{q''_2}{k},$$

$$T_2 = 0, \text{ at } AB \text{ and } T_2 = 1, \text{ at } CD \quad (\text{B.18})$$

$$\frac{\partial T_2}{\partial n} = 0, \quad AC \text{ and } BD$$

The solution to systems (a) and (b) can be written as

$$T_1 = T_1(x, y), \quad T_2 = T_2(x, y) \quad (\text{B.19})$$

Each isotherm T_1 and T_2 thus represents a set of (x, y) and the two solutions get superimposed as a body-fitted curvilinear grid in the domain.

Equation (B.17) and (B.18) can be re-written by interchanging roles of T and (x, y) , thus

$$\begin{aligned} \nabla^2 \xi &= \frac{\partial^2 \xi}{\partial x^2} + \frac{\partial^2 \xi}{\partial y^2} = P(\xi, \eta), \\ \nabla^2 \eta &= \frac{\partial^2 \eta}{\partial x^2} + \frac{\partial^2 \eta}{\partial y^2} = Q(\xi, \eta), \end{aligned} \quad (\text{B.20})$$

Where are (ξ, η) curvilinear coordinates and $P(\xi, \eta)$ and $Q(\xi, \eta)$ are stretching functions and the system is a basic Poisson system of PDE. In order to determine Cartesian coordinates from equation (B.20) they must be inverted. The inverted equation in 2D reads as (*Date*, 2005):

$$\nabla^2 \phi = \frac{1}{J^2} \left[\alpha \frac{\partial^2 \phi}{\partial \xi^2} - 2\beta \frac{\partial^2 \phi}{\partial \xi \partial \eta} + \gamma \frac{\partial^2 \phi}{\partial \eta^2} \right] + P \frac{\partial \phi}{\partial \xi} + Q \frac{\partial \phi}{\partial \eta} \quad (\text{B.21})$$

Replacing ϕ by x and y and $\nabla^2 x = \nabla^2 y = 0$,

$$\alpha \frac{\partial^2 x}{\partial \xi^2} - 2\beta \frac{\partial^2 x}{\partial \xi \partial \eta} + \gamma \frac{\partial^2 x}{\partial \eta^2} = -J^2 \left[P \frac{\partial x}{\partial \xi} + Q \frac{\partial x}{\partial \eta} \right] \quad (\text{B.22})$$

$$\alpha \frac{\partial^2 y}{\partial \xi^2} - 2\beta \frac{\partial^2 y}{\partial \xi \partial \eta} + \gamma \frac{\partial^2 y}{\partial \eta^2} = -J^2 \left[P \frac{\partial y}{\partial \xi} + Q \frac{\partial y}{\partial \eta} \right] \quad (\text{B.23})$$

Where,

$$J = \frac{\partial x}{\partial \xi} \frac{\partial y}{\partial \eta} - \frac{\partial y}{\partial \xi} \frac{\partial x}{\partial \eta}$$

$$\alpha = \left[\left(\frac{\partial x}{\partial \eta} \right)^2 + \left(\frac{\partial y}{\partial \eta} \right)^2 \right]$$

$$\beta = \left[\frac{\partial x}{\partial \xi} \frac{\partial x}{\partial \eta} + \frac{\partial y}{\partial \xi} \frac{\partial y}{\partial \eta} \right]$$

$$\gamma = \left[\left(\frac{\partial x}{\partial \xi} \right)^2 + \left(\frac{\partial y}{\partial \xi} \right)^2 \right]$$

Equation (B.22) and (B.23) are coupled and nonlinear because of α, β and γ . They are solved simultaneously using schemes like Tri-diagonal Matrix Algorithm. The boundary conditions as grid coordinates are specified at $\xi = 0, \xi = \xi_{max}$ and $\eta = 0, \eta = \eta_{max}$. One of the difficulties with elliptic PDE's is that at the boundary either Dirichlet or Neumann boundary conditions are required.

Thompson, Thames and Mastin (1974) have proposed the following stretching function in order to control grid clustering.

$$P(\xi, \eta) = - \sum_{n=1}^N a_n \frac{(\xi - \xi_n)}{|\xi - \xi_n|} e^{-c_n |\xi - \xi_n|} - \sum_{i=1}^I b_i \frac{(\xi - \xi_i)}{|\xi - \xi_i|} e^{-d_i [(\xi - \xi_i)^2 + (\eta - \eta_i)^2]^{1/2}} \quad (\text{B.24})$$

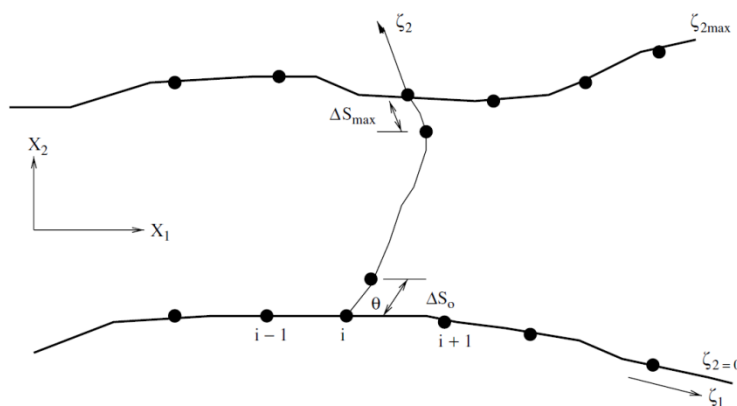
$$Q(\xi, \eta) = - \sum_{n=1}^N a_n \frac{(\eta - \eta_n)}{|\eta - \eta_n|} e^{-c_n |\eta - \eta_n|} - \sum_{i=1}^I b_i \frac{(\eta - \eta_i)}{|\eta - \eta_i|} e^{-d_i [(\xi - \xi_i)^2 + (\eta - \eta_i)^2]^{1/2}} \quad (\text{B.25})$$

Here N is the number of clustering grid lines (coordinate lines $\xi = \xi_n$ and $\eta = \eta_n$) and I is the number of clustering points (with $\xi = \xi_i$, $\eta = \eta_i$, $0 \leq \xi_i, \eta_i \leq 1$) to which the grid is to be attracted. a_n , c_n , b_i and d_i are positive control parameters. The first term in $P(\xi, \eta)$ has the effect with amplitude a_n of attracting ξ -lines towards curves $\xi = \xi_n$ in the physical domain, while the second term attracts ξ -lines with amplitude b_i towards points. Similarly the two terms in $Q(\xi, \eta)$ control the grid line spacing. In each case the attractive effect decays with the distance in the computational space from the lines or points according to the decay parameters c_n and d_i .

The functions $\frac{(\xi - \xi_n)}{|\xi - \xi_n|}$ and $\frac{(\eta - \eta_n)}{|\eta - \eta_n|}$ are function which can take only the value ± 1 and ensure the clustering to take place on both sides of ξ_n -lines and η_n -lines. The amplitude can be set negative to turn attractive effects into repulsive ones.

Sorenson and Steger (1977, 1983), Sorenson (1980) have presented methods for the control of orthogonality at boundaries and the spacing of the first mesh interval of the interior. These procedures use an iterative scheme starting with an approximate grid obtained by algebraic method. Orthogonality or specified angle is strictly enforced only at the boundaries whereas in the interior it is relaxed.

Let ΔS_0 and ΔS_{max} be specified as the first grid spacing at η and η_{max} coordinate lines respectively. Let θ_0 and θ_{max} be specified as the angles of intersection between ξ and η grid lines at $\eta = 0$ and $\eta = \eta_{max}$ respectively. The arrangement is shown in Figure B.6.



Reproduced from: Date (2005)

Figure B.6 Specification of first mesh interval and angle in Sorenson's method

The stretching functions in equations (B.22) and (B.23) are given as

$$P(\xi, \eta) = P(\xi, 0) e^{-a\eta} + P(\xi, \eta_{max}) e^{-c(\eta_{max}-\eta)} \quad (\text{B.26})$$

$$Q(\xi, \eta) = Q(\xi, 0) e^{-b\eta} + Q(\xi, \eta_{max}) e^{-d(\eta_{max}-\eta)} \quad (\text{B.27})$$

a, b, c and d are positive constants that act as damping factors and their values along with S_0, S_{max}, θ_0 and θ_{max} at the boundary nodes are to be provided as inputs for the algorithm.

B.6 Variational grid generation

Variational methods utilize the idea of optimisation of grid characteristics through functions such as grid smoothness, orthogonality factor, cell skewness and cell volume. A function representing a combination of desired grid features is minimised on an initial grid that produces a final grid with balanced grid quality measures selected in the function.

Brackbill and Saltzman (1980, 1982) have developed a technique for constructing an adaptive grid using a variational approach. They have used the properties of grid smoothness, orthogonality and cell volume as the functionals of the minimisation problem.

Smoothness of the transformation can be represented by the integral:

$$I_s = \int_D [(\nabla \xi)^2 + (\nabla \eta)^2] dv \quad (\text{B.28})$$

Orthogonality can be represented by the integral:

$$I_o = \int_D [(\nabla \xi \cdot \nabla \eta)^2 / J^3] dv \quad (\text{B.29})$$

Cell volume measure can be represented by the integral:

$$I_v = \int_D [w J] dv \quad (\text{B.30})$$

The linear combination with coefficient multipliers represents the Euler-Lagrange equations

$$I_t = I_s + I_o + I_v \quad (\text{B.31})$$

If only smoothness is considered,

$$I_s = \iint \left(\frac{x_\xi^2 + x_\eta^2 + y_\xi^2 + y_\eta^2}{J} \right) d\xi d\eta \quad (\text{B.32})$$

The Euler-Lagrange equations corresponding to I_s are of the form:

$$\begin{aligned} \left(\frac{\partial}{\partial x} - \frac{\partial}{\partial \xi} \frac{\partial}{\partial x_\xi} - \frac{\partial}{\partial \eta} \frac{\partial}{\partial x_\eta} \right) \left(\frac{x_\xi^2 + x_\eta^2 + y_\xi^2 + y_\eta^2}{J} \right) &= 0 \\ \left(\frac{\partial}{\partial y} - \frac{\partial}{\partial \xi} \frac{\partial}{\partial y_\xi} - \frac{\partial}{\partial \eta} \frac{\partial}{\partial y_\eta} \right) \left(\frac{x_\xi^2 + x_\eta^2 + y_\xi^2 + y_\eta^2}{J} \right) &= 0 \end{aligned} \quad (\text{B.33})$$

On differentiation these expression yield in the form:

$$\begin{aligned} \alpha \frac{\partial^2 x}{\partial \xi^2} - 2 \beta \frac{\partial^2 x}{\partial \xi \partial \eta} + \gamma \frac{\partial^2 x}{\partial \eta^2} &= 0 \\ \alpha \frac{\partial^2 y}{\partial \xi^2} - 2 \beta \frac{\partial^2 y}{\partial \xi \partial \eta} + \gamma \frac{\partial^2 y}{\partial \eta^2} &= 0 \end{aligned} \quad (\text{B.34})$$

These are equivalent to the Winslow equations of the Laplacian system presented for the differential method of grid generation (equations (B.22) and (B.23)). With inclusion of I_o and I_v the Euler-Lagrange equations are more complicated. Recently a collection of techniques for grid generation using variational methods has been published in *Ushakova et al.* (2007).

Appendix C. Characteristic domain decomposition

A twin screw machine's working chamber is the domain consisting of low pressure port, compression or expansion chamber and high pressure port. The gas flow from suction through compression to discharge happens as a cyclic process and there is no physical isolation because multiple cycles are in progress at a given time. When this is compared to reciprocating machines, here the suction and discharge ports are isolated from the main compression chamber by means of valves. The leakage in reciprocating compressors can occur across the valve seats and through the piston rings. On the other hand in screw compressors the leakage happens from one compression cycle to the adjacent and also from discharge to the suction through the interlobe sealing gap. Because of this nature of operation the suction, compression, leakage and discharge, all have to be accounted in the flow domain without isolation.

Some CFD studies have used 2D representation of these domains in order to simplify the analysis. *Vimmr* (2005) has presented a study on compressible leakage flow through the gap between rotor and casing in a 2D domain. It is necessary to represent the full 3D features of the machine geometry. The suction and discharge ports can be discretised using tetrahedral grid and most commercially available grid generators have good tools for these geometries. However for the rotor domain it is necessary to carefully design the deforming grid. A choice of hexahedral structure allows for ease of database and at the same time ALE formulations in the solver can be utilised that only demand for accurate node positions with time in order to capture grid deformation and its influence on the flow solution. The main difficulty in producing hexahedral grids for the rotor domain is that the geometry of the rotor profile with the casing forms a combination of large main flow regions and very narrow leakage gaps. The twist on the helical rotor in third dimension further makes grid generation difficult and has been the main reason for non-availability of any commercial grid generator for these applications.

Decomposition of the working chamber consists of splitting the flow region into three main blocks as shown in Figure C.1. This gives the flexibility to treat mesh generation in these block independently and also on the choice of the grid generation methods.

- Suction Port, a domain with static grid,
- Rotor + Leakage, a domain with highly deforming grids and
- Discharge Port, a domain with static grid.

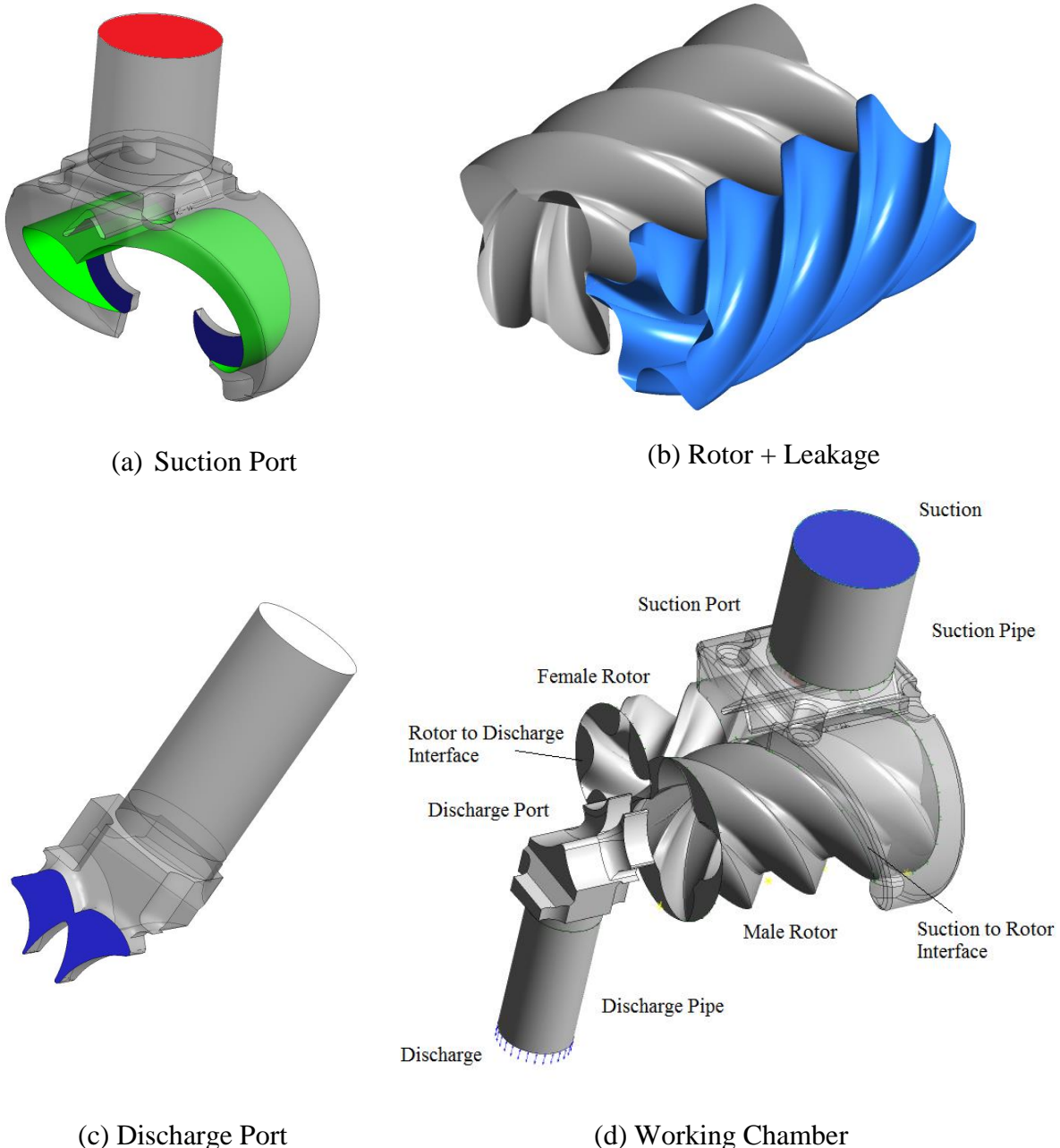


Figure C.1 Characteristic decomposition of a screw compressor

The two rotors together with the casing do not map one to one onto any of the primitive computational domains like rectangular, H, C or O blocks. This demands that special mechanisms need to be used to further decompose the rotor domain so that multi-blocking methods for structured grid generation become applicable. On rotors with parallel axis there is a typical approach used to slice the rotor into number of 2D cross sections and then each section is treated with two O blocks that interface with each other between the two rotors. Each 2D cross section has a different rotor profile position at an instant due to helical rotors but they are related to each other by lead of the rotors. The two O blocks together form a composite grid.

The composite grid can be further completely discontinuous, partially discontinuous, partially continuous or completely continuous. From completely discontinuous to completely continuous, the difficulty goes on increasing and the flexibility goes on decreasing due to more constraints at the interface.

In practise three methods have been utilised to decompose a cross section of the rotor into two O blocks:

- Analytical rack
- Numerical rack
- Differential division line

Below sections describe each of these methods and their application has been presented in Section 4.5 and Section 4.6.

C.1 Analytical rack

Certain families of screw compressor rotor profiles have an analytical definition on the generating rack. *Rinder* (1985) and *Stošić* (1997) ‘N’ profile are some examples of common rack generated profiles. *Kovačević et al.* (2002) were the first to use an analytical rack for decomposition of the rotor cross section. The envelope theory of gearing is used as the basis of rotor generation as both the main and the gate rotor as well as the cutting tool or rack have to be conjugate pairs of each other during meshing and relative motion. The governing theory has been presented in details by *Litvin* (1956) for symmetric circular profiles and later by *Stošić* (1998) for asymmetric profiles. With reference to the meshing condition shown in Figure C.2; if primary curves of definition are given on the rack, their coordinates x_{0r} and y_{0r} as well as their first derivatives $\frac{\partial x_{0r}}{\partial t}$ and $\frac{\partial y_{0r}}{\partial t}$ or $\frac{\partial y_{0r}}{\partial x_{0r}}$ are known.

Using this information the rotor curves are generated from the envelope theory as:

$$\begin{aligned} x_{01} &= x_{0r} \cos\theta - (y_{0r} - r_{1w}) \sin\theta, \\ y_{01} &= x_{0r} \sin\theta - (y_{0r} - r_{1w}) \cos\theta \end{aligned} \quad (\text{C.1})$$

and the meshing condition is of the form:

$$\frac{dy_{0r}}{dx_{0r}} (r_{1w} \theta - y_{0r}) - (r_{1w} - x_{0r}) = 0 \quad (\text{C.2})$$

The solution of the coordinates as a function of θ can be obtained directly from equations (C.1) and (C.2). In practise the above equations are used for known profile coordinates supplied as point data to determine the rack coordinates using inverse equation and this rack is then used to split the rotor cross section into two O blocks as shown in Figure C.3 for one of the rotor positions.

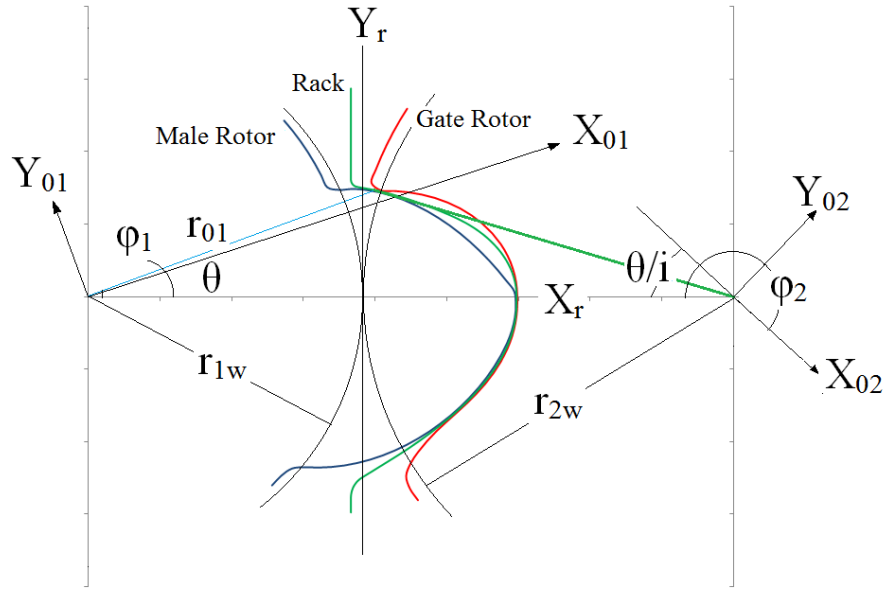


Figure C.2 Main rotor, Gate rotor and Rack curves in meshing condition

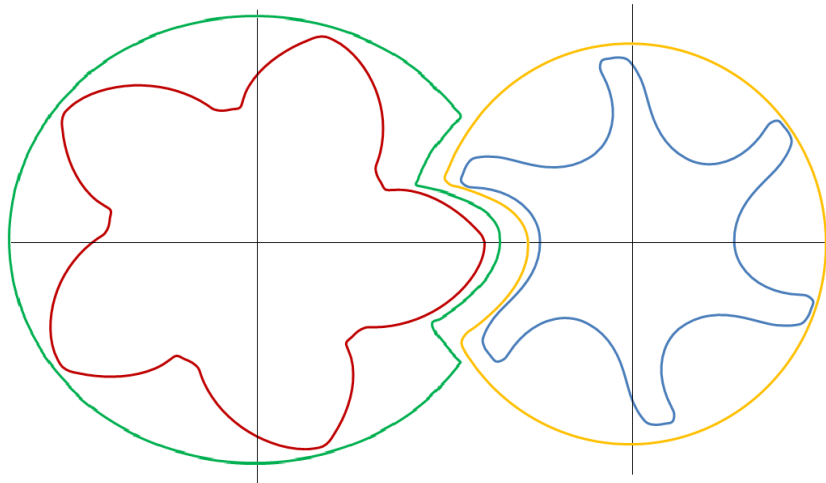


Figure C.3 Analytical rack as a splitting curve for O blocks

C.2 Numerical rack

Commonly CAD models of the rotor or CMM measurements on the manufactured rotor are available as input data for grid generation in the form of point coordinates. Also there are

families of curve which define the rotor profile like involutes, cycloids or a combination as in SRM ‘A’ profiles. In such cases the analytical rack definition may not exist due to singularities. But it is possible to find a conjugate set of points that can serve as the rack. Again from the envelope meshing condition, in special case of uniform lead and parallel rotor axis we have (Stošić, 1998),

$$(p_1 - p_2) \left(x_1 \frac{\partial x_1}{\partial t} + y_1 \frac{\partial y_1}{\partial t} \right) + p_1 C \frac{\partial x_1}{\partial t} = 0 \quad (\text{C.3})$$

$$\frac{dy}{dx} \left(k y_{01} - \frac{C}{i} \sin \theta \right) + k x_{01} + \frac{C}{i} \cos \theta = 0$$

Where, $i = p_2/p_1$ and $k = (1 - \frac{1}{i})$.

For given coordinate of the main rotor (x_{01}, y_{01}) the coordinates of meshing profile can be solved numerically.

$$x_{02} = x_{01} \cos k\theta - y_{01} \sin k\theta - C \cos \frac{\theta}{i} \quad (\text{C.4})$$

$$y_{02} = x_{01} \sin k\theta + y_{01} \cos k\theta + C \sin \frac{\theta}{i}$$

In case of rack, the gear ratio i tends to infinity. Therefore,

$$x_{0r} = x_{01} \cos \theta - y_{01} \sin \theta \quad (\text{C.5})$$

$$y_{0r} = x_{01} \sin \theta + y_{01} \cos \theta - r_1 \theta$$

Equations (C.4) and (C.5) can be used to get the rack coordinates for domain decomposition. The rack generation procedure from specified rotor profile as primary curve is discussed in details by Stošić (1998, 2005).

In some situations where rotor profile has very small fillets or singularities, the equations (C.4) and (C.5) fail to converge. To overcome this, Kovačević (2002) applied an alternative numerical approach also described in literature as Direct Digital Simulation (DDS). DDS has originally been used for CAD modelling of complex gears and their cutting tools in Goldfrab and Voznyuk (1998), Goldfrab, Lunin and Trubachev (2004). Consecutive Boolean operations are used to simulate the rotor cutting process from solid blocks and the cutting tool itself produces the rotor profile. Conversely, given rotor profile can be treated as the cutting tool and the result can be the rack splitting line which falls in between the two rotors as shown in Figure C.4.

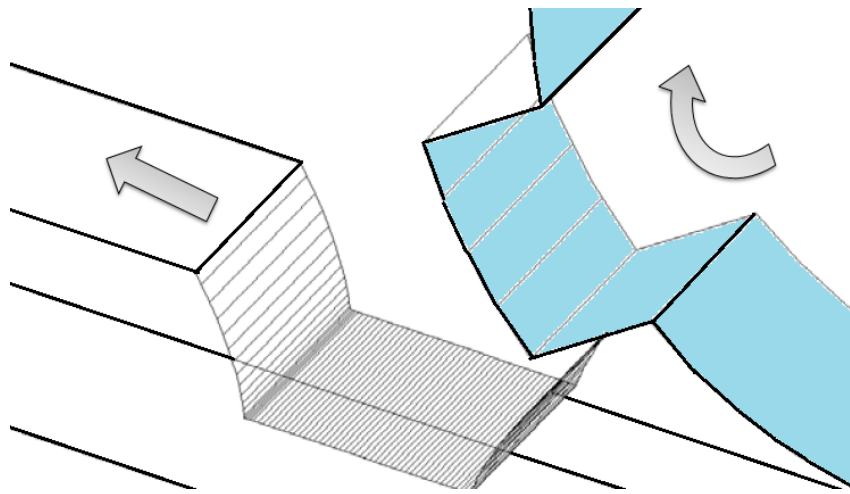


Figure C.4 Rack cut from rotor profile using DDS

The method has been found to be robust for profiles ranging from Asymmetric screw rotors to involutes on Root's blowers and is the principle technique for successful implementation of algebraic grid generation for twin screw machines in the program SCORG (*Kovačević et al., 2002*)

C.3 Differential division line

In 2004, *Vande Voorde, Vierendeels and Dick* presented a grid generation procedure for rotary volumetric pumps and compressors. In this method the rotor cross section was treated initially as a boundary value problem for an elliptic PDE with casing and the two rotors forming a closed domain. The solution to this PDE results in a family of iso-potential and gradient lines. By careful selection of an iso-potential line in between the two rotors it was made possible to split the rotor domain into two O blocks where further structured grid could be constructed. This method is the domain decomposition using differential equipotential curve.

Figure C.5 shows the splitting curve or division line obtained as an example for twin screw rotor profile. *Vande Voorde (2004)* demonstrated the application to double tooth compressor and twin screw compressors. Because of the differential principle the method is generic in nature and can be extended to a variety of domain decompositions.

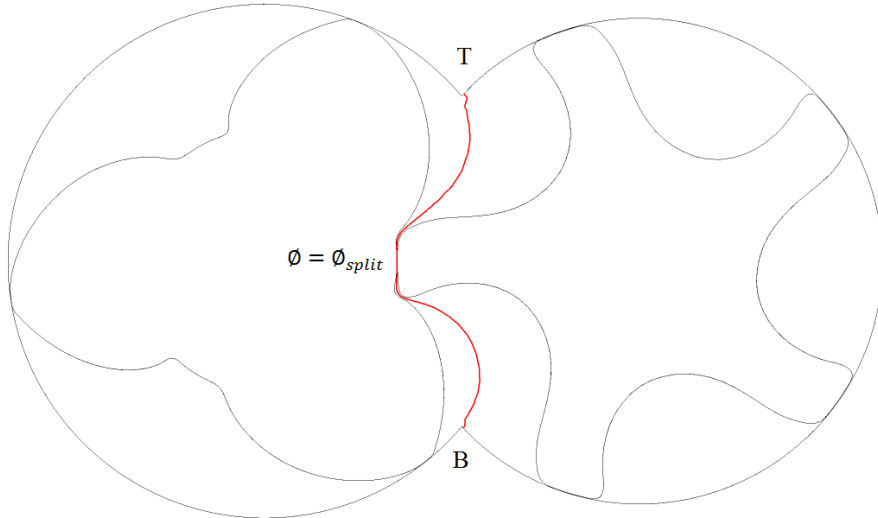


Figure C.5 Differential equipotential as a splitting curve for O blocks

The selected PDE was a Laplace equation $\nabla^2 \Phi = 0$ with no source terms. The solution obtained with fixed boundary conditions is not directly suitable for domain decomposition as the iso-potential lines do not always meet tangentially at the top and bottom CUSP's. For good decomposition it is necessary that the splitting curve meets at points T and B and is also as tangential as possible to one side of the casing to get good grid quality. This was achieved by variable boundary conditions on the casing and iteratively updating so that the splitting iso-potentials become tangential at the points T and B.

Differential decomposition has been successfully applied to a variety of twin rotor machines like lobe pumps, tooth compressors, hook and claw compressor and screw compressor. Out of all these the most difficult profile to achieve is the screw compressor due to the twist on the rotor in the axial direction. The method is generic in nature and can be applied to small fillet radii or singularities in input profiles. The limiting factor is however the time consumed in the initial grid required for iterative solution to the Laplace equation and the solution time itself. The initial grid needs to accurately capture the profile features and small clearances in the leakage gaps. Because of this the initial grid is an unstructured grid. *Vande Voerde et al.* (2004) have used a Delaunay triangulation algorithm (*Riemslagh et al.*, 1998) to achieve high refinements in the clearances. Some details of the procedure are provided in Section 4.6.

Appendix D. Algebraic approach for Grid Generation of Twin Screw Rotors

D.1 Coordinate transformation of interlobe rotor space

Each cross section is split into two O blocks using either the analytical or numerical decomposition technique as described in Appendix C. The next task is to map the physical region X^n to the computational region Ξ^n and to find a transformation function $x(\xi, \eta)$ as shown in Figure D.1.

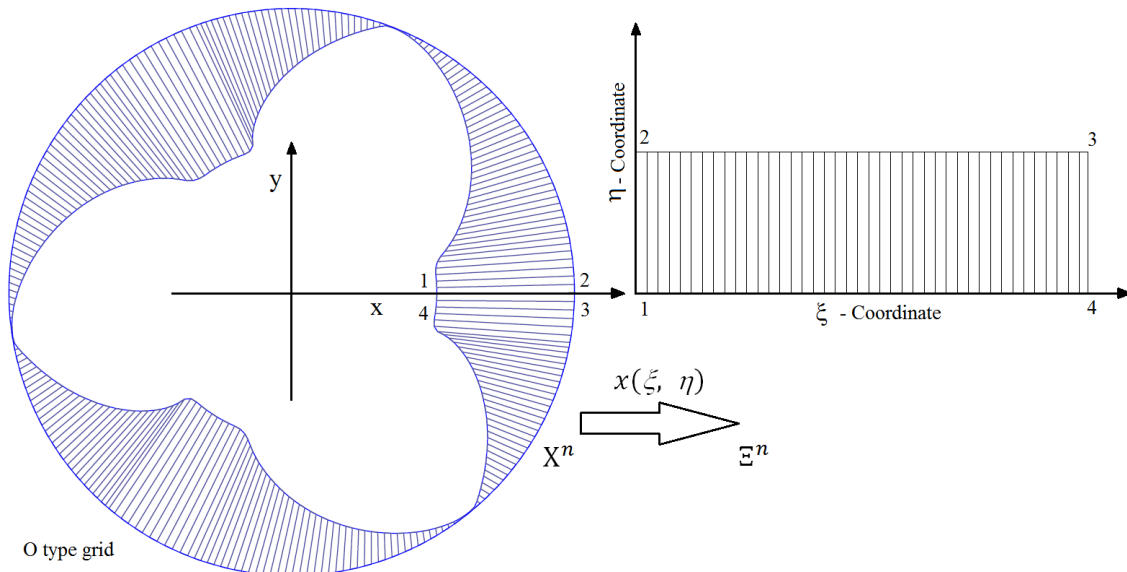


Figure D.1 Coordinate transformation from rotor region to computational region

It is also possible to further treat the rotor domain from tip to tip forming an interlobe space and then map this physical region X^n onto a rectangular computational domain Ξ^n as shown in Figure D.2.

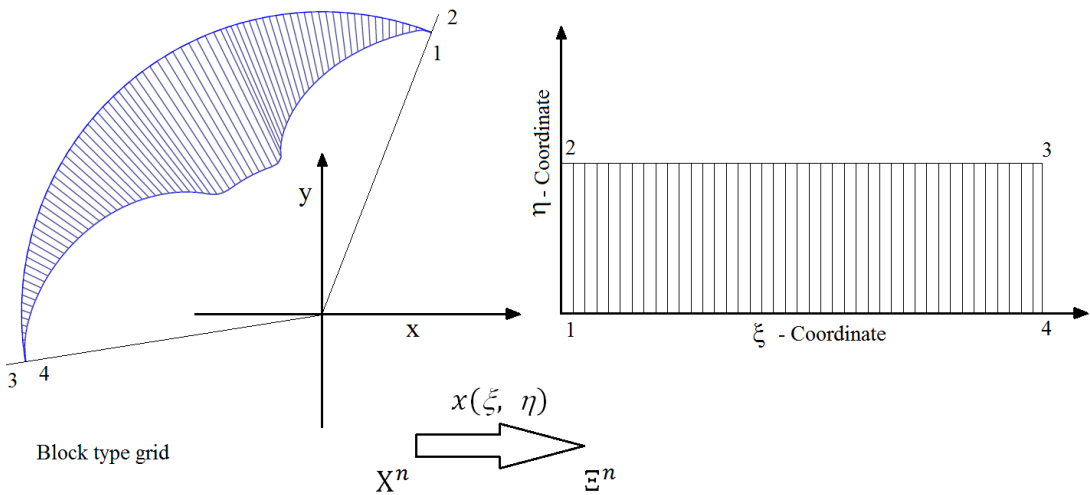


Figure D.2 Coordinate transformation from interlobe region to computational region

Inner boundary of the O grid is the rotor profile and the outer boundary is formed by connecting the casing circles with the rack curve. The interlobe clearances are accounted by offsetting the rack curve from the rotor profile. The radial clearance is accounted by adding the gap to the casing circle. Grid generation continues with the discretisation of the inner and outer boundaries, before they are mapped onto the computational domain. One of the simplest forms of this discretisation would be equidistant distribution of the inner and outer boundaries. The rotor profile curve length is much longer than the casing plus rack curve lengths and this creates crossing of distribution lines if equidistant distribution is applied. Moreover there are small radii present on the rotor profile which need higher resolution by placing more number of nodes. Hence an equidistant distribution on the rotor profile is not ideal in these conditions. *Kovačević* (2002 and 2005) has developed a unique two parameter unidirectional boundary adaptation procedure to be applied for screw rotor profiles that helps in achieving a regular distribution in the transformed space. These procedures have been briefly described below in two parts; Rotor boundary adaptation and Outer boundary regularisation and form key elements in the algebraic grid generation.

D.2 Rotor boundary adaptation

Originally grid adaptation techniques have been developed as static or dynamic methods to improve the solution accuracy without drastically increasing the grid density and placing refinement in preferential zones. The same principles have been used for the screw rotor profile

boundary adaptation so that the boundary distribution can be controlled from the clearance gaps to the core region without substantially increasing the number of nodes on the profile.

The idea of one dimensional equidistribution adaptation (*Lisiken*, 1999) is to place the grid nodes such that the error of the numerical solution is uniformly distributed through the calculation domain. In one dimension the grid spacing X_ξ is specified with a weighting function w selected such that their product is uniform

$$X_\xi w = \text{constant} \quad (\text{D.1})$$

The weight function represents some measure of solution error. As an example for solution the weight function is given by equation (D.2) (*Samareh*, 1987).

$$w = [\alpha + |Q_s|^{2n}]^{1/2n} \quad (\text{D.2})$$

Where,

$$n = \text{constant},$$

$$\alpha = \text{constant},$$

$$Q_s = \text{solution gradient w.r.t arc length } \left(\frac{\partial Q}{\partial s} \right)$$

If, $n = 1$ and $\alpha = 0$ we get, $w = |Q_s|$.

As X_ξ needs to be a monotone function, from equation (D.1), $|Q_s| = \text{constant}$.

This choice of w rearranges the grid points so that the change in solution is constant at consecutive grid intervals. Similarly the second derivative of the solution can also be accounted into w as equation (D.3).

$$w(s) = 1 + \alpha f(Q_s) + \beta g(Q_{ss}) \quad (\text{D.3})$$

Where,

$$\alpha \text{ and } \beta \text{ are positive parameters,}$$

$$f(Q_s) \text{ and } g(Q_{ss}) \text{ are arbitrary functions.}$$

Equation (D.1) integrated with respect to the physical coordinate X gives,

$$\xi(X) = \frac{\int_{X_{min}}^X w(x)dx}{\int_{X_{min}}^{X_{max}} w(x)dx} \quad (\text{D.4})$$

In terms of arc length s ,

$$\begin{aligned}\xi(s) &= \frac{\int_0^s w(s) ds}{\int_0^{S_{max}} w(s) ds} \\ &= \frac{\int_0^s \{1 + \alpha f(Q_s) + \beta g(Q_{ss})\} ds}{\int_0^{S_{max}} \{1 + \alpha f(Q_s) + \beta g(Q_{ss})\} ds}\end{aligned}\quad (\text{D.5})$$

If more than one solution variable needs to be accounted in the adaptation then the weight function can be defined as a summation of all the adaptation functions with respective weighting factors.

$$w(s) = 1 + \sum_{i=1}^I b^i f^i(s) \quad (\text{D.6})$$

Where,

I is the number of variables for adaptation,

b^i are constants,

f^i are adaptation functions,

and 1 is for uniformity.

Equation (D.3) can be written in multi variable form as equation (D.6).

$$\xi(s) = \frac{s + \sum_{i=1}^I b^i F^i(s)}{S_{max} + \sum_{i=1}^I b^i F^i(S_{max})} \quad (\text{D.7})$$

Where,

$$F^i(s) = \int_0^s f^i(s) ds$$

Parameters b^i and F^i have positive values to ensure monotonicity of $\xi(s)$.

In case of screw rotor profiles instead of solution variables, a geometrical property can be selected as the adaptation function. Some properties as specified by Kovačević (2002 and 2005) are listed in Table D.1.

Table D.1 Rotor profile adaptation functions

Adaptation Criteria	Function
The tangent angle on the rotor profile curve at the grid calculation point	$\alpha_p = \tan^{-1} \left(\frac{\partial x_p}{\partial y_p} \right)$
The radius of curvature in the vicinity of the grid calculation point	$r_p = \frac{(1 + y'_p)^{3/2}}{y''_p}$
The distance of the grid calculation point from rotor center	$d_p = \sqrt{x_p^2 + y_p^2}$
Sine distribution	$C_{sin} = \sin(\pi \frac{k_p}{k})$
Cosine distribution	$C_{cos} = \left \cos(\pi \frac{k_p}{k}) \right $

Figure D.3 shows the action of Sinus adaptation function on the gate rotor profile. The weighting of the function has been increased to increase the refinement in the tip leakage gaps.

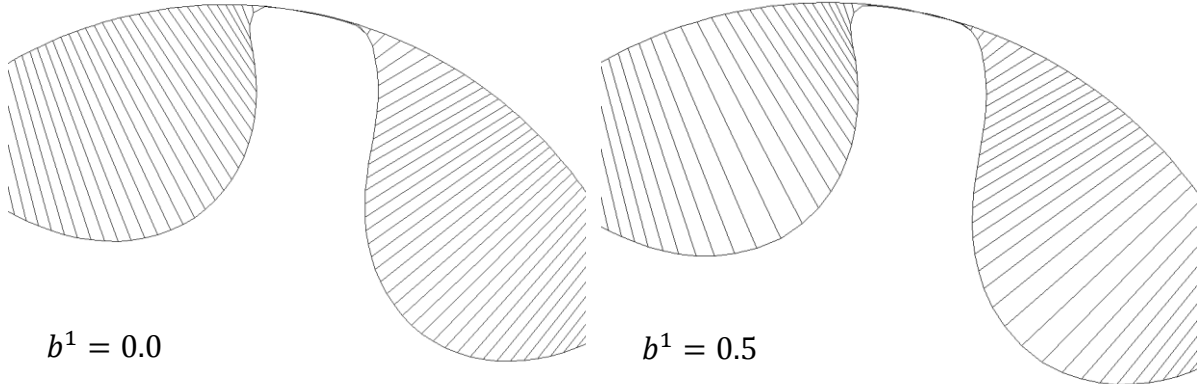


Figure D.3 Sinus adaptation function on the gate rotor profile

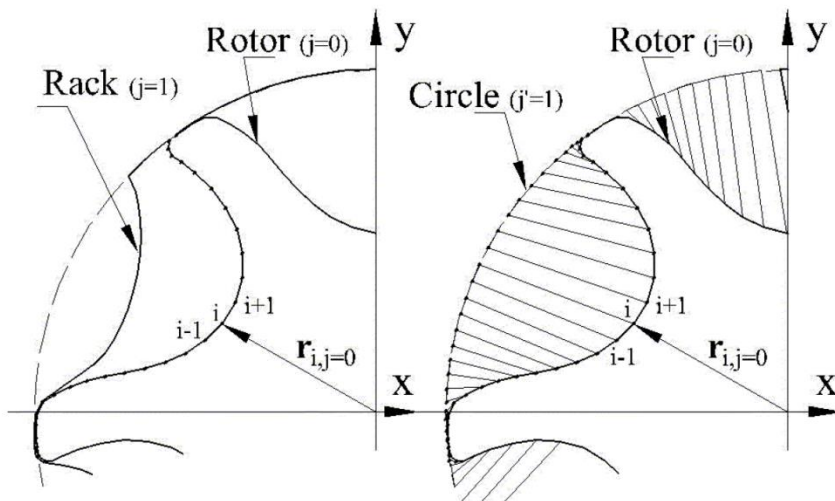
D.3 Outer boundary regularisation

The number of nodes distributed on the casing and the rack curves should be same as number of nodes on the rotor so that structured distribution is achieved between the two boundaries. The requirement of the outer boundary distribution is that it should produce regular cells for a given distribution on inner boundary. After the step of rotor profile adaptation, the nodes on

rotor profile are fixed. They essentially rotate as the rotor turns. But nodes on the casing circles and the rack curve are not fixed. They essentially slide on these curves taking a new position with every rotor turn such that the distribution is always regular.

If the arc length scale on inner boundary is used as a criterion for node distribution of the outer boundary then it is not assured that the cells created will be regular. This is because the aspect ratio between the clearance gap and the core rotor is too large. *Kovačević* (2002) has formulated a special procedure of regularisation of the outer boundary applicable for twin screw rotors.

Suppose that the points distributed on the boundaries are represented in index notation with respect to the physical coordinate system as $\mathbf{r}_{i,j}(x, y)$. Points on the inner boundary are $\mathbf{r}_{i,j=0}(x, y)$ and points on the outer boundary are $\mathbf{r}_{i,j=1}(x, y)$. Additionally if the outer boundary is considered as a full circle instead of a combination with the rack curve then the point distribution is $\mathbf{r}_{i,j'=1}(x, y)$ as shown in Figure D.4.



Reproduced from *Kovačević* (2002)

Figure D.4 Point distribution on inner boundary and outer circle

Based on arc length distribution on the rotor,

$$\mathbf{r}_{i,j'=1}(x, y) = \mathbf{r}_{I,j'=1} \frac{S_i}{S_I} \quad (\text{D.8})$$

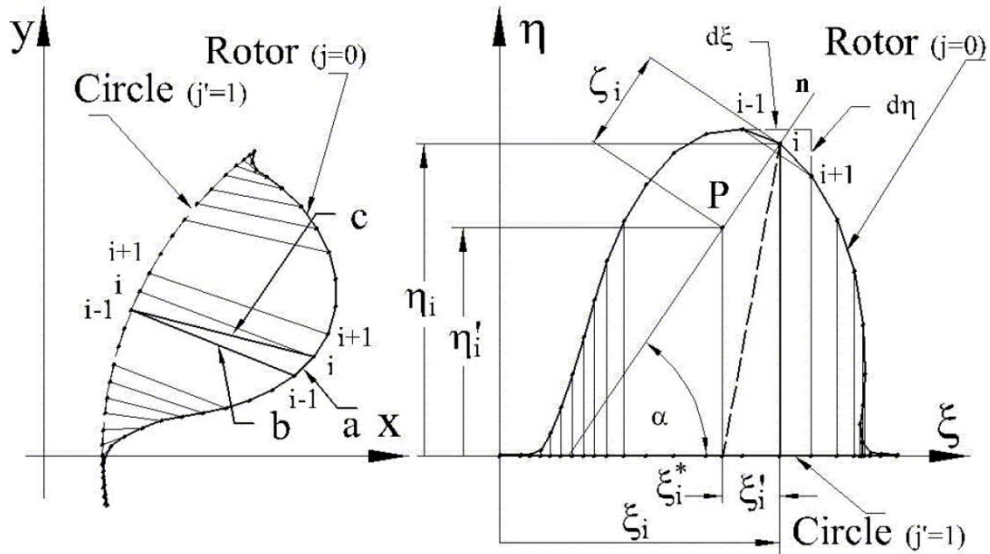
The procedure of outer boundary adaptation starts with a transformation from physical region X^2 onto a computational domain Ξ^2 in which the outer circular boundary becomes a straight line along the ξ coordinate. The transformation is represented by equation (D.9).

$$\xi_{i,j=0} = \xi_{i-1,j=0} + c \cos \alpha_{ac}$$

$$\xi_{i,j'=0} = \xi_{i,j=0} \quad (D.9)$$

$$\eta_{i,j=0} = \eta_{i-1,j=0} + c \cos \alpha_{ac}$$

$$\eta_{i,j'=0} = 0$$



Reproduced from Kovacević (2002)

Figure D.5 Transformation of interlobe region to computational domain

The Figure D.5a shows the physical region X^2 of one interlobe space and Figure D.5b shows the computational coordinate system (ξ, η) with the transformed coordinates of both, the rotor and the outer circle.

Consider point i in the physical domain. The lengths a, b and c are:

$$\begin{aligned} a &= \sqrt{(x_i - x_{i-1})_{j=0}^2 + (y_i - y_{i-1})_{j=0}^2}, \\ b &= \sqrt{(x_{i-1,j=0} - x_{i-1,j'=1})^2 + (y_{i-1,j=0} - y_{i-1,j'=1})^2}, \\ c &= \sqrt{(x_{i,j=0} - x_{i-1,j'=1})^2 + (y_{i,j=0} - y_{i-1,j'=1})^2} \end{aligned} \quad (D.10)$$

and the angle α_{ac} between a and c is determined by the cosine law

$$\cos \alpha_{ac} = \frac{a^2 + b^2 - c^2}{2 a b},$$

The outer circle is a straight line along ξ coordinate and the η coordinate is the distribution of the rotor profile points. On the outer circle the η coordinate is zero for all the points. Right and left boundaries are produced as vertical lines in the transformed space. The equations (D.11) and (D.12) are then used to regularise the cells in (ξ, η) by recalculating the ξ coordinates on the outer circle.

A control point \mathbf{P} is introduced into the system as shown in Figure D.5b. The point is located at a distance ζ_i on the normal at point i . The angle of this normal with ξ axis is

$$\tan \alpha = \frac{d\xi}{d\eta}, \quad \text{at } j = 0 \quad (\text{D.11})$$

Coordinates of point \mathbf{P} are (ξ_i^*, η_i') and ξ_i^* is the required new distribution on the outer circle.

$$\begin{aligned} \xi_i^* &= \xi_i - \xi'_i \\ \eta_i' &= \eta_i - \xi_i \cos \alpha \end{aligned} \quad (\text{D.12})$$

Where ξ'_i is the projection of ζ_i on ξ axis and (ξ_i, η_i) are the coordinates of point i .

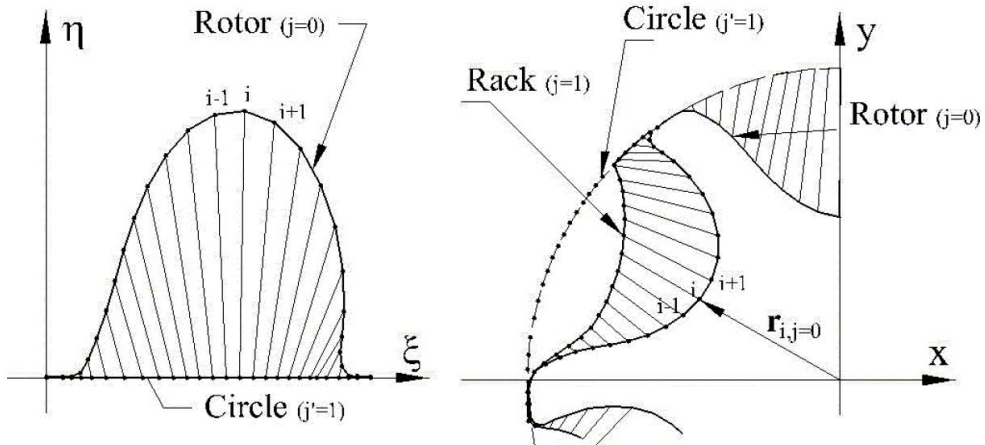
η_i' and ζ_i are related by the parameter k_i ,

$$\begin{aligned} k_i &= \frac{\eta_i'}{\zeta_i}, \quad 0 \leq k_i \leq \infty \\ \xi_i^* &= \xi_i - \eta_i \frac{\cos \alpha}{k_i \sin \alpha} \end{aligned} \quad (\text{D.13})$$

If $k_i \xrightarrow{\text{tends to}} \infty$, P_i corresponds to point i and there is no change in ξ_i .

If $k_i \xrightarrow{\text{tends to}} 0$, P_i is positioned on the ξ axis and will pull the nodes on outer circle towards itself.

In most profiles a factor of $k_i = 1$, regularises the distribution on the outer circle.



Reproduced from *Kovačević* (2002)

Figure D.6 Regularised distribution on the outer boundary

The inverse transformation of ξ coordinates to the circle in the physical domain is with the arc-length factor as in equation (D.14).

$$\mathbf{r}^*_{i,j'=1}(x, y) = \mathbf{r}_{I,j'=1} \frac{\xi_i^*}{\xi_I^*} \quad (D.14)$$

The rack points at ($j = 1$) are obtained by linear interpolation between corresponding points on the outer circle ($j' = 1$) and the rotor($j = 0$). This distribution is also regular as shown in Figure D.6.

D.4 Interior nodes distribution

Once the rotor profile and outer boundary distributions are tested for regularity of computational cells, the algebraic grid generation method uses transfinite interpolation for the distribution of interior nodes. TFI principle has been described in Appendix B.

The coordinates of points on the boundaries generated after adaptation can be written in vector form as equation.

$$\begin{aligned} \mathbf{a}_l(\eta) &= r(\xi_l, \eta), \quad l = 1, 2 \\ \mathbf{b}_l(\xi) &= r(\xi, \eta_l), \quad l = 1, 2 \\ \xi &= \frac{(i-1)}{(I-1)} \text{ and } \eta = \frac{(j-1)}{(J-1)} \end{aligned} \quad (D.15)$$

i and j denote point number on the physical coordinates while I and J are the overall number of points on these coordinates. By application of Simple TFI, the coordinates of the interior points are given by equation (D.15) (*Chawner and Anderson, 1991*).

$$r_1(\xi, \eta) = \sum_{l=1}^2 \alpha_l(\xi) \mathbf{a}_l(\eta), \quad (\text{D.16})$$

$$r(\xi, \eta) = r_1(\xi, \eta) + \sum_{l=1}^2 \beta_l(\eta) [\mathbf{b}_l(\xi) - r_1(\xi, \eta)]$$

And the blending functions satisfy the conditions,

$$\alpha_l(\xi_k) = \delta_{k,l}, \quad k = 1,2 \text{ and } l = 1,2$$

$$\beta_l(\eta_k) = \delta_{k,l}, \quad k = 1,2 \text{ and } l = 1,2$$

In Ortho TFI, in addition to the boundary points, the derivatives at these points are accounted. This gives orthogonality at the boundaries. By definition of Ortho TFI the coordinates of the interior points are given by equation (D.17).

$$r_1(\xi, \eta) = \sum_{l=1}^2 \sum_{n=0}^1 \alpha_l^n(\xi) \mathbf{a}_l^n(\eta),$$

$$r(\xi, \eta) = r_1(\xi, \eta) + \sum_{l=1}^2 \sum_{n=0}^1 \beta_l^n(\eta) \left[\mathbf{b}_l^n(\xi) - \frac{\partial^n}{\partial \eta^n} r(\xi, \eta_l) \right] \quad (\text{D.17})$$

$$\mathbf{a}_l^n(\eta) = \frac{\partial^n}{\partial \xi^n} r(\xi_l, \eta), \quad l = 1,2 \text{ and } n = 0,1$$

$$\mathbf{b}_l^n(\xi) = \frac{\partial^n}{\partial \eta^n} r(\xi, \eta_l), \quad l = 1,2 \text{ and } n = 0,1$$

And the blending functions satisfy the conditions,

$$\frac{\partial^n}{\partial \xi^n} \alpha_l^n(\xi_k) = \delta_{k,l} \delta_{n,m}, \quad k = 1,2 \ l = 1,2 \ n = 0,1 \ m = 0,1$$

$$\frac{\partial^n}{\partial \eta^n} \beta_l^n(\eta_k) = \delta_{k,l} \delta_{n,m}, \quad k = 1,2 \ l = 1,2 \ n = 0,1 \ m = 0,1$$

Some of the blending functions used in practise are:

- Lagrange Blending functions

$$\begin{aligned}\alpha_1(\xi) &= 1 - \xi, & \alpha_2(\xi) &= \xi, \\ \beta_1(\eta) &= 1 - \eta, & \beta_2(\eta) &= \eta\end{aligned}\tag{D.18}$$

- Hermite Blending functions with two boundary method

$$\begin{aligned}h_1(\eta) &= 2\eta^3 - 3\eta^2 + 1 \\ h_2(\eta) &= -2\eta^3 + 3\eta^2 \\ h_3(\eta) &= \eta^3 - 2\eta^2 + \eta \\ h_4(\eta) &= \eta^3 - \eta^2\end{aligned}\tag{D.19}$$

- Blending function based on Tension Spline interpolation

$$\begin{aligned}h_1(s) &= c_1(1-s) + c_2s + c_2 \left[\frac{\sinh[(1-s)\sigma] - \sinh(s\sigma)}{\sinh(s\sigma)} \right] \\ h_2(s) &= c_1s + c_2(1-s) + c_2 \left[\frac{\sinh[(1-s)\sigma] - \sinh(s\sigma)}{\sinh(s\sigma)} \right] \\ h_3(s) &= c_3 \left[(1-s) - \frac{\sinh[(1-s)\sigma]}{\sinh(\sigma)} \right] + c_4 \left[s - \frac{\sinh(s\sigma)}{\sinh(\sigma)} \right] \\ h_4(s) &= -c_3 \left[s - \frac{\sinh[s\sigma]}{\sinh(\sigma)} \right] - c_4 \left[(1-s) - \frac{\sinh[(1-s)\sigma]}{\sinh(\sigma)} \right]\end{aligned}\tag{D.20}$$

Where the coefficients are,

$$c_1 = 1 - c_2, \quad c_2 = \frac{\sinh(\sigma)}{2 \sinh(\sigma) - \sigma \cosh(\sigma) - \sigma}$$

$$c_3 = \frac{-\alpha}{(\beta^2 - \alpha^2)} \sinh(\sigma), \quad c_4 = \frac{\beta}{(\beta^2 - \alpha^2)} \sinh(\sigma),$$

$$\alpha = \sigma \cosh(\sigma) - \sinh(\sigma), \quad \beta = \sinh(\sigma) - \sigma,$$

As $\sigma \xrightarrow{\text{tends to}} \infty$, Blending functions are linear,

And as $\sigma \xrightarrow{\text{tends to}} 0$, Blending functions are cubic.

D.5 Grid orthogonalisation

The process of making grid lines in coordinate directions nearly normal to each other so as to reduce skewness of the cells is referred to as grid orthogonalisation. The orthogonalisation has to be considered at the boundary as well as the interior of the domain. Orthogonalisation procedure presented by *Lehtimaki* (2000) has been adopted by *Kovačević* (2002) in the algebraic grid generation for screw rotor grids.

The weighting factors used in Ortho TFI control the inclusion of boundary gradients in distribution of interior nodes. However they tend to overlap grid lines if the values selected are too large in some regions of the profile. Hence use of an explicit iterative orthogonalisation sequence with damping factor is a more robust approach for screw profiles. Figure D.7 represents the procedure. The initial grid is generated with simple TFI and Hermite blending functions.

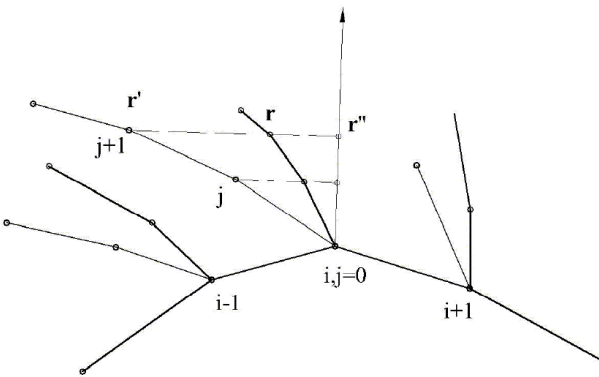


Figure D.7 Explicit orthogonalisation of grid lines

$r'_{i,j}$ are the initial position vectors of the nodes. $r''_{i,j}$ are the projections of the nodes on boundary normal at point i . A weighting factor $w_{i,j}$ is applied and new position is calculated between r' and r'' .

$$r_{i,j} = (1 - w_{i,j}) r'_{i,j} + w_{i,j} r''_{i,j}$$

$$w_{i,j} = e^{\left\{ -c_1 \left[\left(1 - \frac{\hat{\eta}_{i,j}}{\hat{\eta}_{i,j,\max}} \right)^{-2} - 1 \right] \right\}} \left[4 \xi_{i,0} (1 - \xi_{i,0}) \right]^{c_2} \quad (\text{D.21})$$

Where,

$$\hat{\eta}_{i,j} = \sqrt{(\xi_{i,j} - \xi_{i,0})^2 + (\eta_{i,j} - \eta_{i,0})^2} \text{ are arc lengths,}$$

c_1 – damping factor to the interior,

c_2 – damping factor at the boundaries.

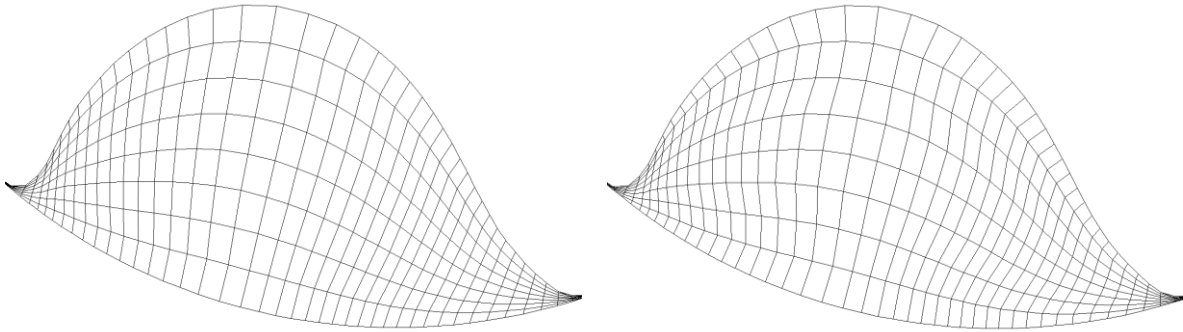


Figure D.8 Orthogonalisation of the gate rotor mesh

Figure D.8 shows the action of orthogonalisation of the gate rotor mesh. The factors c_1 and c_2 in equation (D.21) are decreased to increase the degree of orthogonalisation.

D.6 Grid smoothing

In the regions near top and bottom CUSP's, when the gate rotor transitions into the male rotor there is a sharp discontinuity between the main rotor casing circle and the rack curve. In algebraic interpolations such discontinuities get propagated into the interior node distributions and results in skewness of the cells. An iterative smoothing is applied on the grid in order to move the nodes locally in such regions and improve the cell skewness.

$$\begin{aligned} x_{i,j}^{n+1} &= x_{i,j}^n + c(x_{i+1,j}^n - 2x_{i,j}^n + x_{i-1,j}^n), \\ y_{i,j}^{n+1} &= y_{i,j}^n + c(y_{i+1,j}^n - 2y_{i,j}^n + y_{i-1,j}^n) \end{aligned} \quad (\text{D.22})$$

c is a relaxation constant such that $c \leq 0.5$ for stability in each iteration and $N = 0, 1, 2, \dots, N$ are the number of smoothing iterations.

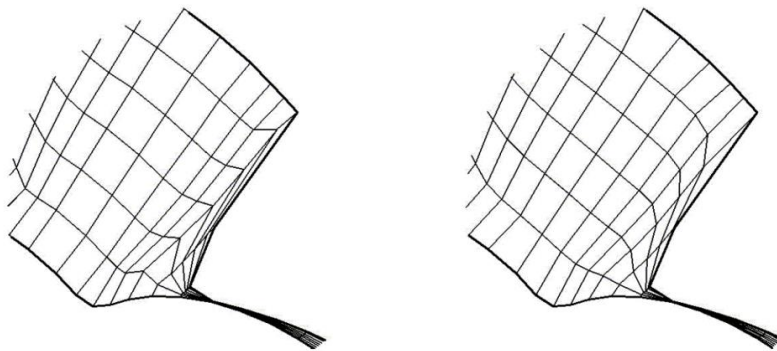


Figure D.9 Influence of iterative smoothing on grid lines

Figure D.9 shows the influence of smoothing in one of the critical regions of the mesh.

With these techniques of boundary regularisation, TFI for interior node distribution followed by orthogonalisation and smoothing, a good quadrilateral cell structure can be constructed in the 2D cross sections of the rotor. Data from 2D cross sections is then combined together to construct the full 3D grid representing the main and gate rotor position. In order to simulate the rotation of the rotors, a set of such 3D grids need to be generated with successive increments in the rotor position and provided to the flow solver during numerical analysis.

Appendix E. Differential approach for Grid Generation of Twin Screw Rotors

E.1 Solution of the Laplace equation

As an example, the boundary conditions for Laplace equation are specified potentials on the rotor curves and on the casing curves as

$$\nabla^2 \phi = 0,$$

With,

$$\phi = 0, \quad \text{Casing} \quad (\text{E.1})$$

$$\phi = +1, \quad \text{Main Rotor}$$

$$\phi = -1, \quad \text{Gate Rotor}$$

The solution is obtained in CFX solver and represented as iso-potential lines in Figure E.1.

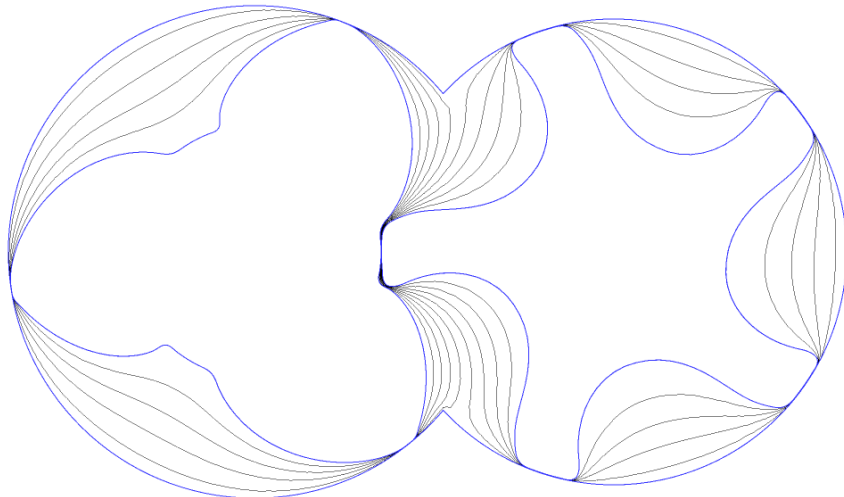


Figure E.1 Solution to Laplace equation with fixed boundary conditions

These iso-potential lines have very favourable characteristics from the point of requirements of grid generation.

- The iso-lines never cross each other.
- They are geometrically well aligned with the boundaries of the domain, which in this case are the two rotor profiles and the casing.

- Iso-potential lines are orthogonal to the gradient lines. The gradient lines are also orthogonal to the boundaries.
- If there are discontinuities on the boundaries, these do not propagate strongly onto the interior iso-lines.

Thus, if the grid points are defined at the intersection of the iso-potential and gradient lines; a naturally smooth mesh will result.

There are a few disadvantages when the method is applied to twin rotor domains.

- The Laplace solution with constant boundary conditions does not produce a unique partition between the two rotors which passes or meets at the top and bottom CUSP points. As seen in Figure E.1, there are discontinuities at the bottom CUSP and if an iso-potential line is extracted at $\emptyset = 0$, it will pass smoothly between the two rotors, but will not meet tangentially to the casing at the CUSP points.
- Because of the nature of the solution, iso-potential lines tend to sparse near convex curves and large spacing are observed between the profile and the adjacent iso-potential lines in the root of the main and gate rotors.
- In Winslow and Crowley's adaptation, no solution was explicitly calculated for the Laplace equation. But in case of screw rotor geometries, a complete solution is required on a very refined mesh. Thus the grid calculation is time consuming.

Vande Voorde et al. (2004) have used a dynamic boundary condition for the potential on the casing in order to get the iso-potential lines at top and bottom CUSP to be produced nearly tangential and coincide with the CUSP points. These iso-potentials are different at the top and bottom and are smoothly connected with the central iso-potential curve at $\emptyset = \emptyset_D$. A transition function is defined in order to establish this division line as shown in Figure E.2. Moreover with the modified potential, the casing is no longer an iso-potential line and some iso-lines can merge with the casing. The transition from top CUSP potential \emptyset_T to bottom CUSP potential \emptyset_B through the central potential \emptyset_D is a combination of segments defined as equation (E.2) and represented in Figure E.2.

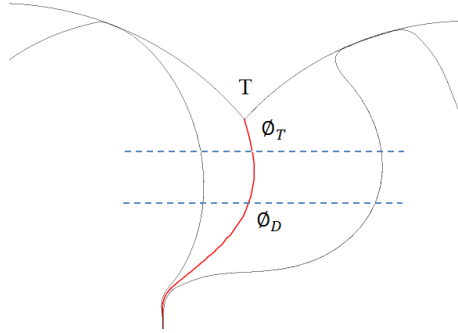


Figure E.2 Transition of division line

$$\begin{aligned}
 y \leq 0, \quad & \emptyset = \emptyset_B \\
 0 \leq y \leq Y_B, \quad & \emptyset(y) = a_B \emptyset_B + (1 - a_B) \emptyset_D \\
 Y_B \leq y \leq Y_T, \quad & \emptyset = \emptyset_D \\
 Y_T \leq y \leq 1, \quad & \emptyset(y) = a_T \emptyset_T + (1 - a_T) \emptyset_D \\
 y \geq 1, \quad & \emptyset = \emptyset_T
 \end{aligned} \tag{E.2}$$

Where,

$$\begin{aligned}
 a_B &= 0.5 \left[1 + \cos\left(\frac{y}{Y_B} \pi\right) \right] \\
 a_T &= 0.5 \left[1 + \cos\left(\frac{(1-y)}{(1-Y_T)} \pi\right) \right]
 \end{aligned}$$

Using this definition the resulting division line splits the 2D domain into two O blocks where internal grid nodes can be distributed. The values of the parameters Y_B and Y_T determine the extent of transition in the division line from \emptyset_B or \emptyset_T to \emptyset_D . The transition in potential results in cell jump and should be limited but if the transition is sharp then the derivative $\frac{\partial \emptyset}{\partial y}$ is large and the curvature of the division line can become large which reduces the cell smoothness. The parameters Y_B and Y_T are defined as in equation (E.3).

$$Y_B = 1 - Y_T = C_1 \Delta x \tag{E.3}$$

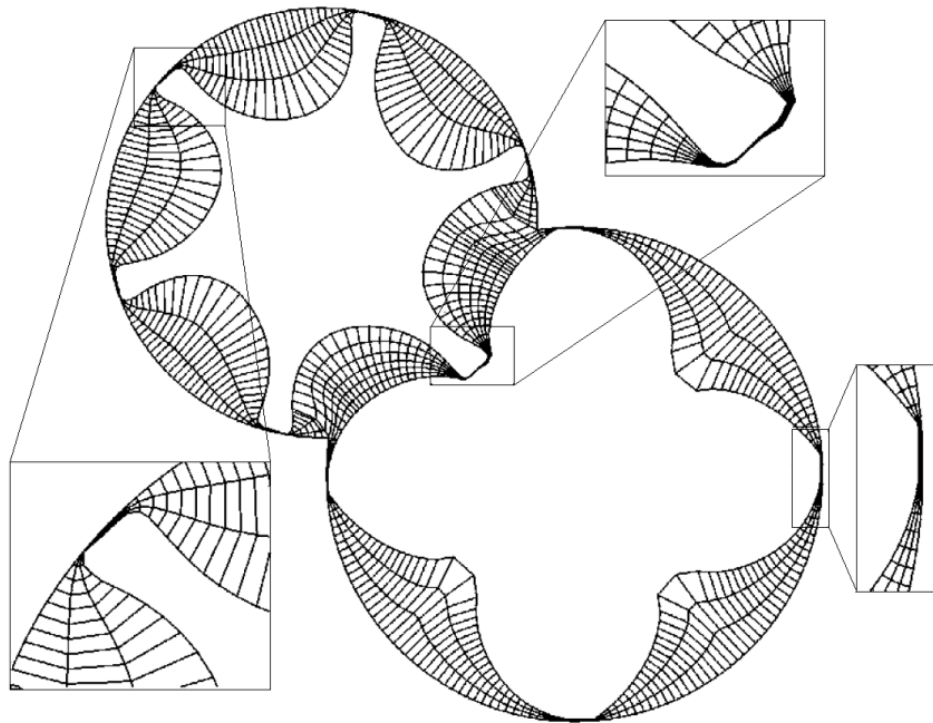
Δx is the horizontal distance from the CUSP to the iso-potential $\emptyset = \emptyset_D$. $C_1 = 1$ has been used in practise. The outer distribution start with discretisation of the division line and the casing curve using equidistant spacing. The nodes are identified by the tangential index i . These nodes have same radial index j . The tangential nodes on rotor profile and interior nodes are placed on gradient lines originating from every node on the outer boundary. Each grid node is identified

by the tangential and radial indices (i,j) . A grid face in 2D is defined by the nodes (i,j) , $(i+1,j)$, $(i+1,j+1)$ and $(i,j+1)$.

Figure E.3 presents the basic grid obtained in a twin screw rotor cross section with some details in the leakage gaps (*Vande Voorde*, 2004).

To improve the quality of the cells, the basic grid is modified by operations such as:

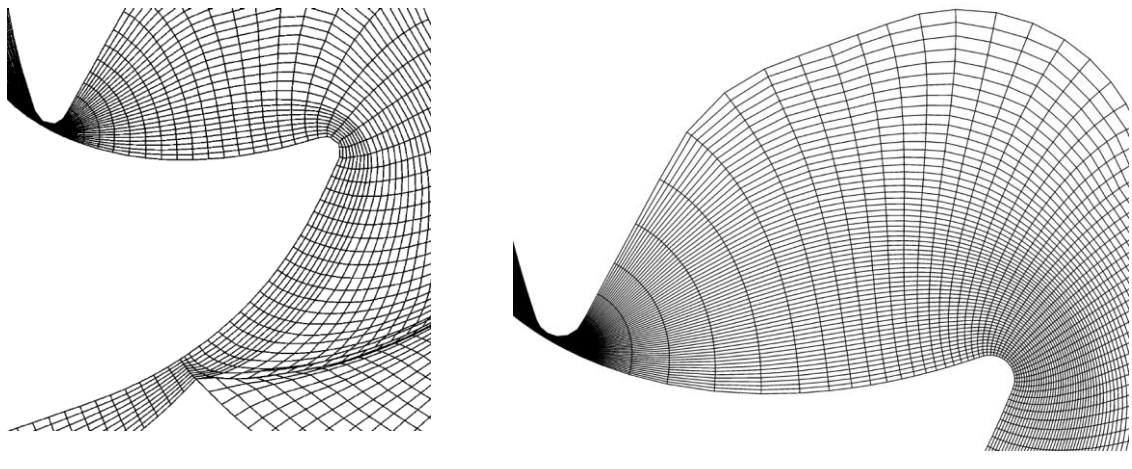
- Radial spacing with equidistant distribution on one O block and geometric distribution on the other O block for each node on the division line. The block with smaller size of an equidistant distribution is selected and this size is applied as the first distance of the geometric distribution in the other O block as shown in Figure E.4 a and b, for a double tooth compressor profile.



Reproduced from *Vande Voorde* (2005)

Figure E.3 Basic grid generated by the differential approach

- Tangential redistribution on the division line so as to concentrate more nodes in the region where rotor tips are present. The division lines radius of curvature is used as the adaptation criteria. To handle the differences in nature of rotor profiles, a damping factor is introduced in the adaptation. The influence is seen in Figure E.4b



Reproduced from *Vande Voorde (2005)*

Figure E.4 Radial spacing with geometric redistribution

- Aspect ratio and grid resolution in the rotor tips is improved by increasing the tangential nodes on the casing in these gaps.
- Local smoothing is applied to a zone consisting of few numbers of nodes tangential from the CUSP along the division line and all radial nodes with these tangential indices to avoid cells with high skewness. In the transition of the division line the potential changes from \emptyset_D to \emptyset_T or \emptyset_B . If the rate of change is high, the gradient lines at points on the division line come very close and this local smoothing relaxes the induced skewness.

With these techniques a good quality quadrilateral cell structure can be constructed in the 2D cross sections of the rotor. Data from 2D cross sections is then combined together to construct the full 3D grid representing the main and gate rotor position and a set of such 3D grids is provided to the flow solver during numerical analysis.